Departamento de
Mineralogía y Petrología

UNIVERSIDAD DE GRANADA

Physico-chemical decay of carbonate stones: the role of atmospheric aerosols and dissolution processes

TESIS DOCTORAL · PhD Thesis ·

Memoria de Tesis Doctoral presentada por Dña. Maja Urosevic
para optar al Grado de Doctor por la Universidad de Granada

Granada, 10 de junio de 2011

Fdo. Maja Urosevic

VºBº del Director

Fdo. Prof. Eduardo M. Sebastián Pardo

VºBº del Director

Fdo. Prof. Carolina Cardell Fernández

Editor: Editorial de la Universidad de Granada
Autor: Maja Urosevic
D.L.: GR 4524-2011
ISBN: 978-84-694-7760-3

Index

3. Methodology: analytical techniques and ageing tests

Appendix I

Ion-specific effects on the kinetics of mineral dissolution

Appendix II

Comparative study of dolomite dissolution rate measured by atomic force microscopy (AFM) and vertical scanning interferometry (VSI)

Appendix III

Assessment of limestone deterioration due to salt formation by micro-Raman spectroscopy: application to architectural heritage

Resumen

Esta Tesis Doctoral aborda el deterioro de rocas carbonatadas debido a procesos de disolución mineral y procesos físico-químicos de alteración desencadenados por su exposición a diferentes tipos de atmósferas (i.e. atmósferas urbanas contaminadas y ambientes costeros). Para ello se han caracterizado diferentes tipos de rocas carbonatadas empleadas en Andalucía en construcciones históricas y civiles actuales, así como para reemplazar materiales geológicos similares en diversos monumentos; en concreto se han estudiado la calcarenita de *Escúzar*, la caliza de *Sierra Elvira*, y el travertino *Olivillo*. El objetivo final de esta investigación es evaluar la idoneidad del uso de estas rocas como "piedra histórica en el Patrimonio Arquitectónico" y su durabilidad como material de construcción. En relación a esto último, se ha prestado especial atención a la modificación del sistema poroso en superficie de las rocas como consecuencia de su diferente terminado superficial, el cual desempeña un papel clave en la adhesión de aerosoles atmosféricos y el cambio de las propiedades mecánicas y estéticas de dichas rocas.

En primer lugar se ha realizado un exhaustivo estudio composicional, petrográfico y físico-químico de las rocas frescas, paso indispensable para poder establecer los cambios originados en las rocas envejecidas debido a diferentes experimentos de alteración (tanto bajo condiciones naturales de exposición como en ensayos de laboratorio). A continuación dicha caracterización se ha efectuado en las rocas envejecidas. En ambos casos se ha aplicado una variedad de técnicas analíticas, a saber: difracción y fluorescencia de rayos-X, microscopía óptica y microscopías electrónica de barrido y transmisión, ensayos hídricos y porosimétricos (i.e. porosimetría de mercurio y adsorción de gases), medidas cromáticas y de propagación de ultrasonidos, así como espectroscopía de infrarrojos por Transformada de Fourier en modo transmitancia y microscopía Raman.

Con objeto de evaluar el impacto de aerosoles atmosféricos procedentes de atmósferas contaminadas y ambientes marinos en las rocas carbonatadas estudiadas, se han realizado los siguientes estudios: i) la caracterización de contaminantes atmosféricos dentro y fuera del Monasterio de San Jerónimo (Granada) y su impacto en el deterioro de los materiales constructivos y decorativos que lo constituyen, ii) un experimento de envejecimiento

acelerado por sales marinas de rocas carbonatadas con distinto terminado superficial en una cámara climática, y iii) un experimento de exposición a largo plazo (ca. 2 años) de rocas carbonatadas en emplazamientos con diferente nivel de contaminación en la ciudad de Granada, con objeto de determinar su ennegrecimiento (*black soiling*). El grado de deterioro de estas rocas se ha estimado mediante la comparación, a diferentes escalas (nano, micro y macro), de los cambios composicionales, petrofísicos y cromáticos ocurridos entre el material de referencia (roca fresca de cantera) y las muestras envejecidas, mediante el empleo de técnicas analíticas complementarias. Además, se han estudiado la naturaleza y morfologías de las sales cristalizadas en las rocas, así como las partículas atmosféricas depositadas tanto en la superficie de las rocas carbonatas como en filtros específicos.

Una de las piedras carbonatadas usadas tanto con fines constructivos como decorativos en el Patrimonio Arquitectónico de la ciudad de Granada es la caliza de *Sierra Elvira*, que presenta cierto contenido en dolomita. Es sabido que la disolución química y los procesos de cristalización de sales solubles en piedras carbonatas de construcción desempeña un papel crítico en su deterioro. No obstante, los procesos físico-químicos involucrados en tal deterioro no son del todo conocidos, particularmente aquellos que conciernen al mineral dolomita. Con objeto de profundizar en el conocimiento de los procesos a nanoescala que gobiernan la interacción dolomita-fluido, se aborda en esta Tesis Doctoral una investigación sistemática *in situ* mediante la aplicación de una técnica novedosa, i.e. la microscopía de fuerza atómica (AFM). Se ha estimado la tasa de disolución de cristales de dolomita en el rango de pH = 3-10, puesto que a día de hoy no consta la publicación de estudios sobre la dependencia de la tasa de disolución de la dolomita con el pH.

Los resultados de esta Tesis Doctoral se discuten en el contexto del campo de la Ciencia del Patrimonio Cultural, con el deseo de que ayuden a establecer políticas de conservación/restauración adecuadas, así como estrategias de conservación preventiva del Patrimonio Arquitectónico construido con rocas carbonatadas. Por último, se presentan las conclusiones generales de este trabajo de investigación y las perspectivas de trabajo futuro.

Summary

This PhD Thesis deals with the deterioration of carbonate stones caused by mineral dissolution processes and physico-chemical weathering processes triggered by their exposure under diverse polluted environments (i.e. urban and marine conditions). To this end, different carbonate stones used to replace similar historic geological materials in monuments in Andalusia, as well as employed in present civil buildings, have been characterized, namely *Escúzar* calcarenite, *Sierra Elvira* (dolomite-bearing) limestone and *Olivillo* travertine. The final goal of this investigation is to evaluate the Cultural Heritage suitability of these stones and their endurability as building materials. In this regard, special attention was paid in the stone pore network modification near surface due to different commercial stone surface finishings, since they play a key role in the uptake of atmospheric aerosols and a major impact on stone mechanical and aesthetic properties.

First, a detailed compositional, petrographic and physico-mechanical characterization of the fresh stones was carried out, which was indispensable for comparing with changes produced on aged stones after different ageing tests (under natural and laboratory conditions). A comprehensive examination was performed by applying on both fresh and aged stone samples a multianalytical approach comprising: X-ray diffraction, X-ray fluorescence, optical microscopy, scanning and transmission electron microscopy, hydric tests, mercury intrusion porosimetry, gas adsorption, ultrasounds and chromatic measurements, transmission-Fourier Transform infrared spectroscopy and micro-Raman spectroscopy.

To address the impact of atmospheric aerosols from polluted and marine environments in the studied carbonate stones, several investigations were carried out: i) the effect of indoor and outdoor atmospheric pollutants in the deterioration of the construction and decorative materials used in the San Jerónimo Monastery (Granada), ii) an *ad hoc* sea-salt ageing test conducted in a controlled-atmosphere chamber, and iii) a long-term ageing tests (ca. 2 years) where stones were exposed under the Granada urban air in different polluted sites to determine their black soiling.

The degree of stone weathering was estimated by comparing changes at macro-, micro- and nanoscale of chemical and mineralogical composition, petrophysical characteristics and chromatic variations between freshly quarried and aged carbonate stones. As well the nature and morphology characteristics of precipitated salts, and the atmospheric particles deposited on aged stone surfaces and on particulate matter filters were studied combining complementary analytical techniques.

Part of the Architectural Heritage of the city of Granada is built with a dolomite-bearing limestone (*Sierra Elvira* limestone). Chemical dissolution and crystallization of soluble salts in building carbonate stones play a critical role in their decay. However the physico-chemical process behind it is not completely understood particularly in the case of the dolomite mineral. To improve our knowledge of the nanoscale processes governing dolomite-fluid interactions, a systematic *in situ* Atomic Force Microscopy (AFM) study was performed in this PhD Thesis. Dissolution rate of dolomite was estimated in the pH range 3-10 since all previous nanoscale studies were conducted at fixed pH conditions and, to date, a systematic study of the dependence of dissolution rates on pH, such as in the case of macroscopic flow-through or batch reaction experiments have been not reported.

The results obtained in this PhD Thesis are discussed in the context of the Cultural Heritage Science field, with the wish to help planning suitable conservation/restoration building stone policies, and preventive conservation strategies for the protection of our invaluable Cultural Heritage. Finally, general conclusions and future work perspectives are presented.

Aims of the Thesis

The main aim of the present PhD Thesis is to contribute to the knowledge of the physico-chemical decay of carbonate stones caused by air pollution and mineral dissolution processes. Particularly, this study has been focused on the following goals:

- To characterize fresh quarried carbonate stones and thus 'unaltered' material, customary used in the Architectural Heritage of Granada. This step is essential to unambiguously appreciate changes induced by stone exposure to polluted urban conditions. A multianalytical approach has been followed to address this goal including a detailed porous network characterization, measurements of elastic properties by using ultrasonic waves, and chromatic measurements among others.

- To monitor and characterize for the first time the indoor/outdoor atmospheric aerosol composition which affects one outstanding architectural monument in the city of Granada, i.e. the San Jerónimo Monastery. The aims of this study were: (a) to relate the composition of atmospheric aerosols and their fluctuation in time with the observed decay patterns in construction/decorative materials in the monuments and (b) to propose conservation policies to mitigate the effect of atmospheric pollutants.

- To describe carbonate decay patterns due to both urban pollution and marine aerosols at different time and spatial scales through two different study approaches. The first approach consisted in reproducing experimentally carbonate stone weathering under marine environment in an accelerated laboratory test by using a climatic chamber. The second approach was to study carbonate stone decay *in situ* through a long-term ageing test (2 years) by placing fresh stone tablets in different sites of the city of Granada. The exposed stone surfaces were characterized as well as particulate matter deposited on filters. This approach has enabled for the first time to determine real weathering rate of carbonate stones in the city of Granada.

- To shed light on the impact of different stone surface finishing in the modification of stone pore network at the near surface and the uptake of aerosols, with a major impact on the stone mechanical and aesthetic properties, and thus on their response to decay.

- To provide new experimental dissolution rate data for dolomite (an important constituent of certain carbonate building stones in the city of Granada) under contrasting pH conditions. To address this topic cutting-edge techniques (atomic force microscopy, AFM, complemented with vertical scanning interferometry, VSI) were used to survey at nanoscale mineral-solution interactions.

- To discuss the implications of all observations and results obtained in this PhD Thesis in the context of Cultural Heritage Science field. The final goal is to better identify problems related to atmospheric aerosols and chemical weathering of carbonate stones which may help proposing suitable conservation policies in the future.

Structure of the Thesis

This PhD Thesis starts with some introductory concepts, presented in Chapter 1, that are relevant to focus the studied problems. Chapter 2 contains the description of stone materials and atmospheric aerosols in the city of Granada. In Chapter 3 the methodology and analytical techniques used in this PhD Thesis are presented. The main body of the text comprises several chapters, i.e. from Chapter 4 to Chapter 9. Each chapter tackles a specific topic related to characterization and weathering of carbonate stones. Briefly, Chapter 4 presents the compositional and physical characteristics of the carbonate stones studied in this PhD Thesis. Chapters from 5 to 9 deal with carbonate stone decay processes due to atmospheric pollutants, marine environment and chemical weathering on dolomite surfaces. Several chapters have been published or submitted for publication to international peer-reviewed journals. A short outline of these chapters is given below for an easier reading of the text. Finally, general conclusions, afterthoughts and future work perspectives are presented.

Chapter 4: '*Physical properties of carbonate rocks used as a modern and historic construction material in Eastern Andalusia, Spain*.' A detailed petrographic and physico-chemical characterization of two carbonate stones commonly used at present in construction in eastern Andalusia (Southern Spain) is presented. The characterization was used to establish their suitability to replace similar ancient geological materials. This chapter has been published in *Materiales de Construcción*, 2011, 61: 93-114.

Chapter 5: '*Characterization of indoor and outdoor atmospheric pollutants impacting architectural monuments: the case of San Jerónimo Monastery (Granada, Spain)*.' This chapter presents the investigation at micro- and nanoscale of indoor and outdoor nature and concentration of atmospheric gaseous pollutants, and composition, size and morphology of particulate matter in the monastery of San Jerónimo in Granada (Spain). This is the first air quality study performed in a monument in the city if Granada with the aim of developing a strategy for preventive conservation. This chapter has been published in *Environmental Earth Sciences*, 2010 (doi: 10.1007/s12665-010-0657-5).

Chapter 6: '*Rough and polished travertine building stone decay evaluated by a marine aerosol ageing test*.' Here, a laboratory ageing test using marine spray in a controlled-atmosphere chamber was applied to examine the implications of rough and polished travertine stone surfaces on their salt decay. The degree of salt damage was estimated by comparing changes in mineralogical composition, petrophysical characteristics and chromatic variations between freshly quarried and aged travertine samples. This chapter has been published in *Construction and Building Materials*, 2010, 24: 1438-1448.

Chapter 7: '*An experimental study on sea spray-induced decay in rough and polished low-porous limestone.'* This chapter deals with a laboratory sea-salt ageing test conducted in a climatic chamber to examine the weathering decay in a low-porous dolomite-bearing limestone (*Sierra Elvira* limestone) widely used as building and decorative stone in Andalusia. The aim was to characterize the precipitated crystalline phases and their morphological variations, and to explore different deterioration behaviors due to contrasting finishings of stone surfaces. This chapter has been submitted to *Construction and Building Materials* (February 2011).

Chapter 8: '*In situ, nanoscale observations of the dissolution of {10-14} dolomite cleavage surfaces.*' It is presented a systematic *in situ* AFM study of dolomite dissolution conducted in the pH range from 3 to 10 aimed to improve our knowledge of the nanoscale processes governing dolomite-fluid interactions. A better understanding of the kinetics and mechanisms of dolomite dissolution at different pH is essential to determine the contribution of dolomite-fluid reactions to the global carbon cycle and CO_2 sequestration strategies, and to design new methods to mitigate the effects of acid rain on carbonate stones. This chapter has been submitted to *Geochimica et Cosmochimica Acta* (April 2011).

Chapter 9: '*Black soiling of an architectural limestone during a long-term urban polluted air exposure in the city of Granada (Southern Spain)*'. This chapter tackles the *Escúzar* calcarenite decay process due to the impact of Granada urban atmosphere during a long-term exposure of ca. 2 years. The soiling process (surface blackening) on the stone surfaces was monitored through chromatic variations (i.e. lightness). Atmospheric particles deposited on the aged stone surfaces and on particulate matter PM10 filters were studied at macro-, micro-

and nanoscale through a multianalytical approach. Cleaning policies can be better planned based on the valuable data obtained in this work. This chapter has been submitted to *Science of the Total Enviroment* (May 2011).

Chapter 1

INTRODUCTION

1.1. Heritage Science field

The development of a scientific approach to address questions of '*Archaeometry*' and '*Conservation*' in Cultural Heritage has received a great attention in the last decades. Certainly, the study of Cultural Heritage is a complex and challenging discipline which involves a broad spectrum of knowledge, classically dealing with Geology, Chemistry, Physics, Biology and Engineering. More outstanding is the fact that this scientific approach must be in symbiosis with archeologists, restorers, architects and art historians to full take advantage of theirs own expertise (e.g. Chiari, 2000; Doehne & Price, 2010). Following the UNESCO definition, 'Cultural Heritage' encompasses several main categories of intangible and tangible heritage that goes from *movable* (e.g. paintings, sculptures, coins and manuscripts), *immovable* (e.g. monuments and archaeological sites) and also underwater cultural heritage (as shipwrecks, underwater ruins and cities). In this work we will restrict ourselves to the movable and immovable Cultural Heritage made of natural stones, more precisely of carbonate stones as it will be described in the following chapters. The role of researchers dealing with Cultural Heritage typically combines a field work and monitoring in a restoration project with a laboratory research approach where representative samples are aged at short timescales compared to nature. Noticeable challenges arise when comparing the results obtained from these two approaches due to the contrasting temporal and spatial scales. The research in the Cultural Heritage field is, therefore, a continuous effort made by a

large scientific and non-scientific community to overcome these obstacles and efficiently preserve this legacy to the future generations (Fig. 1). Earth scientists are actively involved in this goal through the coined term *Environmental Mineralogy* which provides a broad range of analytical and experimental methods (see Vaughan, 2000 and Wogelius & Vaughan, 2000 for a comprehensive review of the scope and analytical methods of this research field). Recently, Buseck (2010) also encouraged geoscientists to take part in atmospheric sciences (largely left to chemists and physics) which, as we will see later, plays a capital role in the preservation of the Cultural Heritage.

As stated before, natural stone – made of mono- or poly- aggregates of minerals – forms an important part of the majority of the historical buildings and is especially prone to decay due to several natural and anthropogenic factors. Stone weathering is the natural and unavoidable response of its constituents to new environmental conditions which differ from that prevailed during its formation (i.e. during diagenesis, metamorphism or magmatism). *Weathering* is defined as a complex interaction of physical, chemical and biological processes that alter the stone in some general or specific way and lead to its decay (Van Grieken *et al*., 1998; Siegesmund *et al*., 2002). In the Conservation field, weathering is considered as any process that results in a change of the physical or aesthetical properties of the stone that differ from those originally conceived. There are a large number of factors that contribute to the natural deterioration of stones including mechanical (e.g. frost action, thermal expansion, wetting and drying or salt decay), chemical (e.g. dissolution, oxidation or hydration) and biological processes. The relative importance of each natural factor varies according to climatic environmental conditions, the stone type, its preservation state and its location on the monument (Papida *et al*., 2000; Cardell *et al.*, 2003a).

In addition to natural processes, stones used in the Cultural Heritage are also exposed to an anthropogenic environment as they are frequently located in the polluted cities or close to them. The relationship between air pollution and stone weathering constitutes one of the subjects studied in this PhD Thesis. It is well known that stones are particularly vulnerable in urban conditions as they provide new sources of weathering agents that accelerate its deterioration rate (Fig. 1). For instance, it is widely known that motor vehicle emission

Figure 1. The restoration of the façade of St. Stephan's Cathedral (Vienna, Austria) is an outstanding example where optimal conservation procedures are essential to preserve the Cultural Heritage. Compare the restored (right) with the aged façade (left).

certainly contributes to the sulfatation of limestone that results in the unaesthetic formation of black crusts and its irreversible deterioration (Rodríguez-Navarro & Sebastián-Pardo, 1996; Van Grieken *et al.*, 2000; Esbert *et al.*, 2001; Moropoulou *et al.*, 2001; Grossi *et al.*, 2003). Such layers of black crusts represent the accumulation areas on the material surface where the deposition of atmospheric gas and aerosol particles takes place. Although part of the Cultural Heritage such as mural paintings and polychromes are preserved from outdoor polluted environment inside buildings, indoor-outdoor air exchange may led to relatively

high gas concentrations. For instance, Kontozova-Deutsch and co-workers (2008) found that the mean concentration of NO_2 was higher at indoor that outdoor (30 $\mu g/m^3$ versus 17 $\mu g/m^3$ respectively) in the Basilica Saint-Urbain in Troyes (France). High concentration of NO_2 may result in severe weathering such as metal corrosion and pigment fading and carbonate dissolution due to formation of nitric acid. Therefore outdoor and indoor microclimatic conditions need to be monitored when integral conservation policies are required.

1.2. Influence of petrophysical properties and surface finishing in stone decay

Petrophysical properties are intrinsic key factors controlling stone decay and are frequently measured by means of several techniques for material characterization (see sections 3.1. and 3.2). Analysis of mineralogical and especially non-compositional petrophysical properties (e.g. texture and pore system) of building and ornamental stones used in the architectural heritage is essential to understand the main factors of decay under real environmental conditions (Hammecker, 1995). Moreover this characterization is also crucial for restorers and conservators to better design replacement strategies when a deteriorated stone building of cultural interest needs to be repaired. Additionally most of the historical quarries commonly used to provide material for architectural purposes have been unavoidable closed or its exact location is nowadays unknown or uncertain. Therefore, the restores are urged to look for new currently exploited materials that need to be characterized and quantitatively compared with those which are going to be replaced (Winkler, 1994; Galán *et al.*, 1999; Gómez-Heras & Fort, 2004; Fort, 2006, 2008; Siegesmund & Snethlage, 2011).

Several surface finishings are provided by manufactures as e.g. polishing, glossing, honing, acid treatment, abrasion, flaming or hammering (Fig. 2). It has not been noticed until very recently that the commercial surface finishing not only affects the aesthetical properties of building stones but also certainly modifies their mechanical properties and thus their suitability for different purposes (Fort, 2008; García del Cura *et al.*, 2008). These properties are essential to eventually define their position and use (e.g. for pedestrian or vehicle traffic).

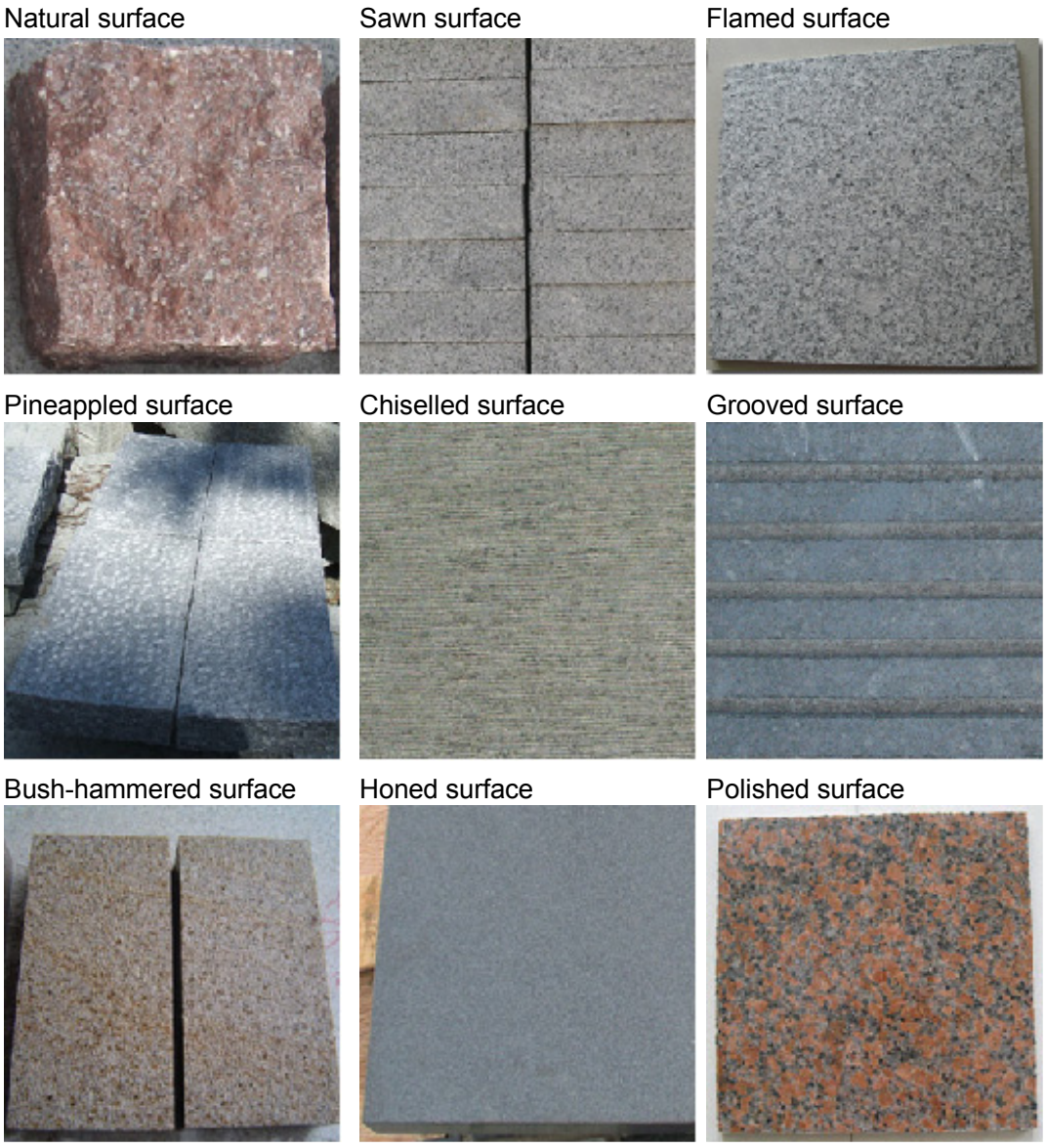

Figure 2. Several commercial surface finishings on granite.

Moreover, the commercial finishing treatment modifies the color of a building material by changing the surface roughness or due to gloss treatments (e.g. García-Talegón *et al.*, 1998; Benavente *et al.*, 2003, García del Cura *et al.*, 2008). For instance, Benavente and co-workers (2003) found that perceptible changes in lightness and chroma but not in hue were induced during the initial stage of surface polishing. Regarding to mechanical properties,

García del Cura *et al.* (2008) observed that the surface finishing treatment may modify in different ways the flexural strength, slip and abrasion resistance depending on the stone type.

Less known is, however, the direct effect of the finishing treatment on the modification of the stone pore network at the near surface due to pore occlusion, which has an important impact on its response to decay, especially in high porous materials (Demirdag, 2009). Roughness modifications of the stone surface due to commercial polishing processes also exert a major impact on the SO_2 uptake in polluted environments and thus on the black crust development (e.g. Bede, 2000). Based on hydric tests, García del Cura *et al.* (2008) suggested that the finishing treatment has nevertheless little influence on water sorption. Monitoring changes in the porous system due to the polishing process are however challenging by conventional techniques because of the unconstrained extending of the modification (which in most of the cases is very limited in depth). To overcome these difficulties, in this PhD research the modification of the stone pore network due to the polishing process has been evaluated based on the contrasting crystal morphologies of soluble salts deposited on the stone surfaces during the sea-salt ageing test (section 3.4.1.).

1.3. Atmospheric aerosols and stone decay: State of the art

The atmospheric environment and mechanisms occurring at the atmosphere-stone interface are key factors controlling stone weathering processes which have paramount cultural and economic consequences. The study of such processes in a polluted atmosphere have attracted the attention of intensive research during decades (e.g. Fassina, 1978; Del Monte *et al.*, 1981; Camuffo *et al.*, 1982, 1983; Sabbioni, 1995; Torfs & Van Grieken, 1997; Chabas & Lefevre, 2000; Charola & Ware, 2002; Mitchell & Searle, 2004; Brimblecombe & Grossi, 2005, 2007; Grossi & Brimblecombe, 2007; Watt *et al.*, 2009; Doehne & Price, 2010) and there are still challenging unresolved questions to be addressed (see recent monographs by Watt *et al.*, 2003, Doehne & Price, 2010 and Smith *et al.*, 2010). In fact, the effect of air pollution on stone decay is still a major problem in Europe even though the

acidic pollutant levels, such as SO_2, have been reduced since the early 1990s (Doehne & Price, 2010).

The direct effects of air pollution on stone decay received enormous attention from the mid-1970s to the early 1990 (Doehne & Price, 2010). Several international projects and conference meetings have been focused on the impact of air pollution on rates of stone soiling from the late 1980s. For instance, the SWAPNET (Stone Weathering and Atmospheric Pollution Network) is an association that brings together scientists from a wide spectrum of disciplines, including stone conservators, geologists, geomorphologists, microbiologists and others, that have special interest in monument heritage and rock weathering (Siegesmund *et al.*, 2008; Doehne & Price, 2010; Siegesmund & Snethlage, 2011). The main results on this topic have been included in the proceeding from several SWAPNET meetings (e.g. Smith & Warke, 1996; Jones & Wakefield, 1999; Přikryl & Viles, 2002; Smith & Turkington, 2004; Gómez-Heras, 2007). A reference conference meeting for Spain was held in Seville in 2003 (Saiz-Jimenez, 2004). In spite of the increasing interest on air pollution and Cultural Heritage only scarce research works on this matter has been conducted in southern Spain (Bernabé *et al.*, 2005), and none in the city of Granada although this city is well known for its outstanding architectural legacy. The aerosol monitoring is essential to unravel the link between the nature of the aerosols and the stone decay response. Recently integrated projects have provided reliable aerosol data which specifically address the link between air pollution and Cultural Heritage preservation in Granada (Kontozova-Deutsch *et al*., 2010, at the San Jerónimo monastery, and Horemans *et al.*– submitted – at the monumental complex of the Alhambra in the framework of the bilateral Hispano-Flemish project '*Assessment of atmospheric environmental risks related to artworks in the UNESCO World Cultural Heritage complex of Alhambra (Granada, Spain) with the emphasis on the analysis of a unique collection of authentic pigment samples*').

The rationale behind the study of the impact of atmospheric aerosols on stone decay and Cultural Heritage conservation is schematically summarized in Fig. 3, which has been, in part, followed in this PhD Thesis.

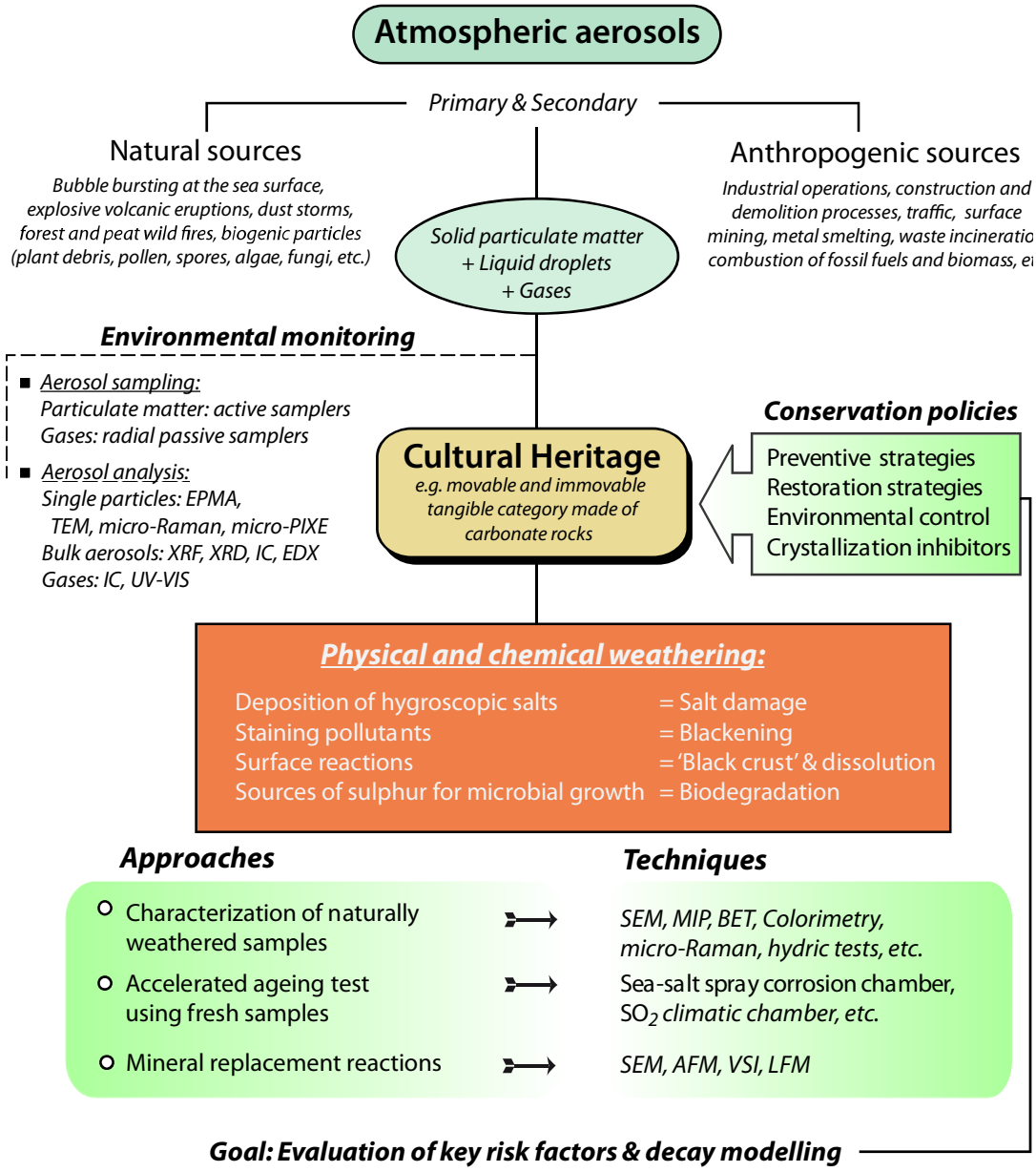

Figure 3. Flow chart summarizing the interactions of atmospheric aerosols with the Cultural Heritage, its sources, its consequences, and the approaches and related techniques that can be followed to address conservation strategies. Analytical techniques abbreviations: EPMA (electron probe microanalyser), TEM (transmission electron microscopy), micro-PIXE (proton induced X-ray emission), XRF (X-ray fluorescence), XRD (X-ray diffraction), IC (ion chromatography), UV-VIS (ultraviolet-visible spectroscopy), EDX (energy-dispersive X-ray spectroscopy), SEM (scanning electron microscopy), AFM (atomic force microscopy), VSI (vertical scanning interferometry), LFM (lateral force microscopy).

The danger to the Cultural Heritage from air pollution comes from several main sources such as the increasing of corrosion induced by gases from the atmosphere or the soiling of light colored surfaces due to black particles (e.g. Grossi *et al.*, 2003 and Hamilton & Crabbe, 2009). The main mechanism of the former occurs when acid chemicals are incorporated into the rain, snow, fog or mist. Sulfur dioxide, SO_2, and nitrogen oxides, NO_x ($NO + NO_2$) are largely products of domestic and industrial fuel burning. These oxides are related to two strong acids: sulfuric acid and nitric acid which are the major agents of the coined term *'acid rain'* (e.g. Grossi *et al.*, 1995, 1999; Charola, 2002; Cardell-Fernández *et al.*, 2002; Delalieux *et al.*, 2002). Sulfur dioxide is very reactive and a corrosive agent known as the main pollutant involved in stone decay (Van Grieken *et al.*, 1998; Böke *et al.*, 1999, 2002; Grossi *et al.*, 2003; Luque, 2010). High concentration of sulfur dioxide in the atmosphere results in sulfate formation from reaction between SO_2 gas and a carbonate-rich surface in humid conditions (e.g. Camuffo *et al.*, 1982, 1983, 1984; Del Monte *et al.*, 1997). Due to high relative humidity and oxidizing conditions, sulfur dioxide reacts with calcite ($CaCO_3$) present in carbonate-rich stones and produces calcium sulfite hemihydrate ($CaSO_3 \cdot 0.5H_2O$) and gypsum ($CaSO_4 \cdot 2H_2O$) (Böke *et al*., 1999, 2002). Most probably, the main process (not yet well constrained) is the heterogeneous oxidation of sulfur dioxide on the stone surface or alternatively before the pollution reaches the stone. Depending on the relative humidity and the pluviometry, the gypsum layer can be washed away and the surface recedes (often at a rate of 10 μm/year or more, according to Van Grieken *et al.*, 1998), since gypsum is more soluble in water than calcite. On the contrary, in areas protected from rain or in drier environments, gypsum starts to accumulate at the surface or inside the stone porous network and forms dense black crusts (Fig. 4).

This black crust development is usually associated with the surface deposition of complex mixtures of atmospheric particulates derived from the combustion of fossil fuels together with a range of environmental dusts, including marine aerosols, a variety of salts and microbial fauna. The blackness of these gypsum crust layers are commonly explained by absorption of carbonaceous particles such as soot. Additionally, it has been discussed that carbon soot and metal-rich particles (e.g. V, Fe, Ni, Cu, Mn and Cr-rich particles derived

Figure 4. Black crust development on the carbonate stone surface of one decorated column of the Cathedral of Granada (*Portada del Perdón*) due to atmospheric pollution (left). The same column after the cleaning process (right).

from anthropogenic sources) exert a critical catalytic action in the oxidation of SO_2 (Camuffo *et al.*, 1984; Rodríguez-Navarro & Sebastián-Pardo, 1996; Maravelaki-Kalaitzaki & Biscontin, 1999; Böke *et al.*, 1999, 2002; Maravelaki-Kalaitzaki, 2005), although the additional catalytic effect of bacteria is not discarded. Moreover, when dolomite $CaMg(CO_3)_2$ occurs in the substrate the resulting crust is more complex and comprise also epsomite, $MgSO_4 \cdot 7H_2O$ (Gauri *et al*., 1992; Gauri & Bandyopadhyay, 1999).

It is widely known that the growth of these types of sulfate salts in pores of stones generate stresses that can lead to serious damage (e.g. La Iglesia *et al.*, 1994; Cardell, 1998; Rodríguez-Navarro & Doehne, 1999; Scherer, 1999; Cardell *et al.*, 2003a; Angeli *et al*., 2007, 2008; Ruiz-Agudo *et al.*, 2007). Salt weathering is, thus, tightly associated with atmospheric pollution and has been the subject of intensive research over the last few decades. A substantial literature exists describing the phenomena associated to salt decay in a variety of individual monuments and building (for a comprehensive review the reader is referred to Evans, 1970; Charola, 2000; Doehne, 2002 and Doehne & Price, 2010 and references therein).

Carbon dioxide, CO_2, is by far the most abundant of all atmospheric gases generated by human activities. Carbon dioxide dissolves in rainwater, forming bicarbonate and carbonate acids which are regarded as a minor culprit in stone decay. Nevertheless, relative importance

of these acids compare to sulfuric, nitric, or other acidic species remains controversial (Lipfert, 1989; Charola & Ware, 2002; Cardell-Fernández *et al.*, 2002; Delalieux *et al.*, 2002). Modest amounts of nitrate are found on stone surfaces, although nitrogen oxides form a significant part of the urban pollute atmosphere. The scarcity of $Ca(NO_3)_2$ on carbonate stones is probably also due to its high solubility in water (Van Grieken *et al.*, 1998). Notwithstanding, the most important role of nitrogen oxides is in the catalytic oxidation of SO_2 at high relatively dry conditions, although the effect of NO_x on SO_2 reactions are poorly understood (Doehne & Price, 2010).

Comparatively less work have been done on the direct effect of marine aerosols on stone decay (however see for example Fassina, 1978; Moropoulou *et al.*, 1995; Zezza & Macri, 1995; Torfs & Van Grieken, 1997; Theoulakis & Moropoulou, 1999; Zendri *et al.*, 2000, 2001; Chabas & Jeannette, 2001; Cardell *et al.*, 2003a, 2003b, 2008; Silva *et al.*, 2007; Silva & Simão, 2009; Angeli *et al.*, 2010). An outstanding exception is the development of honeycomb and tafoni morphologies which seems to be clearly related with a combined effect of wind and salt crystallization with minor chemical weathering (e.g. Rodríguez-Navarro *et al.*, 1999). This combination is obviously enhanced in coastal areas but its effect on inland regions could be also important (Cardell *et al.*, 2003a; Rivas *et al.*, 2003; Anwar Hossain *et al.*, 2009). It is worth to note that naturally produced particulate matter, sea salt and mineral dust (mostly from deserts) are the largest contributors to the global aerosol flux mass (10,130 and 1600 Tg/y, Tg = 10^{12} g, Gieré & Querol, 2010, their Fig. 6, based on Andreae & Rosenfeld, 2008 and Durant *et al.*, 2010). For comparison, primary and secondary anthropogenic particulates are estimated in ~150 Tg/y and ~140 Tg/y respectively. The development of black crust in chemically unrelated substrates such as granites, clearly confirms the importance of atmospheric particulate as sulfate carriers (Prieto *et al.*, 2007; Silva *et al.*, 2009). As a matter of fact, sulfates are major constituent of particulate matter carried by the atmosphere even in non-polluted cities as e.g. Oviedo (northern Spain) studied by Rodríguez *et al.* (2009). Moreover, the atmosphere transports both bioaerosols and food sources for microbial communities such as sulfates. The link between atmospheric aerosols and biodeterioration is, in fact, a promising and still developing research area.

1.3.1. Aerosol particles

The atmosphere of the Earth is a colloidal system that contains a dispersion of particulate matter (solid particles and liquid droplets) suspended in a gas phase. The term aerosol refers to both particulate matters (PM) and gas. PM occur in both the troposphere and the stratosphere and contain small liquid and solid particles in suspension (sub-micron to several microns in size) in the atmosphere. Aerosol particles are ubiquitous and play a pivoting role in the physics and chemistry of the atmosphere and therefore on Earth heat balance, weather, climate, ecosystem processes, and human health (e.g. Pósfai & Molnár, 2000; Buseck *et al.*, 2000; Horemans *et al.*, 2008; Giére & Querol, 2010). Aerosol particles also contribute to atmospheric acidity which, as it will be discuss later, has a paramount adverse effect on carbonate stone weathering. Mineral particles are, by mass, major constituents of aerosols. Their sizes, shapes, composition, and degree of agglomeration can all be determined using transmission electron microscopy (Buseck, 2010). Nevertheless, a difficulty is that deliquescent species lose their water in the vacuum of the electron microscope and therefore these important aerosols types dehydrate and change their character.

The concentration and size distribution are crucial factors that govern the physical and chemical behavior of aerosol particles. The size of aerosol particles is usually given as the diameter (d) of the particle (assuming a spherical shape[1]) and ranges from several nanometers (representing the smallest clusters of atoms and molecules that can be classified as particles) to some tens of micrometers (the largest particles that can be suspended in the air), varying over five orders of magnitude. The sizes of particles from different sources formed by different processes follow distinct log-normal distributions (Fig. 5). Physical size distributions can be characterized by a model consisting of several additive log-normal distributions partially overlapping (*nucleation mode*, *aitken mode*, *accumulation* and *coarse*

[1] Transmission electron microscope (TEM) observations show that the aerosol shape is actually rarely spherical (Buseck, 2010).

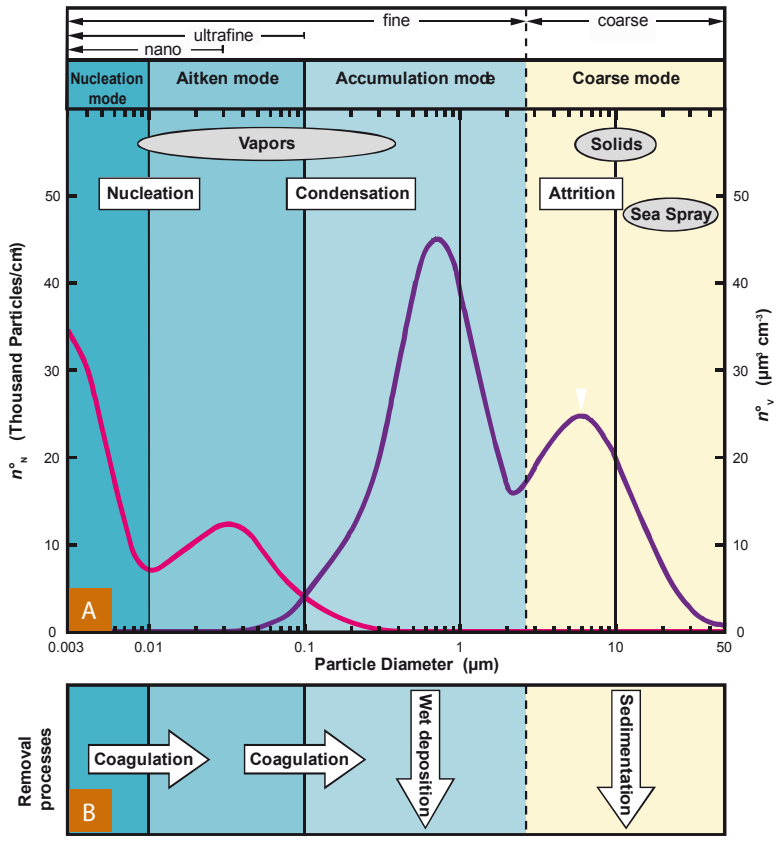

Figure 5. (a) Typical size distributions of the number (n^0_N, magenta line) and the volume (n^0_V, purple line) of atmospheric particles per cubic centimetre of air. Source materials of particles shown in grey ellipses; formation processes of particles shown in white rectangles. **(b)** Particle removal processes. Compiled by Giére & Querol (2010) from several sources.

mode). Particles with d < 2.5 µm ($PM_{2.5}$)[2] are generally described as *fine* and those with larger diameters as *coarse* particles (Fig. 5).

Finer PM is further subdivided into three size fractions based on distinct characteristic and different formation processes. The *nucleation mode* contains particles with diameters from 0.003 to 0.01 µm; these particles result from gas-to-particle conversion, i.e. homogeneous condensation. Particles with d = 0.01-0.1 µm belong to the so-called *Aitken*

[2] Other authors who prefer a value of 1-2 µm for this boundary (e.g. Giére and Querol, 2010).

mode[3] and are formed mostly through coagulation of nucleation mode particles or condensation on them. Particulates belonging to these two modes are the most abundant, but due to their minuscule size, account only for minor proportion of the total PM volume or mass (Fig. 5). Aerosols in the accumulation mode (d = 0.1-2.5 μm) are generally produced by the coagulation of smaller particles and by the *heterogeneous condensation* of gas vapor onto existing aerosol particles. Owing to similar physical processes of formation, the chemical compositions of particles in the nucleation and accumulation mode are similar and constitute the class of fine particles (Fig. 5). The coarse mode (d > 2.5 μm) consists of particles formed by mechanical disintegration and fragmentation, and includes mineral dust, sea-salt, and biogenic particles. Particles from combustion sources also contribute to this size range.

The ideal size distribution shown in Fig. 5 can be dramatically modified in several environments. For instance, in urban areas the highest concentrations are usually observed, exhibiting a distribution dominated by ultrafine particles ($PM_{0.1}$) and a volume distribution with two distinct maxima (accumulation and coarse mode). Typical marine particles have a prominent volume maximum in the coarse fraction, whereas remote continental particles have a volume maximum in the accumulation mode.

Primary particle sources

Sea-salt particles constitute the major fraction of primary coarse particles under marine conditions (O'Dowd *et al.*, 1997). Most sea-salt particles results from the bursting of gas bubbles that reach the water surface although water droplets can also form directly from sea spray. The larger droplets fall back into the water, while the smaller ones remain airborne and can be transported over large distances and high altitudes (Delalieux *et al.*, 2006; Silva *et al.*, 2007).

[3] Named after John Aitken (1839-1919) who was a Scottish meteorologist, physicist and marine engineer and one of the founders of cloud physics and aerosol science.

Large amount of natural primary aerosol particles are additionally emitted on the continents particularly in arid and semiarid areas. The chemical nature of mineral dust particles reflects the composition of Earth's crust. The amount of continental dust is usually inferred from the aluminium content of the aerosol. The most active sources of dust plumes are distributed within the band that includes North Africa, the Middle East, and Central Asia. Satellite data indicate that African dust can be transported over very long distances bringing high 'background' aerosol concentration to large regions of the southern and eastern part of North America (Prospero, 1999). In the context studied here, it is important to note the significant and discontinuous transport of Saharan dust over the Mediterranean Sea depending on the presence of cyclones (Fig. 6). Saharan dust is transported by hot seasonal winds known as *calima* or *scirocco*. This transport is characterized by a regional extension all over the Mediterranean basin resulting in one of the highest dust accretion rates in the world (Dayan *et al.*, 1991; Díaz-Hernández & Párraga, 2008). The mineralogy of Saharan dust is remarkable constant due to well mixing of aerosols over the desert (Moreno *et al.*,

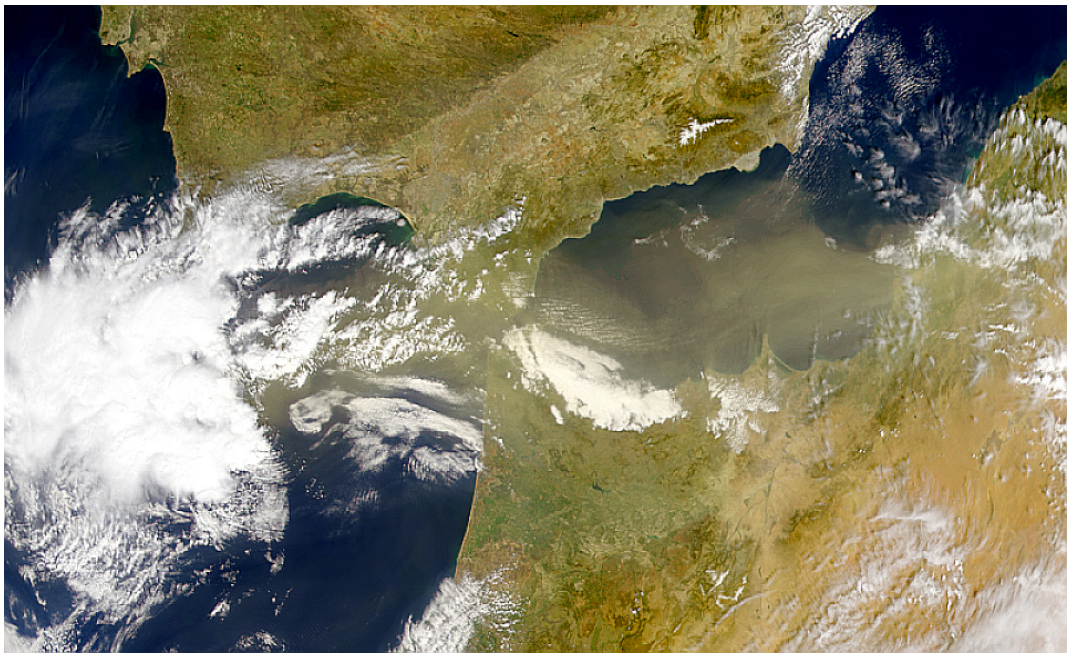

Figure 6. Dust storm blowing out over the Alboran Sea and Gibraltar from northern Africa. Image courtesy of the SeaWiFS Project, NASA/Goddard Space Flight Center, and ORBIMAGE. See http://visibleearth.nasa.gov/

2006). Moreover, Saharan dust delivered to Spain by red rains is comprised mainly of illite, quartz, smectite, palygorskite, kaolinite, calcite, dolomite and feldspar, in order of decreasing abundances (Avila *et al.*, 1997; Moreno *et al.*, 2006).

Díaz-Hernández & Párraga (2008) described a new type of spherical aerosol particle collected in the southern Iberian Peninsula which are larger and morphological different from classic atmospheric aerosols. These particles were called iberulites by these authors (Fig. 7). Iberulites are internally mixed and structured, mechanically generated, with diameter ranging from about 30 to 190 μm, with a low density (0.65 g cm^{-3}) and about 50% mean porosity. Their high specific surface makes them very reactive with atmospheric gases providing reaction sites for many heterogeneous reactions involving SO_2, HO_x and O_3. The appearance of iberulites is a discontinuous phenomenon, occurring mainly during summer and in dry periods corresponding to the highest total suspended particle (TSP) contents.

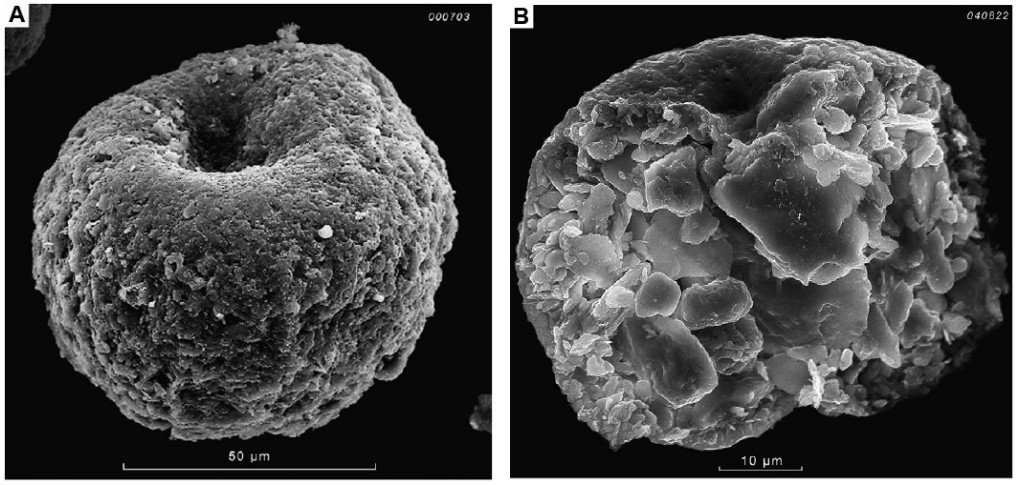

Figure 7. SEM images showing morphological aspects of iberulites. **(a)** External morphology of a single iberulite with one typical vortex on the top. **(b)** Internal view of one iberulite halve formed by mineral particles with angular edges (images from Díaz-Hernández & Párraga, 2008).

The disintegration and dispersion of bulk plant material also produce primary aerosol particles that consist of leaf debris, viruses, bacteria, spores and pollen, protozoa, algae and humic substances. Biological constituents of atmospheric aerosols have been long recognized and can be found even at high altitudes and in remote oceanic and polar regions.

They provide the main source of atmospheric phosphorous, and are important in the cycles of potassium and zinc (Artaxo *et al.*, 1994; Echalar *et al.*, 1998).

Combustion processes produce primary particles that consist mostly of carbonaceous materials such as elemental (black) carbon and organic compounds and represent the fine fraction of the aerosol. Vast quantities of these particles, commonly called soot, are produced by biomass burning during both controlled and wild fires, as well as by industry, automobile, aircraft and ship traffic (Penner, 1995). Fossil fuels contain residual mineral materials, including clays, sulfides, carbonates, chlorides and various trace metals that are also emitted in particulate form within fly ash particles in the coarse size range (Rose *et al.*, 1999). Soot particles emitted by mobile sources, particularly by diesel engines, produce either a unimodal (accumulation) or a bimodal (accumulation and coarse mode) aerosol population (Soot particles have typical morphologies and microstructures, Pósfai & Buseck, 2010). Combustion produces hydrocarbons that condense immediately at the source form 20 to 50-nm large, solid spherules (Lahaye, 1992). These carbonaceous spherules then coagulate and form branching aggregates that are easily recognizable on electron microscope images (Fig 8a). Individual spherules within a soot particle have characteristic microstructures of turbostratic graphitic layers as seen in Fig 8b (Pósfai *et al*., 1999).

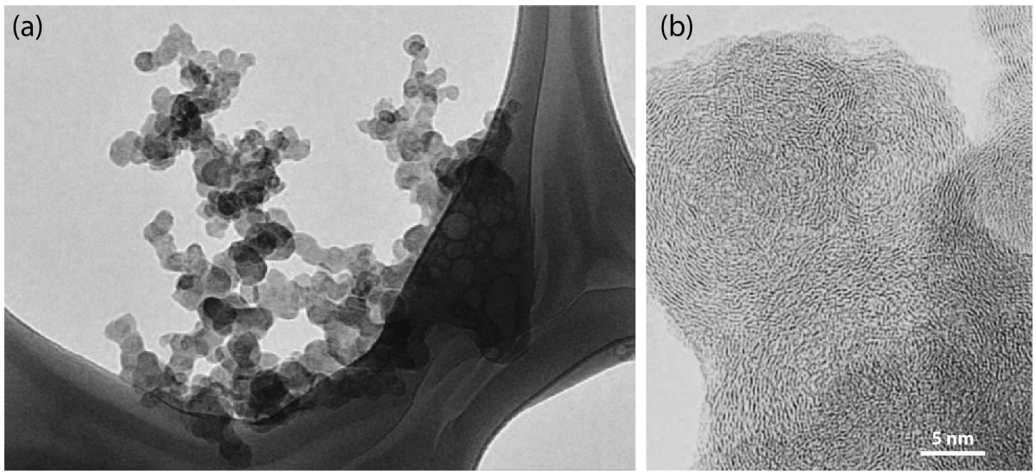

Figure 8. (a) A typical soot aggregate. **(b)** High-resolution TEM image obtained from a soot aggregate. The wavy graphitic layers form onion-like spherules (from Pósfai & Buseck, 2010).

Secondary particle sources

In the atmosphere there is a continuous material exchange between condensed and gas-phase materials. The condensation or nucleation can proceed either homogeneously (when only condensing vapors take part in the process) or heterogeneously on existing aerosol particles (nuclei). Heterogeneous processes are responsible for the formation of a significant fraction of atmospheric sulfate on sea-salt particles (see below) and the nucleation of sulfate on soot particles may be also important (Fitzgerald, 1991 and O'Dowd *et al.*, 1997)

Composition and morphology of aerosol particles

Owing to their different formation mechanisms, the chemical composition of fine and coarse particles, and continental and marine aerosols are substantially different. Also, as the consequence of dynamical and chemical transformation processes, the aerosol generally consists of internally mixed particles (mixtures of different sea salts, silicate and marine minerals and different types of anthropogenic species). Therefore a classification based exclusively on the composition is challenging if not worthless. Following a recent review by Posfái and Buseck (2010), however, a simple classification of major particles types can be established.

- *Sea-salt particles*. They contain primarily Cl^-, Na^+, and SO_4^{2-}, with some Mg^{2+}. Interaction with nitric acid leads to a loss of Cl^- during ageing. Due to the importance of these particles for the purposes of this PhD Thesis a more detailed description of the generation and nature of sea-salt particles is given in the next section.

- *Mineral dust, volcanic ash,* and *industrial dust,* which vary widely in composition (e.g. silicates, oxides, sulfates, carbonates, alloys, glass) due to its different formation mechanisms and source compositions. Particle reactions and internal mixing during transport of mineral dust can substantially change the composition of the original aerosol (Fig. 9a). Carbonate minerals can be a significant fraction of certain source desert areas and commonly react into sulfate or both sulfate and

nitrate during transport and subsequent ageing. Moreover, mineral particles become internally mixed with sea salt, perhaps through cloud processing.

- *Primary biogenic aerosol particles* (PBAP), which comprise biological materials (e.g. pollen, spores, plant fragments) (Fig. 9b). They consist mainly of carbon, but involve also other elements in minor amounts, such as potassium, phosphorus and silicon.

- *Combustion-derived carbonaceous particles*, which consist mainly of organic matter (OM) and elemental carbon. OM is a complex mixture of many different organic compounds with a wide range of physical and chemical properties. The terms elemental carbon (EC) and black carbon (BC), both relatively poorly defined, are used in atmospheric science for those carbonaceous materials that strongly absorb solar radiation (BC) or are highly refractory (EC). In contrast, the term soot is well defined (Pósfai & Buseck, 2010): it refers to a primary combustion-derived particle type with a distinctive structure consisting of concentric graphene-like layers, which are wrapped into spherules that aggregate into characteristic branching clusters (Fig. 8a). Furthermore, a new and distinctive particle type, larger than individual soot spherules and lack of typical graphitic structures, was identified from biomass-burning emissions; they gave it the name tar ball (Posfái & Buseck, 2010).

- *Secondary inorganic compounds*, which consist of salts (mainly of NO^{3-}, SO_4^{2-}, and NH^{4+}) that are formed from precursor gases emitted from natural (e.g. marine dimethylsulfide) or anthropogenic (e.g. SO_2, NO_x, NH_3, HCl) sources (Fig. 9c). These salts may have small contents of other cations as a result of interaction between gaseous precursors and mineral dust or sea-salt particles. Sulfate particles composition range from sulfuric acid to ammonium sulfate and constitute a major aerosol type in the troposphere. They either nucleate homogeneously or are formed by heterogeneous oxidation processes on existing particles from gaseous precursors of both natural (marine dimethylsulfide, DMS) and anthropogenic (SO_2) origins.

- *Secondary organic aerosol* (SOA) particles, which are composed of light elements and formed from reactive organic gases, i.e. volatile organic compounds (VOCs), emitted by the biosphere (mainly forests and phytoplankton), and from anthropogenic sources.

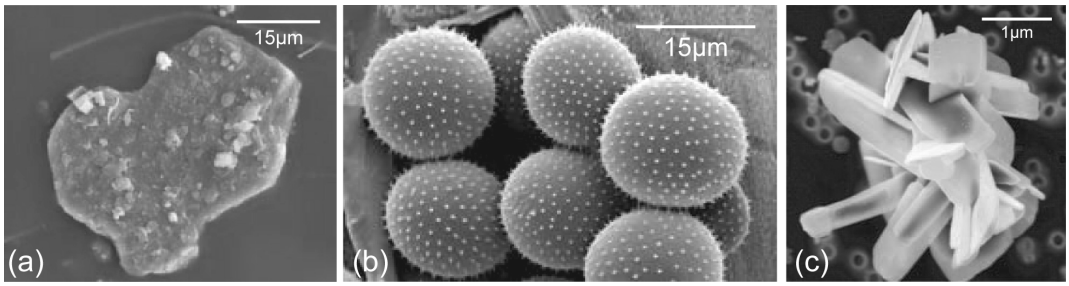

Figure 9. Three examples of natural **(a,b)** and anthropogenic atmospheric **(c)** particles view under scanning electron microscopy. **(a)** *Mineral dust*: illite with attached halite crystals in Saharan dust. **(b)** *Primary biogenic aerosol particle*: spores of wheat leaf rust. **(c)** *Secondary inorganic compounds*: combustion-derived Ca-sulfate crystals (images from Giére & Querol, 2010).

Depending on their origins, particles also differ in shape and physical state. Whereas condensation aerosols are generally liquid and have spherical shapes, particles of surface origin are solid and have irregular shapes (Buseck *et al.*, 2000). Combustion processes produce both solid and liquid particles that can have variable morphologies. New development of TEM techniques such as Electron Tomography (ET) are enabling high-resolution 3D reconstruction of aerosol particle morphology (Posfái & Buseck, 2010 and reference therein).

1.3.2. Marine aerosols

Sea-salt particles are the most abundant aerosol species in the marine atmosphere in terms of mass but can be also transported to great distances above the continents (Prospero, 2002). Owing to their hygroscopic behavior, marine aerosols act as *cloud condensation nuclei,* CCN (O'Dowd *et al.*, 1997). Marine aerosol (Fig. 10) comprises two distinct aerosol types: (1) primary sea-salt aerosol produced by the mechanical disruption of the ocean

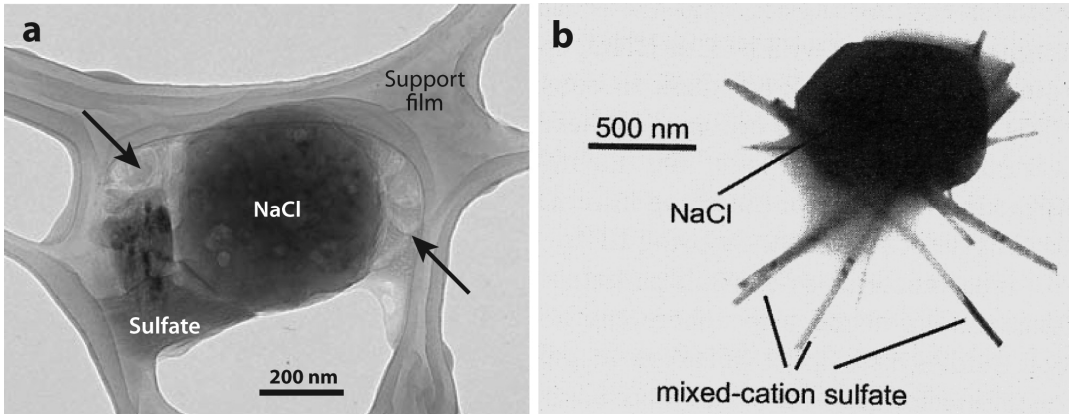

Figure 10. Electron microscope images of particles from the marine atmosphere. **(a)** Sea-salt particle that consists of a NaCl crystal, mixed-cation sulfate, and filamentous organic material, presumably of primary marine origin (marked by arrows) (from Pósfai & Buseck, 2010). **(b)** Image of a sea-salt particle where the mixed-cation sulfates are rod-shaped and contain Na, Mg, K, and Ca in various relative amounts (from Pósfai & Molnár, 2000).

surface and (2) secondary aerosol, primarily in the form of non-sea-salt sulfate and organic species, formed by gas-to-particle conversion processes such as binary homogeneous nucleation, heterogeneous nucleation and condensation (Fitzgerald, 1991 and O'Dowd *et al.*, 1997 and reference therein).

Primary sea-salt aerosol

Sea-salt aerosol particles are produced by the bursting of air bubbles at the surface of the ocean (Fig. 11). The number of sea-salt particles in the *marine boundary layer* is approximately exponentially related to wind speed. When winds are stronger, more whitecaps are produced and a larger number of droplets rises to the surface. A bursting bubble produces up to 10 jet drops (Fig. 11f) with diameters typically between 2-4 μm, and up to several hundreds of submicrometre-sized film drops (Fig. 11d) (Woodcock, 1972; Fitzgerald, 1991, and references therein). Their size distributions are bimodal: one mode at 2.5 μm corresponds to particles produced by jet drops, and another mode at ~0.1 μm corresponds to particles produced by film drops. The initial composition of sea-salt aerosol particles is directly related with the seawater chemistry containing dissolved ions in the same

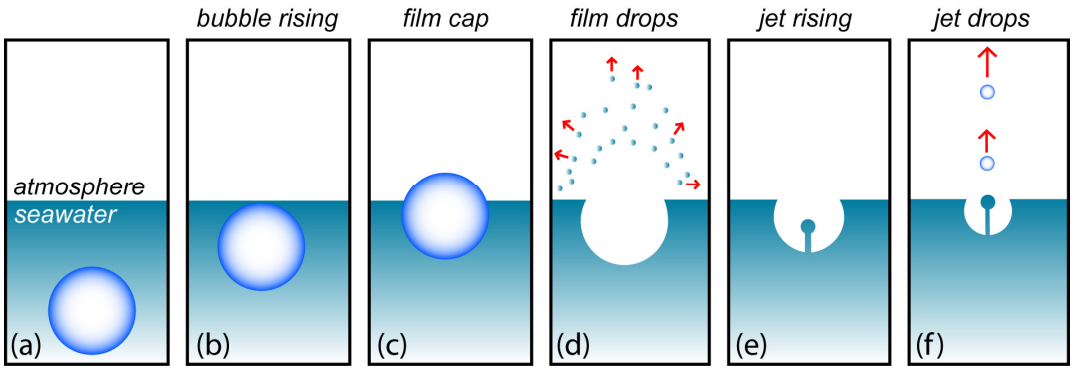

Figure 11. Drop formation from bubble bursting. **(a-c)** Rise of bubble to the surface and formation of the bubble film cap. **(d)** Production of film drops from bursting of the bubble film. **(e)** Shrinkage of the cavity left by the bubble and formation of a jet rinsing from the center of this cavity. **(f)** Further decrease in size of the cavity due to its filling by the surrounding liquid, and formation of several jet drops from breakup of the jet (modified from Lewis & Schwartz, 2004).

relative amounts as seawater. Sea-salt aerosols typically contain some organic compounds in addition to dissolved inorganic ions.

Sea water droplets can be lofted into high altitudes, where relative humidity is lower. It causes water to evaporate from particles producing crystallization of halite and hydrous sulfates. Recrystallized sea-salt particles are commonly observed in the vacuum using TEM (Fig. 10a) although AFM has been also applied to characterize particle morphologies (Pósfai & Buseck, 2010). The bulk composition of unalterated, fresh sea-salt particle is NaCl (e.g. Fig. 10a). In addition, typically rod-shaped or veil-like, thin sulfate crystals commonly occur (Fig. 10b). Sulfates can contain variable ratios of Na, Mg, Ca, K.

Secondary sea-salt aerosol

Sea-salt particles react with gases in the atmosphere, which results in the release of Cl and the formation of additional sulfate and nitrate onto the particles. In distinction to the sulfate that originates from seawater, the excess sulfate is called 'non-sea-salt (*nss*). The mechanism for *nss* sulfate formation in sea-salt particles includes condensation, dissolution, and subsequent oxidation of SO_2 in the water associated with the sea-salt aerosol particles (Pósfai *et al.*, 1995; Pósfai & Molnár, 2000). Nitrogen-bearing species such as NO_x during

the day and HNO_3 at night can also react with sea-salt particles. The result of these reactions produce $NaNO_3$ from NaCl, and Cl is liberated. Fully reacted particles have lost all their Cl contents and form characteristic crystals that can be observed under TEM. The crystal structures of sulfates that are formed from sea-salt are similar to Na_2SO_4 and differ from those of 'mixed-cation sulfate' in unreacted sea-salt particles. Similarly, sea-salt particles that have completely reacted with NO_x or HNO_3 contain $NaNO_3$. Atmospheric reactions do not remove or deposit Na, Mg, K, and Ca ions from or onto the particles and thus the relative amounts of these elements remain constant through time (Fig. 12a). In contrast, the reaction of sea-salt particles with atmospheric gas-phases results in a continuous variation of the Na, S, and Cl ratios (Fig. 12b).

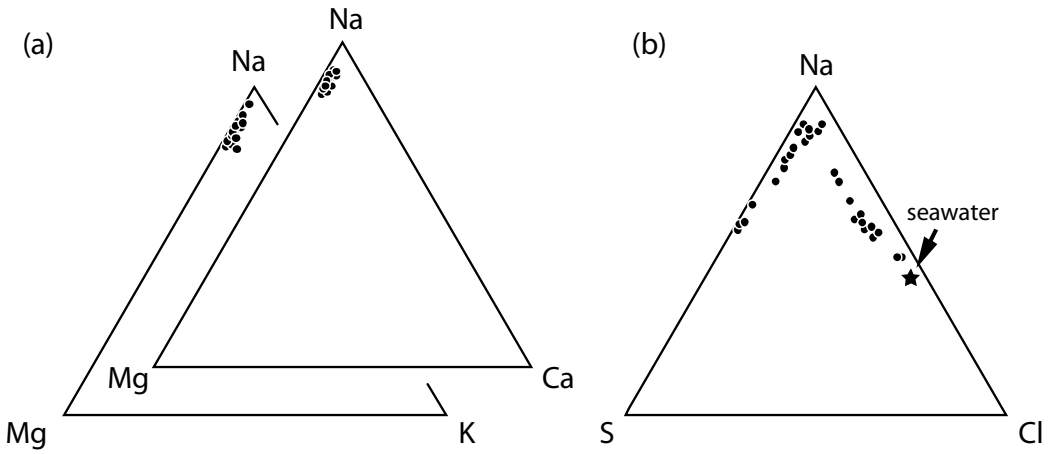

Figure 12. Ternary plots showing sea-salt particles composition (in atomic ratios), obtained from EDX spectra. The three plots represent the same particles collected from the North Atlantic troposphere. Uniform ratios of K, Mg, Ca and Na in **(a)** indicate that these elements remain unchanged during atmospheric reactions, whereas the wide range of compositions in **(b)** shows Cl loss and S excess relative to seawater compositions (Pósfai *et al.*, 1995).

1.4. Chemical weathering of carbonates

Chemical weathering is considered to be the most powerful tool in the destruction of building stone (Winkler, 1973). The effect of chemical weathering on natural building stone is dominated by two related fields of work: the effect of air pollution and acidic deposition and the effect of salt crystallization (Smith, 1999). In general pollutants that affect buildings or monuments can be either in gaseous, liquid or solid phase. Any effect of a pollutant depends on the reactivity of the stone surface with the pollutant and also on its physical properties, durability and chemistry (Smith, 1999). Carbonate-bearing stones are the most sensitive to the effects of pollution (Grossi & Brimblecombe, 2007). The surfaces of carbonate stones heavily and frequently washed by rainwater can suffer dissolution process which is more rapid if the stone has had a prior exposure to air polluted with SO_2 (Cooke & Gibbs, 1994; Cardell-Fernández *et al.*, 2002). Dissolution can be defined as the complete dissociation of a mineral in a solvent, such as water (Winkler, 1973).

Dissolution of carbonates has paramount implications in many geological and biological processes and has attracted the attention of basic and applied research during the last decades. Indeed, about 20% of Phanerozoic (0-547 Ma) sedimentary rocks are made up of the carbonate minerals calcite ($CaCO_3$) and dolomite ($CaMg(CO_3)_2$) (Morse *et al.*, 2007) and therefore constitute also one of the most common building stone applied during many centuries, especially across Europe (Smith *et al.*, 2010 and reference therein). Chemical dissolution and crystallization of soluble salts in building materials play a critical role in the decay of carbonate rocks (Fig. 13) although the physical and chemical processes behind this decay are not completely well understood (e.g. Cardell, 1998; Rodríguez-Navarro & Doehne, 1999). Comparing to physical weathering processes, the effect of dissolution in the preservation of the Cultural Heritage has received less attention due to the complex interrelation of factors that control it. Even more complex is to constrain the time and therefore the *rate* of this process although early attempts date since the end of the 19th century (Winkler, 1997). New high-resolution techniques such as atomic force microscopy (AFM) or vertical scanning interferometry (VSI) devoted to investigate in real time the

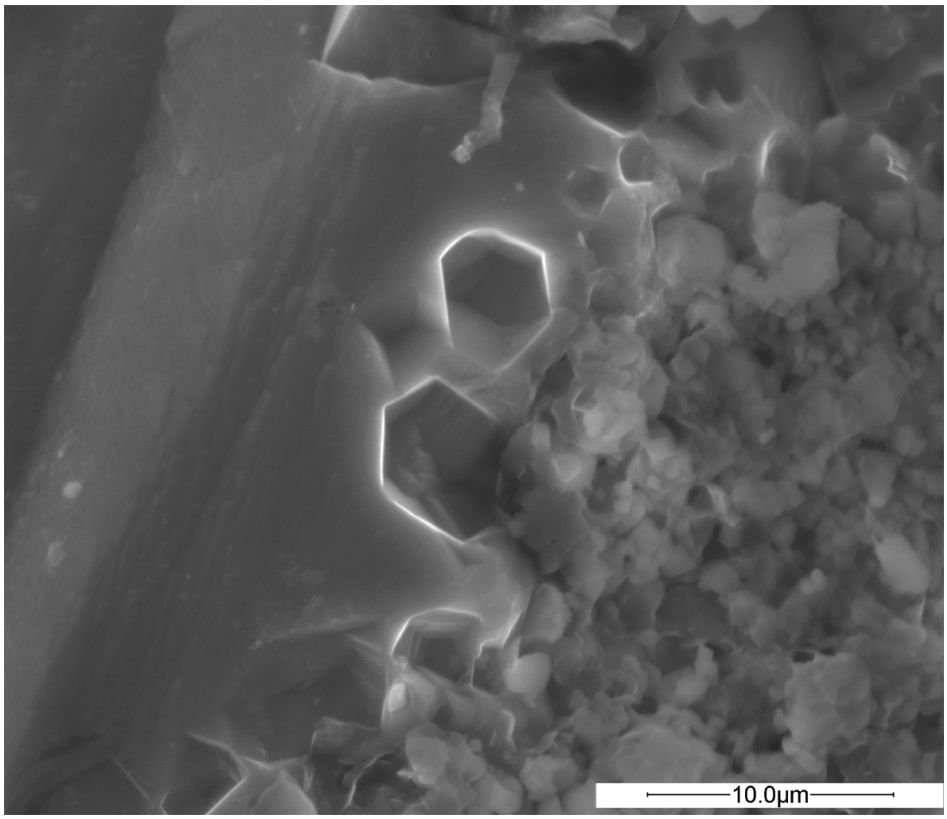

Figure 13. Example of chemical weathering features (deep dissolution pits) under FESEM in the Santa Pudia calcarenite (courtesy of E. Ruiz-Agudo).

interaction of solution with mineral substrates at the nanometer scale, allow new promising perspectives in this research field (Ruiz-Agudo, 2007).

There are three structurally different anhydrous carbonates: the calcite group (hexagonal, $R\bar{3}c$), the aragonite group (orthorhombic, *Pmcn*) and the dolomite group (hexagonal, $R\bar{3}$). Despite their structural simplicity, the behavior of these minerals in solution is complex and primarily reflects the fundamental role of chemical kinetics related to the carbonated substrate (Morse & Arvidson, 2002; Morse *et al.*, 2007) but also to the water structure dynamics and solute hydration in the solution (Kowacz & Putnis, 2008; Ruiz-Agudo *et al.*, 2009, 2010, 2011).

Among other carbonates, calcite and magnesite dissolution has been thoroughly investigated over a range of environmental conditions and solution compositions (for a comprehensive review see Morse & Arvidson, 2002 and Morse *et al.*, 2007). In contrast, dolomite dissolution studies have been traditionally hampered by its low reaction rates compared to calcite and its poorly constrained relationship between cation ordering and reactivity (e.g. Morse & Arvidson, 2002; Lüttge *et al.*, 2003). Nevertheless, dolomite can be the major mineral in certain stones used in the architectural heritage (e.g. Benavente *et al.*, 2007; Cueto *et al.*, 2009; Lopez-Arce *et al.*, 2009; Martínez-Martínez *et al.*, 2011) and the understanding of its behavior under different environmental conditions is essential to better constrain the decay patterns of this building material. In the following paragraphs a brief outline of dolomite structure, chemical composition and its dissolution are described.

Dolomite group comprises double carbonates and includes *dolomite* ($CaMg(CO_3)_2$), *ankerite* ($CaFe(CO_3)_2$) and *kutnahorite* ($CaMn(CO_3)_2$). The structure of dolomite is similar to the calcite structure but with Ca and Mg layers alternating along the c-axis. The large difference in size of the Ca^{2+} and Mg^{2+} ions (ca. 33%) causes cation ordering with the two cations in specific and separate levels in the structure leading to *'ordered dolomite'*. In contrast, magnesium atoms in a *'magnesian calcite'* are not segregated to their own cation plane but randomly substitute for calcium (Morse *et al.*, 2007). The composition of dolomite is intermediate between $CaCO_3$ and $MgCO_3$ although a complete solid solution between these two phases only exists at temperature higher than 1400ºC and about 1100ºC between dolomite and calcite. Naturally occurring dolomite deviates somewhat from Ca:Mg = 1:1 with the Ca:Mg ratio ranging from 58:42 to 48:52 and are commonly termed '*protodolomites'* (Morse *et. al.*, 2007).

Dolomite is found in many parts of the world mainly as extensive ancient sedimentary strata, and crystallized equivalent dolomite marble. Present-day dolomite precipitation is restricted to marginal regimes governed by extreme environmental conditions in terms of temperature, salinity and saturation state (Morse *et al.*, 2007). This is the reason why dolomite as a rock is generally thought to be secondary in origin, formed from limestone by replacement of some of the Ca by Mg. The replacement may be only partial and thus most

dolomite rocks (*dolostone*) are mixtures of dolomite and calcite. Nevertheless the contrast between the abundance of dolomite in ancient carbonates and its rare present-day distributions is still a matter of debate and represent the so-called 'dolomite problem'. This challenging paradox has been, indeed, the subject of scientific research over 200 years and still remains unresolved (Kaczmarek & Sibley, 2007).

The city of Granada is surrounded by extensive outcrops of dolomite in two markedly different geological settings: dolomitic marbles associated to calcite marbles in the internal parts of the Betic Cordillera (e.g. *Macael*, see Luque, 2010) and dolostone and dolomite brecha comprising the lower units of shallow marine-marine carbonate-platforms from the external parts of the Betic Cordillera (e.g. Vera *et al.*, 2005). This fact has promoted the extensive used of dolomite-bearing stone in the architectural heritage of Granada.

Dolomite dissolution rate depends on the saturation state, pH, temperature, ionic strength, total dissolved carbonate, aqueous calcium and magnesium activities, organic and inorganic ligands concentration and hydrodynamic conditions (Busenberg & Plummer, 1982; Herman & White, 1985; Chou *et al.*, 1989; Orton & Unwin, 1993; Gautelier *et al*., 1999, 2007; Pokrovsky & Schott, 2001; Pokrovsky *et al.*, 2005). Most of these relationships have been derived experimentally by monitoring the evolution of the composition of the bulk solution using macroscopic flow-through or batch reaction devices.

In this PhD Thesis the dissolution of dolomite crystals will be studied at nano- and microscale in the pH range 3 to 10 in order to gain knowledge in the behavior of this mineral in the carbonate stones used in the Cultural Heritage field. In addition, the incongruent dolomite dissolution behavior (leading to a Mg-rich surface) is investigated. The incongruent dolomite dissolution has been noticed since early works based on the change of the initial ratio of Ca to Mg released to solution in batch reactors experiments (Busenberg & Plummer, 1982). The existence of this Mg-rich surface has important implications and was argued by these authors to be the rate-limiting factor controlling dolomite dissolution and origin of the observed reaction order. Notwithstanding, a direct observation of this incongruent

dissolution and the nature of the precipitate have not been yet provided and is studied in more detail in this PhD Thesis.

1.5. References

Andreae, M.O. and Rosenfeld, D., 2008. Aerosol-cloud-precipitation interactions. Part 1. The nature and sources of cloud-active aerosols. Earth-Science Reviews, 89(1-2): 13-41.

Angeli, M., Bigas, J.P., Benavente, D., Menéndez, B., Hébert, R. and David, C., 2007. Salt crystallization in pores: quantification and estimation of damage. Environmental Geology, 52: 205–213.

Angeli, M., Benavente, D., Bigas, J.P., Menéndez, B., Hébert, R. and David, C., 2008. Modification of the porous network by salt crystallization in experimentally weathered sedimentary stones. Materials and Structures, 41(6): 1091-1108.

Angeli, M., Hébert, R., Menéndez, B., David, C. and Bigas, J.P., 2010. Influence of temperature and salt concentration on the salt weathering of a sedimentary stone with sodium sulphate. Engineering Geology, 115(3-4): 193-199.

Anwar Hossain, K.M., Easa, S.M. and Lachemi, M., 2009. Evaluation of the effect of marine salts on urban built infrastructure. Building and Environment, 44: 713–722.

Artaxo, P., Gerab, F., Yamasoe, M.A. and Martins, J.V., 1994. Fine mode aerosol composition at three long-term atmospheric monitoring sites in the Amazon Basin. Journal of Geophysical Research, 99: 22857-22868.

Avila, A., Queralt-Mitjans, I. and Alarcón, M., 1997. Mineralogical composition of African dust delivered by red rains over northeastern Spain. Journal of Geophysical Research, 102(D18): 21977-21996.

Benavente, D., Martínez-Verdú, F., Bernabéu, A., Viqueira, V., Fort, R., García del Cura, M.A., Illueca, C. and Ordóñez, S., 2003. Influence of surface roughness on color changes in building stones. Color Research and Application, 28(5): 343-351.

Benavente, D., Martínez-Martínez, J., Cueto, N. and García del Cura, M.A., 2007. Salt weathering in dual-porosity building dolostones. Engineering Geology, 94: 215-226.

Böke, H., Göktürk, E.H., Caner-Saltik, E.N. and Demirci, S.,1999. Effect of airborne particle on SO_2^- calcite reaction. Applied Surface Science, 140: 70-82.

Böke, H., Göktürk, E. H. and Caner Saltik, E. N., 2002. Effect of some surfactants on SO_2-marble reaction. Materials Letters, 57: 935-939.

Brimblecombe, P. and Grossi, C.M., 2005. Aesthetic thresholds and blackening of stone buildings. Science of the Total Environment, 349: 175-189.

Brimblecombe, P. and Grossi, C.M., 2007. Damage to buildings from future climate and pollution. APT Bulletin, 38(2/3): 13-18.

Buseck, P.R., Jacob, D.J., Pósfai, M., Li, J. and Anderson, J.R., 2000. Minerals in the air: an environmental perspective. International Geology Review, 42(7): 577 - 593.

Buseck, P.R., 2010. Atmospheric-particle research: past, present, and future. Elements, 6(4): 208-209.

Busenberg, E. and Plummer, L.N., 1982, The kinetics of dissolution of dolomite in CO_2-H_2O systems at 1.5 to 65ºC and 0 to 1 atm P_{CO2}. American Journal of Science, 282: 45-78.

Camuffo, D., Del Monte, M., Sabbioni, C. and Vittori, O., 1982. Wetting, deterioration and visual features of stone surfaces in an urban area. Atmospheric Environment, 16(9): 2253-2259.

Camuffo, D., Del Monte, M. and Sabbioni, C., 1983. Origin and growth mechanisms of the sulfated crusts on urban limestone. Water, Air, & Soil Pollution, 19(4): 351-359.

Camuffo, D., Del Monte, M. and Ongaro, A., 1984. The pH of the atmospheric precipitation in Venice, related to both the dynamics of precipitation events and the weathering of monuments. The Science of the Total Environment, 40(1): 125-139.

Cardell, C., 1998. Cristalización de sales en calcarenitas. Aplicación al Monasterio de San Jerónimo, Granada. Tesis Doctoral, Departamento de Mineralogía y Petrología, Universidad de Granada.

Cardell, C., Delalieux, F., Roumpopoulos, K., Moropoulou, A., Auger, F. and Van Grieken R., 2003a. Salt-induced decay in calcareous stone monuments and buildings in a marine environment in SW France. Construction and Building Materials, 17(3): 165-179.

Cardell, C., Rivas, T., Mosquera, M.J., Birginie, J.M., Moropoulou, A., Prieto, B., Silva, B. and Van Grieken R., 2003b. Patterns of damage in igneous and sedimentary rocks under conditions simulating sea-salt weathering. Earth Surface Processes and Landforms, 28(1): 1-14.

Cardell, C., Benavente, D. and Rodríguez Gordillo, J., 2008. Weathering of limestone building material by mixed sulfate solutions. Characterization of stone microstructure, reaction products and decay forms. Materials Characterization, 59: 1371–1385.

Cardell-Fernández, C., Vleugels, G., Torfs, K. and Van Grieken, R., 2002. The process dominating Ca dissolution of limestone when exposed to ambient amospheric conditions as determined by comparing dissolution models. Environmental Geology, 43: 160-171.

Chabas, A. and Lefevre, R.A., 2000. Chemistry and microscopy of atmospheric particulates at Delos (Cyclades-Greece). Atmospheric Environment, 34(2): 225-238.

Chabas, A. and Jeannette, D., 2001. Weathering of marbles and granites in marine environment: petrophysical properties and special role of atmospheric salts. Environmental Geology, 40(3): 359-368.

Charola, A.E., 2000. Salts in the deterioration of porous materials: An overview. Journal of the American Institute for Conservation, 39(3): 327-343.

Charola, A.E. and Ware, R., 2002. Acid deposition and the deterioration of stone: a brief review of a broad topic. In: Siegesmund, S., Weiss, T. and Vollbrecht, A. (eds.): Natural stone, weathering phenomena, conservation strategies and cases studies. Geological Society of London, Special Publications, 205(1): 393-406.

Chiari, G., 2000. Mineralogy and cultural heritage. In: Vaughan, D.J. and Wogelius, R.A. (eds.): Environmental Mineralogy, EMU notes in Mineralogy, Eötvös University Press, Hungary, pp. 351-381.

Chou, L., Garrels, R.M. and Wollast, R., 1989. Comparative study of the kinetics and mechanisms of dissolution of carbonate minerals. Chemical Geology 78(3-4), 269-282.

Cueto, N., Benavente, D., Martínez-Martínez, J. and García-del-Cura, M.A., 2009. Rock fabric, pore geometry and mineralogy effects on water transport in fractured dolostones. Engineering Geology, 107: 1-15.

Dayan, U., Heffter, J., Miller, J. and Gutman, G., 1991. Dust intrusion events into the Mediterranean Basin. Journal of Applied Meteorology, 30: 1185-1199.

Delalieux, F., Cardell-Fernández, C., Torfs, K., Vleugels, G. and Van Grieken, R., 2002. Damage functions and mechanism equations derived from limestone weathering in field exposure. Water, Air, & Soil Pollution, 139(1): 75-94.

Delalieux, F., Van Grieken, R. and Potgieter, J.H., 2006. Distribution of atmospheric marine salt depositions over Continental Western Europe. Marine Pollution Bulletin, 52: 606-611.

Del Monte, M., Sabbioni, C. and Vittori, O., 1981. Airbone carbon particulates and marble deterioration. Atmospheric Environment, 15: 645-652.

Del Monte, M. and Rossi, P., 1997. Fog and gypsum crystals on building materials. Atmospheric Environment, 31(11): 1637-1646.

Demirdag, S., 2009. The effect of using different polymer and cement based materials in pore filling applications on technical parameters of travertine stone. Construction and Building Materials, 23: 522–30.

Díaz-Hernández, J.L. and Párraga, J., 2008. The nature and tropospheric formation of iberulites: pinkish mineral microspherulites. Geochimica et Cosmochimica Acta, 72(15): 3883-3906.

Doehne, E., 2002. Salt weathering: a selective review. In: Siegesmund, S., Weiss, T. and Vollbrecht, A. (eds.): Natural stone, weathering phenomena, conservation strategies and cases studies. Geological Society of London, Special Publications, 205: 51-64.

Doehne, E. and Price, C., 2010. Stone Conservation: an overview of current research. (2nd ed.). Getty Conservation Institute, Los Angeles, 174 pp.

Durant, A.J., Bonadonna, C. and Horwell, C.J., 2010. Atmospheric and environmental impacts of volcanic particulates. Elements, 6(4): 235-240.

Echalar, F., Artaxo, P., Martins, J.V., Yamasoe, M., Gerab, F., Maenhaut, W. and Holben, B., 1998. Long-term monitoring of atmospheric aerosols in the Amazon Basin: Source identification and apportionment. Journal of Geophysical Research, 103: 31849-31864.

Esbert, R.M., Díaz-Pache, F., Grossi, C.M., Alonso, F.J. and Ordaz, J., 2001. Airborne particulate matter around the Cathedral of Burgos (Castilla y Leon, Spain). Atmospheric Environment, 35: 441-452.

Evans, I.S., 1970. Salt crystallization and rock weathering: a review. Rev. Geomorphol. Dyn., 19(4): 153-177.

Fassina, V., 1978. A survey on air pollution and deterioration of stonework in Venice. Atmospheric Environment, 12(11): 2205-2211.

Fitzgerald, J.W., 1991. Marine aerosols: a review. Atmospheric Environment. Part A. General Topics, 25(3-4): 533-545.

Fort, R., 2006. Utilización de la piedra natural en restauración, Seminarios de la Sociedad Española de Mineralogía, 2: 155-182.

Fort, R., 2008. Introducción. La Piedra Natural y el Patrimonio construido: Un mismo campo de investigación. Materiales de Construcción, 58(289-290): 7-10.

Galán, E., Carretero, M.I. and Mayoral Alfaro, E., 1999. A methodology for locating the original quarries used for constructing historical buildings: application to Malaga Cathedral, Spain. Engineering Geology, 54: 287-298

García del Cura, M.A., Benavente, D., Bernabéu, A. and Martínez-Martínez, J., 2008. The effect of surface finishes on outdoor granite and limestone pavers. Materiales de Construcción, 58: 65-79.

García-Talegón, J., Vicente, M.A., Vicente-Tavera, S. and Molina-Ballesteros, E., 1998. Assessment of chromatic changes due to artificial ageing and/or conservation treatments of sandstones. Color Research and Application, 23: 46–51.

Gauri, K.L., Tambe, S.S. and Caner-Saltik, E.N., 1992. Weathering of dolomite in industrial environments. Environmental Geology, 19: 55-63.

Gauri, K.L. and Bandyopadhyay, J.K., 1999. Carbonate stone. Chemical behavior, durability and conservation, J.Wiley & Sons, New York, 284 pp.

Gautelier, M., Oelkers, E.H. and Schott, J., 1999. An experimental study of dolomite dissolution rates as a function of pH from −0.5 to 5 and temperature from 25 to 80ºC. Chemical Geology, 157: 13-26.

Gautelier M., Schott J. and Oelkers E.H., 2007. An experimental study of dolomite dissolution rates at 80 °C as a function of chemical affinity and solution composition. Chemical Geology 242(3-4), 509-517.

Giére, R. and Querol, X., 2010. Solid particulate matter in the Atmosphere. Elements, 6(4): 215-222.

Gómez-Heras, M. and Fort, R., 2004. Location of quarries of non traditional stony materials in the architecture of Madrid: the Crypt of the Cathedral of Santa María la Real de la Almudena. Materiales de Construcción, 54(274): 33-49.

Gómez-Heras, M. (ed.), 2007. Abstracts from SWAPNET 2007 and workshop on limestone decay and conservation, Special issue, Stone: Newsletter on Stone Decay (2 August). http://www.qub.ac.uk/geomaterials/weathering/newsletter/issue_2.pdf

Grossi, C.M., Murray, M. and Butlin R.N., 1995. Response of porous building stones to acid deposition. Water, Air and Soil Pollution, 85: 2707-2712.

Grossi, C.M. and Murray, M., 1999. Characteristics of carbonate building stones that influence the dry deposition of acidic gases. Construction and Building Materials, 13: 101-108.

Grossi, C.M., Esbert, R.M., Díaz-Pache, F. and Alonso, F.J., 2003. Soiling of building stones in urban environments. Building and Environment, 38(1): 147-159.

Grossi, C.M. and Brimblecombe, P., 2007. Effect of long-term changes in air pollution and climate on the decay and blackening of European stone buildings. In: Prîkryl, J. and Smith, B.J. (eds.): Building stone decay. From diagnosis to conservation. Geological Society of London, Special Publications, 271: 117-130.

Hamilton, R. and Crabbe, H., 2009. Environment, pollution and effects. In: J. Watt, J. Tidblad, V. Kucera and R. Hamilton (Editors), The effects of air pollution on Cultural Heritage. Springer, pp. 1-28.

Hammecker, C., 1995. The importance of the petrophysical properties and external factors in stone decay on monuments. Pure and Applied Geophysics, 145: 337-361.

Herman, J.S. and White, W.B., 1985. Dissolution kinetics of dolomite: effects of lithology and fluid flow velocity. Geochimica et Cosmochimica Acta 49(10), 2017-2026.

Horemans, B., Worobiec, A., Buczynska, A., Van Meel K. and Van Grieken, R., 2008. Airborne particulate matter and BTEX in office environments. Journal of Environmental Monitoring, 10: 867-876.

Horemans, B., Kontozova-Deutsch, V., Cardell, C. and Van Grieken, R. Atmospheric aerosols at the Alhambra monument, Granada, Spain: composition, sources, and potential risks for conservation. The Science of the Total Environment., submitted.

Jones, M.S. and Wakefield, R.D. (eds), 1999. Aspects of stone weathering, decay and conservation. Proceedings of SWAPNET '97 stone weathering and atmospheric pollution network conference. Imperial College Press, London.

Kaczmarek, S.E. and Sibley, C.F., 2007. A comparison of nanometer-scale growth And dissolution features on natural and synthetic dolomite crystals: Implications for the origin of dolomite. Journal of Sedimentary Research, 77: 424–432.

Kontozova-Deutsch, V., Godoi, R.H.M., Worobiec, A., Spolnik, Z., Krata, A., Deutsch, F. and Van Grieken, R., 2008. Investigation of gaseous and particulate air pollutants at the Basilica Saint-Urbain in Troyes, related to the preservation of the medieval stained glasses windows. Microchimica Acta, 162: 425–432.

Kontozova-Deutsch, V., Cardell, C., Urosevic, M., Ruiz-Agudo, E. and Van Grieken, R., 2010. Characterization of indoor and outdoor atmospheric pollutants impacting architectural monuments: the case of San Jerónimo Monastery (Granada, Spain). Environmental Earth Sciences: 1-13.

Kowacz, M. and Putnis, A., 2008. The effect of specific background electrolytes on water structure and solute hydration: consequences for crystal dissolution and growth. Geochimica et Cosmichimica Acta, 72: 4476–4487.

Lahaye, J., 1992. Particulate carbon from the gas phase. Carbon, 30: 309-314.

La Iglesia, A., García del Cura, M.A. and Ordóñez, S., 1994. The physicochemical weathering of monumental dolostones, granites and limestones; dimension stones of the Cathedral of Toledo (Spain). Science of The Total Environment, 152: 179-188.

Lasaga, A.C. and Lüttge, A., 2001. Variation of crystal dissolution rate based on a dissolution stepwave model. Science, 291(5512): 2400-2404.

Lasaga, A.C. and Lüttge, A., 2003. A model for crystal dissolution. European Journal of Mineralogy, 15: 603-615.

Lewis, E. and Schwartz, S., 2004. Sea salt aerosol production: mechanisms, methods, measurements, and models: a critical review. Washington, D.C.: Am. Geophys. Union. 413 pp.

Lipfert, F.W.,1989. Atmospheric damage to calcareous stones: comparison and reconciliation of recent experimental findings. Atmospheric Environment 23, 415-429.

Lopez-Arce, P., Garcia-Guinea, J., Benavente, D., Tormo, L. and Doehne, E., 2009. Deterioration of dolostone by magnesium sulphate salt: an example of incompatible building materials at Bonaval Monastery, Spain. Construction and Building Materials, 23: 846-855.

Luque, A., 2010. Andalusian marbles: durability criteria applied in its use as ornamental stone. PhD Thesis. Department of Mineralogy and Petrology. University of Granada (Spain).

Lüttge, A.,Winkler, U. and Lasaga, A.C., 2003. Interferometric study of the dolomite dissolution:a new conceptual model for mineral dissolution. Geochimica et Cosmochimica Acta, 67: 1099–1116.

Maravelaki-Kalaitzaki, P. and Biscontin, G., 1999. Origin, characteristics and morphology of weathering crusts on Istria stone in Venice. Atmospheric Environment, 33(11): 1699-1709.

Maravelaki-Kalaitzaki, P., 2005. Black crusts and patinas on Pentelic marble from the Parthenon and Erechtheum (Acropolis, Athens): characterization and origin. Analytica Chimica Acta, 532(2): 187-198.

Martínez-Martínez, J., Benavente, D. and García del Cura, M.A, 2011. Mechanical analysis of multi-textural rocks (brecciated dolostones and limestones): a new micro-compression test for rocks. Key Engineering Materials, 465: 479-482

McMurry, P.H., 2000. A review of atmospheric aerosol measurements. Atmospheric Environment, 34(12-14): 1959-1999.

Mitchell, D.J. and Searle, D.E., 2004. Stone deterioration in polluted urban environments. . Land Reconstruction and Management Series 3. Enfield, NH: Science Publishers.

Moreno, T., Querol, X., Castillo, S., Alastuey, A., Cuevas, E., Herrmann, L., Mounkaila, M., Elvira, J. and Gibbons, W., 2006. Geochemical variations in aeolian mineral particles from the Sahara-Sahel Dust Corridor. Chemosphere, 65(2): 261-270.

Moropoulou, A., Theoulakis, P. and Chrysophakis, T., 1995. Correlation between stone weathering and environmental factors in marine atmosphere. Atmospheric Environment, 29(8): 895-903.

Moropoulou, A., Bisbikou, K., Grieken, R.V., Torfs, K. and Polikreti, K., 2001. Correlation between aerosols, deposits and weathering crusts on ancient marbles. Environmental Technology, 22(6): 607-618.

Morse, J. W. and Arvidson, R. S., 2002. The dissolution kinetics of major sedimentary carbonate minerals. Earth-Science Reviews, 58: 51–84.

Morse, J.W., Arvidson R.S. and Lüttge, A., 2007. Calcium carbonate formation and dissolution. Chemical Reviews, 107: 342-381.

O'Dowd, C.D., Smith, M.H., Consterdine, I.E. and Lowe, J.A., 1997. Marine aerosol, sea-salt, and the marine sulphur cycle: a short review. Atmospheric Environment, 31(1): 73-80.

Orton, R. and Unwin, P.R., 1993. Dolomite dissolution kinetics at low pH: a channel-flow study. Journal of the Chemical Society, Faraday Transactions, 89(21), 3947-3954.

Papida, S., Murphy, W. and May, E., 2000. Enhancement of physical weathering of building stones by microbial populations. International Biodeterioration & Biodegradation, 46(4): 305-317.

Penner, J.E., 1995. Carbonaceous aerosols influencing atmospheric radiation: Black and organic carbon. In: Charlson, R.J. & Heintzenberg, J. (eds.): Aerosol forcing of climate, Wiley, New York, pp. 91-109.

Plummer, L.N., Wigley, T.M.L. and Parkhurst, D.L., 1978. The kinetics of calcite dissolution in CO_2-water systems at 5-60ºC and 0.0–1.0 atm CO_2. American Journal of Science, 278: 179-216.

Plummer, L.N. and Busenberg, E., 1982. The solubilities of calcite, aragonite and vaterite in CO_2–H_2O solutions between 0 and 90ºC, and an evaluation of the aqueous model for the system $CaCO_3$–CO_2–H_2O. Geochimica et Cosmochimica Acta, 46: 1011-1040.

Pósfai, M., Anderson, J.R., Buseck, P.R. and Sievering, H., 1995. Compositional variations of sea-salt-mode aerosol particles from the North Atlantic. Journal of Geophysical Research, 100(D11): 23063-23074.

Pósfai, M., Anderson, J.R., Buseck, P.R. and Sievering, H., 1999. Soot and sulfate aerosol particles in the remote marine troposphere. Journal of Geophysical Research, 104: 21685-21693.

Pósfai, M. and Molnár, Á., 2000. Aerosol particles in the troposphere: a mineralogical introduction. In: Vaughan, D.J. and Wogelius, R.A. (eds.): Environmental Mineralogy, EMU notes in Mineralogy, Eötvös University Press, Hungary, pp. 197-252.

Pósfai, M. and Buseck, P. R., 2010. Nature and climate effects of individual tropospheric aerosol particles. Annual Review of Earth and Planetary Sciences, 38: 17-43.

Pokrovsky, O.S., Schott, J. and Thomas F., 1999. Dolomite surface speciation and reactivity in aquatic systems. Geochimica et Cosmochimica Acta 63(19-20): 3133-3143.

Pokrovsky O.S. and Schott J., 2001. Kinetics and mechanism of dolomite dissolution in neutral to alkaline solutions revisited. American Journal of Science, 301(7), 597-626.

Pokrovsky, O.S., Golubev, S.V. and Schott, J., 2005. Dissolution kinetics of calcite, dolomite and magnesite at 25 °C and 0 to 50 atm pCO_2. Chemical Geology, 217(3-4): 239-255.

Prieto, B., Aira N. and Silva, B., 2007. Comparative study of dark patinas on granitic outcrops and buildings. The Science of the Total Environment, 381(1-3): 280-289.

Přikryl, R. and Viles, H.A. (eds), 2002. Understanding and managing stone decay. Proceedings of SWAPNET 2001 stone weathering and atmospheric pollution network conference. Karolinum Press, Prague.

Prospero, J.M., 1999. Long-term measurements of the transport of African mineral dust to the southeastern United States: Implications for regional air quality. Journal of Geophysical Research, 104(D13): 15917-15927.

Prospero, J.M., 2002. The chemical and physical properties of marine aerosols: An introduction. In: Gianguzza, A., Pellizzetti, E. and Sammarano, S. (eds.): Chemistry of marine water and ediments, Springer-Verlag Berlin, Heidelberg, pp. 35-82.

Rivas, T., Prieto, B., Silva, B. and Birginie, J.M., 2003. Weathering of granitic stones by chlorides: effects of the nature of the solution on weathering morphology. Earth Surface Processes and Landforms, 28: 425–436.

Rivas, T., Prieto, B. and Silva, B., 2008. Artificial weathering tests of granite. Materiales de Construcción, 58(289-290): 179-189.

Rodríguez, I., Galí, S. and Marcos, C., 2009. Atmospheric inorganic aerosol of a non-industrial city in the centre of an industrial region of the North of Spain, and its possible influence on the climate on a regional scale. Environmental Geology, 56: 1551-1561.

Rodríguez-Navarro, C. and Sebastián, E., 1996. Role of particulate matter from vehicle exhaust on porous building stones (limestone) sulfation. The Science of The Total Environment, 187(2): 79-91.

Rodríguez-Navarro, C. and Doehne, E., 1999. Salt weathering: influence of evaporation rate, supersaturation and crystallization pattern. Earth Surface Processes and Landforms, 24(3): 191-209.

Rodríguez-Navarro, C., Doehne, E. and Sebastián, E., 1999. Origins of honeycomb weathering: the role of salts and wind. Geological Society of America Bulletin, 111: 1250-1256.

Rose, N.L., Juggins, S. and Watt, J., 1999. The characterisation of carbonaceous fly-ash particles from major European fossil-fuel types and applications to environmental samples. Atmospheric Environment, 33(17):2699-2713.

Ruiz-Agudo E., 2007. Prevención del daño debido a la cristalización de sales en el patrimonio histórico construido mediante el uso de inhibidores de la cristalización. Tesis Doctoral. Universidad de Granada, Granada (Spain).

Ruiz-Agudo, E., Mees, F., Jacobs, P. and Rodríguez-Navarro, C., 2007. The role of saline solution properties on porous limestone salt weathering by magnesium and sodium sulfates. Environmental Geology, 52: 269-281.

Ruiz-Agudo, E., Putnis, C.V., Jiménez-López, C. and Rodríguez-Navarro, C., 2009. An atomic force microscopy study of calcite dissolution in saline solutions: the role of magnesium ions. Geochimica et Cosmichimica Acta, 73: 3201–3217.

Ruiz-Agudo, E., Kowacz, M., Putnis, C.V. and Putnis, A., 2010. Role of background electrolytes on the kinetics and mechanism of calcite dissolution. Geochimica et Cosmichimica Acta, 74: 1256–1267.

Ruiz-Agudo, E., Urosevic, M., Putnis, C.V., Rodríguez-Navarro, C., Cardell, C. and Putnis, A., 2011. Ion-specific effects on the kinetics of mineral dissolution. Chemical Geology, 281: 364–371.

Sabbioni, C., 1995. Contribution of atmospheric deposition to the formation of damage layers. The Science of the Total Environment, 167(1-3): 49-55.

Saiz-Jimenez, C. (ed.), 2004. Air pollution and cultural Heritage: Proceedings of the international workshop on air pollution and cultural heritage, Taylor & Francis Group, London.

Scherer, G.W., 1999. Crystallization in pores. Cement and Concrete Research, 29(8): 1347-1358.

Siegesmund, S., Weiss, T. and Vollbrecht, A., 2002. Natural stone, weathering phenomena, conservation strategies and case studies: Introduction, 205. Geological Society of London, Special Publications, 1-7 pp.

Siegesmund, S., Snethlage, R. and Ruedrich, J., 2008. Monument futures: climate change, air pollution, decay and conservation—the Wolf-Dieter Grimm-volume. Environmental Geology, 56(3): 451-453.

Siegesmund, S. and Snethlage, R. (eds.), 2011. Stone in architecture: Properties, durability. 4th Edition, Springer, 552 pp.

Silva, B., Rivas, T., García-Rodeja, E. and Prieto B., 2007. Distribution of ions of marine origin in Galicia (NW Spain) as a function of distance from the sea. Atmospheric Environment, 41:4396-4407.

Silva, B., Aira, N., Martínez-Cortizas, A. and Prieto, B., 2009. Chemical composition and origin of black patinas on granite. Science of the Total Environment, 408(1): 130-137.

Silva, Z.S.G. and Simão, J.A.R., 2009. The role of salt fog on alteration of dimension stone. Construction and Building Materials, 23(11): 3321-3327.

Smith, B.J. and Warke, P.A. (eds), 1996. Processes of urban stone decay. Proceedings of SWAPNET '95 stone weathering and atmospheric pollution network conference. Donhead Publishing, London.

Smith, B.J. (ed.), 1999. Stone: building stone, rock fill and armourstone in construction. Geological Society of London, Engeneering Geology Special Publication, 478 pp.

Smith, B.J. and Turkington, A.V. (eds), 2004. Stone decay: its causes and controls. Proceedings of SWAPNET 2000 stone weathering and atmospheric pollution network conference. Donhead Publishing, Shaftesbury.

Smith, B.J., Gómez-Heras, M. and Viles, H.A., 2010. Underlying issues on the selection, use and conservation of building limestone. In: Smith, B.J., Gómez-Heras, M. and Viles, H.A. and Cassar, J. (eds.): Limestone in the built environment: present-day challenges for the preservation of the past. Geological Society of London, Special Publications, 331(1): 1-11.

Theoulakis, P. and Moropoulou, A., 1999. Salt crystal growth as weathering mechanism of porous stone on historic masonry. Journal of Porous Materials, 6(4): 345-358.

Torfs, K. and Van Grieken, R., 1997. Chemical relations between atmospheric aerosols, deposition and stone decay layers on historic buildings at the mediterranean coast. Atmospheric Environment, 31(15): 2179-2192.

Van Grieken, R., Delalieux, F. and Gysels, K., 1998. Cultural heritage and the environment. Pure and Applied Chemistry, 70: 2327-2331

Van Grieken, R., Gysels, K., Hoornaert, P., Joos, J., Osan, J., Szaloki, I. and Worobiec, A., 2000. Characterisation of individual aerosol particles for atmospheric and cultural heritage studies. Water, Air, & Soil Pollution, 123(1): 215-228.

Vaughan, D.J., 2000. The nature and scope of environmental mineralogy. In: Vaughan, D.J. and Wogelius, R.A. (eds.): Environmental Mineralogy, EMU notes in Mineralogy, Eötvös University Press, Hungary, pp. 3-5.

Vera, J.A., 2004. Cordillera Bética y Baleares. In: Vera, J.A. (ed.), Geología de España, SGE-IGME, Madrid, pp. 347-464.

Watt, J., Tidblad, J., Kucera, V. and Hamilton, R., 2009. The effects of air pollution on cultural heritage. Springer, 299 pp.

Winkler, E.M., 1994. Stone in architecture: Properties, durability. 3rd Edition, Springer-Verlag, Berlin, 313 pp.

Wogelius, R.A. and Vaughan, D.J., 2000. Analytical, experimental, and computational methods in environmental mineralogy. In: Vaughan, D.J. and Wogelius, R.A. (eds.): Environmental Mineralogy, EMU notes in Mineralogy, Eötvös University Press, Hungary, pp. 7-87.

Woodcock, A.H., 1972. Smaller salt particles in oceanic air and bubble behavior in the sea. Journal of Geophysical Research, 77(27): 5316-5321.

Zendri, E., Biscontin, G., Kosmidis, P. and Bakolas, A., 2000. Characterization and physico-chemical action of condensed water on limestone surfaces. In: F. Vasco (Editor), Proceedings of the 9th International Congress on Deterioration and Conservation of Stone. Elsevier Science B.V., Amsterdam, pp. 647-656.

Zendri, E., Biscontin, G. and Kosmidis, P., 2001. Effects of condensed water on limestone surfaces in a marine environment. Journal of Cultural Heritage, 2(4): 283-289.

Zezza, F. and Macrì, F., 1995. Marine aerosol and stone decay. The Science of the Total Environment, 167(1-3): 123-143.

Chapter 2

MATERIALS

This chapter contains a summary of the geological materials used for the experimental part of this PhD research. In contrast to other parts of Spain or Portugal where igneous silicate rocks such as granite, gabbro or syenite represent the most common dimensional and ornamental stone used in the architectural heritage (e.g. Rivas *et al.*, 2003, 2008; Simão *et al.*, 2006; Silva & Simão, 2009), in Andalusia carbonate stones form the major part of the Cultural Heritage. This widespread use of carbonate stones is a consequence of their common occurrence in the southern and eastern Spain (corresponding with the mountain range known as Betic Cordillera), and also because of the relative easiness of their cutting and quarrying and their perceived durability (Rodríguez-Navarro, 1994; Cardell, 1998; Gauri & Bandyopadhyay, 1999; Gibbons & Moreno, 2003; García del Cura *et al.*, 2005; Fort, 2006; Sebastián-Pardo *et al.*, 2008; Smith *et al.*, 2010).

In addition to the description of stone materials, a summary of aerosol composition in Granada during the years 2008 and 2009 is presented (Lyamani & Bravo Aranda, 2009, 2010). This period corresponds to the long term natural ageing test performed in diverse carbonate stones placed in the city of Granada.

2.1. Stone materials used in the architectural heritage of Granada

2.1.1. Carbonate stones

Three non-crystalline carbonate stones frequently used in the Architectural Heritage of Granada and Andalusia, as well as in modern buildings, were selected for this study: (a) the *Escúzar* calcarenite, (b) the *Olivillo* travertine and (c) the *Sierra Elvira* limestone.

The *Escúzar* calcarenite is a lithotype variety of the well studied *Santa Pudia* calcarenite, locally known as *Piedra Franca*, which are exploited in diverse quarries situated ~ 20 km to the SW from the city of Granada. Calcarenite is a type of bioclastic limestone composed entirely of carbonate grains in size range of sand (from 0.06 to 2 mm) and therefore known also as carbonate sandstone. Bioclasts of *Santa Pudia* calcarenite are formed by fragmentation of molluscs, echinoderms, briozoan, red algae and foraminifera. The biota association is typical of temperate, shelf carbonates. In the *Escúzar* stone bioclasts grain size commonly ranges from 2 to 5 mm although they can also attain up to 7 mm in length. In the Folk's classification these lithotypes should be classified as *coarse calcarenite* or *fine calcirudite* (Folk, 1981). The *Santa Pudia* calcarenite is also very heterogeneous in calcite grain size ranging from micritic and microsparitic in the matrix and sparitic calcite partially filling large intraclast cavities leading to a bimodal porous size distribution (e.g. Rodríguez-Navarro, 1994). The *Santa Pudia* calcarenite has been commonly exploited as constructive material due to its easiness in terms of labor, although its high open porosity limits its durability. Furthermore, this calcarenite is very well characterized through many research works since it was extensively used as architectural material in the city of Granada, for example in the Cathedral, the Royal Chapel, the Cartuja monastery, the Carlos V Palace, the San Jerónimo monastery and the Royal Hospital (Rodríguez-Navarro & Sebastián-Pardo, 1991, 1996; Sebastián-Pardo *et al*., 1992; Rodríguez-Navarro, 1994; Villegas *et al.*, 1995; Cardell *et al.*, 1998, 2008; Alonso *et al*., 2004; Ruiz-Agudo, 2007; Ruiz-Agudo *et al*., 2007, 2010; Cultrone *et al.*, 2007, Arizzi *et al.*, 2007; Luque *et al.*, 2008; Rodríguez-Navarro *et al.*, 2008; Jroundi *et al.*, 2010). In this work the white calcarenite commercialized by *Áridos Los*

Linos, S.L. has been characterized and used in the different experiments in this Thesis, and will be referred in the following chapters as *Escúzar* calcarenite.

The *Olivillo* travertine exploited in the *Olivillo* quarry (Alhama de Almería, Almería) is commonly used in modern architecture and additionally in restoration works of historic buildings. Travertine is a compact, finely crystalline and often concretionary carbonate rock, formed by rapid chemical precipitation of calcium carbonate from solution in spring waters and rivers. In general, travertine is a mechanically very resistant material and due to its peculiar porous system has the desirable feature of rising damp inhibition. In the Architectural Heritage of Granada the most often travertine used has been the *Alfacar* travertine (Durán et al., 1993; Cardell, 1998; Martín-Algarra *et al.*, 2003), named after the village where it was quarried, situated in the NE of the city of Granada. However, the closing of the quarry stimulated increased exploitation of other colored travertines in southern Spain, such as those from Albox (*Yellow Gold Travertine/ Travertino Oro*), Alhama de Almería (*Red Travertine* and *Olivillo Travertine*) and *Travertino Ágata/Madera* in Huércal-Overa outcropping in the Andarax basin of Almería (García del Cura *et al.*, 2007a, 2007b, 2008a, 2008b). It is worth to note also that light travertine from Muğla Province (Turkey) has been recently imported to Spain because of its similarity with the higher quality Travertino Romano Classico (Benavente *et al.*, 2009). In this work the travertine (Cream Travertine) commercialized by *Travertino Antic S.L.* has been used in the experiments and will be referred in the following chapters as *Olivillo travertine*.

The *Sierra Elvira* limestone represents one of the most common building and ornamental stone used traditionally in the Architectural Heritage of Spain and particularly in Granada. Similar stone varieties in age and geological depositional environment are found in many other Alpine realms and are extensively used throughout Europe. The *Sierra Elvira limestone* is exploited close to the city of Granada in the locality of Atarfe. It is a medium-grain microsparitic limestone mainly composed of well cemented carbonate bioclastic fragments of crinoids (equinoderms) (Sebastián Pardo *et al.*, 2008). It was formed by the deposition of fossil- and algae-carrying calcareous mud or slime in shallow seas or lakes (Braga *et al.*, 1979; Garibaldi, 1999). Thin alternations of parallel- to cross-laminated beds are common in Sierra Elvira limestone and have been interpreted as storm sand layers

(Dabrio & Polo, 1985). It is a crystalline rock, grayish-green in color with some calcite bands and numerous stylolites. Both travertine and limestone are less studied compared to the calcarenite, although they also are very common stones used in the monuments of Granada (Durán Suárez *et al*., 1993; Cardell, 1998; Durán Suárez & García-Casco, 2000).

2.2.2. Geological setting of the quarries

Escúzar calcarenite

This lithotype of the *Santa Pudia* calcarenite is geologically located in the Granada's Neogene sedimentary basin (Fig. 1). Lower Tortonian calcarenic materials were deposited in coastal areas and subjected to different redeposition processes. These calcarenites contain several bioclasts and detritial material as well as metamorphic rock fragments (mainly metapelite and quartz aggregates) from the nearby Palaeozoic basement. The calcarenic materials are exploited at the south edge of the basin in the *Cortijo de Santa Pudia* and *Cortijo de la Escribana* where two important calcarenite quarries are placed, i.e. *La Escribana* and *Escúzar* (Fig. 1). The quarry of *La Escribana* provided until its closing in 1994 one of the most common constructive materials in the Architectural Heritage of Granada (see above). When the quarry of *La Escribana* was closed, exploitation activities moved to an ancient quarry closer to Escúzar, locally named *Las Parideras* (or simply *Escúzar*). The *Escúzar* quarry (Fig. 2), located to the NW of the *La Escribana* quarry may be its prolongation. Its differences in grain size, texture and types of bioclasts could be a consequence of the distance to the original border of the Neogene basin. Coarse grained bioclasts gradually decrease laterally when the basin deepen. At least two color varieties can be distinguished in the outcrop, one more whitish and another more yellowish due to different contents of iron- oxides and hydroxides. *Escúzar* calcarenites were used recently in the restoration of the Great Mosque of Córdoba and the Palace of *Las Cinco Llagas* of Seville (present location of the Andalusian Parliament).

Regional sketch

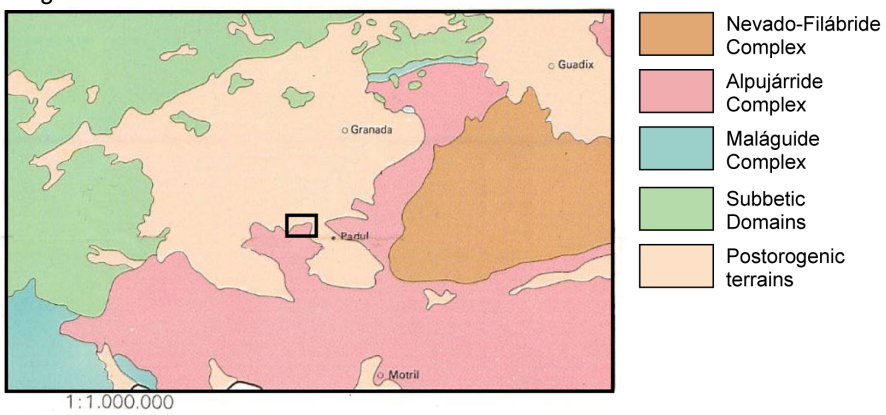

Escúzar calcarenite geological setting

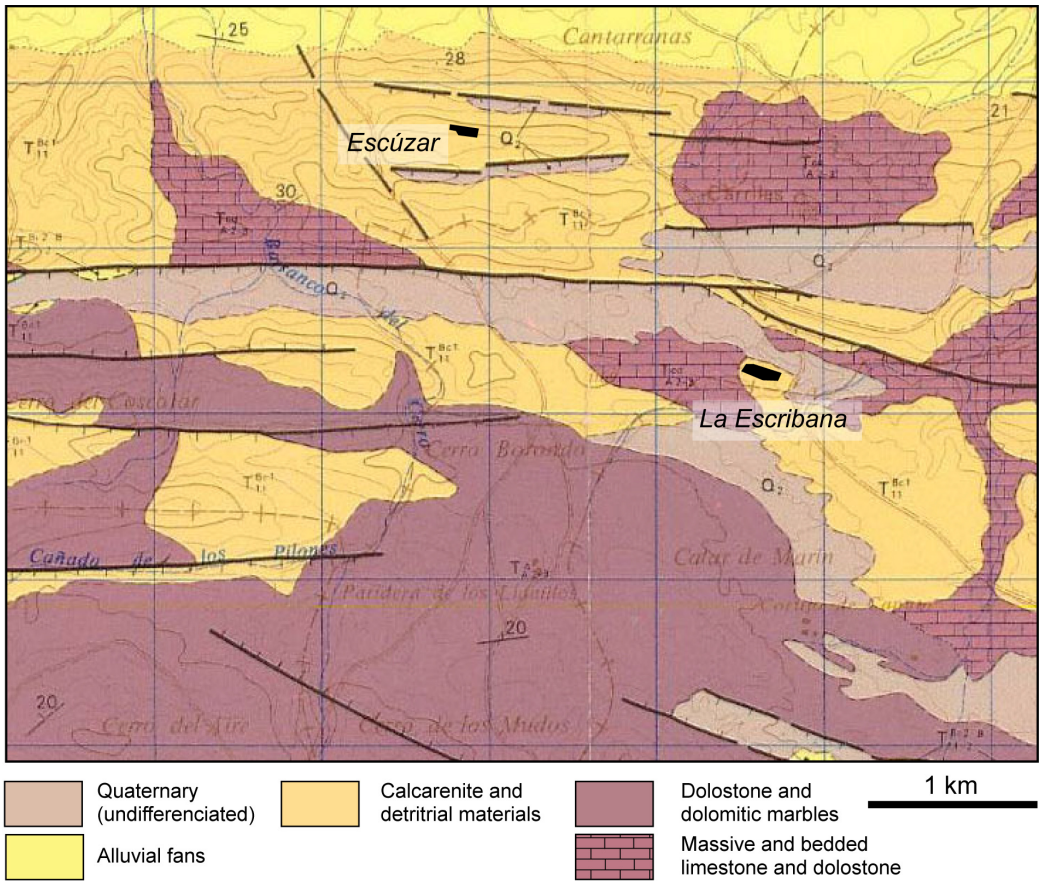

Figure 1. Regional sketch (left) and geological setting (right) for Santa Pudia calcarenite (González Donoso *et al.*, 1980). The old (*La Escribana*) and currently exploited quarries (*Escúzar*) are shown.

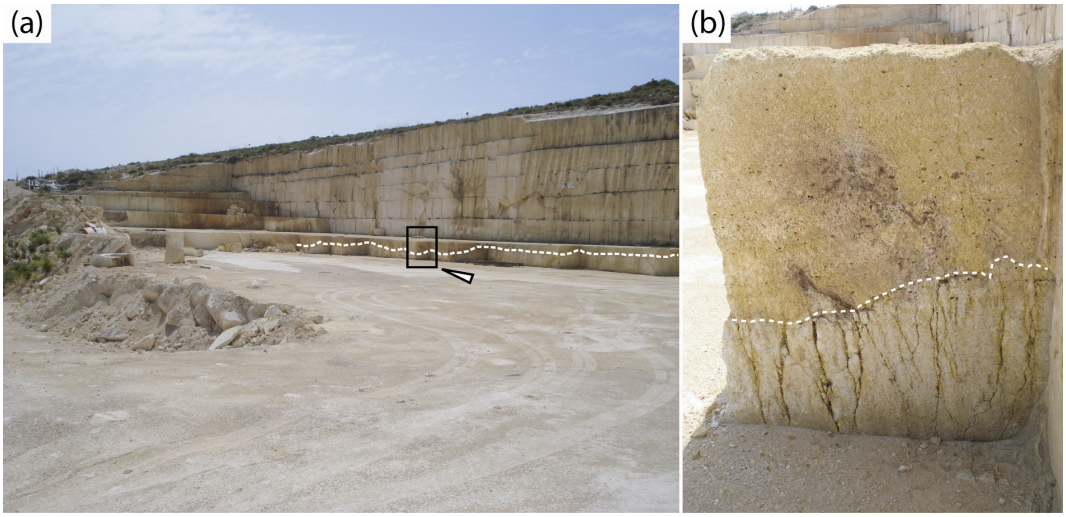

Figure 2. (a) General view of *Escúzar* quarry showing the erosive discontinuity where the exploited baseline level (dashed line) is situated. The frame indicates the position of the picture shown in **b**. **(b)** Detail of the erosive discontinuity. Note the abundance of subvertical joints below the erosive discontinuity. Ashlar height is ca. 1 m.

Olivillo travertine

Relatively large Quaternary travertine formations (> 5 km^2) outcrop near the villages of *Alhama de Almería* and *Alicún* (Fig. 3). These formations were deposited in perched springline and fluvio-lacustrine environments and later locally affected by subaerial exposure processes (Voermans & Baena, 1983). Due to intense fault activity during the travertine deposition different tectonic structures have been further observed over the site, including, stylolitization and fracturation. Furthermore, the travertine beds mainly consist of banded, massive and tufaceous facies. Fenestral porosity, both parallel and perpendicular to the stratification is very common in the banded facies. The size of the pores is from 0.1 mm to 10 mm (micropores to macropores). While the massive facies exhibit intercrystalline micropores (from 0.1 μm to 10 μm), the tufaceous facies are characterized by connected macropores (≥ 5 mm). These later are the least recommended for use as ornamental stone (García del Cura *et al.*, 2008a, 2008b).

Regional sketch

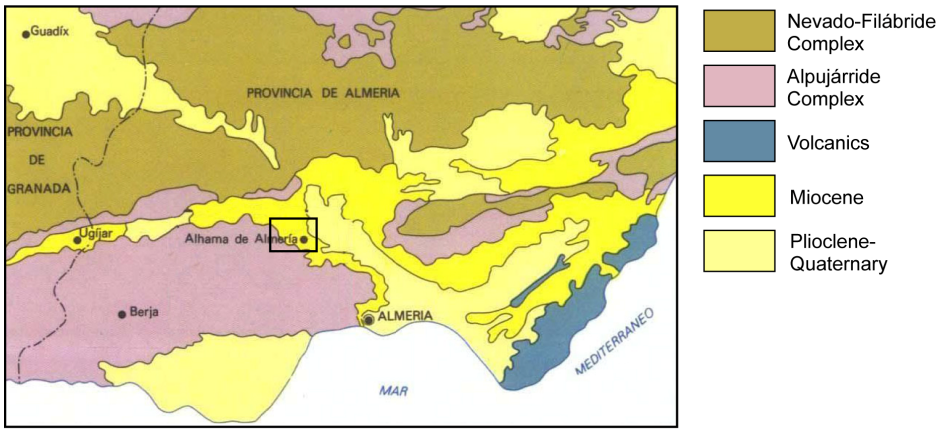

Alhama de Almería geological setting

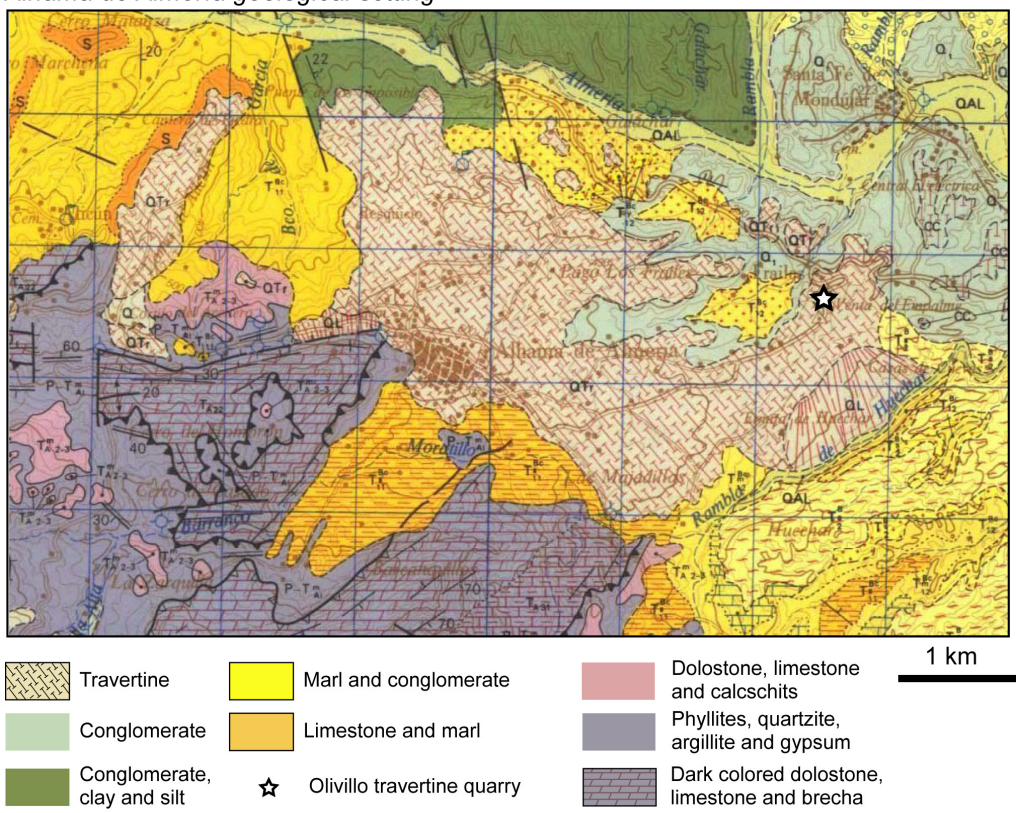

Figure 3. Regional sketch (left) and geological setting (right) for *Alhama de Almeria* travertine (Voermans & Baena, 1983).

The travertines are exploited in several quarries (Fig. 4) in the *Río Andarax* drainage basin (Almería province, southeastern Spain). The travertine selected for this PhD study is commercially known as *Olivillo travertine*, which is commonly used as building stone in modern architecture and restoration interventions in Granada's architectural heritage.

Figure 4. Travertine quarry in *Alhama de Almería* (picture courtesy of M.A. García del Cura)

Sierra Elvira limestone

Sierra Elvira is a small mountain of 1098 m high (Fig. 5), located approximately 10 km to the NW of the city of Granada (southern Spain). Geologically is interpreted as a Mesozoic horst and is part of the most southern part of the Middle Subbetic domain in the central section of the Betic Cordillera (Braga *et al.*, 1979). It comprises Triassic, Jurassic and Cretaceous materials that were deposited on the Tethys realm and is surrounded by Neogene-Quaternary materials of the Granada basin. The Liassic age (Carixian, i.e. 185-190 Ma) crinoid limestone and micritic limestones from the *Sierra Elvira* are very common stones used as building and ornamental materials. Crinoids are equinoderms characterized by a cup-shaped body, feathery radiating arms and either a stalk or clawlike structure used to attach to a substrate. The *Sierra Elvira* crinoid limestone contains also fragments of molluscs,

Figure 5. **(a)** View from the North of the *Sierra Elvira* limestone quarry (*Cerro del Tajillo de la Mina*, *Atarfe*, Granada). **(b)** Minor quarry between *El Tajillo de la Mina* and *Ermita de los Tres Juanes* (behind).

brachiopods and foraminifera. The presence of ammonites is also not rare. In the Sierra Elvira domain two stratigraphic levels can be clearly distinguished. The lower and thicker (about 20 m) is characterized by large-scale unidirectional lamination and a high density of stylolites. The upper level (about 5 m) is characterized by hardground-like cross-lamination associated with polygonal cracks caused by desiccation (Linares & Rivas, 1973; Braga *et al.*, 1979). The *Sierra Elvira* limestone is mainly composed by calcite grains although in some cases the stylolite cavities contain dolomite crystals (Sebastián Pardo *et al.*, 2008). However, the occurrence of dolomite is highly variable and can be the major carbonate mineral in highly dolomitized lithotypes (Lupiani & Soria Mingorance, 1988). The dolomitization process is believed to postdate the diagenesis due to circulation of Mg-rich fluids from the underlying thick sequence of dolostone (ca. 200 m) which are older in age (Hettangian, 197-201 Ma).

The crinoid limestone is commercially known as *piedra de Sierra Elvira* (Sierra Elvira stone) and the less common micritic limestone as *piedra losa* (slab stone) (Durán Suárez & García-Casco, 2000; Sebastián-Pardo, 2000). The crinoid limestone was the last geological formation deposited before the great carbonate platform on the southern rim of the European plate broke due to the formation of the Atlantic Ocean around 180 million years ago (García-Hernández *et al.*, 1979). Sierra Elvira is a key place to observe Middle Triassic crinoid facies

due to the stratigraphic continuity and development of the Liassic formation (Fig. 6). In addition, palaeoenvironmental conditions led to vast accumulation of equinoderms. The *Sierra Elvira* crinoid limestone is by far the most exploited stone variety in the Granada area and widely used in facades, fountains, columns and plinths in some of Granada's most emblematic historic buildings, including the Royal Hospital, the Palace of Charles V (Alhambra), the Royal Chancellery and the Cathedral.

Regional sketch

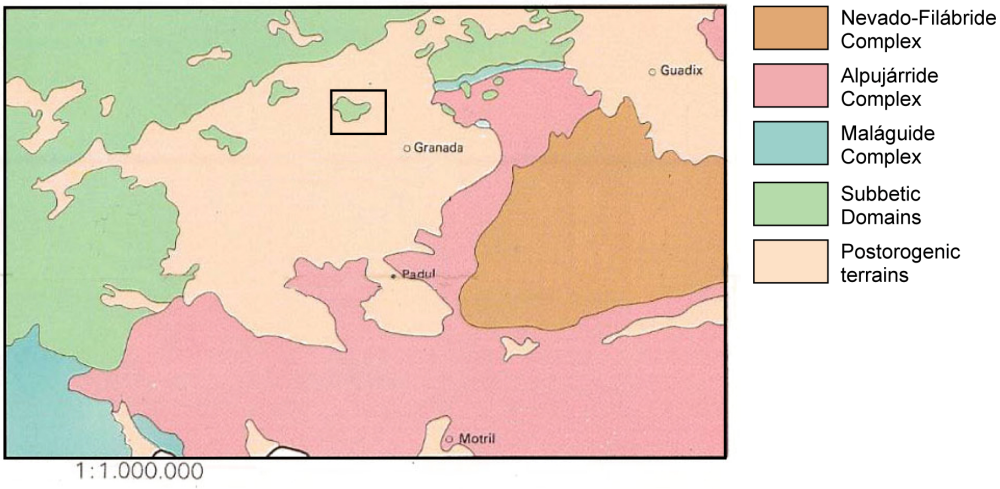

Sierra Elvira geological setting

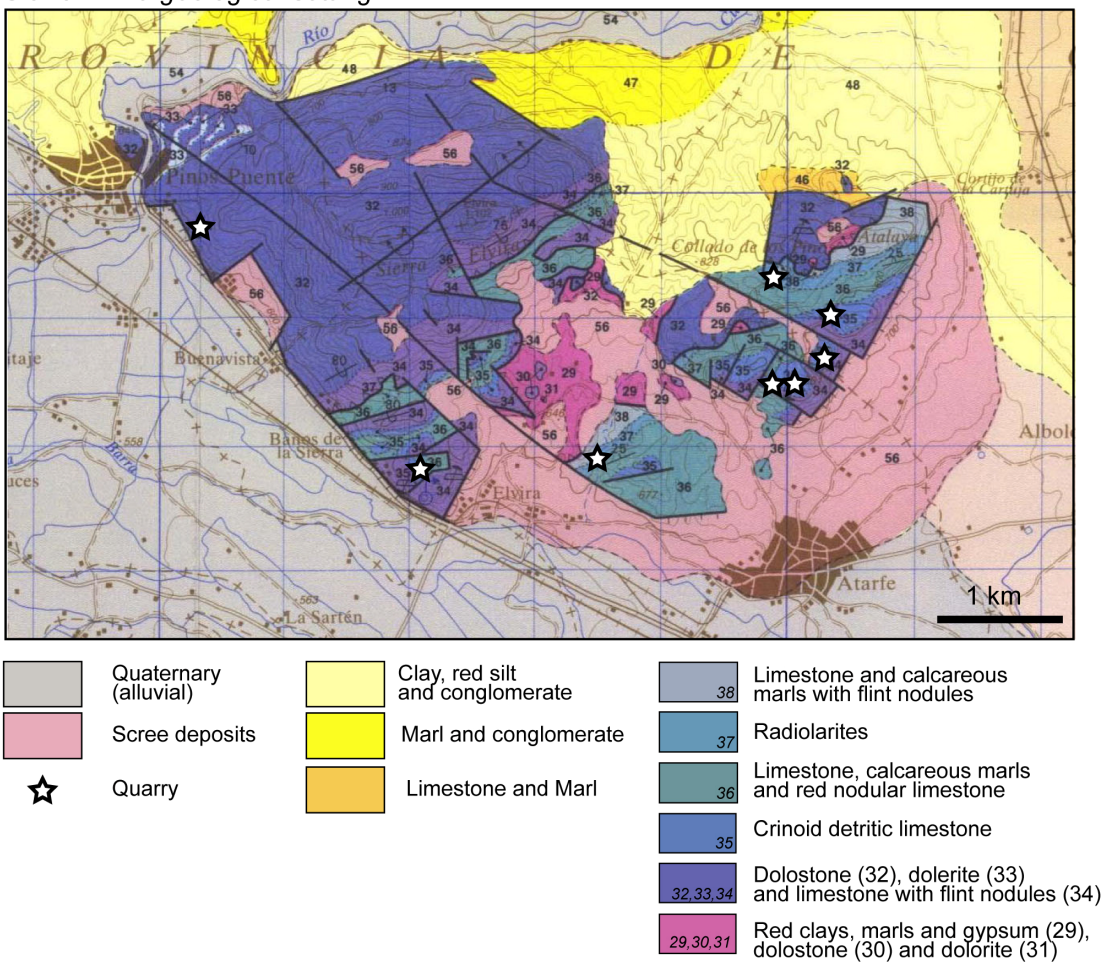

Figure 6. Regional sketch (left) and geological setting (right) for *Sierra Elvira* limestone (Lupiani & Soria Mingorance, 1988).

2.2. Atmospheric aerosols in Granada

Granada is a nonindustrialized, medium size city in southeastern Spain with a population of around 300,000. The population of the entire urban area is estimated to be 600,000. Granada is located in an intraorogenic basin surrounded by mountains with the highest elevations located at the southeast of the basin. Meteorological conditions prevailing in spring and summer favors the arrival of Saharan air masses. During autumn and winter the number of Saharan dust episodes is reduced while Atlantic and continental air mass are dominant (Lyamani *et al.*, 2004, 2006, 2008, 2010). Average climate data for the city of Granada is summarized in Table 1.

Table 1. Climate data for Granada (altitude: 687 m) (source http://www.aemet.es/)

Period: 1971-2000 - **Altitude**: 687 m

Mes	T	TM	Tm	R	H	I
Jan	6.8	12.2	1.3	44	74	161
Feb	8.4	14.1	2.6	36	69	161
Mar	10.7	17	4.3	37	62	207
Apr	12.6	18.8	6.4	40	59	215
May	16.5	23.1	9.8	30	55	268
Jun	21.3	28.8	13.9	16	48	314
Jul	25.3	33.5	17.1	3	41	348
Aug	25.1	33.2	17.1	3	42	320
Sep	21.2	28.5	14	17	52	243
Oct	15.7	21.9	9.5	40	64	203
Nov	10.6	16.2	5.1	46	73	164
Dec	7.9	13.1	2.8	49	76	147
Year	15.2	21.7	8.7	361	60	2751

Caption

T	Average temperature °C	R	Precipitation (mm)
TM	Average of highest temperature °C	RH	Relative humidity (%)
Tm	Average of lowest temperature °C	I	Sunshine hours

The air quality of Granada is permanently controlled (every 10 min 24 h per day) by the Andalusian Centre for Environmental Studies (CEAMA) and the Department of Applied Physics (University of Granada). The air quality is monitored through several stations placed in the city (Fig. 7) and at the Granada's province coast (Motril). Detailed information regarding to several atmospheric gases and the particulate matter measured in these fixed stations are annually summarized and the data are available worldwide. The measured values include: (1) particulate matter with aerodynamic diameter smaller than 10 μm (PM10), (2) light scattering (σ_{sca}), light absorption (σ_{abs}), coarse and fine particle density, scattering albedo (ω_{0A}) measured by means of aerosol optical properties (CEAMA) and (3) NO, NO_2, NO_x, CO, SO_2 and O_3. Next, a short report of these parameters is provided for the period 2008-2009 that corresponds to the natural long-term ageing test (Chapter 9). The report is summarized from internal reports elaborated by Lyamani and Bravo Aranda (2009, 2010).

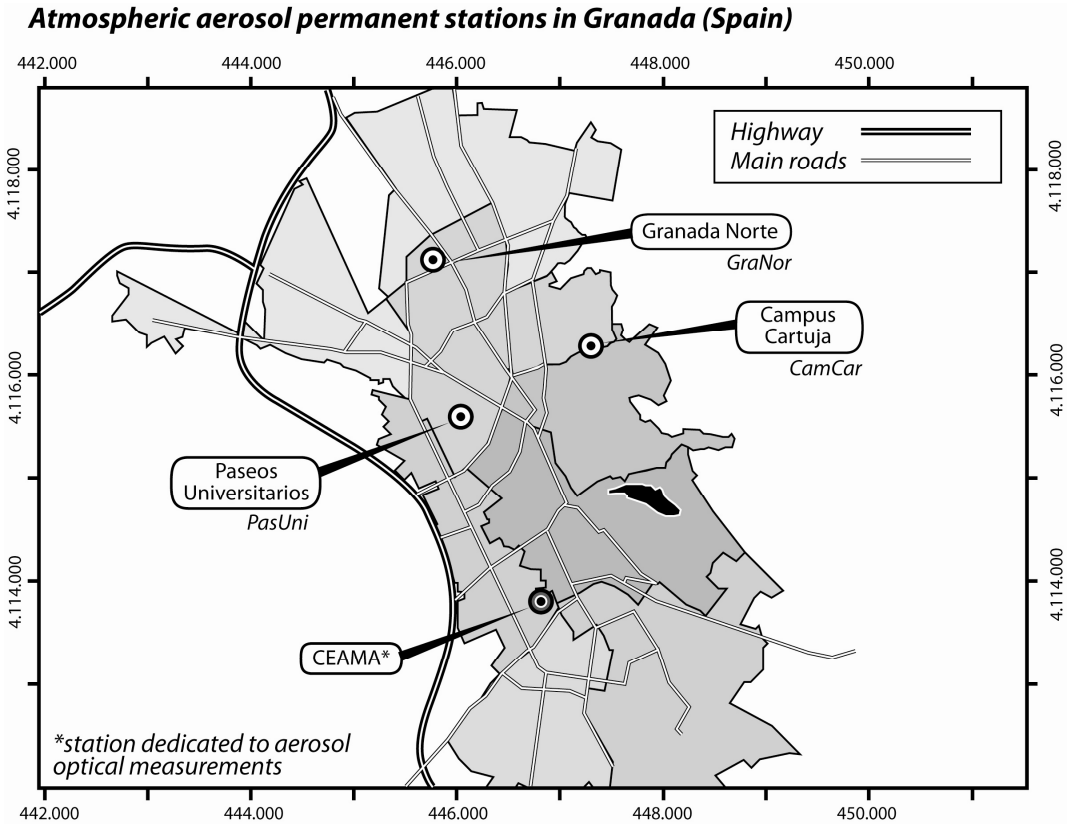

Figure 7. Map of the Granada city with its different suburbs in grey tones. Locations of the aerosol permanent stations are shown with dotted circle. Highways and main roads are also shown.

2.2.1. Particulate matter (PM10)

Spatial variations on the PM10 concentration for 2008 and 2009 are shown in Fig. 8 using Box Whisker diagrams. The notation PM10 is used to describe particles of 10 micrometers or less in aerodynamic diameter. All values measured in Granada city stations, including the one considered as urban background (*Campus Cartuja*), are higher than at the seacoast (*Motril*). This is a clear consequence of higher pollution in the city characterized by a high traffic density. Among the stations from the city of Granada, the lowest PM10 concentrations were found in the *Campus Cartuja* station that is explained by its location far from the traffic density sites. PM10 for *Granada Norte*, *Paseos Universitarios* and *Campus Cartuja* are similar to other spanish stations influenced by traffic. For instance Querol and coworkers (2004) report urban background levels of PM10 ranging from 30 to 40 μg m^{-3} and between 45 and 50 μg m^{-3} in roadside stations.

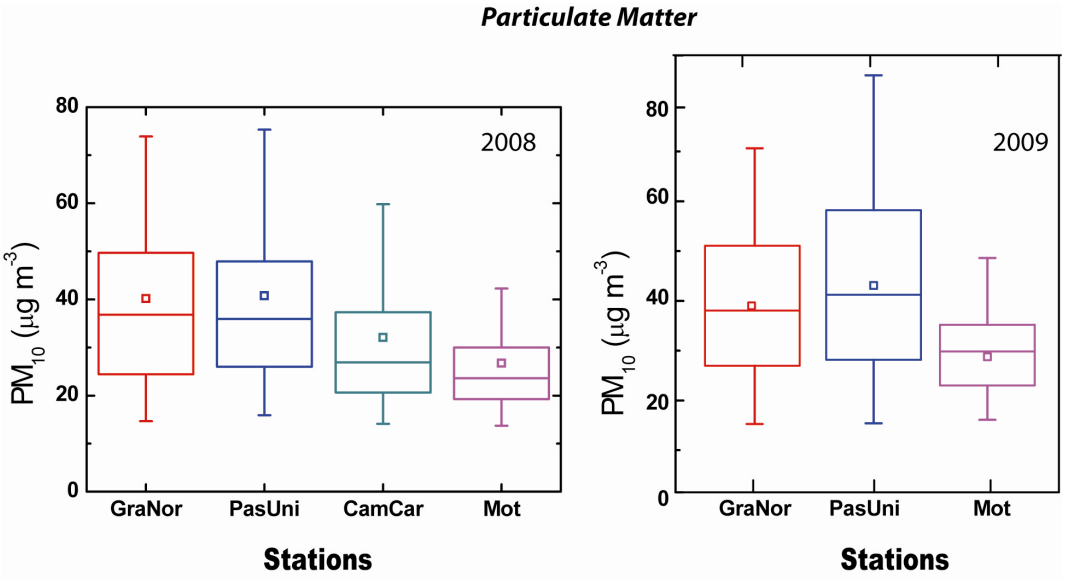

Figure 8. Box-Whisker diagram showing the PM10 concentration for aerosol sampling in Granada during 2008 and 2009. Box limits are 25 and 75 percentile, the line inside the box is the median, the outer limits are the 5 and 95% of the data and the small square the average value. See for acronyms in Figure 7.

Fig. 8 shows that *GraNor* and *PasUni* have the highest PM10 concentrations (ca. 30-50 μg m^{-3}) due to traffic influence. Values are higher in summer due to saharian dust and European air mass intrusions and particle resuspension as a consequence of higher temperature, drier surrounding areas terrain, fires and relatively high wind speeds. Atlantic mass intrusions in winter decrease the PM10 concentration. PM10 values are lower during weekends due to the reduction in traffic, construction and demolition. Highest values of PM10 (60-70 μg m^{-3}) are found during traffic rush hours (at 09.00 and 21.00 h) whereas minimum values (25-35 μg m^{-3}) are observed at 05:00h and 16:00h.

2.2.2. Optical properties

Light scattering and absorption properties of aerosol particles can be interpreted in terms of particle size distributions and by its sources (Lyamani *et al.*, 2008). Coarse particles, with aerodynamic diameter greater than 1 μm, are weak light absorbers and commonly have a mechanical origin, such as erosion or resuspension. On the contrary, particles from the accumulation mode are strong light absorbers and have several sources including combustion.

In the CEAMA station, optical counters measure, in real time, aerosol concentration and particle diameter in range between 0.50 and 20 μm. Aerosol particles are classified as N_F ($0.5<D<1$ μm) and coarse N_C ($1<D<20$ μm) and represented as number of particles per air volume (#/m^3). Based on the measurements of light scattering (σ_{sca}) and light absortion (σ_{abs}), the single scattering albedo at 670 nm, ω_{0A} (670 nm) can be computed, which is the ratio between σ_{sca} and $\sigma_{sca}+\sigma_{abs}$. Purely scattering aerosols (e.g. sulfate) exhibit values of $\omega_{0A} = 1$, while very strong absorbers (e.g. black carbon) have values of 0.3 (Lyamani *et al.*, 2008).

Fig. 9 shows the variation of average values of coarse (N_C) and fine (N_F) particle density and single scattering albedo at 670 nm (ω_{0A}) in the CEAMA station. Fine particle density is

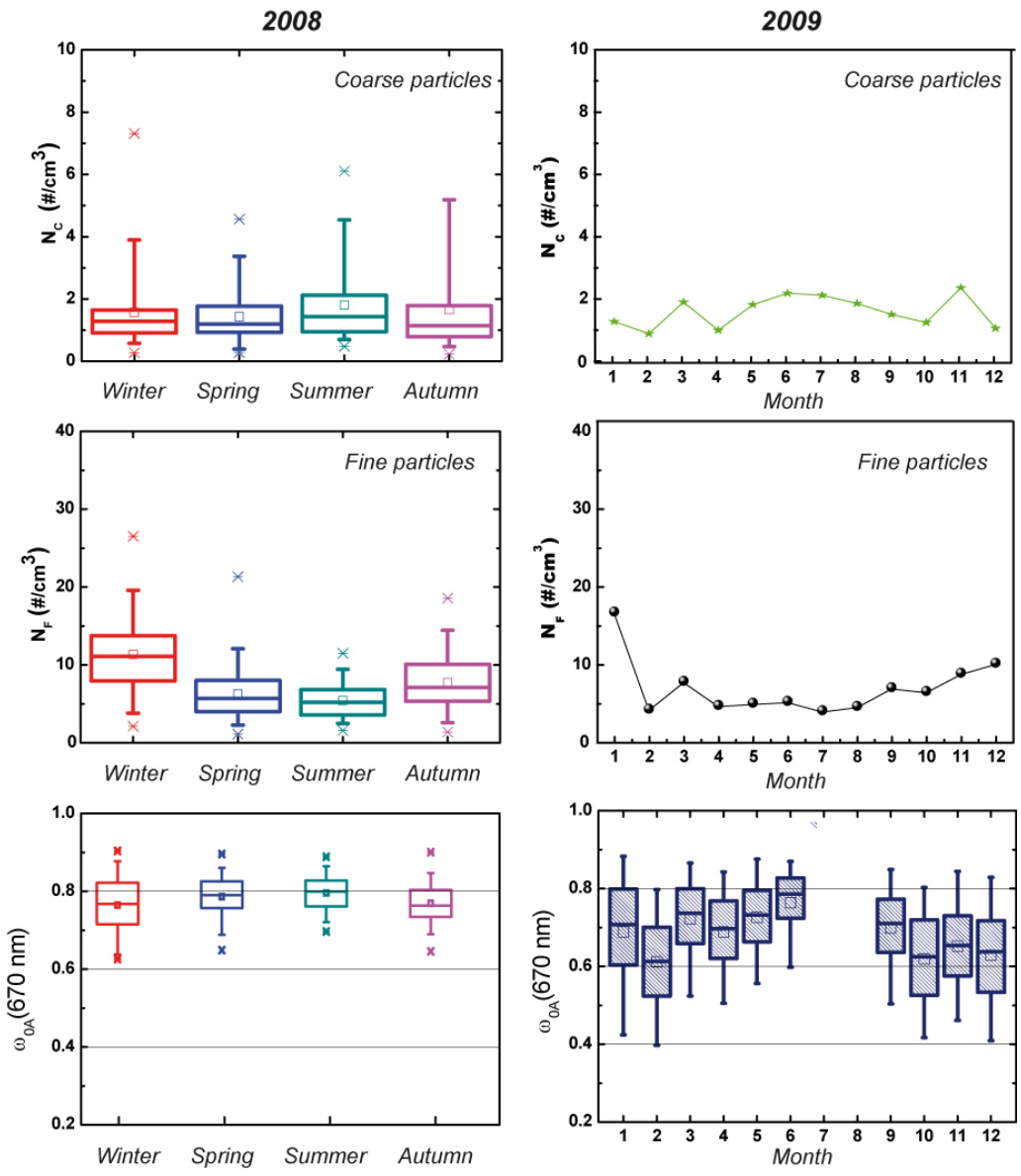

Figure 9. Seasonal values of coarse particle density (N_C), fine particle density (N_F) and scattering albedo (ω_{0A}) which is related to the black carbon concentration in the CEAMA station for 2008-2009.

higher in winter than in summer, and is related to an increase of the anthropogenic activities such as domestic heating (mainly diesel central heating) and meteorological stagnation conditions (reduction of wind speed). On the contrary, coarse particle density is slightly higher in summer than in winter. This increase in N_C is due to the combination of arid conditions and relatively high wind speeds which favour soil particle in suspension.

Average values of single scattering albedo ranged from 0.5 to 0.8 (Fig. 9), indicating that about 35% of the aerosol light extinction was due to absorption. These values are lower compared with other cities like Beijing or Atlanta indicating that the aerosols in Granada contain a large fraction of absorbing material, e.i. black carbon particles (Lyamani *et al.*, 2006, 2008). Single scattering albedo in urban areas is generally related to the black carbon formation from combustion sources, although dust can also contribute to the aerosol light absorption.

2.2.3. Pollutant gases

The spatial variation of pollutant gases NO, NO_2, NO_x, CO and SO_2 for 2008-2009 is shown in Fig. 10. Similarly to the PM10 concentration, the lowest pollutant gases concentration was found at the sea coast (*Motril*). In general the highest values were found in the stations closer to dense traffic (*Granada Norte*) whereas the lowest values correspond to the background station (*Campus Cartuja*).

SO_2 concentration do not show any seasonal variation exhibiting rather constant values thought the year. In general SO_2 is low in all station pointing out that Granada is a non-industrialized city. Also this low concentration addresses the low sulfur content of fuel used for vehicles.

On the other hand, seasonal variations of NO, NO_2, NO_x and CO have been observed in all stations with higher values in winter and lower in summer. The cyclic variation of the concentration of these pollutant gases can be explained by a combination of factors including seasonal variations of vertical distribution of these gases, variation of the sources and meteorological conditions. For instance domestic heating emissions during winter are an active source of pollutant gases in Granada (Lyamani *et al.*, 2008).

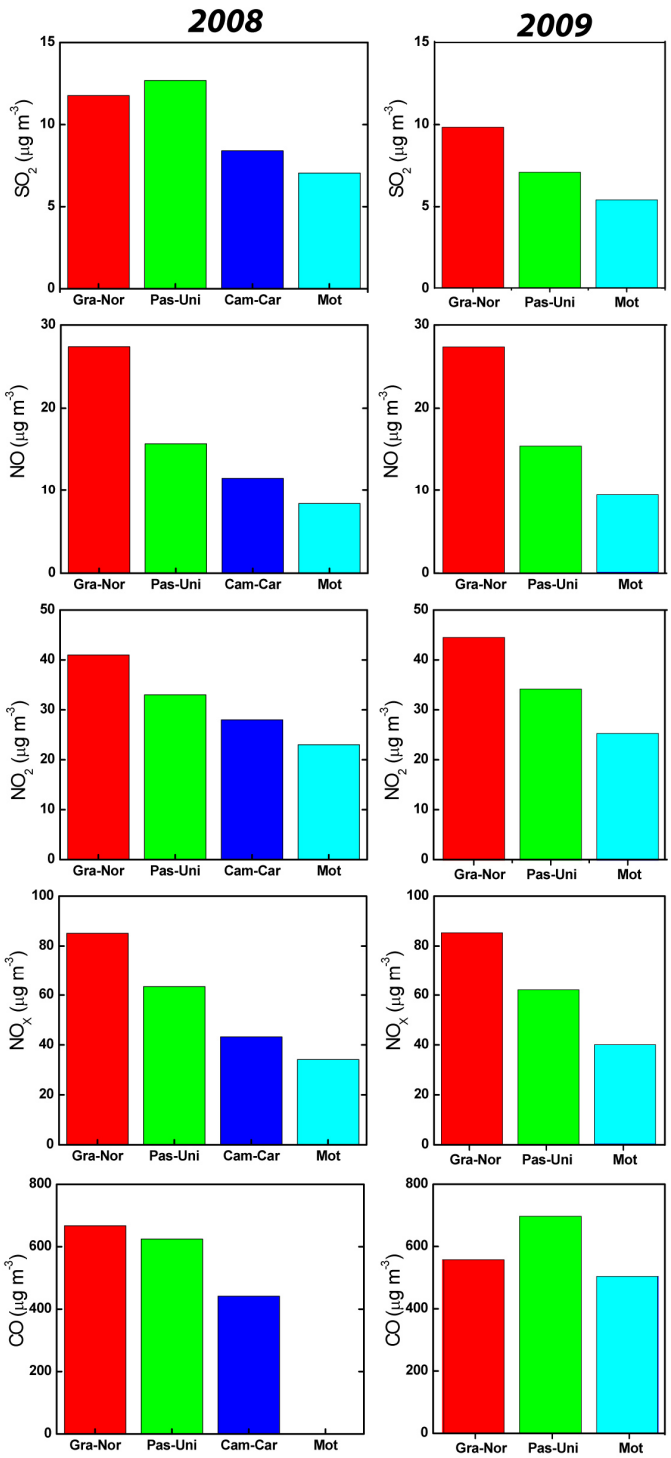

Figure. 10. Spatial variations in the concentration of SO_2, NO, NO_x and CO measured in the Granada province stations for 2008-2009. See for acronyms in Figure 7.

It is well known that ozone (O_3) is a secondary pollutant formed by a complex series of chemical reactions beginning with several pollutant precursors such as NO_x and volatile organic compounds (VOCs) – especially hydrocarbons – in the presence of atmospheric oxygen and sunlight. On the other hand ozone breakdown depends on the occurrence of certain substances in the air. Ozone formation is usually limited by the catalytic effect of NO. The spatial variation in the ozone concentration for 2008 and 2009 is shown in Fig. 11. The concentration of ozone was 30% higher in the background station (*Campus Cartuja*) compared to the other stations with denser traffic. Ozone shows a characteristic behavior that makes it peculiar refer to other atmospheric pollutants. One of these features is its high reactive character. Ozone combines instantaneously with reducing gases, particularly with one of its precursors, NO. Therefore, in dense traffic sites, such as the *Granada Norte* station, the newly emitted NO can be combined with ozone and thus decreasing its concentration. On the other hand, when precursor gases are transported by the wind far from the ozone emission source, higher concentration of ozone can be accumulated due to the lacking of reacting species. This could explain why the *Campus Cartuja* station (which is located in the outer edge of the city) recorded highest ozone values than, the more polluted, *Granada Norte* station.

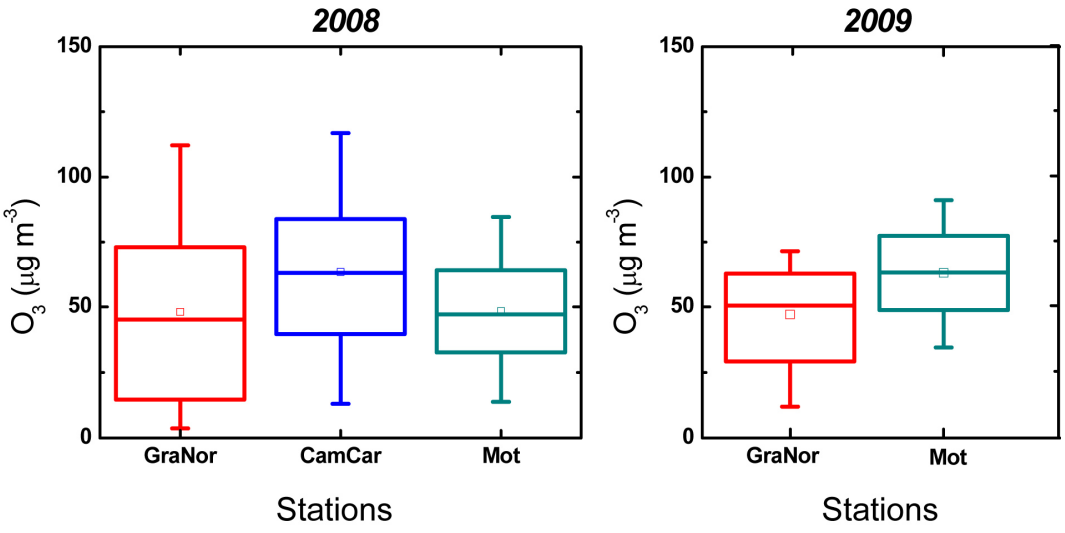

Figure 11. Box-Whisker diagram showing the ozone concentration for Granada's aerosol sampling stations for 2008-2009. Box limits are 25 and 75 percentile, the line inside the box is the median, the outer limits are the 5 and 95% of the data and the small square the average value. See for acronyms in Figure 7.

2.3. References

Alonso, F.J., Esbert, R.M., Ordaz, J. and Grossi, C.M., 2004. Reactivity of laser-cleaned stones to a SO_2 ageing test. Materiales de Construcción, 54(273): 45-55.

Arizzi, A., Belfiore, C.M., Cultrone, G., Rodríguez-Navarro, C., Sebastián Pardo, E. and Triscari, M., 2007. Petro-chemical and physical investigations on the "Santa Pudia Calcarenite" (Andalusia, Spain): New hints for the prevention and conservation of calcarenitic building materials. Geochimica et Cosmochimica Acta, 71(15): A35-A35.

Benavente, D., Martínez-Martínez, J., Cueto, N., García-del-Cura, M.Á. and Medina-Lapeña, J., 2009. Influencia de la petrografía en las propiedades petrofísicas y de durabilidad del Travertino Clásico. Valoración de su anisotropía. Geogaceta, 46: 147-150.

Braga, J.C., Jiménez, A.P. and Rivas, P., 1979. El Jurásico de Sierra Elvira (estudio especial de lias medio y inferior). Cuadernos de geología, Universidad de Granada, 10: 597-604.

Cardell, C., 1998. Cristalización de sales en calcarenitas. Aplicación al Monasterio de San Jerónimo, Granada. Tesis Doctoral, Departamento de Mineralogía y Petrología, Universidad de Granada.

Cardell, C., Benavente, D. and Rodriguez-Gordillo, J., 2008. Weathering of limestone building material by mixed sulfate solutions. Characterization of stone microstructure, reaction products and decay forms. Materials Characterization, 59(10): 1371-1385.

Cultrone, G., Sebastián, E. and Huertas, M.O., 2007. Durability of masonry systems: A laboratory study. Construction and Building Materials, 21(1): 40-51.

Dabrio, C.J. and Polo, D., 1985. Interpretación sedimentaria de las calizas de crinoides del Carixiense Subbético. Mediterránea, 4: 55-77.

Durán-Suárez, J.A., García-Casco, A., Sánchez-Navas, A. and Rodríguez-Gordillo, J., 1993. Caracterización de las alteraciones en pilares de travertino de la Iglesia del Salvador (Granada). Propuestas restauradoras. Boletín de la Sociedad Española de Mineralogía, 16: 1-12.

Durán-Suárez, J.A. and García-Casco, A., 2000. Conservación y restauración de caliza de Sierra Elvira (caliza microesparítica). La Piedra de Sierra Elvira. Historia y estética: 17-27.

Fort, R., 2006. Utilización de la piedra natural en restauración, Seminarios de la Sociedad Española de Mineralogía, 2: 155-182.

García-Hernández, P., Rivas, P. and Vera, J.A., 1979. El Carixiense en la Zona Subbética. . Cuadernos de geología, Universidad de Granada, 10: 375-382.

García del Cura ,M.A., Bernabéu, A., Fort, R., La Iglesia, A. and Ordóñez S., 2005. Use of the microcrystalline limestone as building material: the "Gris Pulpis" case. Materiales de Construcción, 55: 5-23.

García del Cura, M.A., Benavente, D., Bernabéu, A., González–Martín, J.A., Martínez–Martínez. J., Rodríguez M.A. and Sanz–Montero, M.E, 2007a. Porosity features of travertines from SE Spain used as building stone in construction and architectural restoration. Preliminary report. Geophysical Research Abstracts, EGU2007-J-04039-1.

García del Cura, M.A., La Iglesia, A., Benavente, D., Bernabéu, A. and González Martín, J.A., 2007b. Mineralogía de los travertinos pleistocenos de Albox (Almería), importante recurso de materia prima de rocas ornamentales. Macla, 7: 89.

García del Cura, M.A., La Iglesia, A., Ordóñez, S., Sanz-Montero, M.E. and Benavente, D., 2008a. Óxidos de hierro y manganeso en travertinos de Alhama de Almería. Macla, 9: 107.

García del Cura, M.A., Sanz-Montero, M.E., Benavente, D., Martínez-Martínez, J., Bernabéu, A. and Cueto, N., 2008b. Sistemas travertínicos de Alhama de Almería: características petrográficas y petrofísicas. Geotemas, 10: 1555-1558.

Garibaldi, V., 1999. Studio petrografico e fisico - meccanico del calcare a crinoidi utilizzato nell' architetturadi Granada (Andalucía, Spagna), Tesi Sperimentale di Laurea, Università di Pavia.

Gauri, K. and Bandyopadhyay, J.K., 1999. Carbonate stone. Chemical behavior, durability and conservation. J.Wiley & Sons, New York.

González Donoso, J.M., Gallego, J.A. and Sanz de Galdeano, C. (1980). Mapa Geológico de España 1:50.000. Hoja 1026 Padul. Geological and Mining Institute of Spain (IGME), Madrid.

Jroundi, F., Fernández-Vivas, A., Rodriguez-Navarro, C., Bedmar, E. and González-Muñoz, M., 2010. Bioconservation of deteriorated monumental calcarenite stone and identification of bacteria with carbonatogenic activity. Microbial Ecology, 60(1): 39-54.

Linares, A. and Rivas, P., 1973. El Lias medio en la parte sur de la Zona Subbética (Sierra Elvira, Illora e Iznalloz, Provincia de Granada) Cuadernos de geología, Universidad de Granada, 4: 141-154.

Lyamani, H., Olmo, F.J. and Alados-Arboledas, L., 2004. Long-term changes in aerosol radiative properties at Armilla (Spain). Atmospheric Environment, 38: 5935-5943.

Lyamani, H., Olmo, F.J., Alcántara, A. and Alados-Arboledas, L., 2006. Atmospheric aerosols during the 2003 heat wave in southeastern Spain II: Microphysical columnar properties and radiative forcing. Atmospheric Environment, 40: 6465-6476.

Lyamani, H., Olmo, F.J. and Alados-Arboledas, L., 2008. Light scattering and absorption properties of aerosol particles in the urban environment of Granada, Spain. Atmospheric Environment, 42: 2630-2642.

Lyamani, H. and Bravo Aranda, J.A., 2009. Informe de calidad del aire de Granada: año 2008. Informe interno, Universidad de Granada, Granada (Spain).

Lyamani, H. and Bravo Aranda, J.A., 2010. Informe de calidad del aire de Granada: año 2009. Informe interno, Universidad de Granada, Granada (Spain).

Lyamani, H., Olmo, F.J. and Alados-Arboledas L., 2010. Physical and optical properties of aerosols over an urban location in Spain: seasonal and diurnal variability. Atmospheric Chemistry and Physics, 10:239–254.

Luque, A., Cultrone, G., Sebastián, E. and Cazalla, O., 2008. Effectiveness of stone treatments in enhancing the durability of bioclastic calcarenite in Granada (Spain). Materiales de Construcción, 58(292): 115-128.

Luque, A., 2010. Andalusian marbles: durability criteria applied in its use as ornamental stone. Doctoral Thesis. Department of Mineralogy and Petrology. University of Granada (Spain).

Lupiani, E. and Soria Mingorance, J.M., 1988. Mapa Geológico 1:50.000, Hoja 1009 Granada. Geological and Mining Institute of Spain (IGME), Madrid.

Martín-Algarra, A., Martín-Martín, M., Andreo, B., Julia, R. and González-Gómez, C., 2003. Sedimentary patterns in perched spring travertines near Granada (Spain) as indicators of the paleohydrological and paleoclimatological evolution of a karst massif. Sedimentary Geology, 161: 217-228.

Rodríguez-Navarro, C., 1994. Causas y mecanismos de alteración de los materiales calcáreos de la catedrales de Granada y Jaén. Tesis Doctoral, Universidad de Granada, Granada (Spain).

Rodríguez-Navarro, C. and Sebastián, E., 1996. Role of particulate matter from vehicle exhaust on porous building stones (limestone) sulfation. The Science of the Total Environment, 187(2): 79-91.

Rodríguez-Navarro, C. and Sebastián-Pardo, E., 1991. Procesos de alteración de los materiales calcareníticos utilizados en la construcción de la Catedral de Granada: Variación en el contenido de elementos traza. IV Congreso de Geoquimica de España, 1: 312-323.

Rodríguez-Navarro, C., Sebastián-Pardo, E. and Ruiz-Agudo, E., 2008. Plan director del Hospital Real: Estudio de materiales, formas y mecanismos de alteración". Informe interno, Universidad de Granada, Granada (Spain).

Ruiz-Agudo E., 2007. Prevención del daño debido a la cristalización de sales en el patrimonio histórico construido mediante el uso de inhibidores de la cristalización. Tesis Doctoral. Universidad de Granada, Granada (Spain).

Ruiz-Agudo, E., Lubelli, B., Sawdy, A., Van Hees, R., Price, C. and Rodriguez-Navarro, C., 2010. An integrated methodology for salt damage assessment and remediation: the case of San Jerónimo Monastery (Granada, Spain). Environmental Earth Sciences, DOI: 10.1007/s12665-010-0661-9.

Sandrolini, F., Franzoni, E., Cuppini, G. and Caggiati, L., 2007. Materials decay and environmental attack in the Pio Palace at Carpi: A holistic approach for historical architectural surfaces conservation. Building and Environment, 42(5): 1966-1974.

Sebastián Pardo, E., 2000. Características petrográficas y físico-mecánicas de la piedra de construcción de Sierra Elvira. La Piedra de Sierra Elvira. Historia y estética: 11-16.

Sebastián Pardo, E., Zezza, U., Rodríguez-Navarro, C., De la Torre, M.J. and Cardell, C., 1992. La 'Piedra Franca', biocalcarenita, en la construcción de edificios históricos de Granada, . I Cong. Int. Rehabilitacion del Patrimonio Historico y Edificacion, Vol. 1, pp. 329-336.

Sebastián Pardo, E., Cultrone, G., Garibaldi, V., Rodríguez Navarro, C., De la Torre. M.J. and Valverde, I., 2008. La Caliza de Sierra Elvira: comportamiento petrofísico de una piedra significativa del Patrimonio Arquitectónico Andaluz. Materiales de Construcción, 58(289-290): 51-63.

Silva, Z.S.G. and Simão, J.A.R., 2009. The role of salt fog on alteration of dimension stone. Construction and Building Materials, 23(11): 3321-3327.

Simão, J., Ruiz-Agudo, E. and Rodríguez-Navarro, C., 2006. Effects of particulate matter from gasoline and diesel vehicle exhaust emissions on silicate stones sulfation. Atmospheric Environment, 40(36): 6905-6917.

Smith, B.J., Gómez-Heras, M., Viles, H.A. and Cassar, J., 2010. Limestone in the built environment: present-day challenges for the preservation of the past. Geological Society of London, Special Publications, 272 pp.

Voermans, F. and Baena, J., 1983. Mapa geológico de España 1:50.000. Hoja 1.044 Alhama de Almería. Mapa y memoria. Geological and Mining Institute of Spain (IGME), Madrid.

Chapter 3

METHODOLOGY:

ANALYTICAL TECHNIQUES AND AGEING TESTS

Complementary analytical techniques have been used to address at nano-, micro- and macroscale the goals of this PhD Thesis. These techniques are briefly explained in the following paragraphs.

3.1. Chemical and mineralogical characterization of materials

3.1.1. X-ray fluorescence (XRF)

X-ray fluorescence was used to determine major and minor elements of fresh stone samples before being subjected to the ageing tests. Moreover, this technique was also applied to analyze the bulk elemental content of the atmospheric aerosols from the city of Granada collected by Nuclepore® filters (see section 3.3.1.).

The stone samples were analyzed by a Bruker S4 Pioneer X-ray fluorescence spectrometer (IACT-CSIC-University of Granada) with wavelength dispersion equipped with

a goniometer that held analyzing crystals (LIF200/PET/OVO-55) and Rh X-ray tube (60 kV, 150 mA). Semiquantitative scanning spectra were obtained using the software *Spectraplus*. Stone powder (~ 5 g) was blended with wax (Hoestch wax C micropowder Merck) using a 5100 SPEX Mixer/Mill. Then each sample was uniformly deposited onto a cellulose substrate contained in a 40 mm aluminium cup. Finally, the product was pressed at 10 ton (Mignon-S de Nannetti) to obtain a pressed pellet (40 mm sample disc).

The aerosol particles collected on the filters were determined by energy dispersive X-ray fluorescence (EDXRF) during my short research stay at the University of Antwerp, Belgium (Department of Chemistry, Micro and Trace Analysis Center). The details of the applied instrument and analysis conditions are described in section 3.3.1.

3.1.2. X-ray diffraction (XRD)

The mineralogical composition of the fresh stone samples, the stone pore filling in the polished travertine samples and the bulk aerosol samples were determined by powder X-ray diffraction. The stone samples and the stone pore filling were milled in an agate mortar to less than 50 μm particle size. No sample preparation was required for aerosol samples as XRD was applied directly to the Nuclepore® filter surfaces used to collect the bulk aerosol samples. All samples were analyzed by a Philips PW-1710 diffractometer (Department of Mineralogy and Petrology, University of Granada) equipped with an automatic slit window. Analysis conditions were: radiation Cu Kα (λ: 1.5405 Å), 40 kV voltage and 40 mA current intensity. Explored area for stone samples and stone pore filling was between 3º and 60º 2θ and goniometer speed of 0.01º 2θ/s, and for the aerosol samples between 3º and 64º 2θ, with 0.05 scan rate, and 0.80 integration time.

The efflorescences that crystallized on the stone surfaces during the sea-salt ageing test conducted in this PhD Thesis (section 3.4.1) were analyzed using a XPERT-PRO diffractomer (Department of Mineralogy and Petrology, University of Granada). Analysis conditions were: radiation Cu Kα (λ: 1.5405 Å), 45 kV voltage, 40 mA current intensity, explored area between 4º and 70º 2θ and goniometer speed using Si-detector X'Celerator of

0.01º 2θ/s. In addition, grazing incidence X-ray diffraction (GXRD) was applied to characterize the precipitate layer on dolomite crystals (used for the AFM and VSI experiments), which was formed during the dolomite dissolution, at acid conditions, in the AFM experiments (section 3.5.2.). The grazing angle (ω) was 2º and the explored area between 5º and 60º 2θ. Automatic acquisition, evaluation and identification of minerals were performed by Xpowder software (Martín Ramos, 2004).

3.1.3. Optical microscopy (OM)

Petrographic characteristics (texture and mineralogy) of fresh and aged stone samples were examined under polarized optical microscopy using an Olympus BX-60 equipped with digital camera (Olympus DP10). To this aim, polished thin sections were prepared with ethanol to avoid salt dissolution, and stained with red alizarin to differentiate calcite from dolomite (calcite tints to red while dolomite remains unstained).

The microscopic surface features of dolomite crystals subjected to dissolution were also observed using the same optical microscope. Observations were performed both under transmitted and reflected (polarized) light.

3.1.4. Scanning electron microscopy in back-scattered electron mode (SEM-BSE)

Scanning electron microscopy (SEM) operating in back-scattered electron mode was applied to study the chemical composition of the minerals at the fresh carbonate stone surfaces. The samples were investigated under a LEO 1430-VP variable pressure scanning electron microscope (VPSEM) and an Oxford Instruments Inca 350 energy dispersive X-ray (EDX) microanalysis system. The results were processed with INCA® software. The gold- and platinum-coated samples were studied at 15 kV in a high vacuum. The spectra were acquired in a range of 5 to 20 kV.

The chemical composition of precipitated salts on the carbonate stone surfaces after the ageing tests was studied by means of environmental scanning electron microscopy (ESEM) on a Phillips Quanta 400 instrument. Analysis conditions were 20 kV acceleration voltage and 1 nA probe current and working distance of 10 mm.

In addition, polished thin sections (~30 μm thick) of aged calcarenite samples exposed to natural decay were studied. Single point elemental analyses and X-ray maps of carbon coated stone surfaces were acquired. The SEM-EDX working conditions were 500 pA filament current and 10 eV/ch resolution for pinpoint analyses, and 1 nA filament current and 20 eV/ch resolution for map acquisition. The beam energy used was 20 keV. Maps of 1024 × 786 pixels were obtained in selected areas with 500 frames and dwell time of 10 μs. Furthermore, the *Phasemap* tool was applied to identify mineral phases using ternary element plots of specific pixel information from X-ray maps. The procedure for mineral map acquisition involves the use of so-called "ternary phase diagrams". The software generates mineral maps of relative concentrations for up to three elements specified by the user. The element information embedded in each image pixel is rearranged in such a way that regions of similar (ternary) composition can be determined in the phase diagram. Superposition of images obtained from different "ternary phase diagrams," represented as a false color map, then yields a "phase map". To give a realistic reconstruction of mineral distribution in the cross-sectioned sample, the obtained mineral map can be "mixed" into the BSE image. Quantitative analysis was done with the Point & ID tool in the software.

3.1.5. Transmission electron microscopy (TEM)

The composition and morphology of the atmospheric particles deposited on the stone surfaces during long-term natural ageing test and those collected by filters were studied by transmission electron microscopy (TEM). A Philips CM20 equipped with an EDAX solid-state ultrathin-window energy dispersive X-ray (EDX) detector was used. The acceleration voltage of the microscope was 200 kV, and a lens aperture of 40 μm was employed as a compromise between amplitude and phase contrast for the images. The identification of mineral phases was facilitated by collecting selected area electron diffraction (SAED)

patterns. Prior to TEM analysis, particles were dispersed in ethanol, sonicated for 30 s, and placed on Formvar© and C-coated Cu grids.

3.1.6. Transmission-Fourier Transform infrared spectroscopy (T-FTIR)

Transmission-Fourier transform infrared spectroscopy (T-FTIR) was used to characterize the epoxy silicone resin composition used in the polishing treatment of the commercialized *Olivillo* travertine. The T-FTIR spectrum was registered from 3999 to 400 cm^{-1} with a resolution of 2 cm^{-1}. 200 scans were collected using a NICOLET spectrometer 20SXB. The T-FTIR spectrum was obtained from KBr pellet prepared by uniformly mixing 5 mg of powdered sample with KBr (3 wt. %).

3.1.7. Micro-Raman spectroscopy (MR)

Micro-Raman spectroscopy was used to identify tiny crystals precipitated onto the calcarenite slabs after the natural ageing test (see section 3.4.2). The advantage of micro-Raman analysis is that no sample preparation is required enabling an accurate identification of small amount of mineral phases. The calcarenite slabs (10 × 10 × 2 cm) were examined with a Renishaw RM1000 dispersive spectrometer equipped with a Leica DMLM optical microscope (Department of Geology, University of Jaén), a grating with 1200 grooves/mm and a Peltier-cooled CCD detector. Raman spectra were obtained with the 785 nm emission of a diode laser with 30 mW laser power and Leica 20 × and 50 × objectives were used. The wavenumber accuracy was better than 1 cm^{-1} and the spectral resolution was about 2.5 cm^{-1}. The system was operated in the confocal mode, resulting in an approximate lateral resolution of ca. 3 μm.

3.1.8. X-ray photoelectron spectroscopy (XPS)

A thin surface precipitate layer formed on dolomite crystals during dissolution at pH 3 was analyzed with X-ray photoelectron spectroscopy. Optical grade dolomite crystals (3 × 3 × 1 mm) were investigated under a Physical Electronic PHI 5701 spectrometer equipped with

a multi-channel hemispherical electroanalyzer. Non-monochromatic Mg Kα X-ray radiation (300 W, 158 kV, 1253.6 eV) was applied as the excitation source. The spectrometer energy scale was calibrated using Cu 2p3/2, Ag 3d5/2, and Au 4f7/2 photoelectron lines at 932.7, 368.3 and 84.0 eV, respectively. The binding energy of photoelectron peaks was referenced to C 1s core level for adventitious carbon at 284.8 eV. High resolution spectra were obtained at a given take-off angle of 45º by a concentric hemispherical analyzer operating in the constant pass energy mode at 29.35 eV and using a 400 μm diameter aperture. The binding energy of photoelectron peaks was referenced to C 1s core level for adventitious carbon at 284.8 eV. Acquisition and data analysis were performed by a PHI ACCESS ESCA-V8.0C software package. Recorded spectra were fitted using Gauss-Lorentz curves in order to accurately determine the binding energy of the different element core levels. After a Shirley-type background subtraction, atomic concentration percentages of the dolomite elements were determined from high-resolution spectra and the corresponding area sensitive factor for every photoelectron line was taken into account (Moulder *et al.*, 1992). Survey and multiregion spectra were recorded for C 1s, O 1s, Ca 2p and Mg 2p photoelectron peaks. A depth profiling (up to 6 nm deep) was carried out by 4 keV Ar^+ bombardment.

3.2. Determination of physical properties of carbonate stones

3.2.1. Mercury intrusion porosimetry (MIP)

This technique is used to measure the pore size distribution and the open porosity of a solid material. The measurement is based on the non-wetting behavior of the mercury versus the solid surface and its high surface tension. The required pressure to intrude increases as the size of the pore decreases. Therefore, a plot of intruded volume of mercury as a function of the external pressure gives an indication of the pore size distribution (Siegesmund & Snethlage, 2011).

Blocks of ca. 2 cm^3 of fresh and aged stone samples (containing salts) were dried in an oven during 24 h at 60 ºC, and analyzed on a Micromeritics Autopore III model 9410

porosimeter (Department of Mineralogy and Petrology, University of Granada). The instrument consists of two low-pressure and one high-pressure port and works within the pressure range from almost zero up to 60000 psia (414 MPa) that enables measuring pore diameters from 0.003 to 360 μm.

3.2.2. Argon adsorption

This technique was used to study the smallest pores between 1 and 100 nm (10-1000 Å) of fresh and aged samples after the sea-salt ageing test. The aged samples (rough and polished surfaces) were washed in distilled water during one week prior to the measurements. The purpose of this procedure was to discern the binding or cementing effect of the salts in the stones. Different fluids can be used as adsorbates in this technique and the most common is the nitrogen. In stone samples with surface area smaller than 5 m^2/g is more realistic to use argon (Ar) than nitrogen, which usually yield excessively high values (Sing *et al.*, 1985). The Ar adsorption isotherms were obtained at 196 ºC on a Micromeritics Tristar 3000. Prior to measurement, samples were heated to 250 ºC for 8 h and outgassed to 10^{-3} Torr using a Micromeritics Flowprep.

The gas adsorption analysis was used to determine the total specific surface area (Gregg & Sing, 1982; Adamson & Gast, 1997), and the Barret–Joyner–Halenda (BJH) method to obtain pore size distribution curves, the pore volume and the mean pore size of the stone samples (Barret *et. al.*, 1951). Additionally, the surface fractal dimension, D_S, was determined from adsorption data and used to characterize the surface roughness. The analysis of the gas adsorption isotherms using a modified Frenkel–Halsey–Hill (FHH) theory (Tang *et al.*, 2003) allows determination of surface fractal dimension from the slope (A) of the plot of Ln(V) vs. $Ln[Ln(P/P_0)]$, where V is the adsorbed volume of gas, and P and P_0 are the actual and condensation gas pressures. When surface tension (or capillary condensation) effects are important, the relationship between A and D_S is $A = D_S - 3$. Capillary condensation is significant if $\delta = 3(1 + A) - 2 < 0$. The pressure range and therefore the thickness range of the adsorbed layer coverage revealed that samples were purely monolayer (since n = 1–2). This thickness range ensures that the determination of D_S is reliable (Tang *et al.*, 2003).

3.2.3. Hydric tests

Diverse hydric tests (free water absorption, water saturation by the vacuum method, hydrostatic weighting, desorption, capillary ascent and suction) were applied to characterize the porous system and obtain information about the dynamics of fluids inside the quarried stone materials. According to the standards UNE (1999, 2002) and RILEM (1980), cubes of 5 cm in size were prepared for absorption and desorption hydric tests, and blocks of 2x2x10 cm for capillary ascent and suction tests. The samples were dried in an oven during 24 h at 60 ºC to remove the moisture they might contain.

3.2.4. Ultrasonic wave velocity measurements

Ultrasonic measurements were performed in fresh stone samples by Panametrics HV Pulser/Receiver 5058 PR connected to Tektronix TDS 3012B osciloscope. P and S waves were measured in cubes (5 × 5 × 5 cm) by transducers at 25ºC and RH of 50% applying the frequencies of 0.5 MHz (S waves) and 1 MHz (P waves). Afterwards, several parameters were calculated: compression wave velocity (V_P), shear wave velocity (V_S), Young modulus (E_d), Poisson's ratio (v_d) and total and relative anisotropy coefficients (ΔM and Δm) of P and S waves. The equations used to calculate the parameters mentioned above were the following:

Young modulus (E_d) in GPa,

$$E_d = \rho_{bulk} V_P^2 \frac{(1-2\nu_d)(1+\nu_d)}{(1-\nu_d)} \qquad (1)$$

Poisson's ratio (v_d)

$$v_d = \frac{(V_P/V_S)^2 - 2}{2[(V_P/V_S)^2 - 1]} \qquad (2)$$

Total and relative anisotropy for P and S waves in % (ΔM_P, ΔM_S, Δm_P and Δm_S, respectively) according to Guydader & Denis (1986),

$$\Delta M_P = [1 - \frac{2V_{P1}}{(V_{P2} + V_{P3})}] \cdot 100 \quad (3)$$

$$\Delta m_P = \frac{2(V_{P2} - V_{P3})}{(V_{P2} + V_{P3})} \cdot 100 \quad (4)$$

The velocities V_{P1}, V_{P2} and V_{P3} correspond to the minimum, maximum and intermediate velocity measured along three orthogonal directions. Similar expressions are applied also for S waves.

3.2.5. Colorimetry and spectrophotometry

The color of building stones used in the architectural heritage is one of the most important characteristics that define their aesthetic properties. Many aesthetic decays are produced by environmental conditions and urban pollution and therefore, the stone color stability is an essential parameter that must be understood and monitored properly (Benavente *et al.*, 2003). The color depends on the mineral phases present and the texture of the studied materials. Due to atmospheric pollutants the minerals can be replaced with others and the texture can be modified (García Pascual *et al.*, 1999).

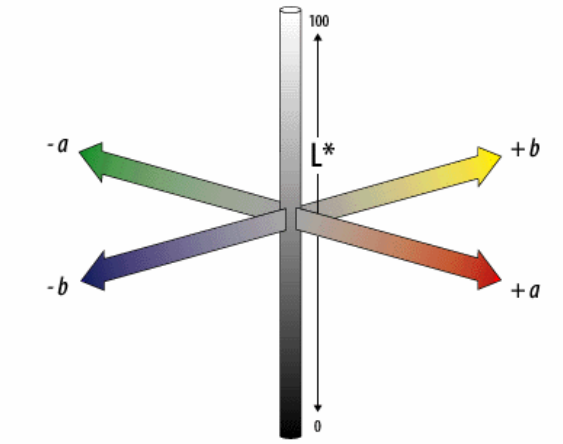

Figure 1. 3D illustration of the CIELAB color system (1976). L* = luminosity (0-100); a* = +a (red), -a (green); b* = +b (yellow), -b (blue).

In this investigation, the chromatic parameters of rough and polished stone samples before and after the sea-salt

ageing test were determined using a Minolta CR 210 colorimeter, with 0º viewing angle and 50 mm diameter measuring area. The CIE illuminant C was applied with a color temperature of 6774 K that simulates the daylight. On the other hand, color changes in calcarenite samples after a long-term ageing test were measured more precisely by a Minolta CM-700d spectrophotometer using a 8 mm diameter. Both C and D65 (color temperature: 6504 K) illuminants were used.

All obtained data were expressed by an alphanumeric code of CIE L*a*b* (Fig. 1) and CIE L*C*H* color systems (Wyszecki & Stiles 1982) where L* represents the color luminosity (brightness, lightness) varying from black with a value of 0 to white with a value of 100; a* varies between +a* (red) and -a* (green), and b* varies between +b* (yellow) and -b* (blue).

The total color difference is described as ΔE* and is calculated using the following equation:

$$\Delta E^* = \sqrt{(\Delta L^*)^2 + (\Delta a^*)^2 + (\Delta b^*)^2} \tag{5}$$

In the CIELCH (L*C*H*) system the same diagram is used as in the previous system with some difference in coordinates. L* represents luminosity, C* color saturation or chroma and H* the hue and are calculated as described below:

$$C^* = \sqrt{(a^*)^2 + (b^*)^2} \tag{6}$$

$$H^\circ = tg^{-1}\frac{b^*}{a^*} \qquad \text{when } a^* > 0 \text{ and } b^* \geq 0 \tag{7a}$$

$$H^\circ = 180^\circ + tg^{-1}\frac{b^*}{a^*} \qquad \text{when } a^* < 0 \text{ and } b^* > 0 \text{ or } a^* < 0 \text{ and } b^* < 0 \tag{7b}$$

$$H^\circ = 360^\circ + tg^{-1}\frac{b^*}{a^*} \qquad \text{when } a^* > 0 \text{ and } b^* < 0 \tag{7c}$$

3.3. Sampling and characterization of atmospheric aerosols

A detailed study of air quality was conducted inside and outside of the Monastery of San Jerónimo that represents one of the main buildings of cultural interest in the city of Granada. Indoor and outdoor concentrations of atmospheric particles and gaseous pollutants were collected and characterized precisely as described in the following paragraphs.

3.3.1. Particulate matter (bulk and single particles)

The most common approach for determining the composition of bulk aerosol particles involves the analysis of deposits collected on filter substrates. During the aerosol sampling in San Jerónimo monastery Nuclepore® filters of 0.4 μm pore-size and 47 mm diameter were used. The filters were fixed on a Millipore filter-unit (Figs. 2 and 3a & b) that was connected to a low-volume vacuum pump. The average sampling time was 24 h and the flow rate approximately 30 L min^{-1}. Bulk elemental content of particles collected on the filters was determined during my short research stay at the University of Antwerp, Belgium (Department of Chemistry, Micro and Trace Analysis Center) by energy dispersive X-ray fluorescence (EDXRF). The measurements were carried out on a Tracor Spectrace- 5000 instrument employing a low-power Rh-anode X-ray tube (17.5 W). For the determination of high-Z elements (starting from K) a tube voltage of 35 kV, a current of 0.35 mA, and an acquisition time of 10,000 s were applied. For low-Z elements (from Al to Cl), the tube voltage was 10 kV, a current 0.35 mA, and an acquisition time 4,000 s. The detection limits were between 5 and 10 ng cm^{-2} on the filters. The measured intensities were converted into elemental concentrations by the application of the AXIL program code (Van Espen *et al.* 1986). Additionally, the mineral composition of bulk particles was analyzed by means of XRD (see section 3.1.2).

Single atmospheric particles were collected using a 7-stage May cascade impactor Fig. 3c. An impactor is a device that classifies particles present in the air into known size ranges. The air is drawn into and through the impactor by a pump where encounters a cascade of progressively finer jets. The jet velocity thus increases from stage to stage and each stage

Figure 2. Field work during an aerosol sampling campaign in the Alhambra (Comares Tower).

collects finer particles than the previous one. The applied May cascade impactor contained aerodynamic cut-off diameters of 8, 4, 2, 1, and 0.5 μm that corresponded to stages 3, 4, 5, 6, and 7 (Fig. 3c). The particles were entrapped on silicon wafers and silver foils. Furthermore the size-segregated particles were analyzed by a JEOL 733 electron probe microanalyzer (EPMA) equipped with an ultra-thin window Si(Li) detector (Oxford). To avoid beam damage of the analyzed particles, the sample holder was cooled of by liquid nitrogen, which is especially important for low-Z elements, starting from C. Approximately 300 particles were measured on each stage, so almost 1,500 individual aerosol particles were analyzed in one sample set. The X-ray spectra were processed using the AXIL software (Van Espen *et al.*, 1986). Moreover, the particles were divided into three representative and main fractions: nano fraction, which contains average results of particles smaller than 1.0 μm, micro fraction, containing particles in the range between 2.0 to 10 μm, and macro fraction, comprising the average results of particles bigger than 10 μm in size. Each fraction was finally analyzed by suitable analytical techniques. The composition and morphology of nano fraction were studied with a Philips CM20 transmission electron microscope (TEM) operated

at 200 kV and equipped with an energy dispersive X-ray spectrometer (EDX). Prior to TEM analysis, particles were dispersed in ethanol and placed on Formvar C-coated Cu grids. On the contrary, micro and macro particles were analyzed by XRD and SEM-BSE (sections 3.1.2. and 3.1.4).

3.3.2. Gas pollutants

SO_2, NO_2 and O_3 were collected by means of radiello® (Fondazione Salvatore Maugeri, Padova, Italy) diffusive samplers, exposed in parallel for one week, both indoors and outdoors (5 samplers indoors, 4 outdoors). The radiello® sampler comprised a chemiadsorbing cartridge which is surrounded by a cylindrical microporous diffusive body, coated with triethanolamine (TEA) and mounted on a supporting plate (Fig. 3d).

NO_2 and SO_2 were chemiadsorbed onto TEA respectively as nitrite (NO^{2-}) and sulfite (SO_2) or sulfate (SO_4^{2-}). They were quantitatively recovered from the cartridges by means of extraction in 5 ml of Milli-Q water (Millipore, Haverhill, USA) followed by two 1-min manual stirring steps. Between them the extracts were left to settle one hour. The nitrite and sulfite contents of the extracts were finally determined by means of ion chromatography (IC). A dual-column Dionex DX-120 ion chromatograph equipped with a Dionex AS50 auto sampler was applied. A 20 μL aliquot of the sample/standard solution was loaded into the eluent-stream (11 mM H_2SO_4 at 1.0 mL min^{-1} and 3.5 mM Na_2CO_3 plus 1 mM $NaHCO_3$ at 1.2 mL min^{-1} for cations and anions, respectively). Background conductance was minimized using ASRS-ULTRA and CSRS-ULTRA suppressors. Data acquisition, construction of calibration curves and peak integration were achieved using the Peaknet® Dionex software package, version 6.11.

The diffusion tube for O_3 sampling consisted of a polyethylene tube, filled up with 4,4'-dipyridylethylene-coated silica gel and closed, at one end, by a PTFE cap. During exposure, the 4,4'-dipyridylethylene is transformed into 4-pyridylaldehyde through ozonolysis. Silica gel ensures the presence of H_2O inside the pores, necessary to complete the ozonolysis reaction. During sample preparation 4-pyridylaldehyde was recovered from the silica gel by

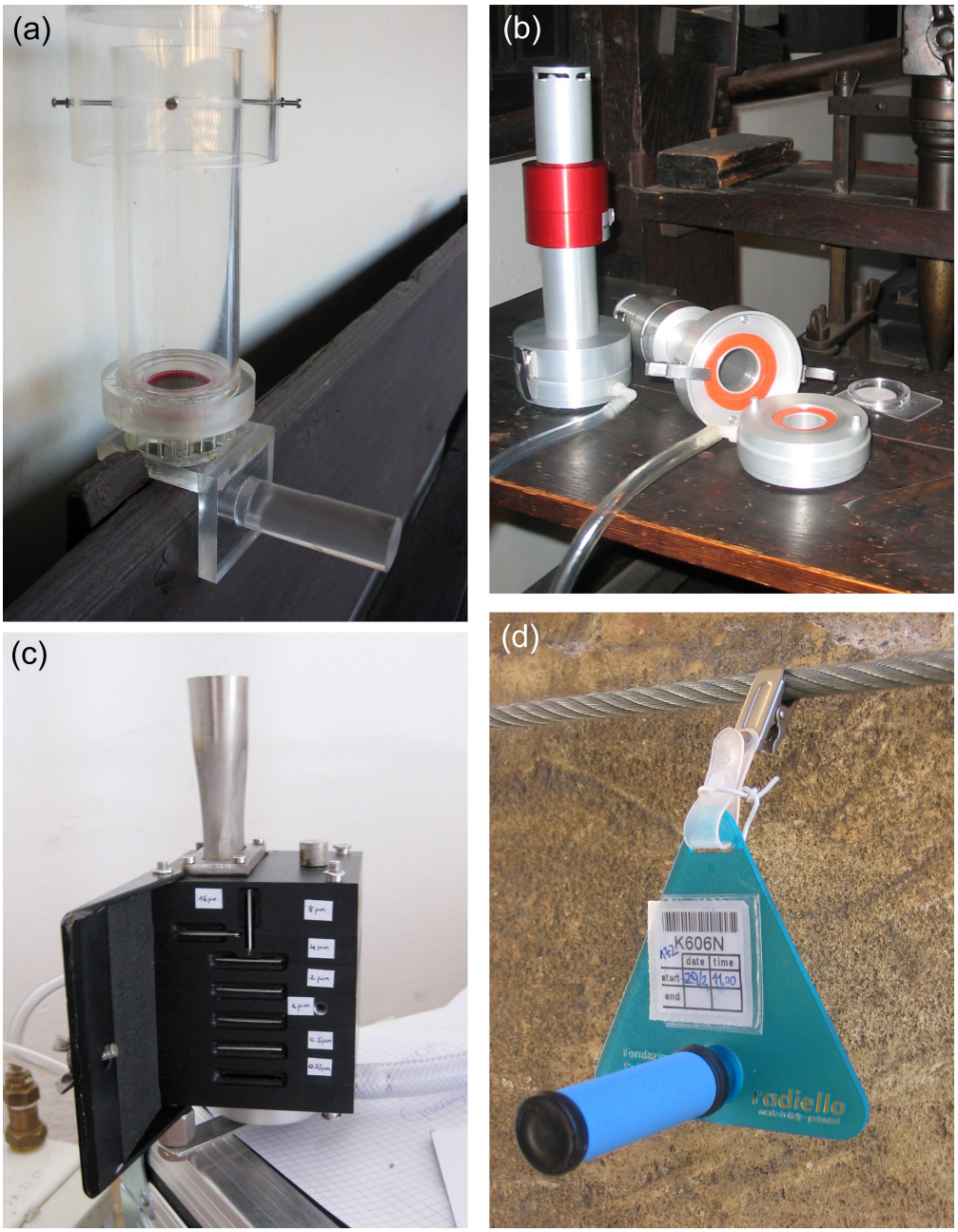

Figure 3. Several devices used in this PhD research to collect aerosol particles and gases in the Monastery of San Jerónimo. **(a)** Millipore filter-unit: Air sampler with Nuclepore® filters of 0.4 mm pore-size and 47 mm diameter, **(b)** Harvard-type impactor to collect aerosol fractions with an equivalent aerodynamic diameter from 0 to 2.5 µm (PM2.5) and 0 to 10 µm (PM10), **(c)** 7-stage May cascade impactor to collect single atmospheric particles and **(d)** Radial passive sampler (Radiello®) used for gas sampling.

adding 3-methyl-2-benzothiazolinone hydrazone (MBTH), followed by two 1-minute mechanical stirring steps, between which the extracts were left to settle one hour. Subsequently 4-pyridylaldehyde was converted into the corresponding yellow-colored azide, analyzed on UVIKON 930 UV-VIS spectrophotometer at 430 nm.

3.4. Ageing tests

3.4.1. Sea-salt ageing test

A saline spray chamber (CCONS series, INELTEC®) was used to investigate the effect of marine aerosol deposition on rough and polished stone surfaces (Figs. 4 and 5). Stone tablets (5 × 5 × 1 cm) were hung on a nylon thread from plastic bars inside the chamber so that all sample faces were exposed to the salt spray (Fig. 4). According to international standards such as e.g. ASTM (B-117), DIN (50021), ISO 9227 or UNE-EN (14147) the standardized 5% solution of NaCl known as NSS (neutral salt spray) is applied. However, in this study to reproduce more realistic conditions of building stone decay in marine environment, seawater was collected from the Mediterranean Sea at the Granada coast (Salobreña, Southern Spain) and used in the ageing test instead of NaCl.

Figure 4. Saline spray chamber (CCONS series, INELTEC®) used in the ageing tests.

The use of a complex solution such as sea water modifies the solubility of NaCl, and therefore the mobility of ions present in the seawater and consequently their deteriorating effects (Rivas *et al.*, 2003).

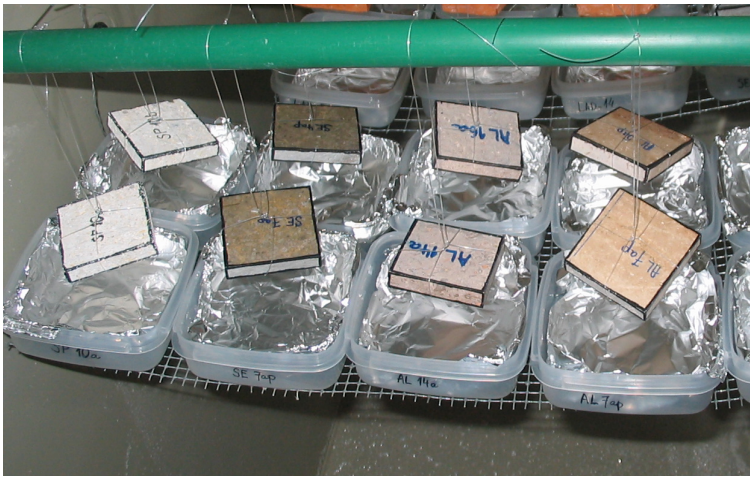

Figure 5. Sample arrangement in the saline spray chamber. Samples were hung to enhance a homogenous weathering (from left to righ, *Escúzar* calcarenite; *Sierra Elvira* limestone, rough and polished *Olivillo* travertine).

The composition of the seawater is shown in Table 1. Cations (Ca^{2+}, K^{+}, Na^{+} and Mg^{2+}) were determined by means of inductively coupled plasma-atomic emission spectrometry (ICP-AES, Leeman Labs PS series) and anions (Cl^{-}, SO_4^{2-}, NO_3^{-}) by ion chromatography (IC, Dionex DX 300). The pH of the seawater was 7.84 at 20 ºC (Eutech 1500).

Table 1. Chemical composition expressed in ppm of seawater used in this ageing test.

Cl^{-}	NO_3^{-}	SO_4^{2-}	Ca^{2+}	K^{+}	Na^{+}	Mg^{2+}
12879	72	2772	330	348.4	10030	1069

The chamber was electronically set to produce 160 cycles corresponding to 60 days. After this period the test was stopped since no significant further macroscopic changes were observed in the stones. Each cycle consisted of 3 h of seawater spray followed by 6 h of drying by forced air at 35 ºC and relative humidity of 70 ± 2%. The chamber remained closed throughout the test, thus during the spray periods the relative humidity was higher (ca. 98%).

3.4.2. Long-term natural ageing test

In order to unravel the initial stages of stone decay under the polluted environment of the city of Granada, representative carbonate stone samples were placed in four sites for a long-time monitoring. This type of approach has been demonstrated to be very useful in understanding stone weathering under realistic conditions (e.g. Cardell *et al.*, 2002; Delalieux *et al.*, 2002; Grossi *et al.*, 2003). The chosen sites in the city of Granada (for site location see Chapter 9) are believed to be representative of low and high pollution levels. The four selected sites differs in terms of sun irradiation times, degree of surface rain-washing and distance to heavy-traffic that ensures a wide spectrum of factors controlling the weathering. Stone slabs (10 × 10 × 2 cm) were placed vertically at outdoor conditions for up to 2 years and were analyzed at 12 and 24 months. The stone decay was characterized by analyzing in depth the thin black crust developed on the stone surfaces by means of ESEM observations, EDX analysis and EDX-mapping, micro-Raman and TEM. To monitor the color change during this long-term experiment, chromatic measurements were also conducted.

3.5. Micro- and nanoscopic study of crystal surface topography

The most common techniques used for studying crystal surface topography are scanning electron microscopy (SEM) and atomic force microscopy (AFM). More recently, vertical scanning interferometry (VSI) has been developed as a new tool to distinguish and trace the reactive parts of crystal surfaces. VSI and AFM are complementary techniques and practically well suited to detect surface changes. However, each method has its own limitations and the proper choice of suitable method depends on features of the analyzed surface and primary goals of research. The main features and differences between SEM, AFM and VSI are summarized in Table 2.

Table 2. A comparison of SEM, AFM and VSI mean features (from Kurganskaya *et al.*, 2009).

	SEM (conventional)	AFM	VSI
Lateral resolution	0.5 - 1 nm	1-5 nm	0.5-1.2 μm
Vertical resolution	Only 2D images	0.05 nm (3D)	2 nm (3D)
Field of view	1-2 mm	100 × 100 μm	500 × 500 μm (10× objective)
Vertical range of scan	-	10 μm	1 mm
Sample preparation	Required coating of a conducted material	-	-
Required environment	Vacuum	Air, liquid	Air

3.5.1. Scanning electron microscopy in secondary electron mode (SEM-SEI)

Scanning electron microscopy in secondary electron mode (SEM-SEI) was applied to study the stone microtexture. Chips of fresh carbonate stones were investigated under a LEO 1430-VP variable pressure scanning electron microscope (VPSEM). The gold- and platinum-coated samples were studied at 15 kV in a high vacuum.

In addition, an environmental scanning microscopy (ESEM) was applied to study the crystal habits of precipitated salts without disturbing their hydration state on the stone surfaces after the sea-salt ageing test (section 3.4.1). Moreover, the ESEM technique was used also to analyze the black crusts formed on the calcarenites during the natural ageing test. In contrast to the conventional SEM, no sample preparation is required for ESEM analysis. Chips of aged stone samples were studied on a Phillips Quanta 400 instrument, applying 20 kV acceleration voltage, 1 nA probe current and working distance of 10 mm.

On the other hand, the study of mineral reaction mechanisms has been revolutionized with the development of new techniques for the nanoscale imaging of mineral surfaces (e.g. Lüttge *et al*., 1999, 2003). Despite the considerable increase in our knowledge about mineral replacement reaction gained with these new techniques, little has been done in its application

to Cultural Heritage conservation field. In the following sections, two of these cutting-edge techniques are described since both were applied to investigate dolomite dissolution in this PhD Thesis.

3.5.2. Atomic force microscopy (AFM)

Atomic force microscopy is a powerful tool allowing a variety of surfaces to be imaged and characterized at the atomic level (Fig. 6). The AFM technique was developed in 1986 and the first commercial devices were produced in 1989 (Blanchard, 1996). AFM provide a number of advantages over conventional microscopy such as the direct representation of three-dimensional images. The most outstanding feature of this technique is its vertical resolution which is about 0.01-0.05 nm on both insulators and conductors and thus providing the imaging of atomic surface variations like dissolution steps or island growth over a large range of materials (Hall & Cullen, 1955; Jordan & Rammensee, 1997; Shiraki *et al.*, 2000; Shtukenberg *et al.*, 2005; Ruiz-Agudo *et al.*, 2009, 2010, 2011). In contrast to conventional SEM, AFM does not require a vacuum environment enabling the imaging at ambient conditions or even in liquid environment with minimal sample preparation.

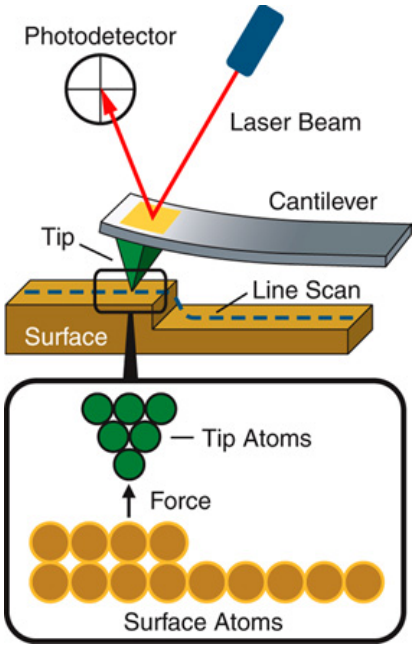

Figure 6. Schematic representation of AFM principles. The repulsive forces between the surface and tip atoms deflect the cantilever which is monitoried by a laser beam and a photodetector.

AFM can work either under 'contact mode' or 'TappingMode™'. In contact mode, a sharp tip (made either of silicon or Si_3N_4) is attached to a low spring constant cantilever. The tips have typically an end radius of 2nm to 20nm, depending on tip type. Either the repulsive force ('contact mode') or the attractive force ('taping mode') is recorded relative to spatial variations and then converted to an analogue image of the sample surface. The deflection of the cantilever-tip assemblage is detected by means of a laser beam and a

split photodiode detector. TappingMode™ AFM consists of oscillating the cantilever at its resonance frequency and lightly "tapping" the tip on the surface during scanning. Therefore TappingMode™ is best suited for image soft, fragile, and adhesive surfaces without risk of damaging. One of the principle drawbacks of the AFM is the relatively small area that can be scanned at any given time. For instance, the maximum scan area for most AFMs is approximately 100 μm^2 (Koyuncu *et al.*, 2006).

In situ AFM observations and measurements were performed in this PhD research to study the dissolution of dolomite crystal surfaces. The analyses were carried out during my short research stay at the *Institute für Mineralogie* (University of Münster, Germany). A Digital Instruments Nanoscope III Multimode AFM working in contact mode was applied under ambient conditions (T=20ºC). Freshly cleaved, optically transparent dolomite crystals from Eugi (Navarra, Spain) were used as substrates. The solutions flowed continuously for 30 min at ca. 100 mL h^{-1} from a syringe coupled to an O-ring sealed fluid cell containing the sample crystal (Fig. 7). AFM images were collected using Si_3N_4 tips (Veeco Instruments, tip model NP-S20). The scanning frequency was 4 Hz, giving an average time of 1.5 min per scan over 9 (3 × 3) μm^2 dolomite surfaces. After flowing through the fluid cell, aliquots of solutions were collected for cation analysis by inductively coupled plasma optical emission spectrometry (ICP-OES, Auto Scan 25 Thermo Jarrell Ash). Furthermore, AFM images were analyzed with the Nanoscope software (Version 5.12b48). Measurements of step retreat velocity (or etch pit spreading rate) were made from sequential images scanned in the same direction. The retreat velocity, v_{sum}, was calculated by measuring the length increase per unit time between opposite parallel steps in sequential images.

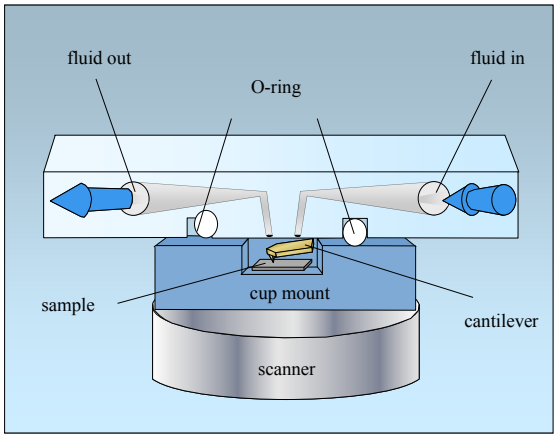

Figure 7. Arrangement of the O-ring sealed fluid cell used in the AFM experiments (courtesy of J.M. Astilleros)

3.5.3. Vertical scanning interferometry (VSI)

Optical interferometry is a type of microscopy where nanometer level characteristics of a sample surface topography may be characterized through the interpretation of light reflected from a surface (Fig. 8). With optical interferometry it is possible to obtain scan-sizes of up to a square millimeter with a vertical resolution of approximately 2 nm (Koyuncu *et al.*, 2006). Depending on the roughness of the surface two working modes can be used, namely phase shifting interferometry (PSI) and vertical scanning interferometry (VSI). The PSI mode allows measurements on smooth surfaces at the angstrom level, while the VSI mode enables to measure rough surfaces and steps at the nanometer level up to the micrometer level.

In this PhD Thesis, dolomite dissolution rates obtained by AFM were further constrained at different spatial scale with VSI measurements. VSI experiments were conducted during my short research stay at the Department of Earth Science, Rice University (Houston, Texas, USA). VSI was used to measure surface-normal retreat of single dolomite crystal faces relative to a fixed (unreacted) reference surface. Optically transparent dolomite crystals from Eugui (Navarra, Spain) were cleaved in air along $\{10\bar{1}4\}$ planes with a knife blade and then covered in few places on the surface with small spots of Pertex HI-T RTV, a high-temperature silicone rubber. The rubber spots can be taken off easily at any later stage of the experiment. The crystal with reference masks was left in the temperature-controlled, flow-through cell system for a long period of time due to the extremely slow dissolution rate of dolomite. The total run time of each experiment was up to 6 days, with measurements taken after 72 h and 144 h. To perform the measurements, the sample was taken out of the fluid cell and dried at ambient temperature. All measurements were taken *ex situ* on a MicroXam MP-8 VSI (ADE Phase Shift Inc.) with 20× 40× 50× and 80× Mirau objectives and a white light source. Measurements were acquired at constant time intervals before and after the reaction of the crystal substrate with a fluid.

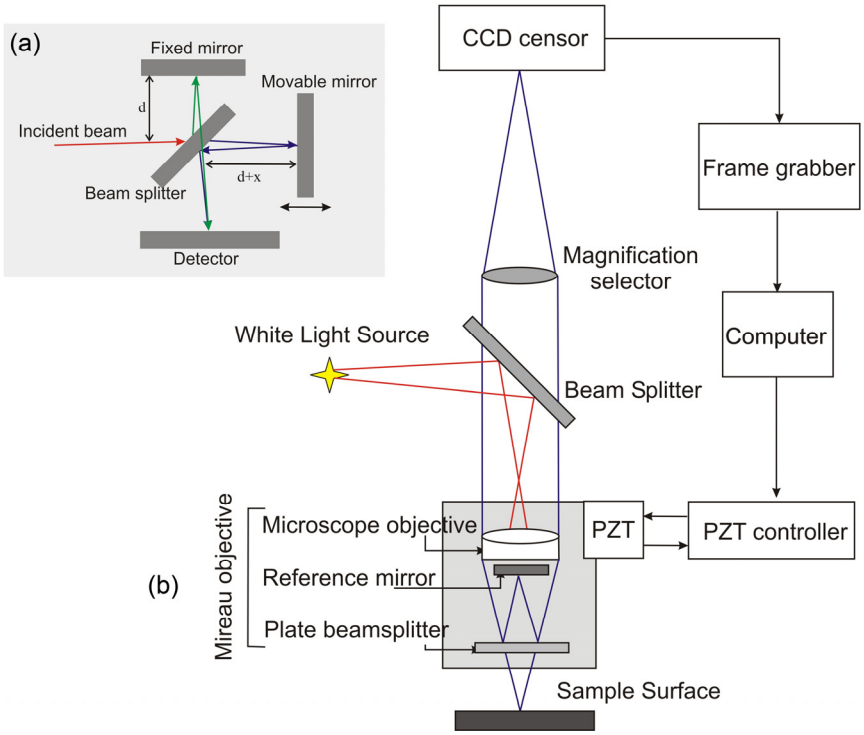

Figure 8. **(a)** Interferometry principle as used in the Michelson interferometer. Interference fringes are produced by splitting a beam of monochromatic light (red line) so that one beam strikes a fixed mirror and the other a movable mirror. An interference pattern results when the reflected beams (blue and green lines) are brought back together in the detector. **(b)** Schematic representation of the Vertical scanning interferometry (VSI) system, where the Mireau objective is based on a Michelson interferometer (Kurganskaya *et al.*, 2009).

Vertical changes in the surface topography were quantified by taking images, which were digitized with a CCD camera and converted into a topographic map with Mapvue software, ADE Phase Shift Inc. (see Lüttge *et al.*, 1999, 2003 for more experimental methods details). The resulting topographies were then compared to compute absolute dissolution rates. A large number of data for a relatively large surface areas (e.g. 140 x 156 μm) was recorded in very short acquisition times allowing robust statistical results. Therefore, VSI is considerate as an invaluable tool linking the nanoscale observations from AFM with traditional bulk solution chemistry. The change in height, h, of a given point (x,y) on a surface during the time interval from t_1 to t_2 is:

$$\frac{\Delta h}{\Delta t} = \frac{h_2 - h_1}{t_2 - t_1} = v_{\perp}$$

where $v_{\perp}$ is the velocity of surface retreat in units of e.g., cm·s^{-1}. Alternatively the change in height can be also computed using data from height profiles and a reference surface. In this case an average height difference can be calculated ($\overline{\Delta z}$). The intrinsic rate constant, R_{VSI} (in mol cm^{-2} s^{-1}) is then calculated dividing the average velocity of the surface retreat by the molar volume of the material dissolved (V_{dol}), as following:

$$R_{VSI} = \frac{\overline{\Delta z}}{\Delta t \cdot V_{dol}}$$

The preliminary results of VSI experiments at circumneutral pH solution are described and compared with AFM data in Appendix II.

3.6. References

Adamson, A.W. and Gast, A.P., 1997. Physical chemistry of surfaces. J. Wiley & Sons, New York.

ASTM B-117, 1997. Standard practice for operating salt spray (fog) apparatus. American Society for Testing and Materials, Philadelphia.

Barrett, E.P., Joyner, L.G. and Halenda, P.P., 1951. The determination of pore volume and area distributions in porous substances. I. Computations from nitrogen isotherms. Journal of the American Chemical Society, 73(1): 373-380.

Benavente, D., Martínez-Verdú, F., Bernabéu, A., Viqueira, V., Fort, R., García del Cura, M.A., Illueca, C. and Ordóñez, S., 2003. Influence of surface roughness on color changes in building stones. Color Research and Application, 28(5): 343-351.

Blanchard, C.R., 1996. Atomic Force Microscopy. The Chemical Educator, 1(5): 1-8.

Cardell, F., Vleugels, Torfs and Van Grieken, R., 2002. The processes dominating Ca dissolution of limestone when exposed to ambient atmospheric conditions as determined by comparing dissolution models. Environmental Geology, 43(1): 160-171.

Delalieux, F., Cardell-Fernández, C., Torfs, K., Vleugels, G. and Van Grieken, R., 2002. Damage functions and mechanism equations derived from limestone weathering in field exposure. Water, Air, & Soil Pollution, 139(1): 75-94.

DIN 50021, 1988. Spray tests with different sodium chloride solutions. Deutsches Institut für Normung E.V.

García Pascual, N., Sánchez de Rojas, M. and Frias, M., 1999. Medidas de color en diferentes materiales de construcción. La restauración en edificios de arenisca. Materiales de Construcción, 49: 29-45.

Gregg, S.J. and Sing, K.S.W., 1982. Adsorption surface area and porosity. Academic Press, London.

Grossi, C.M., Esbert, R.M., Díaz-Pache, F. and Alonso, F.J., 2003. Soiling of building stones in urban environments. Building and Environment, 38(1): 147-159.

Guydader, J. and Denis, A., 1986. Propagation des ondes dans les roches anisotropes sous contrainte évalution de la qualité des schistes ardoisiers. Bulletin of Engineering Geology and Environment, 33(49-55).

Hall, C. and Cullen, D.C., 1955. Scanning force microscopy of gypsum dissolution and crystal growth. AIChE Journal, 42 (1): 232-238.

ISO 9227, 2006. Corrosion tests in artificial atmospheres – salt spray tests. International Organization for Standardization.

Jordan, G. and Rammensee, W, 1997. Growth and dissolution on the CaF_2 (111) surface observed by scanning force microscopy. Surface Science, 371(2): 371-380.

Koyuncu, I., Brant, J., Lüttge, A. and Wiesner, M.R., 2006. A comparison of vertical scanning interferometry (VSI) and atomic force microscopy (AFM) for characterizing membrane surface topography. Journal of Membrane Science, 278(1-2): 410-417.

Kurganskaya, I., Luttge, A. and Barron, A., 2009. The application of VSI (vertical scanning interferometry) to the study of crystal surface processes. Connexions web site. http://cnx.org/content/m22326/1.4/, March 8, 2011.

Lüttge, A., Bolton, E.W. and Lasaga, A.C., 1999. An interferometric study of the dissolution kinetics of anorthite; The role of reactive surface area. American Journal of Science, 299: 652-678.

Lüttge, A.,Winkler, U. and Lasaga, A.C., 2003. Interferometric study of the dolomite dissolution:a new conceptual model for mineral dissolution. Geochimica et Cosmochimica Acta, 67: 1099–1116.

Martín Ramos, J.D., 2004. A software package for powder X-ray diffraction analysis, Lgl. Dep. GR 1001/04.

Moulder, J.F., Stickle, W.F., Sobol, P.E. and Bomben, K.D., 1982. Handbook of X-ray photoelectron spectroscopy. In: Chastain, J. (ed.), Perkin-Elmer Corporation, Minneapolis.

Rivas, T., Prieto, B., Silva, B. and Birginie, J.M., 2003. Weathering of granitic rocks by chlorides: effect of the nature of the solution on weathering morphology. Earth Surface Processes and Landforms, 28(4): 425-436.

RILEM: Recommended test to measure the deterioration of stone and to assess the effectiveness of treatment methods, Commision 25-pem: Protection et Erosion des Monuments (1980), pp. 175-253.

Ruiz-Agudo, E., Putnis, C.V., Jiménez-López, C. and Rodríguez-Navarro, C., 2009. An atomic force microscopy study of calcite dissolution in saline solutions: the role of magnesium ions. Geochimica et Cosmichimica Acta, 73: 3201–3217.

Ruiz-Agudo, E., Kowacz, M., Putnis, C.V. and Putnis, A., 2010. Role of background electrolytes on the kinetics and mechanism of calcite dissolution. Geochimica et Cosmichimica Acta, 74: 1256–1267.

Ruiz-Agudo, E., Urosevic, M., Putnis, C.V., Rodríguez-Navarro, C., Cardell, C. and Putnis, A., 2011. Ion-specific effects on the kinetics of mineral dissolution. Chemical Geology, 281: 364–371.

Shiraki, R., Rock, P.A. and Casey, W.H., 2000. Dissolution kinetics of calcite in 0.1 M NaCl solution at room temperature: An atomic force microscopic (AFM) study. Aquatic Geochemistry, 6 (1): 87-108.

Shtukenberg, A.G., Astilleros, J.M. and Putnis, A., 2005. Nanoscale observations of the epitaxial growth of hashemite on barite (001). Surface Science, 590: 212–223.

Siegesmund, S. and Snethlage, R. (eds.), 2011. Stone in architecture: Properties, durability. 4th Edition, Springer, 552 pp.

Sing, K.S.W., Everett, D.H., Haul, R.A.W., Moscou, L., Pierotti, R.A., Rouquérol, J. and Siemieniewska, T., 1985. Reporting physisorption data for gas/solid systems with special reference to the determination of surface area and porosity (recommendations 1984). Pure and Applied Chemistry, 57: 603-619.

Tang, P., Chew, N.Y.K., Chan, H.K. and Raper, J.A., 2003. Limitation of determination of surface fractal dimension using N_2 adsorption isotherms and modified Frenkel-Halsey-Hill theory. Langmuir, 19(7): 2632-2638.

UNE-EN 14147, 1994. Natural stone test methods. Determination of resistance to ageing by salt mist. Spanish Association for Standardisation and Certification (AENOR), Madrid.

UNE-EN 1925, 1999. Método de ensayo para piedra natural. Determinación del coeficiente de absorción de agua por capilaridad. AENOR, Madrid.

UNE-EN 13755, 2002. Método de ensayo para piedra natural. Determinación de la absorción de agua a presión atmosférica. AENOR Madrid.

Van Espen, P., Janssens, K. and Nobels, J., 1986. AXIL-PC software for the analysis of complex X-ray spectra. Chemometrics and Intelligent Laboratory Systems, 1: 109-114.

Wyszecki, G. and Stiles, W.S., 1982. Colour science. Concepts and methods, quantitative data and formulae. 2nd ed. J. Wiley & Sons, New York.

Chapter 4

Materiales de Construcción 61 (2011) 93-114

Physical properties of carbonate rocks used as a modern and historic construction material in Eastern Andalusia, Spain

Maja Urosevic, Eduardo Sebastián-Pardo, Encarnación Ruiz-Agudo, Carolina Cardell*

Department of Mineralogy and Petrology, Faculty of Science, University of Granada, Campus Fuentenueva s/n, 18071 Granada, Spain

Article history:

Received 15 July 2009

Accepted 22 March 2010

Available online 9 April 2010

doi: 10.3989/mc.2010.53809

ABSTRACT

We present a detailed characterization of two calcareous stones from Andalusia (Southern Spain), namely *Escúzar* calcarenite and *Olivillo* travertine. Both materials can replace two stones extensively used in the architectural heritage of Andalusia, i.e. *La Escribana* calcarenite and *Alfacar* travertine. To establish the suitability of the replacement of ancient materials, detailed examination was performed. X-ray diffraction, X-ray fluorescence, optical and scanning electron microscopy, hydric tests, mercury intrusion porosimetry, gas adsorption, ultrasounds and colourimetry were applied. The *Escúzar* calcarenite has large pore cavities and higher open porosity than *La Escribana* calcarenite. From a chromatic point of view both calcarenites are rather similar. The *Olivillo* travertine is a massive well cemented and heterogeneously coloured rock. The ultrasounds velocities for this material are very homogeneous and elevated, indicating excellent mechanical properties. However the hydric and chromatic differences between both travertines point to reduced adequacy of *Olivillo* travertine as substitutive material for *Alfacar*.

KEYWORDS

Calcarenite, travertine, ornamental rocks, physical properties, mercury porosimetry.

4.1. Introduction

While in other regions of Spain most of the monumental heritage is based on plutonic rock (primarily granite), the geological context of Eastern Andalusia favoured the frequent use of carbonate rock throughout its architectural history (1, 2). Although the mineralogical composition of carbonate rocks is relatively simple, a wide range of lithological varieties can be identified as a result of differences in texture and sedimentary structure. This variability is reflected in the dispersion of the values of the physical properties (3-10) that determine the aptness of these materials for use in construction (9, 11, 12). Consequently, minor textural variations may lead to significant changes in the physical properties of such stone, modifying its usability as an architectural material (13). Since these textural variations are found between quarries exploiting the same rock, the physical properties of each material extracted must be assessed separately.

Replacement stone must be suitable for the monument to be restored and compatible with the original stone, in terms of both its petrophysical characteristics and outer appearance (13). Nonetheless, the stone used in restoration work should be chromatically different from the stone replaced, although this contrast should be moderate only so as not to detract from the aesthetics of the monument.

A number of factors render the use of natural stone as a replacement material in heritage structures somewhat difficult. These include the shortage of quarrymen, a competitive society that induces the use of lower cost materials (specifically, artificial materials that imitate natural stone), the closure or non-usability of the original quarries due to their location in urban areas or protected natural parks or their scant profitability (13).

The frequent decline in profitability as the extraction front advances prompts quarry closure or relocation to nearby areas where the operating conditions are more advantageous. This is the case of two quarries that supplied a large amount of stone widely used in the architectural heritage of Eastern Andalusia: the *La Escribana* calcarenite and the *Alfacar*

travertine quarries, both in the Spanish province of Granada, very close to the provincial capital.

La Escribana constitutes a typical example of relocation to a more profitable extraction area. Until its closure in 1994 it supplied one of the construction materials most commonly used in monumental buildings in Granada. "Piedra Franca", a calcarenite quarried at *La Escribana* (on the Santa Pudia Estate), was used to build Granada's Cathedral, the Palace of Charles V, San Jerónimo Monastery, the Royal Hospital and the Royal Chancellery (3, 14-16). After *La Escribana* closed, quarrying operations were initiated at the Escúzar site, also known as *Las Parideras* and likewise located on the Santa Pudia Estate. The calcarenite extracted from the new site has recently been used to restore the mosque at Cordoba and The Five Wounds Palace at Seville (current headquarters of the Andalusian Parliament).

A second, scantly studied example is to be found in the travertine once quarried at *Alfacar* and used to build San Jerónimo Monastery, the Royal Hospital and three churches: San Justo, San Justo y Pastor and El Salvador. In some restoration interventions, *Alfacar* travertine has been replaced by *Albox* and *Alhama*, quarried at a number of sites in the province of Almería (Eastern Andalusia).

The present study aimed to characterize the aforementioned new stone varieties, *Escúzar* calcarenite from Granada and *Olivillo* travertine from Almería, to determine their suitability as replacement stone in future restoration work on monuments in Eastern Andalusia.

4.2. Materials and methods

4.2.1. Materials

Santa Pudia calcarenite was widely used to build the most significant historic buildings in the city of Granada. The characteristic that makes this rock particularly apt for construction is its ready workability. Nonetheless, its high porosity limits its durability

considerably (7, 14, 15, 19-22). Geologically speaking, Santa Pudia calcarenite is located in the inter-mountain basin of the Granada depression. Lower Torteniense calcarenite materials are quarried primarily on the southern rim of that basin. This is the site of the so-called Santa Pudia Estate, home to two large calcarenite quarries, *La Escribana* and *Escúzar*. The *Escúzar* quarry, located NW of *La Escribana*, comprises a series of calcarenite banks with characteristic texture, bioclast size and macroscopic heterogeneity. *La Escribana* calcarenite, by contrast, has a more homogeneous pore distribution and bioclast size than the calcarenite that outcrops at *Escúzar*, which exhibits centimetre-scale pores and xenoclasts and variations in macroscopic porosity from one 10-cm (approximately) layer to another (Figures 1a and 1b). This study focused on *Escúzar* calcarenite, supplied by the *Los Linos* factory (23) located at Padul in SW Granada.

Olivillo travertine (Figure 1c), quarried at *Alhama* in the province of Almería, is commonly used in modern architecture and a candidate for use in the restoration of historic buildings (24). From a construction standpoint, travertine stone is a high-strength, abrasion-resistant material. Moreover, thanks to its pore system, it responds well to water, preventing capillary rise. *Alfacar* travertine (Figure 1d) has been used in Eastern Andalusia since antiquity. This stone is quarried in the municipal district of that name NE of the city of Granada (15, 18). It was deposited over materials in the intermountain basin on the NE rim of the Granada depression during the Quaternary Period. The closure of the *Alfacar* quarries led to more intensive exploitation of other travertine stones such as *Albox* and *Alhama* in Almería, as well as a rise in Roman travertine imports. A substantial number of fairly extensive (> 5 km^2) travertine Quaternary formations, appearing over Pleistocene, Pliocene and Miocene materials, outcrop near the town of *Alhama* in Almería, as well as at *Alicún*. Characterized by scant macroscopic porosity and weak compositional banding, they have greater aesthetic appeal than *Alfacar* travertine (Figures 1c and 1d). These travertine formations were deposited during upwelling in fluvial-lacustrine environments and subsequently underwent brecciation and, more recently, surface alteration (24-26). Travertine, including the *Olivillo* variety, is extracted in several quarries. The object of the present study was *Olivillo* travertine, purchased at the *Mármoles Nevado* factory (27) at *Atarfe* in NW Granada.

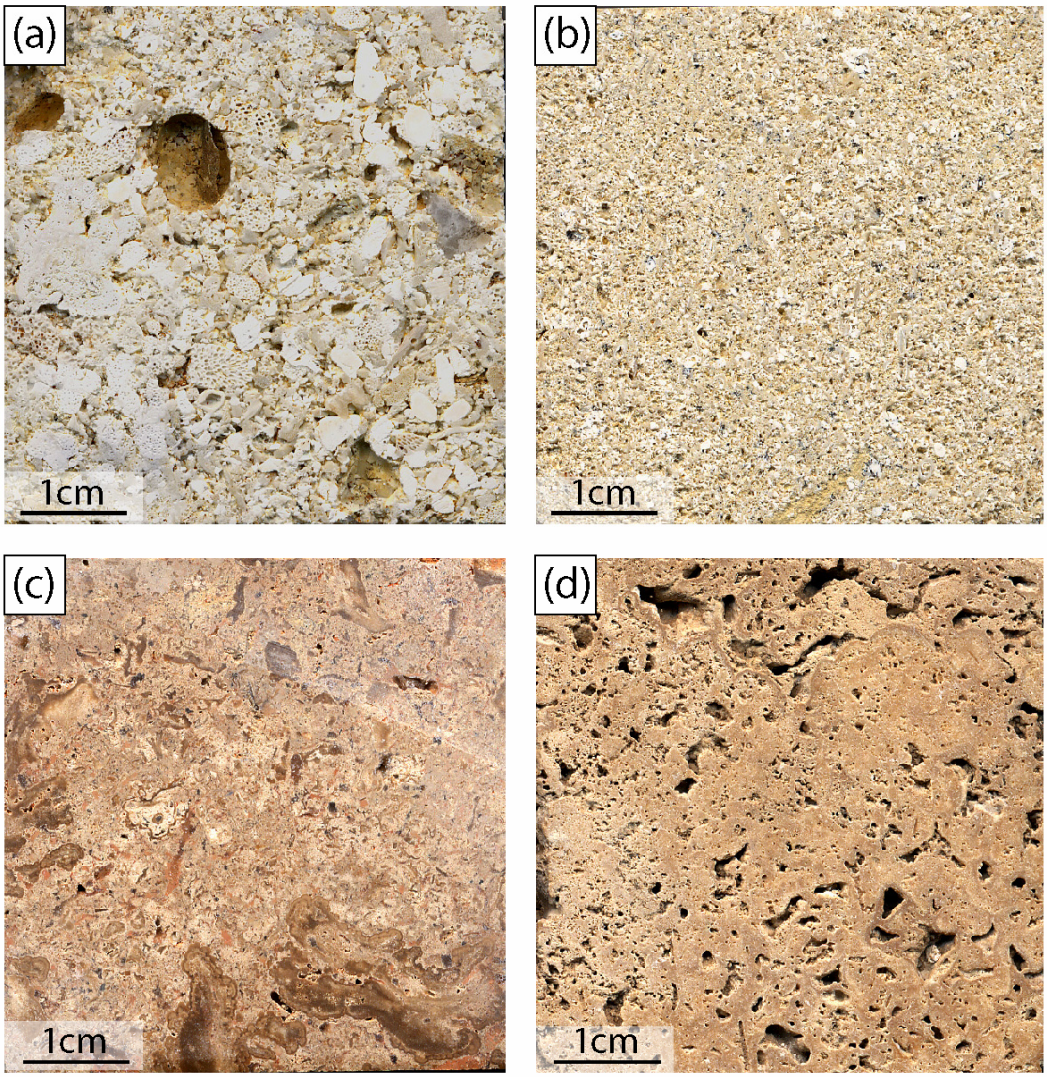

Figure 1. Macroscopic view of (a) *Escúzar* calcarenite; (b) *La Escribana* calcarenite; (c) *Olivillo* travertine; and (d) *Alfacar* travertine.

4.2.2. Methods

The mineralogical composition of these stone materials was determined with X-ray diffraction (XRD). Quarry sample fragments were ground in an agate mortar and the resulting powder, with a particle size of under 50 μm, was analysed with a Philips PW-1710 diffractometer fitted with an automatic slit. The working conditions were: CuKα radiation (λ:

1.5405 Å), 40 kV and 40 mA. The 2θ scan angle ranged from 3º to 60º, while the goniometer speed was 0.01º 2θ/s. Semi-quantitative analysis of the mineral phases was performed with Xpowder software (28).

The major and the trace minor elements in the rocks studied were analysed with an S4 Pioneer-Bruker wavelength dispersive X-ray fluorescence spectrometer fitted with a (60 kV, 150 mA, Rh anode) tube, LIF200/PET/OVO-55 crystals, proportional gas detectors and scintillation. Semi-quantitative spectra were obtained with Spectraplus® software. The powder samples (~5 g) were homogenized with a 5100 Spex Mixer/Mill and then evenly spread over a cellulose substrate on a 40-mm diameter aluminium container. The powder sample was compacted under a 10-t load with a Nannetti Instrument Mignon-S press to obtain 40-mm diameter wafers.

The petrographic and mineralogical study was conducted on thin sections under an Olympus BX-60 transmitted light optical microscope fitted with an Olympus DP10 digital camera. To distinguish calcite from dolomite, the samples were dyed with alizarin red, which dyes calcite selectively.

Sample microtexture and composition were studied under a LEO 1430-VP variable pressure scanning electron microscope (VPSEM) fitted with a wolfram filament and an Oxford Instruments Inca 350 energy-dispersive X-ray (EDS) microanalysis system. The results were processed with INCA® software. The gold- and platinum-coated samples were studied at 15 kV in a high vacuum. The spectra were acquired in a range of 5 to 20 kV.

The pore system in the rock samples was characterized with mercury intrusion porosimetry (MIP) and argon adsorption. Two-cm^3 samples were prepared for the mercury porosimetry analyses, kiln-dried at 60 ºC for 24 hours and subsequently analyzed with a Micromeritics Autopore III 9410 porosimeter. Argon adsorption and desorption isotherms were obtained at -196 ºC with a Micromeritics TriStar 3000 analyzer. The most common of the several fluids that can be used as adsorbates when studying stone materials is nitrogen. Nonetheless, for surface areas of under 5 m^2/g, the values delivered by nitrogen are higher

than the actual quantities. Consequently, argon is more suitable in these cases (29). The samples were heated at 250 ºC for 7 hours and degassed at 10^{-3} Torr in a Micromeritics Flow Prep station before the measurements were taken. The surface area of each sample was determined by BET linearization (30, 31) while the pore size distribution, pore volume and mean pore size were found with the BJH method (32). The surface fractal dimension, D_S, was used to characterize pore system surface roughness. The gas adsorption isotherms were studied applying the modified Frenkel-Halsey-Hill (FHH) equation, which determines the surface fractal dimension from the slope (A) of the Ln(V) vs the Ln[Ln(P/P_0)] graph, where V is the volume of the adsorbed gas and P and P_0 are the gas pressure measured and the condensation pressure, respectively. When the surface tension (or capillary condensation) has significant effects, the ratio between A and D_S is $A = D_S - 3$. The effects of capillary condensation are significant when $\delta < 0$ ($\delta = 3\ (1 + A) - 2$). Given that in the cases studied the value of δ was consistently greater than one, the expression $A = D_S - 3$ could be used. Single layer, or close to single layer, adsorption is required for the value of D_S found to be comparable among different samples (33). Consequently, the range of pressures used to calculate slope (A) in the Ln(V) vs Ln[Ln(P/P_0)] graph was limited to values that ensured that the number of layers adsorbed was close to one.

The following hydric trials were conducted to characterize the pore system and determine the fluid dynamics inside the stones studied: free water absorption and desorption, vacuum water saturation, hydrostatic weight, and capillary rise and suction. Pursuant to Spanish and European standards UNE-EN 1925 (34) and UNE-EN 13755 (35) and RILEM (36), 5 × 5 × 5 cm cubes were cut from quarry slabs to determine free water sorption, while 2 × 2 × 10 cm prismatic specimens were used for the capillary rise and suction trials. Before conducting the trials, the samples were kiln-dried at 60 ºC for 24 hours to remove any moisture they might contain.

The ultrasound velocity analyses were conducted on a Panametrics 5058 PR HV Pulser/Receiver operating in conjunction with a Tektronix TDS 3012B oscilloscope. Cubes measuring 5 cm on each side were prepared and the P and S waves measured with 0.5 HMz (S waves) and 1 MHz (P waves) transducers. The ultrasound velocity was determined at a

temperature of 25 ºC and relative humidity of 50%. The parameters calculated from a digital analysis of the signals transmitted were: compression (V_P) and shear (V_S) wave velocity, Poisson's ratio (ν_d), Young's modulus (E_d) and the total (ΔM) and relative (Δm) P and S wave anisotropy indices, calculated from the indices proposed by Guydader and Denis (37).

The chromatic characteristics of the stone varieties were studied on a Minolta CR 210 colorimeter with a 0º view angle and a 50-mm diameter. A xenon arc lamp inside a mixer compartment diffused the reflected light even when beamed on a 50-mm area. The measurements were taken with C illuminant having a daylight simulating colour temperature of 6774 K. The data obtained were expressed in a CIE L*a*b* and CIE L*C*H* (38) colour system alphanumeric codes. The mean values of the L*a*b* coordinates were determined for each 10 × 10 × 2 cm specimen, where L* is colour lightness, which varies from black with a value of 0 to white with a value of 100; a*, which varies from +a* (red) to -a* (green) and b*, ranging from +b* (yellow) to -b* (blue). The CIELCH (L*C*H*) system uses the same diagram as above but with cylindrical instead of Cartesian coordinates, where L* is lightness, C* is colour saturation or chroma and H* is hue.

4.3. Results and discussion

4.3.1. Mineralogical and chemical composition

Table 1 gives the chemical analysis of all major and certain minor elements (Cu, Zn, Sr and Zr) obtained with XRF for *Escúzar* calcarenite and *Olivillo* travertine. It also shows the analysis for the stones extracted from the historic quarries, namely the *La Escribana* calcarenite and *Alfacar* travertine traditionally used on monuments in the city of Granada.

According to the XRF data (Table 1), calcium was the main element in all the stones, an indication that they consist primarily of calcium carbonate (calcite). This was confirmed by the XRD findings. *Escúzar* calcarenite contained slightly less silicon, aluminium, iron,

Table 1. Chemical analysis of major and minor elements in calcarenite and travertine stone.

	Calcarenites				Travertines	
	Escúzar	*La Escribana**			*Olivillo*	*Alfacar**
wt. %		E1	E2	E3		
SiO_2	0.31	2.83	1.79	2.38	0.96	14
TiO_2	**	0.02	0.01	0.01	0.02	-
Al_2O_3	0.12	0.64	0.35	0.34	0.32	2.05
Fe_2O_3	0.12	0.14	0.27	0.49	0.12	0.86
MnO	0.01	0.02	0.04	0.07	**	-
MgO	0.28	0.3	0.46	0.44	0.72	2.15
CaO	56.01	52.8	54.8	54.1	54.24	43.9
K_2O	0.02	0.09	0.06	0.07	0.06	0.38
P_2O_5	0.05	0.09	0.07	0.1	0.01	0.08
SO_3	0.03	-	-	-	0.19	-
Cl	**	-	-	-	0.01	-
ppm						
Cu	43	4.2	3.4	4.9	40	6.4
Zn	**	15.8	60.6	24.3	1000	30.2
Sr	185	318	457	358	1416	317
Zr	7	< 10	< 10	< 10	55	27

The detection threshold is 0.005 %wt for major elements and 3 ppm for Zr, 2 ppm for Sr and 1 ppm for Cu and Zn.

* Extracted from (14) and (15). ** Below the detection threshold. - Not measured.

magnesium, zinc and strontium, and more copper and slightly more calcium than the *La Escribana* stone. *Olivillo* travertine had higher values of CaO and lower values of SiO_2, Al_2O_3, Fe_2O_3, MgO and K_2O and higher concentrations of copper, zinc, strontium and zirconium than the *Alfacar* material (Table 1). The high zinc and strontium concentrations may be attributed to small amounts of detrital materials (possibly sphalerite and celestite) trapped in the travertine formations at *Alhama* (Spanish province of Almería) during genesis (24).

The XRD findings confirmed that calcite was the main mineral phase in all the rocks. The mineralogical composition proved to be similar, in the *Escúzar* rock and subtype E-1 La

Escribana calcarenite (14, 15), which consists primarily of calcite (100-90%), quartz (~10%) and clay (< 1%). This distinguishes it from the E-2 and E-3 varieties, which exhibit a higher clay (> 2.5%) and feldspar (< 5% in E-3) content. Travertine was found to consist mostly of calcite, although in lower proportions in the *Alfacar* stone (84-100%), which also contains quartz (up to ~14%), dolomite (< 5%) and feldspar (< 1%).

4.3.2. Petrographic characteristics

Escúzar calcarenite was observed to comprise fossil fragments in a clast-supported matrix, generated by the fragmentation of mineralized organic remains, primarily of bivalves, echinoderms, foraminifers, serpulids, bryozoans and red algae. The bryozoan and red alga clasts were found to be fairly well preserved, as shown in Figures 2a and 2b. Also observed were extraclasts, whose origin can be traced to the erosion of metamorphic materials from the nearby reliefs of Baetic Mountain Internal Units. The abundance of these extraclasts formed by fragments of mica- and quartz-rich metamorphic rock, together with a much higher proportion of red algae and bryozoans than serpulids and echinoderms, make the material quarried here readily distinguishable from *La Escribana* calcarenite (14). Another distinct characteristic of the *Escúzar* stone is the presence of vugs up to 2 cm in diameter, as depicted in Figure 1a.

Historic *La Escribana* calcarenite has more foraminifers and serpulids and fewer bioclasts than the *Escúzar* variety, as Figures 2c and 2d show. Two types of primary porosity can be distinguished in both calcarenite stones studied: (a) intraclast porosity in foraminifers and bryozoans, characterized by small, partially cemented pores; and (b) irregular interclast porosity with larger, uncemented pores. Moreover, scant interconnection was observed between intra- and interclast porosity.

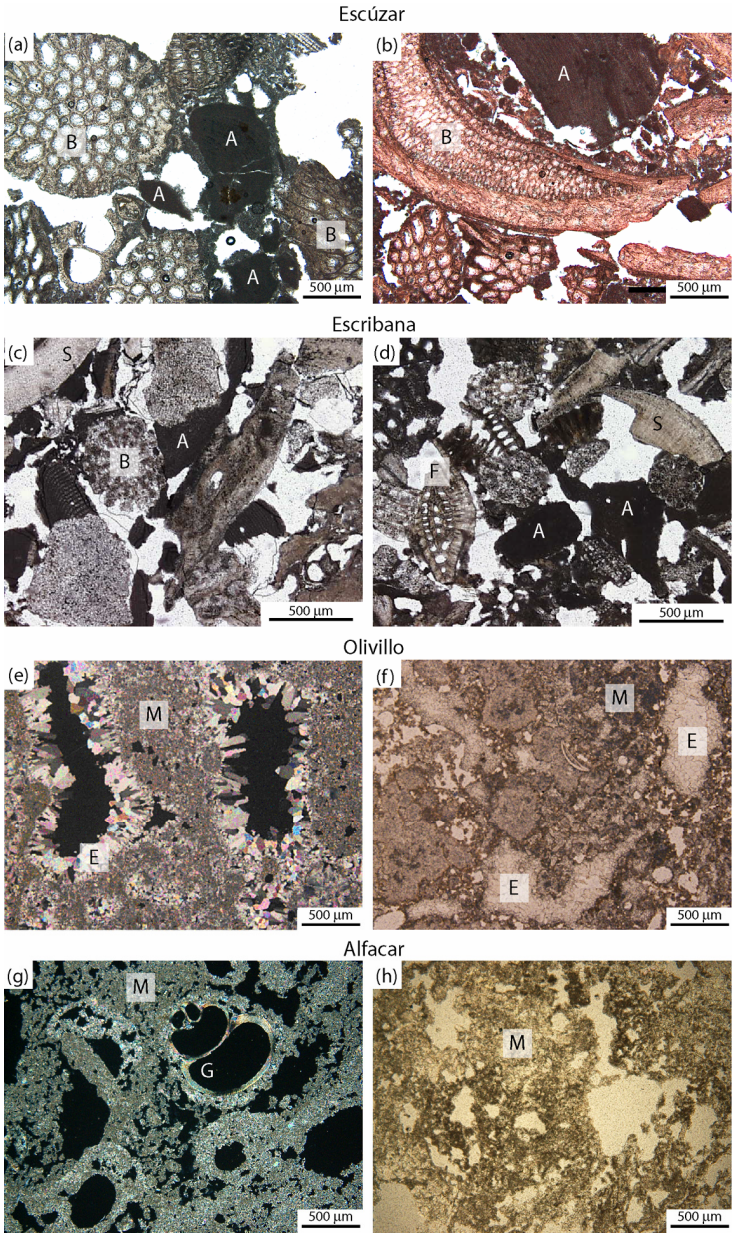

Figure 2. Microphotographs of thin sections. **(a)** and **(b)** *Escúzar* calcarenite (parallel Nicol prisms) showing large-scale (3-4 cm) red alga (A) and bryozoan (B) bioclasts; (b) dyed with alizarin red; **(c)** and **(d)** *La Escribana* calcarenite (parallel Nicol prisms) showing (0.5-1 mm) red alga (A), bryozoan (B), serpulid (S) and foraminifer (F) bioclasts; **(e)** *Olivillo* travertine showing micritic calcite matrix and elongated (~2x1 mm) vugs lined with sparitic calcite crystals (fenestral porosity = intersecting Nicol prisms); **(f)** *Olivillo* showing irregular distribution of the proportions of micritic (M) and sparitic (E) calcite; **(g)** *Alfacar* travertine showing an exclusively micritic matrix (M) (intersecting Nicol prisms) and large pores due to the presence of an abundance of gastropod fossils (G); and **(h)** *Alfacar* showing a detail of irregular and heterogeneous porosity (parallel Nicol prisms).

The pore size in *Olivillo* travertine was fairly small and the pores generally well cemented. The light and dark bands characteristic of the texture of this travertine were found to be due to changes in the relative proportion of sparitic, microsparitic and micritic calcite. The large (~2 × 1 mm), irregular and elongated vugs observed in Figures 2e and 2f resemble the organic structures of plants that were partially or wholly filled with sparitic calcite grains around 200 μm in size. The grains of carbonate material originally deposited between the voids left by the vegetation were much smaller (~20 μm).

Petrographic studies show that the historic stone from *Alfacar* is a very porous calcitic travertine. The texture is indicative of chemical precipitation on plant remains, in which gastropod fossils can be identified (Figure 2g). The matrix consists essentially of micritic calcite. Its porosity is very heterogeneous, with some centimetre-scale pores (vugs). Unlike *Olivillo* travertine, the *Alfacar* variety exhibits fenestral porosity characterized by a scant or nil sparitic calcite lining (Figures 2g and 2h).

4.3.3. Pore system characteristics

4.3.3.1. Mercury intrusion porosimetry

The distribution and volume of pores with access radii of 0.003 to 100 μm were measured with mercury intrusion porosimetry (MIP). The findings are set out in Table 2 and Figure 3, along with the lithological data for historic *La Escribana* calcarenite and *Alfacar* travertine.

The MIP findings given in Table 2 show that *Escúzar* calcarenite proved to be slightly more porous than the *La Escribana* variety, with values of 29.3 ± 7.6% and 24.50 ± 6.75%, respectively. The two rocks exhibited the same bulk density. As Figures 3a and 3b show, the calcarenite stones studied had a clearly bimodal pore distribution. The curve for *Escúzar*

Table 2. Pore system characteristics determined by mercury porosimetry (MIP) and Ar adsorption.

	Calcarenites		Travertines	
Hg porosimetry	*Escúzar*	*La Escribana* *	*Olivillo*	*Alfacar* *
Effective porosity (%)	29.30 ± 7.60	24.50 ± 6.75	8.16 ± 1.21	20.8
Real density (g cm^{-3})	2.52 ± 0.25	2.46 ± 0.21	2.65 ± 0.04	2.57
Bulk density (g cm^{-3})	1.96 ± 0.39	1.96 ± 0.25	2.43 ± 0.04	2.04
Ar adsorption				
Specific surface area (m^2/g)	0.7137 ± 0.1077	1.6506 ± 0.0060	0.5601 ± 0.1042	0.6246 ± 0.0022
Total pore volume (cm^3/g)	0.00049 ± 0.00006	0.0013	0.00037 ± 0.00007	0.00061
Pore diameter (Å)	19.72 ± 1.54	19.04	20.53 ± 1.48	19.01
Single layer volume (cm^3/g)	0.1667 ± 0.0326	0.4165 ± 0.0228	0.1468 ± 0.0270	0.1637
Fractal surface dimension (D_S)	2.6	2.7	2.52	2.64
Linear correlation coefficient (r^2)	0.9835	0.9912	0.9974	0.9923

The values shown are the mean of 3 measurements and the respective standard deviation.
- Values not available, * Historic rocks. Values extracted from (14).

calcarenite had an absolute peak at 0.3 μm and a fairly diffuse second peak between 3 and 100 μm. By contrast, the proportion of 3- to 100-μm pores was larger in *La Escribana* calcarenite, although this stone also exhibited a significant presence of 0.3-μm pores (39).

The pore system accessible to mercury differed greatly between the *Olivillo* and *Alfacar* travertine stones (Table 2). *Olivillo* travertine proved to be much less porous than the *Alfacar* stone, with a value of 8.16 ± 1.21% compared to 20.8%. *Olivillo* travertine was characterized by a much higher bulk density, attributed to the higher actual density of its constituent minerals and its smaller effective porosity, mentioned above. Figures 3c and 3d show that the pore size distribution differed in the travertine and calcarenite rocks studied. In the travertine materials it was unimodal. The *Olivillo* travertine peaked at 0.02 to 0.07 μm,

whereas in the *Alfacar* travertine most of the pores accessible to this technique measured around 1 μm.

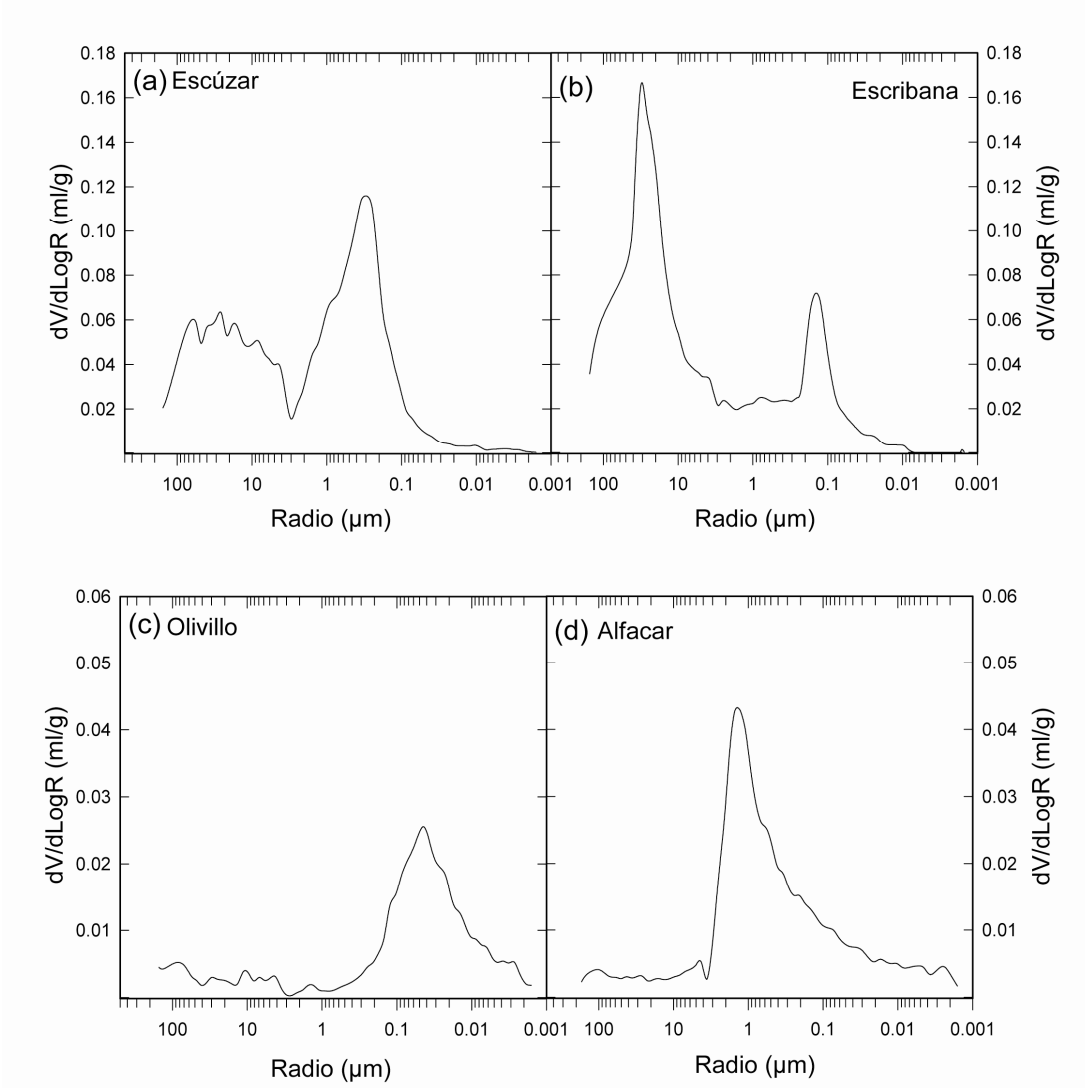

Figure 3. Pore size distribution found with mercury intrusion porosimetry (MIP) for **(a)** *Escúzar* calcarenite; **(b)** *La Escribana* calcarenite; **(c)** *Olivillo* travertine; and **(d)** *Alfacar* travertine; **(b)** taken from (39).

4.3.3.2. Argon adsorption

The pore system with access radii ranging from 0.001 to 0.006 μm (10-60 Å) was characterized in depth by argon adsorption. The findings in Table 2 show that *Escúzar* calcarenite had a smaller surface area (0.7137 ± 0.1077 m^2/g) than the historic rock (1.6506 ± 0.0060 m^2/g), as well as a smaller total volume of pores accessible to this technique (Table 2). Clear differences were found between the pore systems of the two calcarenite stones, as reflected in their surface fractal dimension. The higher values of this index in the *La Escribana* (2.70) than in the *Escúzar stone* (2.60) are indicative of a more complex micropore system, more liable to deterioration in the former (40, 41).

The differences in the micropore systems in the two travertine rocks were found to be smaller. The two materials have similar surface area and total pore volume values. The *Alfacar* stone has a more complex pore system than the *Olivillo* variety, however. The inference of the above findings is that the rocks potentially able to replace the historic materials are less prone to chemically induced (i.e., dissolution of the carbonate cement by salts or aqueous acid solutions) deterioration than the historic stone (40, 41).

4.3.4. Hydric parameters

Hydric parameters such as free water absorption and desorption and capillary rise and suction determine the suitability of a given construction material as a replacement of another in architectural structures (6, 13). Table 3 and Figure 4 show that, 168 hours into the trial, mean free water absorption in the *Escúzar* calcarenite was 16.30 ± 2.42%. This is higher than the 12.75% reported for the historic *La Escribana* stone (14). Figures 4a and 4b show that the two calcarenite rocks followed similar patterns, respectively reaching free water absorption values of ~14 and 12% shortly after (~ 4 min) the trial began. *Olivillo* travertine, in turn, exhibited slow water absorption in the first segment of the curve, which slowed further throughout the trial, with a value of only 2-2.5% after 47 hours (Figure 4c). These values were similar to the findings reported by Karaca (43) for Turkish travertine. The

Table 3. Values determined by hydric trials.

	Calcarenites		Travertines	
	Escúzar	*La Escribana**	*Olivillo*	*Alfacar*
Effective porosity (%)	31.86 ± 3.09	20.43	6.83 ± 0.82	23.7 ± 3.00
Real density (g/cm^3)	2.48 ± 0.05	2.46	2.60 ± 0.01	2.37 ± 0.05
Bulk density (g/cm^3)	1.69 ± 0.06	1.96	2.43 ± 0.02	1.81 ± 0.11
Free water absorption (%)	16.30 ± 2.42	12.75	2.28 ± 0.23	10.46 ± 1.62
Free water desorption (%)	14.80 ± 1.37	-	2.53 ± 0.26	11.46 ± 1.92
Saturation (%)	78.36 ± 1.72	73.98	82.31 ± 2.17	72.96 ± 4.23
Rate of capillary rise (cm/h$^{1/2}$)	3.24 ± 0.81	2.96	-	-
Capillary suction (g/cm^2*h$^{1/2}$)	0.76 ± 0.26	0.68	0.03 ± 0.01	0.12

Values determined by hydric trials.

- Values not available. * Historic rock. Values extracted from (14) and (42).

hydraulic behaviour of the *Alfacar* travertine differed considerably, reaching free water absorption values of over 8% in the first hour of the trial (Figure 4d).

The free water desorption curves for the calcarenite stones (Figures 4a and 4b) differed significantly. The curve for *Escúzar* calcarenite had an initial segment in which barely any drying was detected (Figure 4a). The *La Escribana* calcarenite curve, by contrast, had a single and higher desorption rate (Figure 4b). Historic *La Escribana* calcarenite dried after 49 hours, compared to the over 121 hours needed to dry the *Escúzar* stone.

The free water desorption curve for *Olivillo* travertine stabilized, and the rock was still moist 196 hours after the trial started (Figure 4c). The *Alfacar* curve, in contrast, has two distinct segments, with quicker drying taking place in the first 25 hours and total drying recorded after 144 hours (Figure 4d). The hydraulic behaviour of *Olivillo* travertine would be explained by the presence of many isolated micropores. The water reaching the micropores during forced vacuum absorption would be retained in these pores, preventing complete

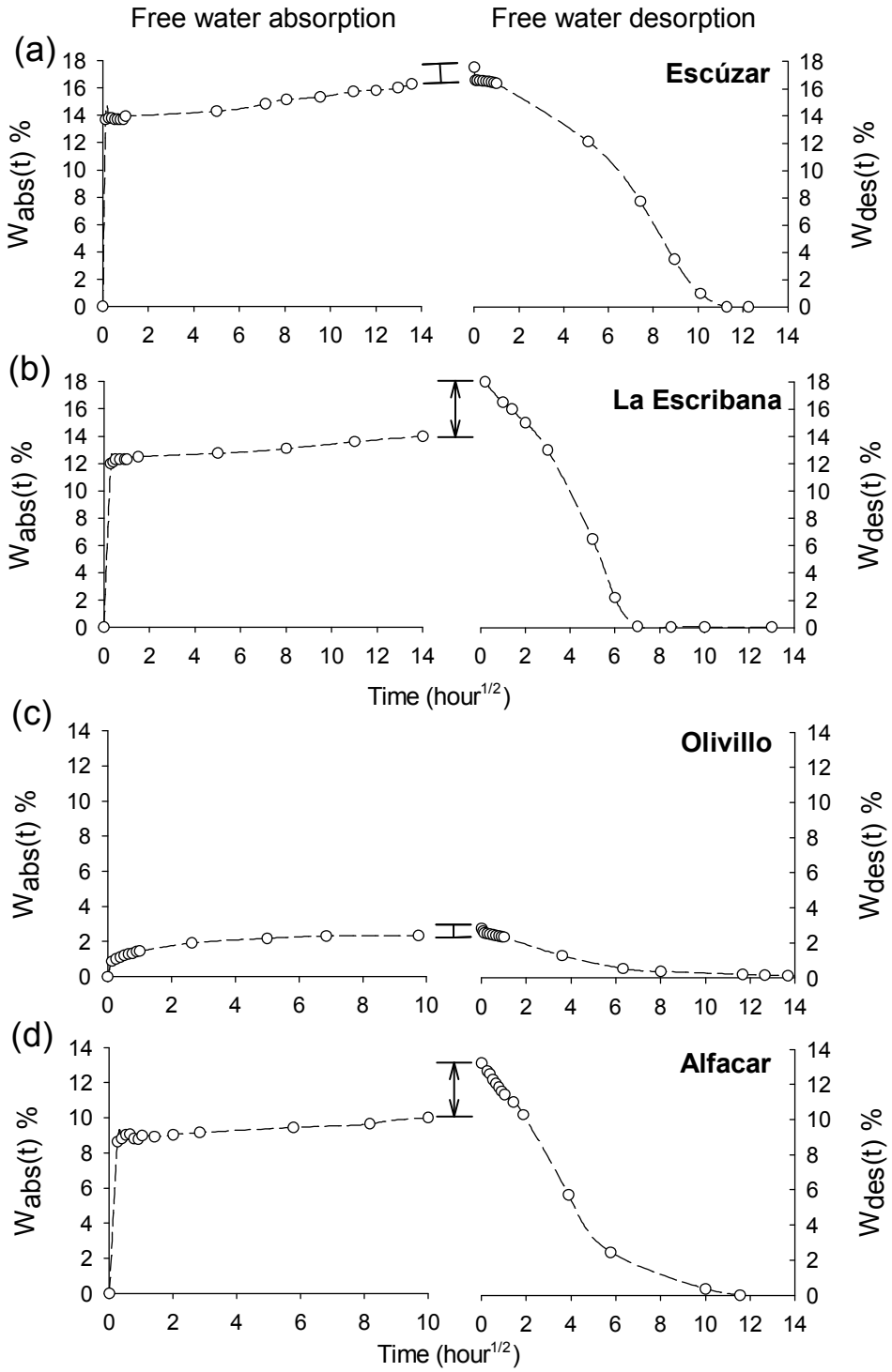

Figure 4. Hydric parameters: free water absorption and desorption curves for **(a)** *Escúzar* calcarenite; **(b)** *La Escribana* calcarenite; **(c)** *Olivillo* travertine; and **(d)** *Alfacar* travertine; **(b)** taken from (14).

desorption. The larger pore size in the *Alfacar* travertine, by contrast, would favour total drying.

As Table 3 shows, capillary rise could only be determined or the calcarenite stones. The *Escúzar* variety had a value of 3.24 ± 0.81 cm/h$^{1/2}$, which was slightly higher than the 2.96 cm/h$^{1/2}$ found for the *La Escribana* stone. This finding revealed substantial differences in the physical properties of the two materials extracted from the same lithological unit. The capillary suction coefficient (Table 3) could be measured in all four rock varieties from the slope of the first straight segment on the suction curve during the first hour of the trial (Figure 5). Table 3 shows that the capillary suction coefficient in *Escúzar* calcarenite (0.76 ± 0.26 g/cm^2·h$^{1/2}$) was, while higher, similar to the value for the *La Escribana* stone (0.68 g/cm^2·h$^{1/2}$).

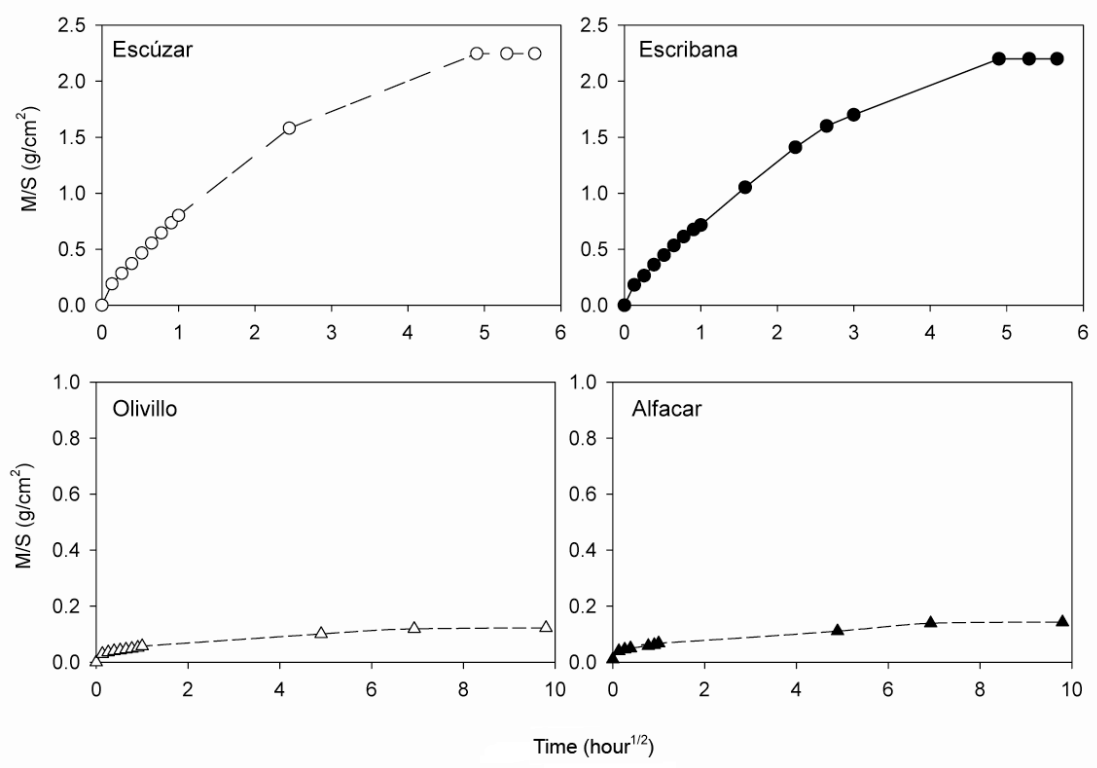

Figure 5. Capillary water suction curves for **(a)** *Escúzar* calcarenite; **(b)** *La Escribana* calcarenite; **(c)** *Olivillo* travertine; and **(d)** *Alfacar* travertine; **(b)** taken from (14).

4.3.5. Ultrasound parameters

The mechanical properties of a number of rocks have been determined by measuring the propagation velocity of ultrasound waves, a technique for evaluating force resistance in materials (6, 8, 37, 44, 45). These properties were determined in the rocks studied by measuring the P and S wave velocity in the three spatial directions. The findings are given in Table 4. The S wave velocity could not be measured in historic *La Escribana* calcarenite, for want of samples of a size suitable for the trial. Nor were data on this material found in the literature.

The P wave velocity in *Escúzar* calcarenite was grater than the velocity measured in the *La Escribana* material, and the standard deviation in these measurements was higher than for the S waves (Table 4). This high value can be attributed to the great textural heterogeneity of this stone, visible to the naked eye. Both calcarenite rocks had moderate to low anisotropy, and higher total than relative anisotropy, especially in the *Escúzar* variety. Total anisotropy (ΔMp) was higher, in turn, in the *Escúzar* than in the *La Escribana* rock, with values of 9.2 and 5%, respectively. Higher total than relative anisotropy values are an indication that a rock has greater anisotropy in one of the three spatial directions, attributable to a slightly laminar orientation that may not be macroscopically detectable (37). The present results showed that such laminar orientation was present in both calcarenite materials, although textural orientation or grain classification was more accentuated in the *Escúzar* than the *La Escribana* variety.

Similar total anisotropy values were obtained by Pardo et al. (46) in "Piedra Franca" calcarenite quarried near Baeza in the Spanish province of Jaén (9.8% for P waves). Other biocalcarenites quarried in the province of Granada, however (such as "Piedra Asperón") have extremely low anisotropy, with values of ~ 0.20% (47). Similarly low values (0.27-0.61%) were reported by Cultrone et al. (48) in compact limestone in Eastern Sicily, Italy.

Olivillo travertine, in turn, had very homogeneous P and S values, with low standard deviation and higher values than measured in the *Alfacar* material. Moreover, the total

Table 4. Ultrasound velocity (V_P, V_S), dynamic elasticity constants (E_d, v_d) and S and P wave total and relative anisotropy coefficients along the three spatial axes.

	ρ_{bulk} (g/cm^3)		V_P (m/s)	± 1σ	V_S (m/s)	± 1σ	V_P/V_S	E_d (GPa)	v_d	ΔM_P (%)	Δm_P (%)	ΔM_S (%)	Δm_S (%)
Calcarenites													
Escúzar	1.86	x	3994	(692)	2028	(76)	1.97	20.3	0.33	9.2	2.7	2.4	0.5
		y	4459	(613)	2083	(114)	2.14	22.0	0.36				
		z	4342	(454)	2072	(78)	2.10	21.6	0.35				
*La Escribana**	1.85	x	3328	-	-	-	-	-	-	5.0	3.6	-	-
		y	3566	-	-	-	-	-	-				
		z	3441	-	-	-	-	-	-				
Travertines													
Olivillo	2.43	x	5627	(95)	3035	(29)	1.85	58.0	0.29	2.4	0.7	1.8	0.5
		y	5787	(54)	3100	(61)	1.87	60.7	0.30				
		z	5746	(87)	3083	(3)	1.86	60.0	0.30				
*Alfacar**	1.81	x	4571	-	2149	-	2.13	22.7	0.36	1.5	1.6	3.2	2.9
		y	4679	-	2253	-	2.08	24.8	0.35				
		z	4603	-	2188	-	2.10	23.5	0.35				

The values shown are the mean of 3 measurements and the respective standard deviation. ρ_{bulk}: bulk density; V_P: compression wave velocity; V_S: shear wave velocity; E_d: Young's modulus; v_d: Poisson's ratio; ΔMp: total anisotropy coefficient; Δmp: relative anisotropy coefficient.
- Values not available. * Values extracted from (14) and (16).
Axes x, y and z are defined in terms of minimum, maximum and intermediate velocity, respectively.

anisotropy was higher than the relative anisotropy in *Olivillo*, contrasting in this respect with the *Alfacar* travertine, in which the two indices are very similar (1.5 and 1.6%, respectively). These findings are indicative of the existence of textural orientation in the *Olivillo* stone, which is in fact macroscopically visible in the form of the colour banding induced by differently sized calcite crystals.

Moreover, *Olivillo* rock exhibited homogeneous and very high Young's modulus values (E_d ~ 60 GPa), which were nearly triple the *Alfacar* values (Ed < 25 GPa). The deduction to be drawn from the foregoing is that the physical-mechanical properties of *Olivillo* travertine

make it a high quality construction material. Nonetheless, the presence of anisotropy conditions its durability and onsite placement

4.3.6. Colourimetry

While the chromatic parameters of construction materials depend essentially on their composition, such as the presence of small amounts of iron or manganese oxides, they are also affected by textural variations such as pore size or the existence of banding (49). The chromatic parameters of the rocks studied and the stone varieties from historic quarries are given in Table 5. The table shows that while the lightness (L*) values in the calcarenite stones were fairly similar, the datum for *Escúzar* (90.34 ± 0.74) was lower than for *La Escribana* (97.74 ± 0.06) calcarenite. The former, moreover, was yellower, with a b* value of 5.42 ± 0.07 compared to 1.90 ± 0.96, and greener (more negative a* values) than *La Escribana*. *Escúzar* also exhibited greater colour saturation (C*= 5.45 ± 0.07) than *La Escribana* calcarenite (2.00 ± 0.83).

The travertine stones showed more accentuated colour differences, particularly in terms of saturation (C*) and hue (H*). The findings for the chromatic coordinates a* and b* indicated that Olivillo is yellower and more reddish than Alfacar travertine, and has a higher C* value (C*= 7.54 ± 0.45 vs 2.02 ± 1.08). The total chromatic difference (ΔE) between the two travertine stones was highly significant, at 28.01. The contrast between the calcarenite materials was much more moderate (8.20). According to these results, replacing *Alfacar* with *Olivillo* travertine would entail undesirable visual effects and a concomitant deterioration of monument aesthetics (13). In contrast, replacing historic calcarenite with the *Escúzar* variety would not involve such an intense visual impact. More than that, the chromatic contrast would make the two readily distinguishable, which is a highly recommended feature of replacement stone.

Table 5. Chromatic parameters: luminosity (L*), chromatic coordinates (a* y b*), chroma (C*), hue (H*) and differences in luminosity (ΔL*), chromatic coordinates (Δa* and Δb*), chroma (ΔC*) and total colour (ΔE*).

Type	L*		a*		b*		C*	
Calcarenites								
Escúzar	90.34	±0.74	-0.60	±0.01	5.42	±0.07	5.45	±0.07
La Escribana	97.74	±0.06	-0.47	±0.24	1.90	±0.96	2.00	±0.83
Travertines								
Olivillo	69.78	±2.18	1.83	±0.30	7.31	±0.33	7.54	±0.45
Alfacar	97.16	±0.73	-0.58	±0.15	1.92	±1.11	2.02	±1.08

Type	H*		ΔL*	Δa*	Δb*	ΔC*	ΔE*
Calcarenites							
Escúzar	96.29	±0.09					
La Escribana	108.88	±17.76	-7.40	-0.13	3.52	3.45	8.20
Travertines							
Olivillo	75.92	±0.56					
Alfacar	111.89	±14.28	-27.39	2.41	5.39	5.52	28.01

a*: red-green components; b*: yellow-blue components. $\Delta E^* = \sqrt{(\Delta L^*)^2+(\Delta a^*)^2+(\Delta b^*)^2}$

4.4. Conclusions

This study addressed the petrographic and physical-mechanical characterization of two carbonate rocks commonly used in construction in Eastern Andalusia, Spain. The two varieties, *Escúzar* calcarenite and *Alhama* (or *Olivillo*) travertine, quarried in the provinces of Granada and Almería, respectively, were examined to determine both their technical quality and their suitability as replacement stone in future restoration work on the architectural heritage. The data obtained were compared with the information on the historic stone widely used in monuments in Granada, namely *La Escribana* calcarenite and *Alfacar* travertine (both quarried in Granada).

Replacement stone must meet suitability requirements and be compatible with the original material: the two rocks must exhibit similar hydraulic behaviour, mechanical strength and visible features. Further criteria include durability (resistance to alteration) and

sufficient colour contrast to ensure that the original and replacement stones can be distinguished.

The outer appearance of the calcarenite stones compared differed visibly. The Escúzar variety is characterized by vugs of up to 2 cm in diameter and centimetre-scale clasts, unlike the historic material, which exhibits substantially smaller and more homogeneous pores and bioclasts. The chromatic difference between the two is perceptible to the naked eye (ΔE = 8.20), but not overly accentuated. This is of particular interest, for it contributes to making the replacement stone distinguishable from the original material in the monument with no detriment to the overall aesthetics.

Escúzar also has higher effective porosity (31.86% vs 20.43%), free water absorption (16.30% vs 10.96%) and saturation (78.36% vs 73.98%) than historic *La Escribana* calcarenite, while capillary rise and suction are similar in the two materials. Escúzar calcarenite exhibits greater textural heterogeneity than the historic *La Escribana* rock, and higher total than relative anisotropy. This translates into the existence of textural orientation that conditions its durability, depending on its position when laid. In other words, the hewing and positioning of this rock with respect to the orientation of its stratification planes determine the intensity and morphology of its deterioration. If *Escúzar* calcarenite is to be used in future restorations as a replacement stone for the *La Escribana* variety, account should be taken of its greater anisotropy and (minimally) different hydraulic behaviour.

The outer appearance of the two travertine stones compared differs substantially. *Olivillo* is a massive travertine, with light and dark colour banding and smaller pore sizes than in the *Alfacar* rock. The latter is characterized by significant and very heterogeneous porosity and the presence of vugs. The chromatic contrast between these two materials is so accentuated ($\Delta E \sim 28$) that replacing the historic travertine with *Olivillo* would entail an undesirable aesthetic effect.

The hydraulic behaviour of the two stones likewise differs substantially, with the massive *Olivillo* exhibiting much lower free water absorption and desorption and effective

porosity (6.83% vs 23.7%) values than the *Alfacar* variety. These findings, along with greater real density, ultrasound velocity and a higher Young's modulus in the *Olivillo* stone than in the historic *Alfacar* travertine denote the higher quality of the former. Further to such findings, the excellent mechanical properties of this rock make it a highly suitable construction material. Nonetheless, the presence of more accentuated anisotropy in one spatial direction (greater total than relative anisotropy), visible to the naked eye in the form of banding, is indicative of the need to take special on-site measures when it is laid. The foregoing suggests that the joint presence of the two travertine stones in restoration works is not advisable, in light of both the differential deterioration this would entail and the accentuated chromatic difference that would detract from the aesthetic value of the monument as a whole.

4.5. References

(1) Cantó, A. M.: "Avances sobre la explotación del mármol en la España romana", Archivo Español de Arqueología, vol. 50-51 (1977-1978), pp. 165-188.

(2) Beltrán Fortes, J.: "Expertos universitarios investigan el uso de los marmora en la Bética romana", PH Boletín del Instituto Andaluz del Patrimonio Histórico, vol. 59, (2006), pp. 4-17.

(3) Sebastián, E.; Zezza, U.; Rodríguez-Navarro, C.; De la Torre, M. J.; Cardell, C.: "La Piedra Franca, biocalcarenita, en la construcción de edificios históricos de Granada", I Congreso Internacional Rehabilitación del Patrimonio Histórico y Edificación (1992), Islas Canarias, Spain, pp. 329-336.

(4) Birginie, J. M.; Rivas, T.; Prieto, B.; Auger, F.: "Comparación de la resistencia a la alteración por niebla salina de dos calizas utilizadas en la construcción mediante métodos ponderales, métodos acústicos y tratamiento de imágenes", Materiales de Construcción, vol. 50, nº 259 (2000), pp. 27-43. doi:10.3989/mc.2000.v50.i259.397

(5) Arizzi, A.; Belfiore, C. M.; Cultrone, G.; Rodríguez-Navarro, C.; Sebastián Pardo, E.; Triscari, M.: "Petro-chemical and physical investigations on the 'Santa Pudia

Calcarenite' (Andalusia, Spain): New hints for the prevention and conservation of calcarenitic building materials", Goldschmidt Conference Abstracts, A35 (2007).

(6) Buj, O.; Gisbert, J.: "Caracterización petrofísica de tres variedades comerciales de areniscas miocenas del valle del Ebro", Materiales de Construcción, vol. 57, nº 287 (2007), pp. 63-74.

(7) Luque, A.; Cultrone G.; Sebastián, E.; Cazalla, O.: "Evaluación de la eficacia de tratamientos en el incremento de la durabilidad de una calcarenia bioclástica (Granada, España)", Materiales de Construcción, vol. 58, nº 292 (2008), pp. 115-128.

(8) Martínez-Martínez, J.: "Influencia de la alteración sobre las propiedades mecánicas de calizas, dolomías y mármoles. Evaluación mediante estimadores no destructivos (ultrasonidos)", Tesis Doctoral, Universidad de Alicante (2008).

(9) Sebastián Pardo, E.; Cultrone, G.; Garibaldi, V.; Rodríguez Navarro, C; de la Torre, M. J.; Valverde, I.: "The Sierra Elvira limestone: petrophysical features of a widespread Andalusian decorative material", Materiales de Construcción, vol. 58, nº 289-290 (2008), pp. 51-63.

(10) Cueto, N.; Benavente, D.; Martínez-Martínez, J.; García del Cura, M. A.: "Rock fabric, pore geometry and mineralogy effects on water transport in fractured dolostones", Engineering Geology, vol. 107, nº 1-2 (2009), pp. 1-15. doi:10.1016/j.enggeo.2009.03.009

(11) Sáez Pérez, M. P.: "Estudio de elementos arquitectónicos y composición de materiales del Patio de los Leones. Interacciones en sus causas de deterioro", Tesis Doctoral, Universidad de Granada (2003).

(12) Barrios Neira, J.; Montealegre, L.; Ortega, A.; Meroño, J. E.; Aguilera, M. J.: "Biocalcarenites as construction materials in Santa Marina de Aguas Santas church at Cordoba, Spain", Materiales de Construcción, vol. 59, nº 293 (2009), pp.125-134.

(13) Fort González, R.: "Utilización de la piedra natural en restauración", Seminarios de la Sociedad Española de Mineralogía, vol. 2 (2005), pp. 155-182.

(14) Rodríguez-Navarro, C.: "Causas y mecanismos de alteración de los materiales calcáreos de las catedrales de Granada y Jaén", Tesis Doctoral, Universidad de Granada (1994).

(15) Cardell, C.: "Cristalización de sales en calcarenitas. Aplicación al Monasterio de San Jerónimo", Tesis Doctoral, Departamento de Mineralogía y Petrología, Universidad de Granada (1998).

(16) Rodríguez-Navarro, C.; Sebastián-Pardo, E.; Ruiz-Agudo, E: "Plan Director del Hospital Real: Estudio de materiales, formas y mecanismos de alteración", informe interno, Universidad de Granada (2008).

(17) Guardia Olmedo, J.; Gómez Moreno, J. M.; López Guzmán, R.; Prieto Moreno, J.: "Arte y deterioro en los monumentos granadinos. Catedral, Chancillería y Palacio de Carlos V", Universidad de Granada, Junta de Andalucía (1986).

(18) Durán-Suárez, J. A.; García-Casco, A.; Sánchez-Navas, A.; Rodríguez-Gordillo, J.: "Caracterización de las alteraciones en pilares de travertino de la Iglesia del Salvador (Granada). Propuestas restauradoras", Boletín de la Sociedad Española de Mineralogía, vol. 16 (1993), pp. 1-12.

(19) Cardell-Fernández, C.; Rodríguez-Gordillo, J.: "A comparative study of calcarenite salt crystallisation and weathering in laboratory conditions and in a monument", 8th International Conference on Non Destructive Investigations and Microanalysis for the Diagnostics and Conservation of the Cultural and Environmental Heritage, Lecce, Italy (2005).

(20) Velilla Sánchez, N.: "Caracterización petrográfica de rocas ornamentales y de construcción de uso en los edificios históricos", Metodología de diagnóstico y evaluación de tratamientos para la conservación de los edificios históricos (Cuadernos técnicos), Junta de Andalucía (2003), pp. 22-35.

(21) Ruiz-Agudo, E.: "Prevención del daño debido a la cristalización de sales mediante el uso de inhibidores de la cristalización", Tesis Doctoral, Universidad de Granada (2007).

(22) Cardell, C.; Benavente, D.; Rodríguez-Gordillo, J.: "Weathering of limestone building material by mixed sulfate solutions. Characterization of stone microstructure, reaction products and decay forms", Materials Characterization, vol. 59, nº 10 (2008), pp. 1371-1385. doi:10.1016/j.matchar.2007.12.003

(23) www.loslinos.es

(24) García del Cura, M. A.; Sanz-Montero, E.; Benavente, D.; Martínez-Martínez, J.; Bernabéu, A.; Cueto N: "Sistemas travertínicos de Alhama de Almería: características petrográficas y petrofísicas", Geotemas, vol. 10 (2008), pp. 456-459.

(25) Voersman, F.; Baena, J.: Mapa geológico de España escala 1:50.000. Hoja 1.044 Alhama de Almería, Mapa y Memoria, IGME, Madrid (1983).

(26) García del Cura, M. A.; La Iglesia, A.; Ordóñez, S.; Sanz-Montero, E.; Benavente, D: "Óxidos de hierro y manganeso en travertinos de Alhama de Almería", Macla, vol. 9 (2008), pp. 107.

(27) www.marmolesnevado.es

(28) Martín Ramos, J. D.: XPowder. A software package for powder X-ray diffraction analysis, Lgl. Dep. GR 1001/04, Granada (2004).

(29) Sing, K. S. W.; Everett, D. H.; Haul, R. A. W.; Moscou, L.; Pierotti, R. A.; Rouquérol, J.; Siemieniewska, T.: "Reporting Physisorption Data for Gas/Solid Systems", Pure and Applied Chemistry (IUPAC), vol. 57 (1985), pp. 603-619. doi:10.1351/pac198557040603

(30) Gregg, S. J.; Sing, K. S. W.: Adsorption Surface Area and Porosity, Academic Press, London (1982).

(31) Adamson, A. W.; Gast, A. P.: Physical Chemistry of Surfaces, J. Wiley & Sons, New York (1997).

(32) Barret, E. P.; Joyner, L. G.; Halenda, P. P.: "The Determination of Pore Volume and Area Distributions in Porous Substances. I. Computations From Nitrogen Isotherms", Journal of the American Chemical Society, vol. 73 (1951), pp. 373-380. doi:10.1021/ja01145a126

(33) Tang, P.; Chew, N. J. K.; Chan, H-K.; Raper, J. A.: "Limitation of determination of surface fractal dimension using N2 adsorption isotherms and modified Frenkel-Halsey-Hill theory", Langmuir, vol. 19 (2003), pp. 2632-2638. doi:10.1021/la0263716

(34) UNE-EN 1925: Método de ensayo para piedra natural. Determinación del coeficiente de absorción de agua por capilaridad, AENOR, Madrid (1999).

(35) UNE-EN 13755: Método de ensayo para piedra natural. Determinación de la absorción de agua a presión atmosférica, AENOR, Madrid (2002).

(36) RILEM: Recommended test to measure the deterioration of stone and to assess the effectiveness of treatment methods, Commision 25-pem: Protection et Erosion des Monuments (1980), pp. 175-253.

(37) Fort, R.; Fernández-Revuelta, B.; Varas, M. J.; Álvarez de Buergo, M.; Taborda-Duarte, M.: "Influencia de la anisotropía en la durabilidad de las dolomías cretácicas de la Comunidad de Madrid frente a la cristalización de sales", Materiales de Construcción, vol. 58, nº 289-290 (2008), pp. 161-178. doi:10.3989/mc.2008.v58.i289-290.74

(38) Wyszecki, G.; Stiles, W. S.: Colour Science. Concepts and Methods, Quantitative Data and Formulae (2nd Edition), J. Wiley & Sons, New York (1982).

(39) Ruiz-Agudo, E.; Mees, F.; Jacobs, P.; Rodríguez-Navarro, C.: "The role of saline solution properties on porous limestone salt weathering by magnesium and sodium sulfates", Environmental Geology, vol. 52 (2007), pp. 269-281. doi:10.1007/s00254-006-0476-x

(40) Pérez Bernal, J. L.; Bello López, M. A.: "The fractal dimension of stone pore surface as weathering descriptor", Applied Surface Science, vol. 161 (2000), pp. 47-53. doi:10.1016/S0169-4332(00)00031-3

(41) Urosevic, M.; Sebastián Pardo, E.; Cardell, C.: "Rough and polished travertine building stone decay evaluated by a marine aerosol ageing test", Construction and Building Materials (2010). doi:10.1016/j.conbuildmat.2010.01.011

(42) Cultrone, G.: "Stone deterioration and conservation treatments in Cultural Heritage", Marie Curie Fellowship of the European Community Programme "Energy, Environment and Sustainable Development", Universidad de Granada (2004).

(43) Karaca, Z.: "Water absorption and dehydration of natural stones versus time", Construction and Building Materials, (2009). doi 10.1016/j.conbuildmat.2009.10.029

(44) Martínez-Martínez, J.; Benavente, D.; Ordóñez, S.; García del Cura, M. A.: "Multivariate statistical techniques for evaluating the effects of brecciated rock fabric on ultrasonic waves propagation", International Journal of Rock Mechanics and Mining Sciences, vol. 45 (2008), pp. 609-620. doi:10.1016/j.ijrmms.2007.07.021

(45) Sáez Pérez, M. P.; Rodríguez-Gordillo, J.: "Structural and compositional anisotropy in Macael marble (Spain) by ultrasonic, XRD and optical microscopy methods", Construction and Building Materials, vol. 23, nº 6 (2009), pp. 2121-2126. doi:10.1016/j.conbuildmat.2008.10.013

(46) Sebastián Pardo, E.; Martín Clavo, J.; Zezza, U.: "The "Piedra Dorada" calcarenite in the cultural built heritage of Baeza (andalusian province of Jaen, Spain)", Atti Ticinesi di Scienze della Terra, vol. 38 (1995), pp. 205-213.

(47) Sebastián Pardo, E.; De la Torre, M. J.; Cazalla, O.; Cultrone, G.; Rodríguez-Navarro, C.: "Evaluation of treatments on biocalcarenites with ultrasound", The e- Journal of Nondestructive Testing & Ultrasonics, vol. 4, nº 12 (1999).

(48) Cultrone, G.; Russo, L. G.; Calabrò, C.; Urosevic, M.; Pezzino, A.: "Influence of pore system characteristics on limestone vulnerability: a laboratory study", Environmental Geology, vol. 54 (2008), pp. 1271-1281. doi:10.1007/s00254-007-0909-1

(49) Gökay, M. K.; Gundogdu, I. B.: "Color identification of some Turkish marbles", Construction and Building Materials, vol. 22, nº 7 (2008), pp. 1342-1349. doi:10.1016/j.conbuildmat.2007.04.016

Chapter 5

Environmental Earth Sciences, DOI 10.1007/s12665-010-0657-5

Characterization of indoor and outdoor atmospheric pollutants impacting architectural monuments: the case of San Jerónimo Monastery (Granada, Spain)

Velichka Kontozova-Deutsch[1], Carolina Cardell[2,*], Maja Urosevic[2], Encarnación Ruiz-Agudo[2], Felix Deutsch[3], René Van Grieken[1]

[1] Micro and Trace Analysis Centre, Department of Chemistry, University of Antwerp, Universiteitsplein 1, 2610 Antwerp, Belgium

[2] Department of Mineralogy and Petrology, Faculty of Science, University of Granada, Campus Fuentenueva s/n, 18071 Granada, Spain

[3] Environmental Modeling Unit, Flemish Institute for Technological Research (VITO), Boeretang 200, 2400 Mol, Belgium.

Article history:

Received 15 April 2010

Accepted 5 July 2010

doi: 10.1007/s12665-010-0657-5

ABSTRACT

Indoor and outdoor concentrations of atmospheric gaseous pollutants as well as composition, size, and morphology of particulate matter have been investigated at the monastery of San Jerónimo in Granada (Southern Spain). Complementary micro- and nano-analytical techniques were applied; elemental and mineralogical composition and morphological characteristics of particulate matter were investigated combining electron probe microanalysis at the single particle level, and bulk aerosol samples were analyzed using energy-dispersive X-ray fluorescence, X-ray diffraction, scanning electron microscopy with energy-dispersive X-ray analyzer and transmission electron microscopy (TEM). Microclimatic conditions at the monastery were monitored, and gas concentrations were assessed by means of diffusion tubes subsequently analyzed with ion chromatography. Results revealed high abundances of soil dust particles (aluminosilicates, calcite, dolomite, quartz), salt aerosols (chlorides, sulfates and ammonium-rich salts), and NO2 and SO2 both outdoors and indoors. Amorphous black carbon particles had surprisingly high abundances for Granada, a non-industrialized city. The composition of indoor particles corresponds to severe weathering affecting the construction materials and artworks inside the church; moreover their composition promotes a feedback process that intensifies the deterioration. Chemical reactions between chloride-rich salts and pigments from paintings were confirmed by TEM analyses. Indoors, blackening of surface decorative materials is fostered by particle re-suspension due to cleaning habits in the monastery (i.e. dusting). This is the first air quality study performed in a monument in the city of Granada with the aim of developing a strategy for preventive conservation.

KEYWORDS

Atmospheric aerosols, Architectural monument, SEM–EDX, EPMA, TEM, Preventive conservation

5.1. Introduction

Most buildings of cultural interest are located in urban environments, where pollution caused by road traffic, residential heating systems, and industry has harmful consequences for outdoor and indoor construction and decorative materials (Pérez-Rodríguez et al. 1998; Van Grieken et al. 2000; Esbert et al. 2001; Moropoulou et al. 2001; Jordan et al. 2009). On the exterior of buildings, black crusts are formed and dust is deposited due to impact of gases and particles, leading to undesirable aesthetic effects and also compromising the integrity of the materials (Pérez-Rodríguez et al. 1998; Esbert et al. 2001; Moropoulou et al. 2001; Bonazza et al. 2005; Sanjurjo Sánchez et al. 2009; Xu et al. 2010). The aggressiveness of particles depends on their composition, size, hygroscopicity, and solubility; for example, deposition of acids such as sulfuric and nitric acid can lead to local corrosion processes on certain stones, glass, paintings, and metals (Nazaroff et al. 1993; Sabbioni et al. 2003; Tétreault 2003). On the other hand, indoor air pollution, a result of both indoor and outdoor phenomena, can cause soiling and chemical weathering of decorative materials via adsorption of gases or particulate matter (Sánchez-Moral et al. 1999; Gysels et al. 2004; Worobiec et al. 2006; Spolnik et al. 2007; Kontozova-Deutsch 2007; Jordan et al. 2009).

Currently, preventive conservation measures are acknowledged as important for safeguarding cultural heritage (CH), both in terms of preserving CH and also reducing the cost of future conservation measures. Preventive conservation requires knowledge of a variety of parameters connected to a specific CH site, including microclimatic conditions, concentration, and character of caustic gases and particles in the surrounding air, as well as management of the CH site (Cataldo et al. 2005; Kontozova-Deutsch et al. 2008a; Worobiec et al. 2008; Brimblecombe et al. 2009). Hence, monitoring and sampling campaigns for air pollutants and microclimatic parameters have to be performed to identify possible threats and thereby remedies (Delalieux et al. 2001; Esbert et al. 2001; Camuffo et al. 2002; La Gennusa et al. 2005; Corgnati et al. 2009; García-Diego and Zarzo 2010).

There is a vast body of literature tackling the impact of outdoor and indoor air composition and microclimate on damaging our CH, in which diverse analytical techniques

are applied to characterize and quantify atmospheric aerosols, such as, e.g., electron probe microanalysis (EPMA), X-ray fluorescence (EDXRF), scanning electron microscopy (SEM), ion chromatography (IC), gas chromatography–mass spectrometry (GC–MS), transmission electron microscopy (TEM), and X-ray diffraction (XRD), Fourier transform infrared spectroscopy (FTIR) and recently Raman spectroscopy (RS) (Weinbruch et al. 1997; Van Grieken et al. 2000; Delalieux et al. 2001; Ro et al. 2001; Murr and Bang 2003; Liu et al. 2005; De Hoog et al. 2005; Simão et al. 2006; Ivleva et al. 2007).

Most of these studies have been carried out in wellprotected buildings like museums (Camuffo et al. 2002; Gysels et al. 2004; La Gennusa et al. 2005: Corgnati et al. 2009), which differ from numerous churches that are required to be open for congregation and which commonly use incense and candles in liturgical practices (Worobiec et al. 2006, 2008; Spolnik et al. 2007; Kontozova-Deutsch et al. 2008b; García-Diego and Zarzo 2010). This is the case of the church of the monastery of San Jerónimo (Granada, Spain). The purpose of this work was to characterize at micro and nano-scale, outdoor and indoor air composition at the monastery of San Jerónimo in Granada (Southern Spain). To this end qualitative and quantitative analyses of atmospheric particulates and gases were performed by combining complementary mineralogical and elemental analytical techniques to typify the levels, composition, and also size and morphology of particulates. The origin of the outdoor and indoor aerosols and their contribution to damaging the artworks exposed inside the church of the monastery are assessed.

5.2. Experimental

5.2.1. Sampling location

The city of Granada in Southern Spain has a population of around 300,000 (agglomeration 600,000). It is about 50 km from the Mediterranean Sea and approximately 200 km from the African continent. The city is situated in a natural basin surrounded by mountains with altitudes up to 3,500 m. Due to this topography and the prevailing low wind

speeds, in combination with traffic emissions, pollution-derived particulate matter often accumulates in the urban air of Granada (Lyamani et al. 2010). The city has a near-continental climate with cool winters, hot summers, and high diurnal temperature variability. Most rainfall occurs during winter and spring seasons, leading to re-suspension of dust particles predominantly in the dry seasons.

The investigated monastery of San Jerónimo is located in the city center of Granada, surrounded by busy streets. Its construction started in 1496 and was directed by two famous architects: Jacobo Florentino until 1526 and later by Diego de Siloé, the most famous Spanish architect at that moment. It is a splendid Renaissance temple with an extraordinary church, one of the best representative works of the Spanish Baroque with a spectacular altar piece and choir, considered one of the masterpieces of Spanish sculpture. The interior of the temple is entirely covered with polychromes. The monastery was plundered during Napoleon's invasion and converted into cavalry barracks. Numerous restorations of the remains have been undertaken, most recently in 1998. At present, the monastery of San Jerónimo constitutes a historic building where numerous scientific investigations have been realized, as for example salt weathering characterization and investigations on salt inhibitors (Cardell 1998; Laiz et al. 2000; Cardell and Rodríguez-Gordillo 2003; Ruiz-Agudo 2007). However, prior to this study no research on air quality in the framework of a CH study had been carried out in this or other monuments in the city of Granada.

The sampling campaign was carried out in the period of February–March 2008. Samples of gaseous (NO_2, SO_2, O_3) and particulate pollutants (bulk and single particles) were taken indoors and outside the monastery. The sampling locations are shown in Fig. 1. Outdoor samples were taken at two different heights at the church and the major cloister. Inside the church sampling sites were selected considering orientation and height in order to establish possible differences in both quantity and composition of particles. The altar and lateral rooms are the most distant from the entrance, which is situated in the NW of the church connected to the major cloister. Hence, less deposition of outdoor-derived particulate matter can be expected at those locations. The organ is found on the first floor above the entrance at approximately 5 m above ground level (a.g.l.). Some of the stained glass

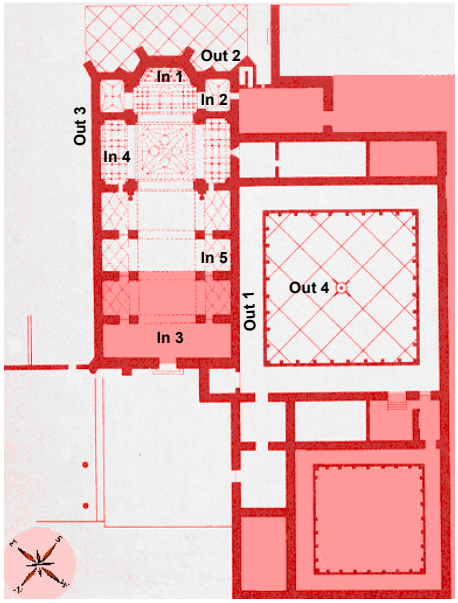

Sample	Sample location	Type of sample
In 1	Altar, h=1m	gases
In 2	Lateral room, W altar h=1m	gases
In 3	Organ, h~5m	gases, bulk and single particles
In 4	Side chapel E, h=1m	gases, bulk and single particles
In 5	Side chapel W, h=1m	gases
Out 1	Cloister, 1st floor h~5m	gases, bulk and single particles
Out 2	Apse, h~20m	gases
Out 3	Roof, h~20m	gases, bulk particles
Out 4	Cloister, garden h=1m	gases

Fig. 1 Sampling locations and outline ground-plan of the monastery of San Jerónimo (Granada, Spain). Map reproduced with permission (Cardell 1998)

windows of the church are broken and the main entrance remains open during visiting hours (in winter from 10^{00} to 18^{30} and in summer from 10^{00} to 19^{30}). Hence, pigeons can fly inside and the indoor–outdoor air exchange can be expected to be quite large. In addition, in this work a PM10 sample (AER-GR) was taken at the roof of the Andalusian Centre for Environmental Studies (CEAMA), located in Granada.

5.2.2. Analysis of gaseous pollutants

SO_2, NO_2, and O_3 were collected by means of radiello® (Fondazione Salvatore Maugeri, Padova, Italy) diffusive samplers, exposed in parallel for 1 week, both indoors and outdoors. The radiello® sampler consists of a chemically adsorbing cartridge, surrounded by a cylindrical microporous diffusive body (5.8 mm diameter, 60 mm height) coated with triethanolamine (TEA) and was mounted on a supporting plate.

NO_2 and SO_2 were chemically adsorbed onto TEA, respectively, as nitrite (NO_2^-) and sulfite (SO_3^{2-}), or sulfate (SO_4^{2-}). They were quantitatively recovered from the cartridges by means of extraction in 5 mL of Milli-Q water (Millipore, Haverhill, USA). Nitrite and sulfite contents were determined by means of IC. Analysis of aqueous extracts was performed on a dual-column Dionex DX-120 ion chromatograph (Dionex, Sunnyvale, USA) equipped with a Dionex AS50 auto sampler. Suppression of background conductivity was achieved with a Dionex self-regenerating suppressor model ASRS-ULTRA (anions) with neutralization of the eluent by exchanging its counter ions with H^+ (generated by the electrolysis of H2O). The separation of the anions was attained on an AG14 guard column, preceded by an AS14 analytical column. The eluent was composed of 3.5 mM Na_2CO_3/1.0 mM $NaHCO_3$ at 1.2 mL min-1 flow rate. Calibration was performed using certified standard multi-ion solutions (Combined Seven Anion Standard II, Dionex, USA), diluted to obtain effective concentrations of 20, 10, 5, 2.5, and 1 ppm standard solutions. Data acquisition, calibration curve, and peak integration were done using the Peaknet software package, version 6.11.

The diffusion tubes for O_3 sampling consisted of a polyethylene tube, filled with 4,40-dipyridylethylene-coated silica gel and closed, at one end, by a PTFE cap. During exposure, the 4,40-dipyridylethylene was transformed into 4-pyridylaldehyde through ozonolysis. A silica gel ensured the presence of H_2O inside the pores, necessary to complete the ozonolysis reaction. During sample preparation, 4-pyridylaldehyde was recovered from the silica gel by adding 3-methyl-2-benzothiazolinone hydrazone (MBTH). Subsequently, 4-pyridylaldehyde was converted into the corresponding yellow-colored azide, analyzed by means of UV–Vis spectrophotometry (UVIKON 930, Kontron Instruments) at 430 nm.

5.2.3. Analysis of single particles

For the collection of size-segregated aerosol samples, a 9-stage May cascade impactor was applied with aerodynamic cut-off diameters of 8, 4, 2, 1, and 0.5 μm for stages 3, 4, 5, 6, and 7. As collection substrates Si wafers and Ag foils were chosen. The size-segregated samples were analyzed by an electron probe microanalyser (EPMA, JEOL 733, Tokyo, Japan) equipped with an ultra-thin window Si(Li) detector (Oxford). To avoid beam damage

of the analyzed particles, cooling of the sample holder by liquid nitrogen was applied, which is especially important for low-Z elements. Approximately 300 particles were measured on each stage, so almost 1,500 individual aerosol particles were analyzed in one sample set. The X-ray spectra were processed using the *AXIL* software for both EDXRF and EPMA (Van Espen et al. 1986). For EPMA, quantitative calculations of the particle composition (including light elements such as C, N and O) were performed using a method based on iterative Monte Carlo simulations using the in-house program Elementary (Ro et al. 2003). The large data set from the single-particle analysis was treated by statistical methods. To compare the different aerosol sample sets, all particles were classified by non-hierarchical clustering analysis based on the Forgy algorithm (Massart and Kaufmann 1983). The initial centroids were selected by a sequence of hierarchical cluster analyses using the homemade software *IDAS* (Bondarenko et al. 1996). The results for the five stages were divided into three representative and main fractions: the fine fraction, which contains average results of particles with cut-off diameter of 0.5 and 1 μm (and thus suitable to be characterized at nanoscale by TEM), the middle-sized fraction, which contains average results of particles with cut-off diameter of 2 and 4 μm, and the coarse fraction comprising the average results of particles with cut-off diameter of 8 m. These last two fractions were suitable to be analyzed by micro (SEM–EDX) and mineralogical (XRD) analytical techniques as well.

5.2.4. Bulk aerosol particles

For the collection of bulk aerosol samples from the monument, Nuclepore® filters of 0.4 μm pore-size and 47 mm diameter were used in a Millipore filter-unit connected to a low-volume vacuum pump. The average sampling time was 24 h and the flow rate about 30 L min-1. Bulk concentrations were analyzed for up to 20 elements by energydispersive X-ray fluorescence (EDXRF) analysis. The measurements were carried out with a Tracor Spectrace-5000 instrument employing a low-power Rh-anode X-ray tube (17.5 W). For the determination of high-Z elements (starting from K) a tube voltage of 35 kV, a current of 0.35 mA, and an acquisition time of 10,000 s were selected. For low-Z elements (from Al to Cl), the tube voltage was adjusted to 10 kV; a current of 0.35 mA, and an acquisition time of

4,000 s were used. The detection limits were between 5 and 10 ng cm-2 on the filters. The measured intensities were converted into elemental concentrations by the application of the *AXIL* program code (Van Espen et al. 1986).

Conventional powder XRD was used to determine the mineral composition of the bulk aerosol samples taken from the monastery (indoors and outdoors), as well as the PM10 (AER-GR) sample collected from the CEAMA. The PM10 (AER-GR) sample was collected during 12 h by means of a high-volume sampler MCV-CAV with DIGITEL DH-80 and with a flow rate of 30 m^3 h^{-1}, using circular glass fiber filters (15 cm, QF20 Schleicher and Schuell, Dassel, Germany). To perform the XRD analyses, a Philips PW-1710 diffractometer was used with the Bragg–Brentano focusing geometry, a graphite secondary monochromator, CuKa radiation (k = 1.5405), and automatic divergence 1º slit. The voltage was 40 kV and the tube current 40 mA. Diffraction patterns for the total suspended aerosols were obtained using continuous scan mode exploring an area over 3º–64º 2θ, with 0.05 scan rate, and 0.80 integration time. XRD was applied directly to the Nuclepore® filter surface (no sample preparation was required). Automatic acquisition, evaluation, and identification of minerals were carried out with the Xpowder software (Martín-Ramos 2004).

To study the chemical composition and micro-morphology of the bulk aerosol samples taken from the monastery and the PM10 sample (AER-GR), a scanning electron microscope (SEM Leo 1430VP, VP-SEM) coupled with an EDX microanalyzer (Inca 350 version 17, Oxford Instruments) was used. Analyses were carried out in secondary electron (SE) and backscattered electron (BSE) mode. Both operating modes are complementary, as SE-mode provides information on texture and structure and BSE-mode on elementary composition. The SEM–EDX working conditions were 500 pA filament current, 20 keV beam energy, 10 eV/ch resolution, and an acquisition time of 50 s for pinpoint analyses. Samples requiring no preparation were mounted on a tee and coated with carbon for microanalysis purposes, and with gold to better visualize the morphology.

Transmission electron microscopy (Philips CM20) equipped with an EDAX solid-state ultrathin-window energy dispersive X-ray (EDX) detector was used to investigate the composition and morphology at nanoscale of the indoor and outdoor samples from the monastery and the PM10 sample (AER-GR). The acceleration voltage of the microscope was 200 kV, and a lens aperture of 40 μm was used as a compromise between amplitude and phase contrast for the images. The identification of phases was facilitated by collecting selected area electron diffraction (SAED) patterns. Quantitative analytical electron microscopy analyses were performed in scanning TEM mode using a 10-nm diameter beam and a 20 × 100 nm scanning area. A low-background condenser aperture and an analytical Be sample holder were employed to improve spectrum quality. Prior to TEM analysis samples were dispersed in ethyl alcohol and deposited on Formvar© and carbon-film coated Cu grids.

Microclimatic parameters, namely temperature (T) and relative humidity (RH) were monitored during the sampling period by means of Signatrol SL502 (Signatrol Ltd, Gloucestershire, UK) sensor. The data were collected every 20 min indoors (altar, In 1) and outdoors (major cloister, Out 1).

5.3. Results and discussion

5.3.1. Microclimatic parameters

Figure 2 shows the trend of T and RH recorded outside and inside the monastery during the sampling campaign. Outdoors, the means of T and RH were 10.5 ± 6.6□C and 44.3 ± 22.6%, respectively. It should be recalled that the city of Granada has a near continental climate with large day/night amplitudes of temperature and RH (Cardell 1998; Lyamani et al. 2010). These fluctuations cause high thermal stress to stone materials accelerating their deterioration (Rodríguez-Gordillo and Sáez-Pérez 2006). As result, particles are easily generated and subsequently may enter the studied building and cause

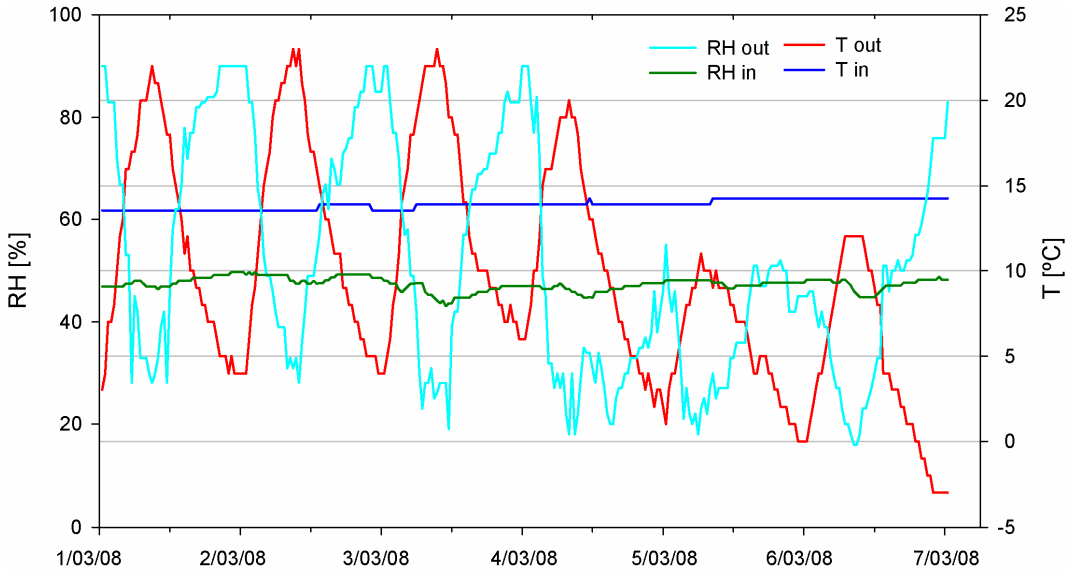

Fig. 2 Temperature and relative humidity at the monastery of San Jerónimo (Granada, Spain)

soiling and deterioration of artworks exposed indoors. In the interior of the church the mean T (13.9 ± 0.3ºC) and mean RH (47.5 ± 1.5%) stayed almost constant due to the buffering effect of the high volume of the building. This circumstance is certainly advantageous for the preservation of the artworks in the church.

5.3.2. Gaseous pollutants

The results obtained for concentrations of NO_2, SO_2, and O_3 are shown in Fig. 3. Indoor and outdoor mean concentrations of NO_2 were found to be similar. The average indoor value of NO_2 was 29 μg m^{-3}, whereas a mean outdoor value of 32 μg m^{-3} has been measured. NO_2 is a gas with largely outdoor sources (via NO_x, mainly from road traffic). The comparable NO_2 values could be attributed to the considerable indoor–outdoor air exchange in the church (due to circumstances mentioned above, see sampling location), and the lower deposition velocity compared with that of O_3. However, indoor sources have to be considered as well, such as burning candles and incense, the latter particularly during

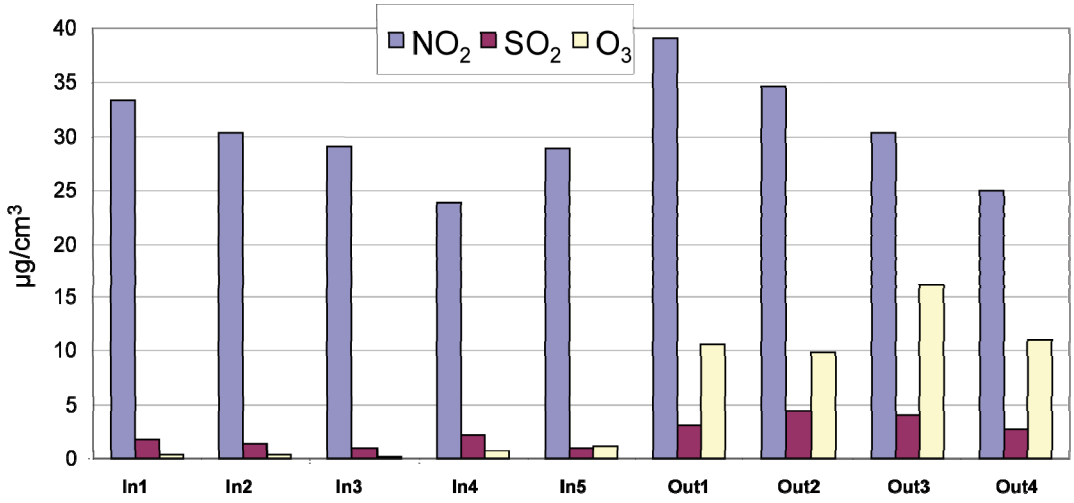

Fig. 3 Indoor and outdoor concentrations of NO_2, SO_2 and O_3 at the monastery of San Jerónimo (Granada, Spain).

weekends. Similar trends have been identified in other churches (Spolnik et al. 2005; Worobiec et al. 2006; Kontozova-Deutsch et al. 2008b).

As expected, indoor SO_2 concentrations were lower than outdoors. The average SO_2 value was 1.6 µg m^{-3} for indoors, and 3.6 µg m^{-3} for outdoors. Surprisingly, the SO_2 concentrations in the interior of the church were higher than others reported in the literature, which were near the detection limit (Spolnik et al. 2005; Worobiec et al. 2006; Kontozova-Deutsch et al. 2008b). Again, the considerable indoor–outdoor air exchange in the church likely plays an important role as no significant indoor SO_2 sources have been identified.

The average outdoor O_3 concentrations were much higher than those indoors. The calculated O_3 mean value for outdoors was 12 µg m^{-3}, versus only 0.6 µg m^{-3} indoors. This result has to be attributed to the high-deposition velocity and reactivity of the O3, and the absence of an indoor ozone sources. The obtained O_3 values (both indoors and outdoors) are rather low in comparison with indoor O_3 concentrations measured during winter in other churches (Worobiec et al. 2006; Kontozova-Deutsch et al. 2008b). The location of the monastery in the city center of Granada, near busy streets, should be responsible for these

low O_3 concentrations since high NO_x (mainly NO) emissions by traffic lead to substantial ozone titration.

The literature reports that NO_2 causes formation of nitric acid (HNO_3) leading to decomposition of lime-containing materials, fading of pigments, and corrosion of metals (Tétreault 2003). On the other hand, SO_2 oxidizes quickly to sulfur trioxide (SO_3) and sulfuric acid (H_2SO_4), which leads to damage of basic construction and decorative materials like limestone, plaster, and frescoes. The interior of the church of San Jerónimo is covered with mural paintings and polychromes (on a substrate of gypsum based plaster), severely damaged by salt crystallization at particular sites, thus exposing the limestone used to build the church (Cardell 1998; Cardell and Rodríguez-Gordillo 2003). Hence, the high indoor concentrations of NO_2 and SO_2 are a potential threat for the construction and artwork materials contained in the monastery.

5.3.3. Single particles

The results of the size-segregated single particle analysis performed with EPMA are shown in Fig. 4. The samples were divided into three fractions (fine, middle and coarse) according to their aerodynamic cut-off diameters (8, 4, 2, 1 and 0.5 μm for stages 3, 4, 5, 6 and 7). Soil dust particles, i.e., aluminosilicates (AlSi + Fe-oxid) were found in particles of the middle size-fraction and in coarse particles. Aluminosilicates derive from the geological materials present in the vicinity of the city, e.g., limestones and metamorphic rocks (Puga et al. 2007). In addition, sources such as windblown soil dust, road traffic, and fly ash aerosols have to be considered (Lyamani et al. 2010). Aluminosilicates showed higher abundances in indoor versus outdoor samples. This fact has to be attributed to the intense sanding-off of various construction materials used to build the monastery, such as renders, mortars and, to a smaller extent, bricks, all severely altered as described elsewhere (Cardell 1998) (Fig. 5). Additionally, transport of these particles by the shoes of visitors and monastery nuns may also contribute to the observed high indoor abundances. Inside the building, re-suspension of particles plays an important role as inferred from the cleaning habits (dusting instead of

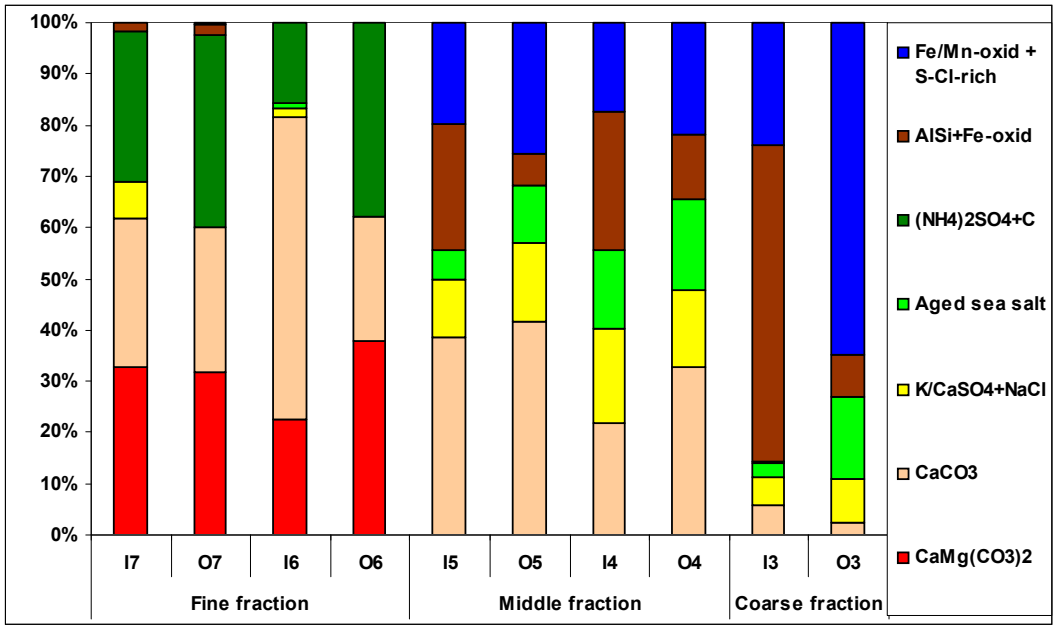

Fig. 4 Relative abundances of particle types in indoor and outdoor samples of the fine, middle-sized, and coarse size fraction in the monastery of San Jerónimo (Granada, Spain).

vacuum cleaning or moist wiping) and the high amounts of dust deposited at unreachable places. The high abundance of soil dust particle type certainly represents a threat to the indoor environment, since these particles can accelerate the soiling of material surfaces, although they are not considered to be chemically aggressive. Dust accumulation is an important management and conservation problem in monuments (Brimblecombe et al. 2009).

Calcite ($CaCO_3$) was the most abundant mineral found in particles of the fine and middle size-fractions, while dolomite ($CaMg(CO_3)_2$) was detected only in the fine size fraction. Calcite particles of the fine and coarse fractions showed slightly higher abundances indoors. Limestone (calcite-bearing rock) and dolostone (dolomite-bearing rock) are abundant near the city of Granada and have been used profusely as construction materials in ancient and modern buildings such as the monastery of San Jerónimo (Cardell 1998). However, the high abundance of these minerals inside the church suggests a source from deterioration of construction materials (limestone and mortars; already visible to the naked

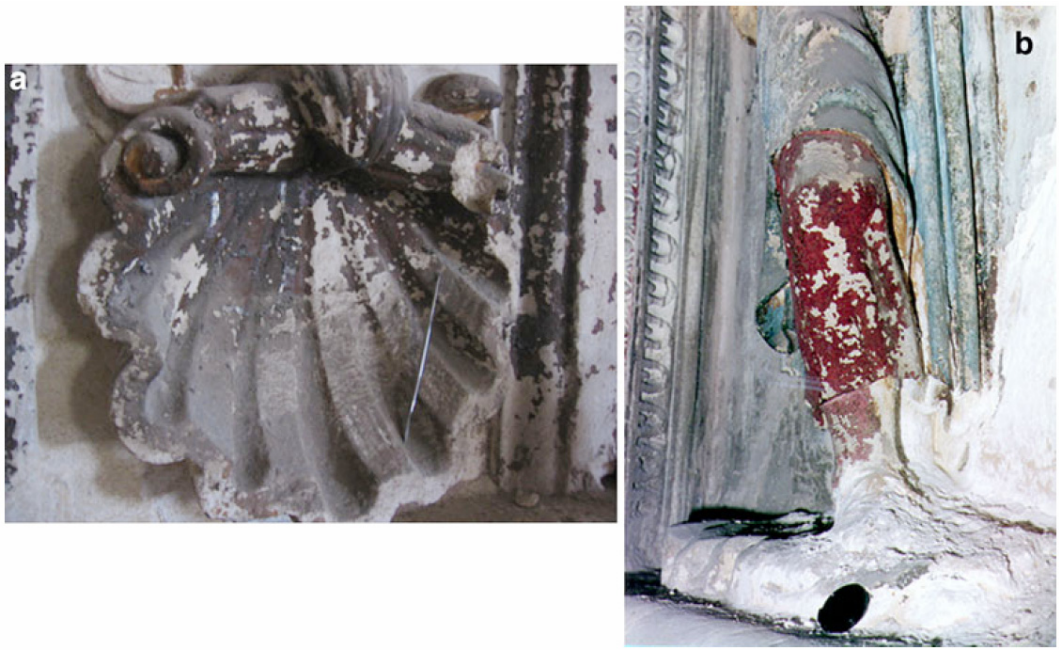

Fig. 5 a Photograph of a weathered, polychromed ornament covered with a thin layer of dust. **b** Photograph of polychromed sculpture intensively deteriorated showing massive formation of sulfate-rich salts (epsomite and gypsum) and detachment of the paintings. Both ornaments are placed in the church of San Jerónimo at ~15 m a.g.l

eye), in addition to mineral particles originating from outdoor sources entering by the indoor–outdoor air exchange.

Ammonium sulfate ($(NH_4)_2SO_4$) particles clustered with carbon (C) were found only in the fine fraction and predominantly in the smallest particles. Abundances were slightly higher for outdoor versus indoor samples. This particle type is potentially threatening for the decorative materials of the monastery due to its hygroscopicity. Aged sea salt (a mixture of sodium chloride, sodium nitrate and sodium sulfate) had rather higher abundances in the middle and coarse-sized fractions, being slightly more predominant in outdoor samples. Clusters of calcium sulfate with potassium and sodium chloride were also found in most of the samples. In the middle- and coarse-sized fractions abundances were comparable indoors and outdoors, though in the fine fraction this cluster was only found in the indoor samples. Indoor sources for these sulfate/nitrate/chloride containing particles also must be considered. This is supported by the results of previous studies in the church of San Jerónimo (Cardell

1998; Ruiz-Agudo 2007) showing intense weathering of the limestone used in walls, windowsills, vaults, and carved figures as a result of the massive presence of salts. Gypsum ($CaSO_4 \cdot H_2O$), halite (NaCl), Mg/Na-rich sulfate efflorescences (mostly epsomite), and minor amounts of nitrates (niter, KNO_3, and nitratine, $NaNO_3$) were found in the building in these studies, mainly in the outer layer of the walls (Fig. 5b). As Mg-sulfates were not detected in outdoor aerosol samples, they most probably originate from indoor sources, such as infiltration of ground water and subsequent interaction with building materials in the walls (joining mortars, stone and paintings), which contain significant amounts of Mg. Regarding other sulfates, nitrates, and chlorides, both aerosols and indoor sources may contribute to their presence inside the church.

Finally, a cluster containing particles comprised of iron (Fe), manganese (Mn), sulfur (S), and chlorine (Cl) was found predominantly in the outdoor samples of the middlesized and coarse fraction. The origin of this particle type can be attributed to soil dust sources (aluminosilicates), and a marine source for Cl.

5.3.4. Bulk particles

The bulk aerosol concentrations obtained indoors and outdoors at the monastery of San Jerónimo by EDXRF analysis are presented in Table 1. The concentrations of all elements, except for S and Pb, were observed to be significantly higher outside the building. This suggests that these two elements have an indoor source. As stated above, the higher level of S indoors can be attributed to the high amount of sulfate-rich salts such as epsomite, hexahydrite, and gypsum present in the interior of the church, as found in earlier studies (Cardell 1998; Ruiz-Agudo 2007), while the higher amount of Pb should be due to the intense deterioration of the paintings (totally covering the interior of the church) containing Pb-based pigments (Cardell and Rodríguez-Gordillo 2003).

The highest outdoor and indoor concentrations were found for Ca and Si, followed by S, K, and Al. The origin of the outdoor particles can be attributed to geological materials from the vicinity of the city as limestones and metamorphic rocks (Puga et al. 2007).

Table 1. Elemental concentrations of bulk particles at the monastery of San Jerónimo (Granada, Spain)

	In 1 ng m^{-3}	Out 1 ng m^{-3}	In 2 ng m^{-3}	Out 2 ng m^{-3}
Al	166	304	111	231
Si	400	742	271	578
Si	469	339	352	179
Cl	4.1	24.1	1.8	82
K	233	358	311	335
Ca	388	1790	310	2004
Ti	15	30	9.1	24
V	5.1	7.7	8.3	4.2
Mn	2.2	5.7	1.9	5.2
Fe	108	283	92	215
Ni	2.9	2.6	5.1	1.5
Cu	3.1	7.2	2.8	4.8
Zn	8.5	18	6.7	8.2
Pb	4.0	2.1	5.3	1.8

Indoors, lower concentrations of these elements were detected. The sampling period was characterized by dry weather conditions leading to rather high outdoor particulate matter concentrations. The results suggest that there was considerable indoor–outdoor air exchange rate leading to transport of ambient particles into the monastery. However, indoor sources cannot be excluded for these particle types. In fact, the severe weathering of the construction (stone and mortars) and decorative materials (paintings), and the related efflorescence affecting the interior of the church should be one of the major (indoor) sources for S, Ca, Si, and K (Cardell 1998). In addition, K and S can also be connected to the burning candles and incense inside the church (Kontozova-Deutsch et al. 2008b). From a preventive conservation perspective, the high concentration of sulfates in indoor aerosols is a threatening factor for pigments, metals, and other acid-sensitive artworks. Thus, the results obtained in this work confirm a feedback process inside the church that enhances further weathering of the indoor construction and decorative materials.

The analysis of the samples with XRD revealed a broad hump in the diffractograms due to the presence of amorphous black carbon particles (~9%), in agreement with previous

studies (Rodríguez-Navarro and Sebastián 1996; Lyamani et al. 2010). The basin-like geography of the Granada basin favors weak wind speeds that, in combination with pollutant emissions, mainly from traffic, lead to heavy accumulations of particles. Moreover, the monastery of San Jerónimo and the CEAMA are located in the southern part of the city near the highway that rings it. Considering that Granada is a non-industrialized city, local aerosol sources are mainly heavy traffic (mostly diesel vehicles) together with re-suspension of material available on the ground. In addition, during winter domestic heating (typically oil burning central heating) represents an additional important source of anthropogenic aerosols. These aerosols contain significant amounts of carbonaceous particles, in agreement with our results of XRD analysis. As a consequence a dark haze can be observed frequently above the city, especially during morning hours, indicating the presence of soot particles as important pollutant in the basin.

The identified crystalline phase consists largely of calcite ($CaCO_3$, ~28%), muscovite (~27%), i.e., a phyllosilicate mineral known as common mica with formula $KAl_2(AlSi_3O_{10})(F,OH)_2$, and dolomite ($CaMg(CO_3)_2$, ~12%). Minor phases include Na feldspar ($Na(AlSi_3O_8$, ~9%), gypsum ($CaSO_4 \cdot 2H_2O$, ~8%), paragonite (~5%) which is a phyllosilicate with empirical formula $NaAl_2$ $(Si_3Al)O_{10}(OH)_2$, and quartz (SiO_2, ~3%). This composition is consistent with the results obtained elsewhere (Rodríguez-Navarro and Sebastián 1996), as well as with the mineralogy of the geological materials in the vicinity of Granada, namely limestones, dolostones, gypsum, and metamorphic rocks (e.g. micaschists) proceeding from the Sierra Nevada mountains and the surrounding basins (Puga et al. 2007).

The microanalysis of the samples (with particle size above 2 μm) performed with SEM–EDX showed that the major constituents were O, Si, Ca, Mg, and Al; the K content was also noteworthy. Minor constituents were Na, S, Cl, and Fe in decreasing order of abundance, and more rarely Br and P in sample AER-GR (Fig. 6). The spectra suggest the presence of clay minerals (phyllosilicates) accompanied by calcite, dolomite, and gypsum in a lower amount, in agreement with the mineralogical results obtained with XRD. In addition, minor amounts of chlorine-based salts such as KCl and NaCl, Fe oxides, K-based sulfates and Fe-rich, and aluminosilicate-rich (Si and Al) particles can be inferred from the spectra, in accordance

with the EPMA results. This composition is consistent with results published elsewhere for the city of Granada (Rodríguez-Navarro and Sebastián 1996) and results of airborne particulate matter deposited on the exterior of other monuments (Esbert et al. 2001). Iron (Fe) can be related to diesel exhaust, mainly composed of soot and metallic particles bearing Fe and Fe–S as major elements, while Br can be ascribed to emissions from gasoline engines composed of minor amounts of soot and Br-rich particles (Simão et al. 2006). Figure 7 shows several SEM images of the outdoor samples. In the outdoor samples taken at the monastery (Fig. 7a, b), soil erosion particles were observed, composed of calcite, dolomite, and quartz, as well as minor amount of Fe-rich particles and salts made of NaCl, KCl, and gypsum. Figure 7c, d corresponds to AER-GR sample revealing the presence of Fe-rich spherical particles, clay minerals, calcite, quartz, gypsum, chlorine, and sulfate-based salts as well as the so-called iberulite particle. This is a new type of spherical aerosol particle with a vortex, detected in Southern Spain, made of a complex mineral assemblage that also contains biological remains (Díaz-Hernández and Párraga 2008). The most likely source areas based on inherent mineral components are the Sahara and Sahel, while other minerals are the results of atmospheric neoformation. The appearance of iberulites is a discontinuous phenomenon, occurring mainly during summer and in dry periods corresponding to the highest total suspended particle (TSP) contents. Thus a correlation between amounts of dust and iberulites can be established; indeed, often their presence coincides with red dust rains and periods with no heavy rains. The sampling period of our study was characterized by dry weather conditions that lead to high outdoor particulate matter concentration.

Outdoor and indoor particles below 1 μm in size from the monument and the PM10 sample (AER-GR) were studied by TEM (Fig. 8). The main particles found in the aerosols sampled outside the church were salts, in particular chlorides and sulfate-rich salts. Also ammonium chloride (i.e. sal-ammoniac) was a common component; its origin may be related to the existence of guano deposits in the upper part of the church (Cardell 1998). Ammonium-rich salts were also identified by EPMA in the smallest particles of the fine fraction inside and outside the church. It should be noted that pigeon feathers and excrement are abundant not only in the exterior of the church in the upper parts at around 15 m a.g.l., but also in the interior due to open doors and broken stained-glass windows.

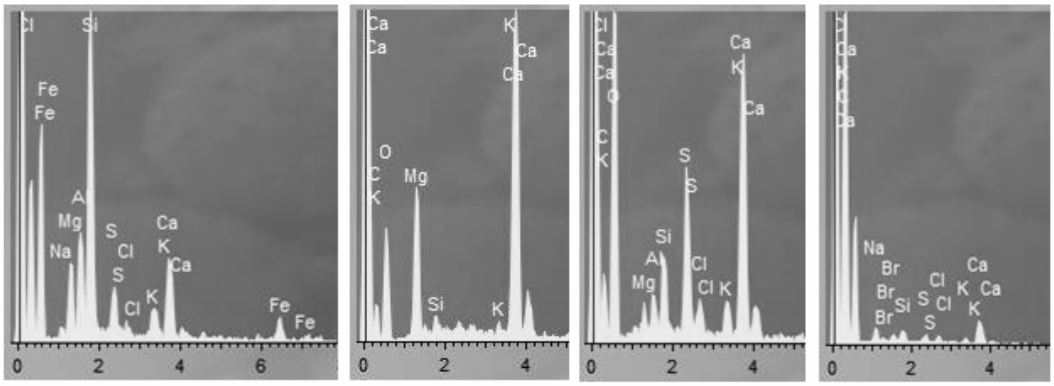

Fig. 6 SEM–EDX spectra representative for the composition of the outdoor PM10 sample (AER-GR)

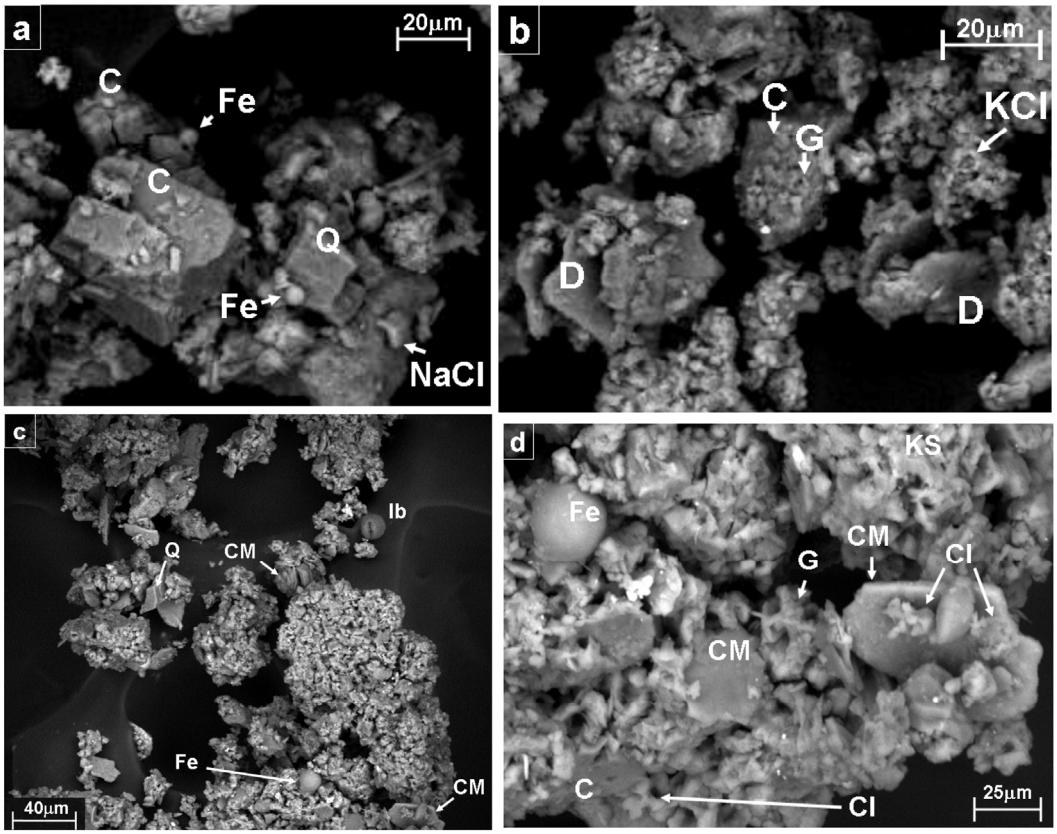

Fig. 7 SEM images of outdoor samples showing different particles. Sample Out-3 (**a**, **b**, outside the monastery) and sample AER-GR (**c**, **d**). Clay mineral (*CM*), calcite (*C*), dolomite (*DO*), quartz (*Q*), gypsum (*G*), Fe-rich particle (*Fe*); iberulite (*Ib*), chloride-based salts (*KCl*) and K-based sulfates (*KS*)

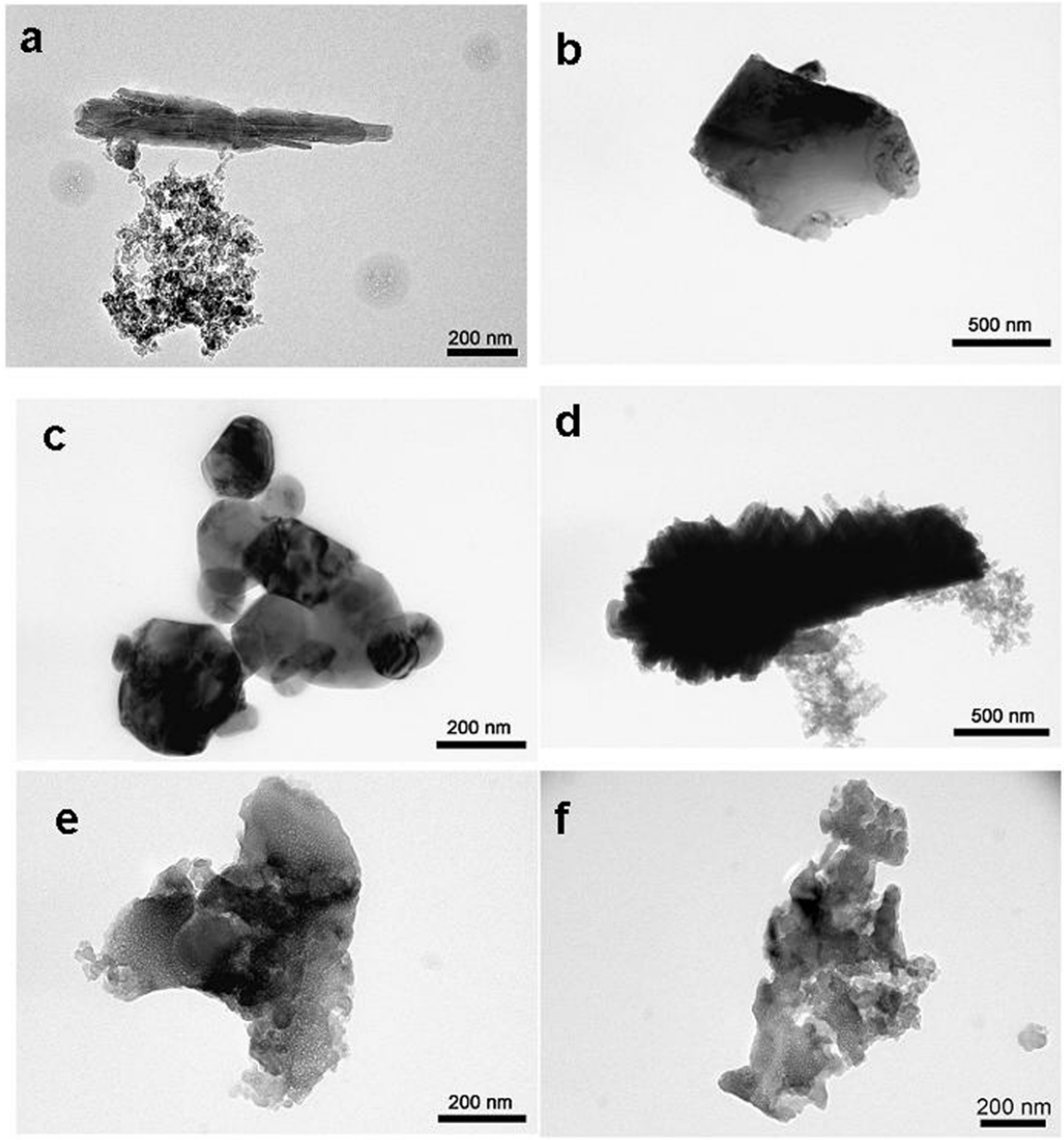

Fig. 8 Representative TEM images of particles found in aerosols. Sample AER-GR: **a** phyllosilicate particle and aggregate of amorphous carbon particles and **b** calcite; sample Out-3: **c** rutile, **d** iron oxide; sample In-4: **e** NaCl and **f** calcium–potassium double sulfate particles

Particles of Ca–K–S and Ca–Na–K–S were also frequently detected, in agreement with the aged salts analyzed with EPMA inside and outside the monastery, as well as in the AER-GR sample. Their presence may be attributed to transport of marine aerosols to the city, although in-cloud processes cannot be neglected as a possible source (Liu et al. 2005). Oxidation of atmospheric SO_2 in the presence of water leads ultimately to the formation of sulfates. Aluminosilicates were also found in the fine fraction of these samples as revealed by EPMA, XRD, and SEM–EDX in the coarser fractions. In particular, fibrous paragonite was detected with TEM which corroborated the XRD results. The presence of calcite, as well as the detected silicates could originate from windblown dust released during natural erosion of limestone rocks and clay formations surrounding the city of Granada. Aggregates of amorphous carbon particles and particles of amorphous SiO_2 were also identified with TEM in outdoors samples. These aggregates, randomly oriented and poorly crystalline, are composed of graphite particles, typically present in particulate matter from diesel motor vehicles exhaust emissions (Simão et al. 2006).

Regarding the indoor particles, again the main particles found were chlorides and sulfates, essentially ammonium chloride and Ca–K–S-rich particles (Fig. 8e, f). The composition of the indoor samples obtained with TEM can be related to that of the outdoor aerosols, in accordance with the EPMA results. However, as stated above, indoors sources such as the sanding-off of salt-containing building stone may also contribute to some extent to the presence of these particles in indoors aerosols. The identification of iron chloride particles inside the church reveals interaction between chloride-based particles (e.g. salt-rich particles) and Fe-rich pigments and clay-based pigments present in the wall paintings (Cardell and Rodríguez-Gordillo 2003). However, interaction with iron-rich particles from diesel motor vehicle exhaust emissions present in outdoor aerosols (entering the church by air exchange) cannot be neglected, although it is highly unlikely as these particles were not observed in outdoor samples, which also contain Cl-rich particles. Finally, silicates such as talc ($H_2Mg_3(SiO_3)_4$), carbonates like calcite and dolomite, and rutile (TiO_2) were also found (Fig. 9). As mentioned earlier, the indoor origin of these minerals can be attributed to the debris released during the sanding-off process that affects the construction materials (limestone, renders and mortars).

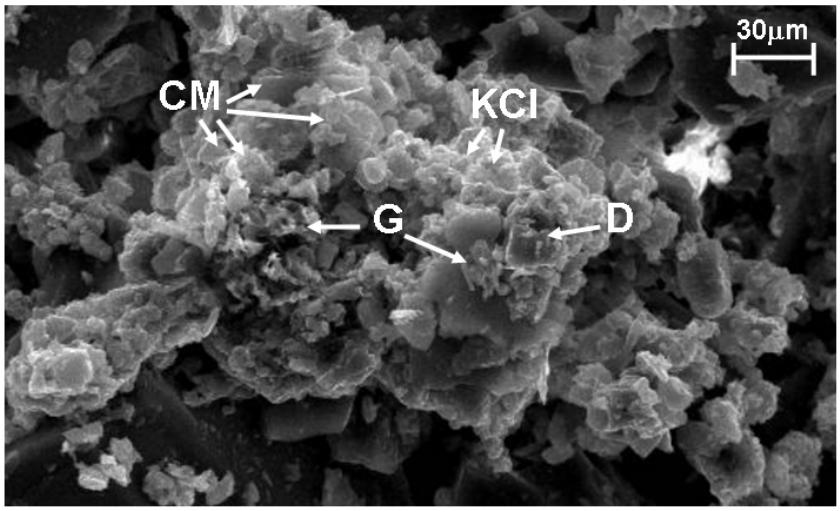

Fig. 9 SEM image of indoor samples showing dolomite (*D*), clay minerals (*CM*), gypsum (*G*), and KCl salt (*KCl*)

5.4. Conclusions

An outdoor and indoor air quality study was carried out at the monastery of San Jerónimo (Southern Spain) allowing characterization of atmospheric aerosols at nano- and microscale. Detected outdoor atmospheric aerosols are related to the geographical characteristics and climate of the city. Severe day/night temperature fluctuations contribute to soil dust generation. In addition, the basin-like shape of Granada surrounded by high mountains, in combination with heavy traffic, enhances the accumulation of soot particles. Also, an influx of marine particles can be expected when the wind direction is southerly (S and SW are the prevailing wind patterns).

In accordance with these characteristics, abundant soil dust particles (aluminosilicates, calcite, dolomite, quartz and clay minerals) and ca. 9% of black carbon particles (soot particles) were detected outside the monument. Other abundant particle types such as $(NH_4)_2SO_4$ clustered with C, and Fe/Mn oxides plus S–Cl rich particles were identified, as

well as minor amounts of Br and Fe-rich rounded particles (related to traffic) and iberulites (a new type of spherical aerosol particle identified in Southern Spain). TEM analyses identified salt aerosols (chloride, sulfate and ammonium-rich salts) and aggregates of both amorphous C and SiO_2 particles.

Inside the church of San Jerónimo, high NO_2 and SO_2 concentrations were detected, implying both indoor sources and an indoor–outdoor air exchange. The impact of both gases in the murals of the church is particularly aggressive. Abundances of C and soil dust particles, and ammonium and calcium sulfate and chloride-rich aerosols were found to be similarly high indoors and outdoors. In addition, high levels of S, Pb, and chloride- and sulfate-rich aerosols further showed that the source of these particles was related to the intense weathering of the construction and decorative materials, and to the copious efflorescences inside the church. Chemical reactions between Fe-rich pigments from paintings and chloride-rich salts were identified through the recognition of iron chloride particles. All of these particles promote a feedback process that triggers further weathering of the mentioned indoor materials. In addition, although stable indoor microclimatic conditions were registered, the inappropriate cleaning habits foster the re-suspension of particles which play a key role in the darkening of distant and isolated places inside the church.

8.5. References

Bonazza A, Sabbioni C, Ghedini N (2005) Quantitative data on carbon fractions in interpretation of black crusts and soiling on European built heritage. Atmos Environ 39:2607–2618

Bondarenko I, Treiger B, Van Grieken R, Van Espen P (1996) IDAS: a Windows based software package for cluster analysis. Spectrochim Acta B51:441–456

Brimblecombe P, Thickett D, Hun Yoon Y (2009) The cementation of coarse dust to indoor surfaces. J Cult Herit 10:410–414

Camuffo D, Bernardi A, Sturaro G, Valentino A (2002) The microclimate inside the Pollaiolo and Botticelli rooms in the Uffizi Gallery, Florence. J Cult Herit 3:155–161

Cardell C (1998) Salt crystallization in calcarenites: application to the Monastery of Saint Jerome, Granada (Spain). Dissertation, University of Granada (in Spanish)

Cardell C, Rodríguez-Gordillo J (2003) Polychromes in the Church of the Monastery of San Jerónimo in Granada: composition, alteration and applied techniques. Bol Soc Esp Mineral 26:113–121 (in Spanish)

Cataldo R, De Donno A, De Nunzio G, Leucci G, Nuzzo L, Siviero S (2005) Integrated methods for analysis of deterioration of cultural heritage: the Crypt of "Cattedrale di Otranto". J Cult Herit 6:29–38

Corgnati SP, Fabi V, Filippi M (2009) A methodology for microclimatic quality evaluation in museums: application to a temporary exhibit. Build Environ 44:1253–1260

De Hoog J, Osán J, Szalóki I, Eyckmans K, Worobiec A, Ro C-U, Van Grieken R (2005) Thin-window electron probe X-ray microanalysis of individual atmospheric particles above the North Sea. Atmos Environ 39:3231–3242

Delalieux F, Cardell C, Todorov V, Dekov V, Van Grieken R (2001) Environmental conditions controlling the chemical weathering of the Madara Horseman monument, NE Bulgaria. J Cult Herit 2:43–54

Díaz-Hernández JL, Párraga J (2008) The nature and tropospheric formation of iberulites: pinkish mineral microspherulites. Geochim Cosmochim Acta 72:3883–3906

Esbert RM, Díaz-Pache F, Grossi CM, Alonso FJ, Ordaz J (2001) Airborne particulate matter around the Cathedral of Burgos (Castilla y Leon. Spain). Atmos Environ 35:441–452

García-Diego FJ, Zarzo M (2010) Microclimate monitoring by multivariate statistical control: the renaissance frescoes of the Cathedral of Valencia (Spain). J Cult Herit. doi:10.1016/j.culher.2009.06.002

Gysels K, Delalieux F, Deutsch F, Van Grieken R, Camuffo D, Bernardi A, Sturaro G, Busse HJ, Wieser M (2004) Indoor environment and conservation in the Royal Museum of Fine Arts, Antwerp, Belgium. J Cult Herit 5:221–230

Ivleva NP, McKeon U, Niessner R, Pöschl U (2007) Raman microspectroscopic analysis of size-resolved atmospheric aerosol particle samples collected with an ELPI: soot, humic-like substances, and inorganic compounds. Aerosol Sci Technol 41:655–671

Jordan MM, Sanfeliu T, Gómez ET, Pallarés S, Vicente AB (2009) A valuation of the influence of particulate atmospheric aerosol in constructions of the cultural and architecture patrimony of the urban area of Castellon (NE, Spain). Water Air Soil Pollut 200:245–251

Kontozova-Deutsch V (2007) Characterisation of indoor gaseous and particulate pollutants for conservation in museums and churches. Dissertation, University of Antwerp

Kontozova-Deutsch V, Deutsch F, Godoi RHM, Spolnik Z, Wei W, Van Grieken R (2008a) Application of EPMA and XRF for the investigation of particulate pollutants in the field of cultural heritage. Microchim Acta 161:465–469

Kontozova-Deutsch V, Godoi RHM, Worobiec A, Spolnik Z, Krata A, Deutsch F, Van Grieken R (2008b) Investigation of gaseous and particulate air pollutants at the Basilica Saint-Urbain in Troyes, related to the preservation of the medieval stained glasses windows. Microchim Acta 162:425–432

La Gennusa M, Rizzo G, Scaccianoce G, Nicoletti F (2005) Control of indoor environments in heritage buildings: experimental measurements in an old Italian museum and proposal of a methodology. J Cult Herit 6:147–155

Laiz L, Cardell C, Rodríguez-Gordillo JF, Saiz-Jiménez C (2000) Bacteria in the efflorescences of Saint Jerome church, Granada, Spain. In: 5th international symposium on the "The Conservation of Monuments in the Mediterranean Basin", Seville, Spain, 15–16

Liu X, Zhu J, Van Espen P, Adams F, Xiao R, Dong S, Li Y (2005) Single particle characterization of spring and summer aerosols in Beijing: formation of composite sulfate of calcium and potassium. Atmos Environ 39:6909–6918

Lyamani H, Olmo FJ, Alados-Arboledas L (2010) Physical and optical properties of aerosols over an urban location in Spain: seasonal and diurnal variability. Atmos Chem Phys 10:239–254

Martín-Ramos JD (2004) Using XPowder: a software package for powder X-ray diffraction analysis. http://www.xpowder.com. D.L.; 2004. GR 1001/04, ISBN 84-609-1497-6

Massart D, Kaufmann L (1983) The interpretation of analytical chemical data by the use of cluster analysis. Wiley, New York

Moropoulou A, Bisbikou K, Van Grieken R, Torfs K, Polikreti K (2001) Correlation between aerosols, deposits and weathering crusts on ancient marbles. Environ Technol 22:607–618

Murr LE, Bang JJ (2003) Electron microscope comparisons of fine and ultra-fine carbonaceous and non-carbonaceous, airborne particulates. Atmos Environ 37:4795–4806

Nazaroff WW, Ligocki MP, Salmon LG, Cass GR, Fall T, Jones MC, Liu HIH, Ma T (1993) Airborne particles in museums, research in conservation. The Getty Conservation Institute, USA

Pérez-Rodríguez L, Maqueda C, Jiménez de Haro MC, Rodríguez-Rubio P (1998) Effect of pollution on polychromed ceramic statues. Atmos Environ 32:993–998

Puga E, Díaz de Federico A, Nieto JM, Díaz Puga MA (2007) Petrology, geodynamic evolution and georesources of the Natural Space of Sierra Nevada. Est Geol 63:19–40 (in Spanish)

Ro CU, Oh K-Y, Kim H, Kim YP, Lee CB, Kim K-H, Kang CH, Osán J, de Hoog J, Worobiec A, Van Grieken R (2001) Single-particle analysis of aerosols at Cheju Island, Korea, using low-Z electron probe X-ray microanalysis: a direct proof of nitrate formation from sea salts. Environ Sci Technol 35:4487–4494

Ro CU, Osan J, Szaloki I, de Hoog J, Worobiec A, Van Grieken R (2003) A Monte Carlo program for quantitative electron-induced X-ray analysis of individual particles. Anal Chem 75:851–859

Rodríguez-Gordillo J, Sáez-Pérez MP (2006) Effects of thermal changes on Macael marble: experimental study. Constr Build Mater 20:355–365

Rodríguez-Navarro C, Sebastián E (1996) Role of particulate matter from vehicle exhaust on porous building stones (limestone) sulfation. Sci Total Environ 187:79–91

Ruiz-Agudo EM (2007) Prevention of salt damage to the built cultural heritage by the use of crystallization inhibitors. Dissertation, University of Granada (in Spanish)

Sabbioni C, Ghedini N, Bonazza A (2003) Organic anions in damage layers on monuments and buildings. Atmos Environ 37:1261–1269

Sánchez-Moral S, Soler V, Cañaveras JC, Sanz-Rubio E, Van Grieken R, Gysels K (1999) Inorganic deterioration affecting the Altamira Cave, N Spain: quantitative approach to wall-corrosion (solutional etching) processes induced by visitors. Sci Total Environ 243–244:67–84

Sanjurjo Sánchez J, Alves CAS, Vidal Romaní JR, Fernández Mosquera D (2009) Origin of gypsum-rich coatings on historic buildings. Water Air Soil Pollut 204:53–68

Simão J, Ruiz-Agudo E, Rodríguez-Navarro C (2006) Effects of particulate matter from gasoline and diesel vehicle exhaust emissions on silicate stones sulfation. Atmos Environ 40:6905–6917

Spolnik Z, Bencs L, Worobiec A, Kontozova V, Van Grieken R (2005) Application of EDXRF and thin window EPMA for the investigation of the influence of hot air heating on the generation and deposition of particulate matter. Microchim Acta 149:79–85

Spolnik Z, Worobiec A, Samek L, Bencs L, Belikov K, Van Grieken R (2007) Influence of different types of heating systems on particulate air pollutant deposition: the case of churches situated in a cold climate. J Cult Herit 8:7–12

Tétreault J (2003) Airborne pollutants in museums, galleries and archives: risk assessment, control strategies, and preservation management. Canadian Conservation Institute, Ottawa

Van Espen P, Janssens K, Nobels J (1986) AXIL-PC software for the analysis of complex X-ray spectra. Chemom Intell Lab Syst 1:109–114

Van Grieken R, Gysels K, Hoornaert S, Joos P, Osán J, Szalóki I, Worobiec A (2000) Characterisation of individual aerosol particles for atmospheric and cultural heritage studies. Water Air Soil Pollut 123:215–228

Weinbruch S, Wentzel M, Kluckner M, Hoffmann P, Ortner HM (1997) Characterization of individual atmospheric particles by element mapping in electron probe microanalysis. Microchim Acta 125:137–141

Worobiec A, Samek L, Spolnik Z, Kontozova V, Stefaniak E, Van Grieken R (2006) Study of the winter and summer changes of the air composition in the church of Szalowa, Poland, related to conservation. Microchim Acta 156:253–261

Worobiec A, Samek L, Karaszkiewicz P, Kontozova-Deutsch V, Stefaniak EA, Van Meel K, Krata A, Bencs L, Van Grieken R (2008) A seasonal study of atmospheric conditions influenced by the intensive tourist flow in the Royal Museum of Wawel Castle in Cracow, Poland. Microchem J 90:99–106

Xu F, Tang J, Gao S (2010) Characterization and origin of weathering crusts on Kylin carved-stone, Kylin countryside, Nanjing—a case study. J Cult Herit 11:228–232

Chapter 6

Construction and Building Materials 24 (2010) 1438–1448

Rough and polished travertine building stone decay evaluated by a marine aerosol ageing test

Maja Urosevic, Eduardo Sebastián-Pardo, Carolina Cardell*

Department of Mineralogy and Petrology, Faculty of Science, University of Granada, Campus Fuentenueva s/n, 18071 Granada, Spain

Article history:

Received 17 April 2009

Received in revised form 14 January 2010

Accepted 15 January 2010

Available online 4 February 2010

doi:10.1016/j.conbuildmat.2010.01.011

ABSTRACT

Tablets of rough and polished travertine were aged in a sea-salt spray corrosion chamber to explore potentially contrasting stone decay behaviour due to different surface finishing processes. This paper presents a multianalytical approach to characterise the chemical, mineralogical, textural, porosimetric and colourimetric features of quarried and weathered travertine after the test. Rough and polished stone surfaces behave differently according to salt-spray absorption, newly formed pore networks, composition and habits of salts, and chromatic changes. Roughness and irregularities of the unpolished travertine favour salt inputs that in turn increase the open porosity. By contrast, the smooth finish of the polished travertine helps to protect it against salt decay, since this finishing blocks the pore system in the near surface stone. This information is crucial to establish maintenance and conservation construction practices.

KEYWORDS

Travertine**,** stone finishing processes**,** marine aerosol**,** ageing test, pore system, colourimetric features.

6.1. Introduction

For the goal of detecting and preventing salt deterioration on construction materials placed in architectural heritage, civil constructions and in present-day buildings, it is crucial to improve knowledge concerning weathering mechanisms involved in salt damage. Salt induced deterioration of natural and artificial building materials (e.g. stones, mortars, bricks and ceramics) is drastically accelerated in coastal areas due to the action of marine aerosols, with significant cultural and economic implications [1–4]. In fact, the sizeable investment to preserve the architectural heritage, as well as to repair damage on ornamental and building materials used in modern constructions, makes necessary application of scientific knowledge due to salt weathering processes. Despite the abundant literature concerning this topic [5,6], little attention has been paid to ascertain the effect of different stone surface finishing processes to mitigate stone decay caused by marine aerosols.

In this regard great advances have been achieved as result of investigations conducted in the field of Heritage Science. In particular, laboratory tests have helped to shed light on causes and mechanisms involved in salt weathering of construction materials, as well as to allow easier recognition of key factors that trigger or mitigate their damage [1,7–12]. Though there are diverse international standard salt crystallisation tests (ASTM B-117 [13], DIN 50021 [14], ISO 9227 [15] and UNE-EN 14147 [16]), researchers have frequently designed *ad hoc* salt corrosion tests in an attempt to reproduce more realistic environmental conditions for better understanding the synergistic action of factors causing salt decay in construction materials. Thus different environmental conditions and solutions, as pure NaCl solutions [11,17], mixed solutions [9,17–19] or seawater spray [8,11] have been tested. In order to create a more realistic atmosphere for building stone decay in marine environments, a modified standard sea-salt spray test has been used in the present study to investigate the susceptibility of polished and rough surfaces of travertine stone samples due to the impact of marine aerosols.

Travertine has been an important building material for monuments and civil constructions from Roman times until present throughout Europe and near east [20–22]. It

has been used as structural stone (ashlars and plane surfaces) and also in ornamental elements such as sculptures. In fact, travertine is one of the most frequently used stones in modern architecture worldwide, and is commonly seen in tile sizes as façade material, wall cladding, and flooring (for instance modern buildings such as the Getty Center in Los Angeles and Barcelona's Prat airport are cladded with travertine). Despite its widespread use, travertine has been investigated less than other carbonate stones like marbles and limestones, particularly in Andalusia (Southern Spain) where local travertines have been used in numerous monuments [17,23], and in public buildings at present times.

Travertine stone is a natural chemical precipitate of carbonate minerals deposited from the water of mineral springs saturated with dissolved calcium bicarbonate [24]. As a consequence, the stone is characterised in general by pitted holes in its surface. However various types of travertine exist due to variation in depositional environment and components. Two broad lithotypes are porous travertine with large irregular pores, and the less porous massive travertine. In this work the studied *Olivillo* travertine belongs to this latter group. Since travertine can have many nooks and crannies, it can be effectively polished to a smooth, shiny finish (honed travertine) or unpolished, as well as unfilled or filled with different polymer and cement-based materials [25].

Physical properties and compositional characteristics of travertine have been studied in naturally weathered travertine buildings to investigate their response to diverse atmospheric conditions [26,27]. However laboratory analyses and tests of physical and chemical weathering of travertine remain scarce. Thus, there are still interesting open questions to be investigated, such as the effects of different finishing processes in travertine stone buildings on marine aerosols absorption.

This paper presents a laboratory ageing test using marine spray in a controlled-atmosphere chamber to examine the implications of rough and polished travertine stone surfaces on their salt decay. The degree of salt damage was estimated by comparing changes in mineralogical and chemical composition, petrophysical characteristics and chromatic variations between freshly quarried and aged samples. The results obtained have significance

for the design of proper processing, protection, maintenance and intervention protocols for civil and historic buildings.

6.2. Materials and methods

6.2.1. Stone material

This research focuses on a travertine type currently used as building stone extracted in Andalusia (Almería province, Southern Spain). Relatively large travertine formations outcrop (>5 km^2) near the villages *Alhama* de Almería and *Alicún* [28]. This formation was deposited in perched springline and fluvio-lacustrine environments and later affected locally by subaerial exposure process [29,30]. Travertines are exploited in several quarries and commercialised as *Olivillo* travertine (hereafter referred as AL travertine), commonly used as building stone in modern architecture as well as stone restoration in the Granada (Southern Spain) cultural heritage [17,23].

The sawing direction of the selected material was perpendicular to the layering (vein cut). Two finishing surface types of AL travertine are commercialised, namely as rough surface and polished surface. Polished travertine is treated before the polishing process in order to increase its strength. This treatment consists of a two-step process where large pores are first filled with a beige coloured gypsum-based plaster, and then the surface is dressed with an epoxy silicone mixed resin. After the strengthening, the surface of the travertine tiles is finally polished.

In this work, two sets of travertine samples with rough and polished surfaces were cut as tablet samples (50 × 50 × 10 mm) for the sea-salt spray ageing test. Later on, stone samples were prepared according to the requirement of each analytical technique applied, as specified in Section 6.2.3.

6.2.2. Sea-salt spray ageing test

A saline spray chamber (CCONS series, INELTEC□) was used to investigate the effect of marine aerosol deposition on rough and polished travertine surfaces. To reproduce more realistic conditions of building stone decay in marine environment, seawater was collected from the Mediterranean Sea at Granada coast (Salobreña, Southern Spain), instead of using the standardised 5% solution of NaCl known as NSS (neutral salt spray) advised by international standards such as e.g. ASTM (B-117) [13], DIN (50021) [14], ISO 9227 [15] or UNE-EN (14147) [16]. However the NaCl concentration of these tests can differ (e.g. 10% or 20% NaCl) upon laboratory request.

Standard salt spray tests are widely used in the industrial sector including automotive, construction and aerospace industries to evaluate the corrosion resistance of finished surfaces or parts (coatings, metals, alloys, stones, etc.). These standards describe the essential procedures to perform each test specifying temperature, relative humidity, concentration and pH of the solution, air pressure of the sprayed solution, sample dimension, testing hours in NSS (e.g. 100 h in [13], 96 h in [15]), etc., which differ among the tests. The basic principle of long-term salt spray (fog) ageing tests consists of a continuous salt solution pulverisation (ASTM (B-117) [13]), although cycle tests are preferred to simulate ageing due to the cyclic nature of real environmental conditions. For example, the UNE-EN (14147) test [16] requires 60 cycles, each consisting of 4 h ± 15 min of salt spray (pH = 6.5–7.2) followed by 8 h ± 15 min of drying at 35 ± 5 ºC.

Test requirements should be agreed between customer and laboratories or manufacturer. Test duration depends on the corrosion resistance of the studied material (e.g. construction stones); the more corrosion resistant the material, the longer the period needed to show signs of deterioration. Thus, testing periods range from a few hours (e.g. 8 or 24 h) to more than a month. Results can be represented as mass loss [16], although the usual ageing test criteria is the visual estimation of degradation, as salts precipitation, stone colour changes or other types of damages such as creation of fissures, cracks, pits, etc. Therefore at first it is difficult

to predict the number of hours or cycles needed for a salt spray test, so generally a high number is chosen to ensure material degradation.

In this work, the travertine tablets were subjected to a modified UNE-EN (14147) ageing test [16] to re-create more realistic environmental conditions of coastal areas. Stone tablets were hung on a nylon thread from plastic bars inside the chamber so that all sample faces were exposed to the salt spray. Care was taken to avoid direct exposure of the samples to the salt spray atomizer. The chamber was electronically programmed to produce 160 cycles corresponding to 60 d. After this period the test was judged to have finalised since no significant further macroscopic changes were observed in the stones. Each cycle consisted of 3 h of seawater spray followed by 6 h of drying by forced air at 35 ºC and relative humidity of 70 ± 2%. The chamber remained closed throughout the test, thus during the spray periods the relative humidity was higher (c.a. 98%). The composition of the seawater is shown in Table 1. Cations (Ca^{2+}, K^{+}, Na^{+} and Mg^{2+}) were determined by means of inductively coupled plasma-atomic emission spectrometry (ICP-AES, Leeman Labs PS series) and anions (Cl^{-}, SO_4^{2-} and NO_3^{-}) by ion chromatography (IC, Dionex DX 300). The pH of the seawater was 7.84 at 20 ºC (Eutech 1500). Water composition used in the present ageing test is relatively lower in chlorine, potassium and sodium compared to those used elsewhere whereas nitrate, sulphate and magnesium content is slightly higher [8,11]. Upon conclusion, travertine samples were removed from the chamber and analysed using various techniques.

Table 1. Sea-salt water composition (expressed in ppm) used in the artificial ageing test of the present study and from [8].

	This study	[8]
Cl^{-}	12,879	22050
NO_3^{-}	72	50
SO_4^{2-}	2772	2713
Ca^{2+}	330	345
K^{+}	348	1020
Na^{+}	10,030	19920
Mg^{2+}	1069	945
HPO_4^{2-}	-	28

- not measured

6.2.3. Analytical techniques

The following methods and analytical techniques were used to characterise the pore filling in the polished stone, the freshly quarried travertine and to evaluate modifications induced by the test. Before and after the test the blocks were weighed. Throughout the test, macroscale observations and photographic records were made to assess the presence of efflorescences, evolution of crystalline habits, drying and decay of stone samples, as presented in Sections 6.3.3.1 and 6.3.3.2.

The mineralogical composition of the travertine, the stone pore filling and the crystallised efflorescences were determined by powder X-ray diffraction (XRD) using a Philips PW-1710 diffractometer equipped with an automatic slit window. For this aim, the samples were milled in an agate mortar to less than 50 μm particle size. Analysis conditions were: radiation Cu Kα (λ: 1.5405 Å), 40 kV voltage, 40 mA current intensity, explored area between 3º and 60º 2θ and goniometer speed of 0.01º 2θ/s. Automatic acquisition, evaluation and identification of minerals were performed by Xpowder software [31]. To identify the epoxy silicone resin composition, transmittance Fourier transform-infrared spectroscopy (T-FTIR) was applied. The T-FTIR spectrum registered from 3999 to 400 cm^{-1} with a resolution of 2 cm^{-1} and 200 scans, were collected using a NICOLET spectrometer 20SXB. The T-FTIR spectrum was obtained from KBr pellet prepared by uniformly mixing 5 mg of powdered sample with KBr (3 wt.%).

Major and trace elements of fresh travertine were analysed using a Bruker S4 Pioneer X-ray fluorescence spectrometer (XRF) with wavelength dispersion equipped with a goniometer that held analysing crystals (LIF200/PET/OVO-55) and Rh X-ray tube (60 kV, 150 mA). Semiquantitative scanning spectra were obtained using the software Spectraplus. Stone powder (~5 g) was blended with wax (Hoestch wax C micropowder Merck) using a 5100 SPEX Mixer/Mill. After that each sample was uniformly deposited on a cellulose substrate contained in a 40 mm aluminium cup. Finally, the product was pressed at 10 ton (Mignon-S de Nannetti) to produce a pressed pellet (40 mm sample disc).

Petrographic characteristics of fresh and aged travertines presenting rough and polished surfaces were examined under optical microscopy (OM) using an Olympus BX-60 equipped with digital camera (Olympus DP10). To this aim polished thin sections were prepared with ethanol to avoid salt dissolution, and stained with red alizarin to differentiate calcite from dolomite (calcite tints to red while dolomite remains unstained). Chips of these stone samples were also analysed with an environmental scanning microscope (ESEM) to study the stone microtexture, as well as crystal habits and chemical composition of precipitated salts without disturbing their hydration state. No sample preparation is required for ESEM analysis [12]. A Phillips Quanta 400 was used applying 20 kV acceleration voltage, 1 nA probe current and working distance of 10 mm.

The travertine pore system was characterised by means of mercury intrusion porosimetry (MIP) and gas sorption isotherms (BET). Blocks c.a. 2 cm^3 of fresh and aged samples (containing salts) were dried in an oven during 24 h at 60 ºC, and analysed on a Micromeritics Autopore III model 9410 porosimeter. In addition, aged samples (rough and polished surfaces) were washed in distilled water during one week after the ageing test, and studied by means of gas Ar sorption. The purpose of this procedure was to discern the binding or cementing effect of salts in the stone. In samples with less than 5 $m^2\ g^{-1}$ surface area, Ar sorption measurements are more realistic than using N2, which usually yield excessively high values [32]. The Ar sorption isotherms were obtained at ~196 ºC on a Micromeritics Tristar 3000 under continuous adsorption conditions. Prior to measurement, samples were heated to 250 ºC for 8 h and outgassed to 10^{-3} Torr using a Micromeritics Flowprep. The BET analysis was used to determine the total specific surface area [33,34]. The Barret–Joyner–Halenda (BJH) method was used to obtain pore size distribution curves, the pore volume and the mean pore size of the travertine samples [35]. The surface fractal dimension, D_S, was determined from adsorption data and used to characterise the surface roughness. The analysis of the gas sorption isotherm using a modified Frenkel–Halsey–Hill (FHH) theory [36] allows determination of surface fractal dimension from the slope (A) of the plot of Ln(V) vs. Ln[Ln(P/P_0)], where V is the adsorbed volume of gas, and P and P_0 are the actual and condensation gas pressures. When surface tension (or capillary condensation) effects are important, the relationship between A and D_S is $A = D_S - 3$. Capillary

condensation is significant if $\delta = 3(1 + A)–2 < 0$. The pressure range and therefore the thickness range of the adsorbed layer coverage revealed that we were dealing only with monolayer (since n = 1–2). This thickness range ensures that the determination of DS is reliable [36].

Chromatic characteristics of rough and polished surface samples before and after the ageing test were determined using a Minolta CR 210 colorimeter, with 0º viewing angle and 50 mm diameter measuring area. The CIE 1976 chromatic scale was used to measure the parameters L*, a* and b* [37].

6.3. Results and discussion

The results of the pore filling analysis in the polished travertine are presented first. Then, to facilitate the comprehension of this work, the results of freshly quarried samples that display both surface finishing (i.e. polished and rough samples) are presented first, followed by the results for the corresponding surfaces of the aged travertine samples. However, all the results (from rough and polished stones) are shown together in the figures and tables to avoid unnecessary repetitions and to facilitate understanding of the text.

6.3.1. Surface finishing treatment

The XRD analysis revealed that the beige coloured gypsum based plaster was composed of ~67% quartz (SiO_2), ~31% calcite ($CaCO_3$) and <2% illite (a type of phyllosilicate or layered alumino-silicate). T-FTIR analysis of polymeric materials provides highly precise measurements that are widely interpretable in terms of chemical structure. Most common epoxy resins are produced from a reaction between epichlorohydrin and bisphenol-A to obtain a polymer. The T-FTIR spectrum of the epoxy silicone resin analysed in this work (Fig. 1) is comparable to other epoxy silicone resins reported elsewhere [38]. Fig. 1 shows the carbonyl band at 1730 cm^{-1}, the C–H stretch at 2930 cm^{-1} and the C–H scissoring and

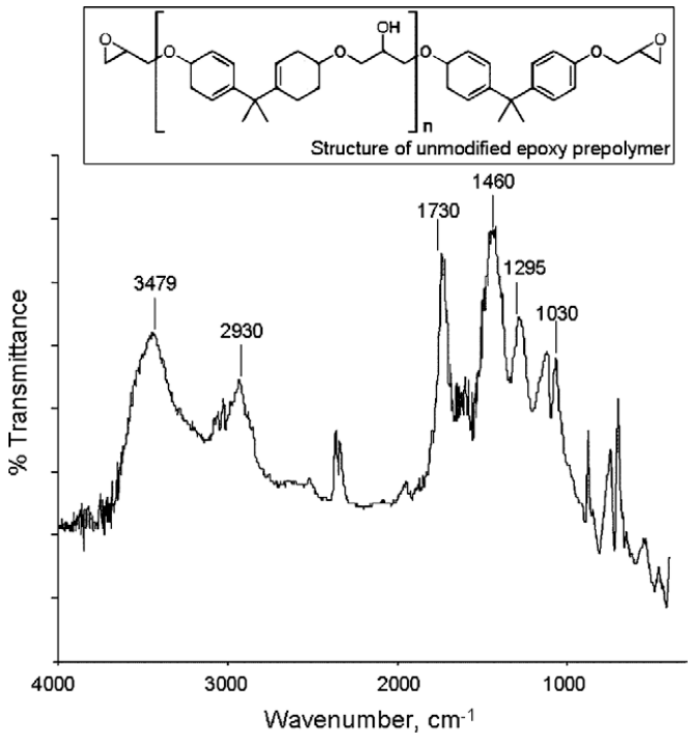

Fig. 1. T-FTIR spectrum of the epoxy silicone resin and its structure used in the finishing treatment of the polished travertine.

bending at 1460 cm^{-1}. The characteristic band of hydroxyl group was identified at 3479 cm^{-1} and the presence of C–O bands was observed in the region between 1030 and 1295 cm^{-1}.

6.3.2. Fresh stone

6.3.2.1. Macroscale observations

The AL travertine is a massive travertine, mostly well cemented and heterogeneously coloured, varying from pale yellow to brown. It shows relatively small pores of c.a. 2–3 mm in size and larger ones at c.a. 20 mm. Also, a laminated structure is distinguished particularly when the material is polished, and the colour contrast of layers is enhanced (Fig. 2).

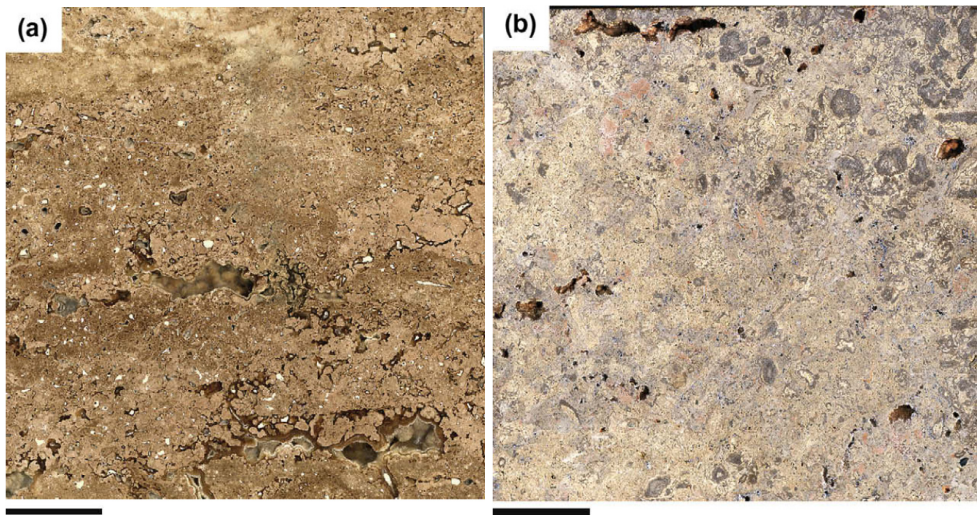

Fig. 2. Polished **(a)** and rough **(b)** surface of fresh *Olivillo* travertine. Note the porous laminated structure in (a). Bars = 10 mm.

6.3.2.2. Bulk stone composition

The AL travertine bulk stone major composition and trace elements determined by XRF are presented in Table 2. Also for the purpose of comparison, chemical results from others travertine lithotypes from Southern Spain and Italy are provided. AL travertine is low in siliciclastic components (i.e. SiO_2 and Al_2O_3) compared to other travertines (Table 2), being composed of almost pure calcite. Whereas the zirconium (Zr) value content is in the range of other travertines from Granada [17] and Italy [39,40], AL travertine is significantly enriched in copper (Cu) and zinc (Zn) and slightly in strontium (Sr). In the same locality (Alhama de Almería) iron (Fe) and manganese (Mn) oxides have been reported in another type of travertine displaying an intense red colour, known as Red Alhama travertine. However in this study MnO concentration was below detection limit of XRF. Contrasting depositional environment and different degrees of subaerial exposition (brecciation and karstification) have been noted in the same travertine formation exploited in several quarries [29]. Therefore the differences in MnO content and other minor elements measured can be ascribed to this heterogeneous distribution of facies and alterations.

Table 2. Representative major bulk stone composition and trace elements of *Olivillo* and *Alfacar* travertine (Granada, Southern Spain; [17]) and mean values of some Italian travertines [39,40].

wt. %	*Olivillo*	*Alfacar*	Roman travertine chiaro	Santa Sabina	Orvieto district	Cetona	Saturnia
SiO_2	0.96	1.93	0.68	1.75	8.69	5.23	0.05
TiO_2	0.02	-	-	0.02	0.10	0.08	*
Al_2O_3	0.32	0.44	0.54	0.54	2.52	1.94	0.08
Fe_2O_3	0.12	0.21	0.06	0.17	1.12	0.67	0.05
MnO	*	-	-	0.04	0.04	0.03	0.04
MgO	0.72	1.16	0.18	0.38	0.77	0.47	0.42
CaO	54.24	51.40	54.77	52.99	46.48	50.25	55.07
K_2O	0.06	0.10	-	0.11	0.59	0.27	*
P_2O_5	0.01	0.59	0.01	0.57	0.26	0.11	0.50
SO_3	0.19	-	0.45	-	-	-	-
Cl	0.01	-	-	-	-	-	-
ppm							
Cu	40	9	-	6	22	17	14
Zn	1000	49	-	11	31	34	6
Sr	1416	343	-	478	1546	826	749
Zr	55	< 10	-	17	83	38	13

Detection limit is 0.005 wt.% for major elements and for trace elements 3 ppm for Zr, 2 ppm for Sr and 1 ppm for Cu, Zn, Zr. * below detection limit, - not measured.

6.3.2.3. Mineralogical and textural characteristics

The XRD data showed that calcite was the most abundant mineral in AL travertine (95–100%) with trace amounts (less than 5%) of quartz and phyllosilicates (illite-type). Detailed OM observations revealed that the lamination of AL travertine was related to changes in the ratio of sparitic (>10 μm in size) and microsparitic (4–10 μm)/micritic (<4 μm) calcite (Fig. 3). Higher proportion of the sparitic calcite leads to lighter band colour, vs. darker bands for higher proportion of the micritic calcite. Furthermore, the lamination can be a consequence of seasonal rhythmic growth; the spring bands are darker and thinner [24]. Some large irregular cavities (2 × 1 mm in size) appear as organic structures of plants that were

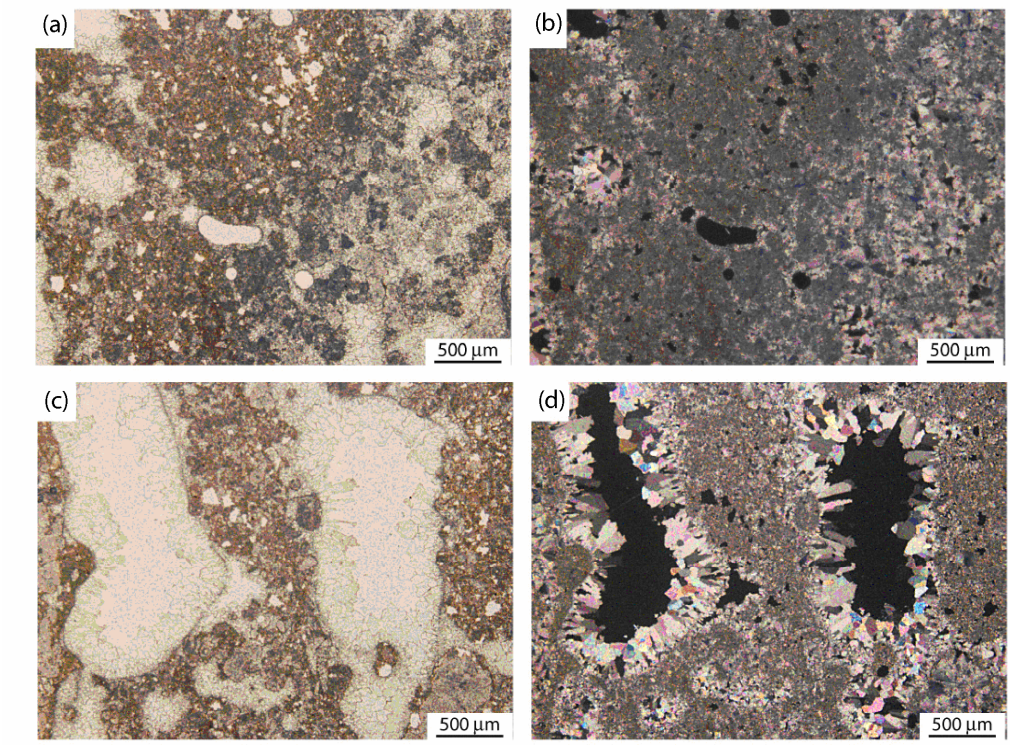

Fig. 3. Optical microphotographs showing the representative textures of freshly quarried travertine stained with red alizarin: **(a)** colour layering due to contrasting sparitic and micritic calcite content (parallel polarised light), **(b)** same as **(a)** under crossed polarised light where sparitic calcite (right) is clearly observed, **(c)** detail of irregular and elongated pores (2 × 1 mm in size) under parallel polarised light, **(d)** pores are incompletely filled by coarse grain sparitic calcite (>150 µm)(crossed polarised light).

associated to travertine deposition. Large cavities may be filled by mosaic calcite of secondary origin [26,41].

These cavities were observed also by means of ESEM allowing discernment of pore gradation (pores from 4 µm up to 700 µm) and irregular abrasion of calcite crystals in the polished surface. The abrasion can be interpreted as a result of mechanical polishing of the stone, where calcite crystals were unpinned from the stone surface thus favouring the differential erosion of the stone surface. Moreover, the uneven abrasion could be enhanced by the different crystals sizes, as well as by their different crystallographic orientation – on the stone surface – that could generate asymmetrical decay [42].

6.3.2.4. Pore system

Table 3 shows the porosimetric parameters of fresh rough and polished travertine samples determined by MIP. The mean open porosity for rough fresh samples was ~8.16% characterising AL travertine as a medium porous stone. After the polishing process this value slightly decreased to ~7.26%, a fact attributed to the filling process with the resin used in the polishing process. Fig. 4a and b shows the pore size distribution obtained by means of MIP for rough and polished freshly quarried samples. Both curves are bimodal and strongly asymmetric. The main pore size range for the rough surface is comprised between 0.02 and 0.07 μm (radius size) with a secondary peak centered at 100 μm (Fig. 4a). By contrast the polished travertine displays a pore size distribution where the main peak is centered at 100 lm and the secondary peak appears in the range of 0.02–0.05 μm (Fig. 4b). The decrease of the main pore size range could be assigned to the sealing effect of the resin used to improve the stone endurance during polishing. Moreover, the increase of pores centered at ~100 μm could be related to the induced stone damage during the polishing process (small detached crystal grains can scratch the stone surface) as well as to small bubbles or defects inherent to the resin used to fill travertine voids.

Table 3. Mercury intrusion porosimetry parameters: n_0 = open porosity (%); ρ_A = apparent (skeletal) density (g cm^{-3}); ρ_B = bulk density (g cm^{-3}).

Surface	Type	n_0	ρ_A	ρ_B
rough	fresh	8.16 ± 1.21	2.65 ± 0.04	2.43 ± 0.04
	aged	10.65 ± 0.57	2.70 ± 0.06	2.48 ± 0.06
polished	fresh	7.26 ± 0.25	2.66 ± 0.04	2.42 ± 0.01
	aged	8.34 ± 0.93	2.70 ± 0.03	2.49 ± 0.01

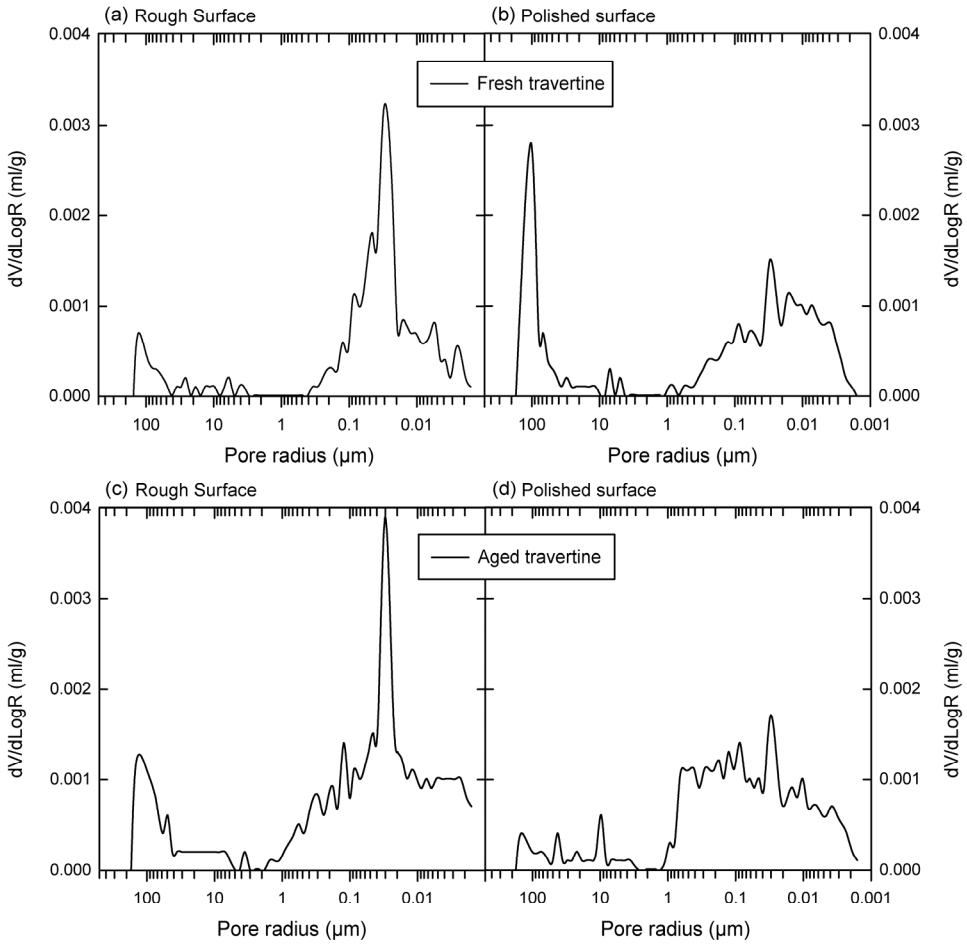

Fig. 4. Pore size distribution measured by MIP of freshly quarried travertine with rough **(a)** and polished **(b)** surface. Note that the main pore size range for **(a)** is comprised between 0.02 and 0.07 µm (radius) whereas in **(b)** is centred at 100 µm. Pore size distribution after the sea-salt spray test for the aged travertine with rough **(c)** and polished **(d)** surface.

Ar sorption was applied to investigate the smallest pore sizes of fresh polished and non-polished samples (Fig. 5 and Table 4). Representative Ar sorption isotherms of these samples are shown in Fig. 5a and b. Both isotherms are of type II [32] and indicate the non-microporous nature of these samples; this is further confirmed by the very low surface area, i.e. 0.5601 ± 0.1042 m^2/g vs. 0.2387 ± 0.0853 m^2/g respectively for rough and polished travertine samples (Table 4). Table 4 also shows that the porosity of both travertine types is

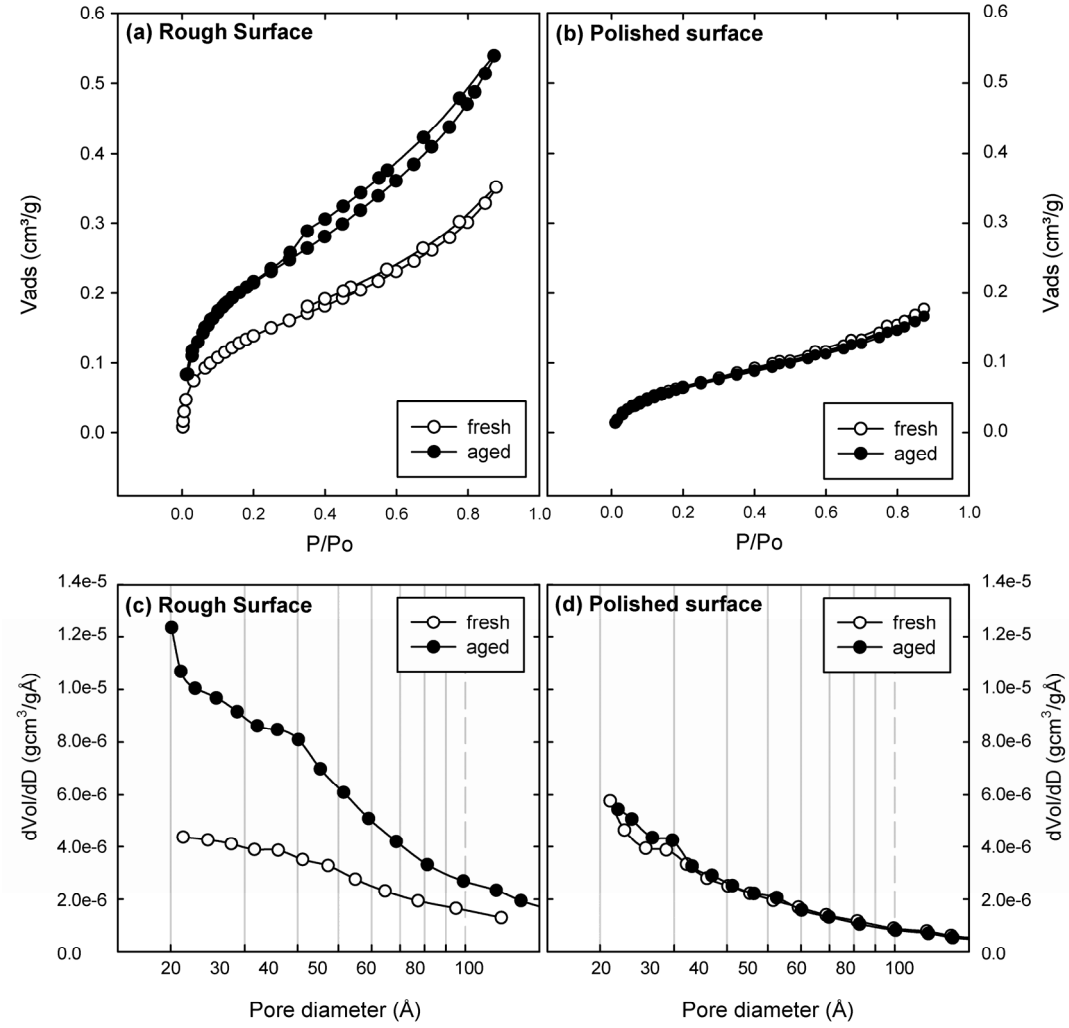

Fig. 5. Ar (~196 ºC) physisorption isotherms for fresh (empty dots) and aged (filled dots) travertine with rough **(a)** and polished **(b)** surface. BJH pore size distribution plot of Ar physisorption curve for fresh (empty dots) and aged (filled dots) travertine samples with **(c)** rough and **(d)** polished surface.

Table 4

Pore system characteristics determined by Ar-sorption (BET) of samples with rough and polished surface before and after the ageing test.

	Fresh samples		Aged samples	
	Rough surface	Polished surface	Rough surface	Polished surface
Surface area (BET), m^2/g	0.5601 ± 0.1042	0.2387 ± 0.0853	0.9133 ± 0.2789	0.2245 ± 0.0193
Total pore volume, cm^3/g	0.00037 ± 0.00007	0.00022 ± 0.00007	0.00076 ± 0.00007	0.00022 ± 0.00007
Average pore diameter, Å	20.53 ± 1.48	20.60 ± 0.75	20.64 ± 0.74	21.07 ± 1.42
Monolayer volume	0.1468 ± 0.0270	0.0624 ± 0.0363	0.2394 ± 0.0739	0.0589 ± 0.0050
Surface fractal dimension, D_S	2.52	2.51	2.54	2.51
Linear correlation coefficient, r^2	0.9974	0.9912	0.9978	0.9934

Reported values are the mean and standard deviation of 3 measurements.

concentrated in the mesopore range, with an average pore diameter of 20.53 ± 1.48 Å for the rough surface and 20.60 ± 0.75 Å for the polished surface.

Finally, the BJH plots (pore size distribution curves named after Barret–Joyner–Halenda) are almost equivalent (Fig. 5c and d). Total pore volume is lower in polished samples than in rough ones (due to filling with resin as explained above), although the complexity of the pore system expressed as the surface fractal dimension (D_S = 2.52 vs. D_S = 2.51 for rough and polished samples respectively) is virtually similar (Table 4).

6.3.2.5. Colourimetry

The study of the chromatic characteristics presented in Table 5 showed that the polishing process of the travertine caused a decrease of the brightness parameter L* (69.78 vs. 62.00) and an increase of the chromatic parameters a* (1.83 vs. 5.52) and b* (7.31 vs.15.69). This means that after polishing the travertine becomes more reddish and yellowish.

6.3.3. Aged samples

6.3.3.1. Macroscale observations

During the sea-salt ageing test no stone detachments were observed. The first efflorescences crystallised as crusts after 48 h exposure into the test chamber in all samples, most profusely in the rough ones. Salt crusts started to grow at the upper borders of each tablet and afterwards extended and covered the tablets completely (Fig. 6). The weight of all samples increased slightly after the test (0.65% for rough travertine and 0.60% for polished travertine). The salt crusts were thicker in the polished travertines.

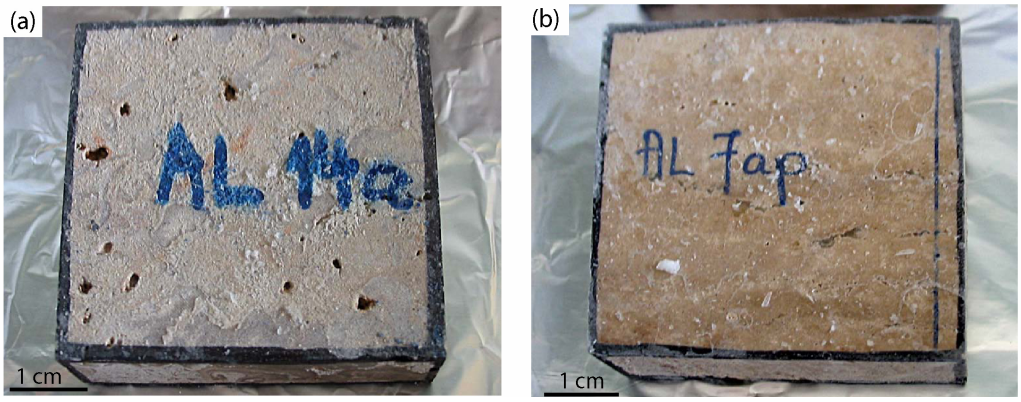

Fig. 6. Macroscopic features of the aged travertine with rough **(a)** and polished **(b)** surface after the sea-salt ageing test.

6.3.3.2. Mineralogical and textural characteristics

Halite (NaCl) was the only salt detected by means of XRD. No other minority phases (detectable at 5% or more) as for example sulphates – detected in the seawater used in the test, see Table 1 – were found by XRD.

Detailed OM observations of the aged samples revealed no important microtextural differences, neither between fresh and aged travertine nor between rough and polished surfaces. In some parts of the aged rough samples a slight reduction of the sparitic calcite that covered the cavities was observed. In addition it was confirmed that the marine aerosol affected only the most superficial part (first 200 μm) of the stone samples.

By ESEM small unconnected and discontinuous salt crusts of xenomorphic or anhedral halite crystals (no crystal faces present) formed in the rough travertine were observed (Fig. 7a). These crusts partially covered original coarse-grained calcite crystals. Crystalline habits formed in polished travertine surfaces were more diverse since homogeneous and continuous halite crusts developed (Fig. 7b). In fact, four crystalline habits of halite could be recognised (Fig. 7c): (1) small subhedral crystals (some faces present); (2) dendritic crystals (with a typical multi-branching tree-like form) with a hole in the centre (hopper crystals); (3) transition into oblong (column) crystals with scarce holes and (4) crystals that tend to form cubes (50–100 μm in size) in the upper part of the crust, where desiccation fissures were observed. This sequence suggests a change in the supersaturation of the saline solution which promotes the halite crystallisation. While the presence of abundant small subhedral and dentritic crystals are indicative of high growth rates and supersaturation values, the development of hopper and cubic crystals in this test suggests stable growth at medium/low supersaturation in last crystallisation stages [17,43–45].

Furthermore, pseudo-hexagonal tabular crystals of gypsum were locally identified in the polished stone surface (Fig. 7d). It should be recalled that gypsum was present in the plaster used in the polishing process, thus it is possible that gypsum crystals appear after the salt ageing test on the polished travertine. However the observed morphology is not typical of

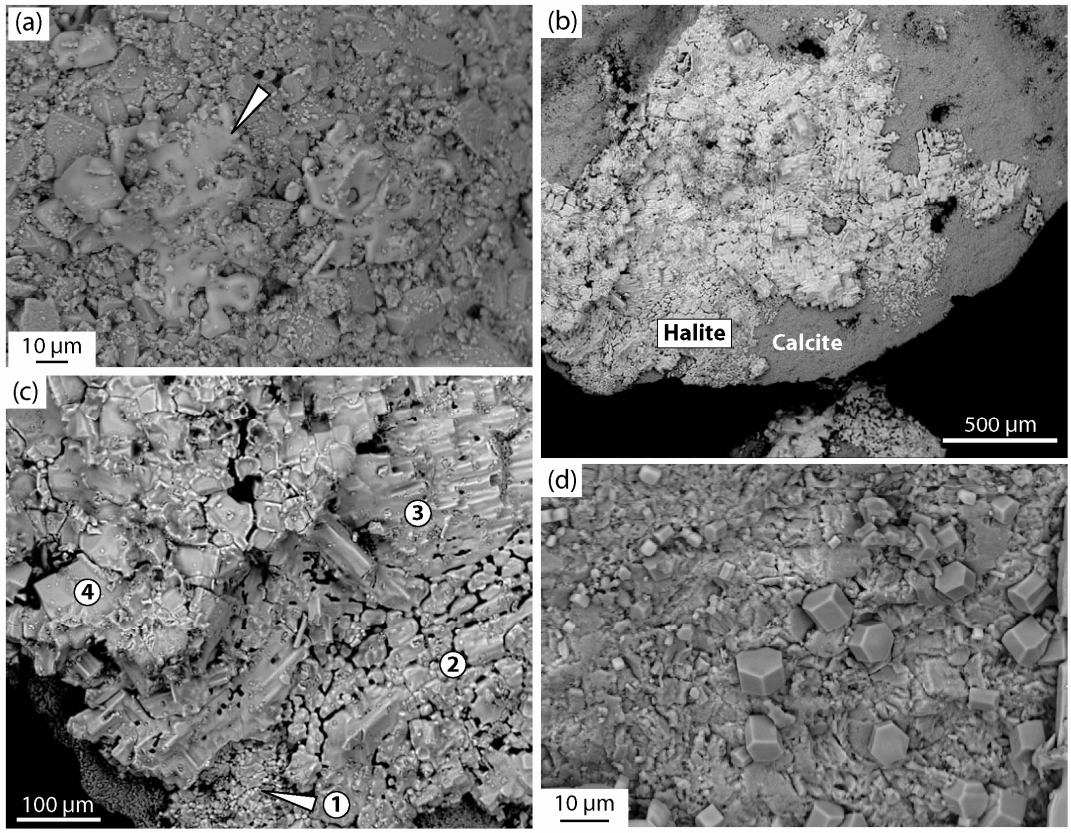

Fig. 7. Electron backscattered images of the aged travertine with **(a)** rough surface where coarse sparitic calcite is covered by thin xenomorphic halite crust (arrow), **(b)** polished surface where halite crystals form a thick (>2 mm) homogeneous crust with dendritic textures indicating medium to high supersaturation, **(c)** detail of these crusts where up to four different halite textures can be distinguished (see text for the explanation) and **(d)** pseudo-hexagonal gypsum crystals on the polished surface of travertine.

gypsum which crystallized in the monoclinic system. It has been reported that pedogenic gypsum can exhibit diverse crystal morphologies that may be controlled by a variety of environmental conditions including pH, temperature, salinity, organic matter and clays. In particular, tabular pseudo-hexagonal gypsum crystals (like those observed in this study) have been associated with organic matter and microorganisms [46]. Already these specific conditions can be attained in this work via the organic matter and microorganisms present during the travertine formation and those possibly contained in the seawater used in the test.

6.3.3.3. Pore system

The modification of the pore system due to the salt ageing test differs for rough and polished samples (Table 3). In rough samples the increase of the open porosity was higher (from ~8.16% toward ~10.65%) compared to the polished samples (from ~7.26% towards ~8.34%). Nonetheless no important modifications of the pore size distribution occurred as shown in Fig. 4, although a slight increase of the pore volume for all pore sizes was observed compared to the fresh travertine samples.

In other carbonate stones as for instance limestone several authors have observed a decrease of the open porosity after diverse salt crystallisation tests, which was attributed to pores infilling by salts [9,17,19]. In the samples of this work, the slight increase in the open porosity could be related either to the textural heterogeneity of this type of travertine or to (chemical) dissolution processes. In fact, the small increase in pores around 100 μm (Fig. 4c) could be justified by dissolution of the calcite that refills pores of such size, as confirmed by OM and ESEM. Calcite cement dissolution due to the action of marine aerosols on limestones placed in monuments has already been reported elsewhere [2]. Additionally, the open fabric of the studied travertine could have enhanced the salt spray attack stimulate by the surface roughness.

On the contrary the small increase in the open porosity of the polished samples (~7.26% vs. ~8.34%, Table 3) falls within the measurement error, and suggests that these stones were less deteriorated by the marine spray than the non-polished stones. When comparing Fig. 4b and 4d it is observed that after the test, pores around 100 lm almost disappeared, which is attributed to infilling with salts, while pores between 0.001 and 1 μm remained essentially unaffected (see Fig. 4b vs. Fig. 4d). The study of the aged polished travertine with ESEM and the Ar sorption analysis (regarding the pore system modification explained below) already confirmed the minor alterations that took place in the polished samples after the salt spray test.

The different behaviour of both surface finishings in response to the sea-salt spray action was particularly highlighted by the modification of pores (1–100 nm) analysed with Ar sorption. As shown in Fig. 5a a significant increase of the isotherm slope for the rough samples after the test occurred. It is known that roughness and complexity of the surface define the isotherm slope, which can be further related to the surface fractal dimension [47–49]. Salt crystallisation inside stones causes an increase of both roughness and surface complexity, which leads to an increase in the fractal dimension (D_S) values. Conversely, crack opening and widening produce a decrease of DS [49]. In this work the significant increase of the isotherm slope of the aged travertine (Fig. 5a) gives rise to an increase of the fractal dimension compared to that of the fresh travertine (D_S^{fresh} = 2.52 vs. D_S^{aged} = 2.54, Table 4). Calcite dissolution induced by salt crystallisation may account the increase of the fractal dimension [50]. Increase of fractal dimension can be used to estimate damage degrees of a material [51]. In this work, this damage degree was also confirmed by the large increase of the total pore volume for the rough travertine samples after the test as shown in Table 4 (i.e. ~0.00037 vs. ~0.00076 cm^3/g before and after the test respectively). The total pore volume increase can be related to the crack opening and chemical attack produced during the salt ageing test.

In contrast to rough samples, no changes of the isotherm adsorption slope were observed for polished aged samples (Fig. 5b). Therefore, the fractal dimension remained constant after the ageing test owing to the protecting effect of the resin (D_S^{fresh} = D_S^{aged} = 2.51, Table 4). Similarly, total pore volume and surface area did not change (Table 4) and values were below those of rough samples, showing that the resin also filled pores with radius below than 50 nm. All these results indicate that the pore system characteristics measured by Ar sorption were not modified after the sea-salt ageing test.

6.3.3.4. Colourimetry

Chromatic parameters of the rough and polished aged travertine surfaces were determined using the following approach: (1) measurements on surfaces covered by salt crusts, (2) measurements on surfaces where efflorescences were mechanically removed and

(3) measurements on aged stone surfaces washed in distillate water during one week. The second and third approach can be useful to evaluate the efficiency of cleaning interventions to recuperate the original stone chromatic characteristics. Table 5 shows the chromatic parameters of all the studied samples (these are average values of three measurements). Perceptible visual changes are achieved only when ΔE* (total colour difference = $\sqrt{(\Delta L^*)^2 + (\Delta a^*)^2 + (\Delta b^*)^2}$) exceeds three units. Thus colour alterations were observed for all aged samples, particularly in the polished samples and more precisely in those where salts were mechanically removed, i.e. ΔE* = 17.67 (Table 5).

Table 5
Mean values of chromatic parameters and their variations in travertine samples before and after the test, and after mechanical and distillate water cleaning of salts from the stone surface.

Surface	Type	L*	a*	b*	C*	H*	ΔL*	Δa*	Δb*	ΔC*	ΔE*
rough	fresh	69.78	1.83	7.31	7.54	75.9					
	aged	77.04	1.31	3.17	3.43	67.6	7.26	-0.53	-4.14	-4.11	8.38
	rasped	80.13	1.16	2.96	3.18	68.6	10.35	-0.67	-4.35	-4.36	11.25
	washed	79.78	1.24	2.89	3.15	66.7	10.00	-0.59	-4.42	-4.39	10.95
polished	fresh	62.00	5.52	15.69	16.63	70.6					
	aged	71.20	2.69	8.47	8.89	72.4	9.20	-2.83	-7.22	-7.75	12.03
	rasped	78.31	2.64	9.54	9.90	74.5	16.31	-2.88	-6.15	-6.73	17.67
	washed	79.35	2.07	9.07	9.30	71.15	17.35	-3.45	-6.62	-7.33	18.89

L* brightness; a* red-green components; b* yellow-blue components; C* chroma, $C^*=\sqrt{(a^*)^2+(b^*)^2}$; H* hue; $\Delta E^*=\sqrt{(\Delta L^*)^2+(\Delta a^*)^2+(\Delta b^*)^2}$.

Furthermore, after the ageing test and elimination of salt crusts the ΔL* (brightness difference) was higher in polished samples than in rough ones (10.35 vs. 16.31, Table 5) (Fig. 8a). Moreover, the alteration caused all samples to become more green and blue (cold tones) as parameters a* and b* decreased (Table 5).

Chromatic parameter variations related to the fresh travertine can be quantified together by means of chroma differences. Fig. 8b shows the decrease of chroma after the ageing test which remained nearly constant after mechanical cleaning of the surface. Interestingly the development of salt cleavage planes during the surface rasping caused a luminosity increase in both rough and polished samples (Fig. 8a). Moreover chroma and brightness differences

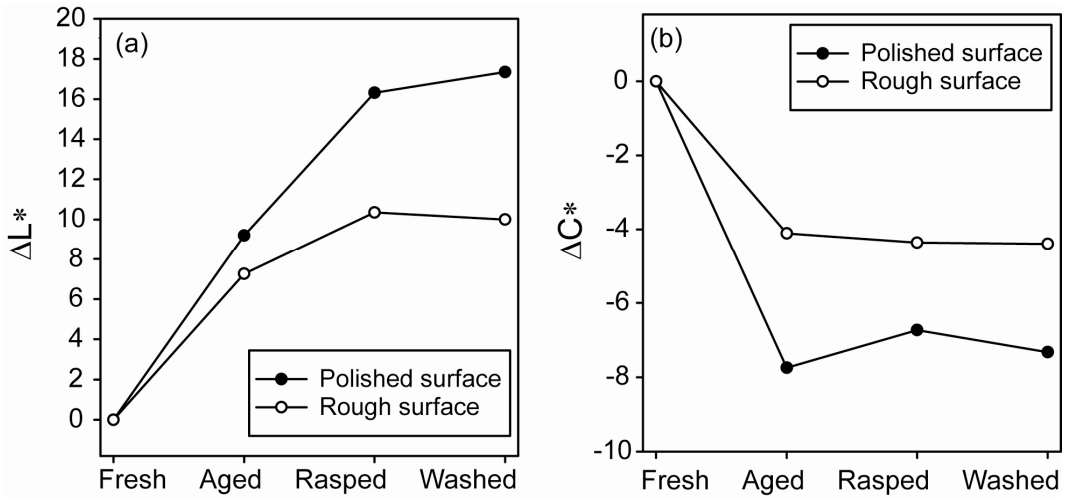

Fig. 8. Changes in the chromatic parameters of the travertine with rough (empty dots) and polished surface (filled dots) between fresh samples, aged ones and aged samples after salt cleaning: (a) variation of brightness (ΔL*) and (b) variation of chroma (ΔC*).

remained constant after surface cleaning with distillate water indicating that the chromatic effect of the salt damage is irreversible (Fig. 8a and b).

6.4. Conclusions

Results from a realistic sea-salt spray test on the massive *Olivillo* travertine (Southern Spain) have revealed that stone damage due to the impact of marine aerosols is strongly related to the stone surface finishing (i.e. rough or polished surface stone). In fact, the polished finishing – combined with a gypsum-based plaster and an epoxy silicone resin infilling – protects the travertine against marine salt corrosion. On the basis of surface fractal dimension analyses, it is clear that this finishing process effectively blocks the pore system in the near-surface zone of the travertine, thus preventing penetration of the saline spray into the stone. By contrast, on the irregular rough travertine surface, salt crystallization is more abundant and induces larger open porosity and also greater surface fractal dimension than in the polished stones, which in turn make it more vulnerable to further salt spray attack.

Apart from this, in terms of chromatic alteration, on rough surfaces chromatic changes are less intense than on polished stones. In fact, the latter become brighter and lose their valued warm tonality, since chromatic parameters were found to be displaced toward more blue and green values. Therefore, salt cleaning interventions based on mechanical removal of efflorescences are not advisable.

This study emphasises that prior to establishing conservation or maintenance practices, it is advisable to characterise the materials used in filled travertines (as well as in other stone types), since undesirable products such as gypsum salt can activate weathering mechanisms. Also, in coastal areas it is recommended to apply *ad hoc*, long-term salt-spray ageing tests on construction and decorative materials to optimise conservation interventions for buildings exposed to marine aerosols.

6.5. References

[1] Anwar Hossain KM, Easa SM, Lachemi M. Evaluation of the effect of marine salts on urban built infrastructure. Build Environ 2009;44:713–22.

[2] Cardell C, Delalieux F, Roumpopoulos K, Moropoulou A, Auger F, Van Grieken R. Salt-induced decay in calcareous stone monuments and buildings in a marine environment in SW France. Constr Build Mater 2003;17:165–79.

[3] Mottershead D, Gorbushina A, Lucas G, Wright J. The influence of marine salts, aspect and microbes in the weathering of sandstone in two historic structures. Build Environ 2003;38:1193–204.

[4] Stefanis N-A, Theoulakis P, Pilinis C. Dry deposition effect of marine aerosol to the building stone of the medieval city of Rhodes, Greece. Build Environ 2009;44:260–70.

[5] Charola AE. Salts in the deterioration of porous materials: an overview. J Am Inst Conserv 2000;39:327–43.

[6] Doehne E. Salt weathering: A selective review. In: Siegesmund GS, Vollbrecht A, Weiss T, editors. Natural stone, weathering phenomena, conservation strategies and case studies. London: Geological Society; 2003. p. 205–19.

[7] Benavente D, García del Cura MA, Bernabeu A, Ordóñez S. Quantification of salt weathering in porous stones using an experimental continuous partial immersion method. Eng Geol 2001;59:313–25.

[8] Cardell C, Rivas T, Mosquera MJ, Birginie JM, Moropoulou A, Prieto B, et al. Patterns of damage in igneous and sedimentary stones under conditions simulating sea-salt weathering. Earth Surf Process Land 2003;28:1–14.

[9] Cardell C, Benavente D, Rodríguez Gordillo J. Weathering of limestone building material by mixed sulfate solutions. Characterization of stone microstructure, reaction products and decay forms. Mater Charact 2008;59(10):1371–85.

[10] Rivas T, Prieto B, Silva B, Birgine JM, Auger F. Comparison between traditional and chamber accelerated ageing tests on granitic stones. In: Proceedings of 9th international congress on deterioration and conservation of Stone, Venice, 2000. p. 171–80.

[11] Rivas T, Prieto B, Silva B, Birginie JM. Weathering of granitic stones by chlorides: effects of the nature of the solution on weathering morphology. Earth Surf Process Land 2003;28:425–36.

[12] Rodríguez-Navarro C, Doehne E. Salt weathering: influence of evaporite rate, supersaturation and crystallisation pattern. Earth Surf Process Land 1999;23(3):191–209.

[13] ASTM B-117: Standard practice for operating salt spray (fog) apparatus. Philadelphia: Am Soc Testing Mater; 1997.

[14] DIN 50021: spray tests with different sodium chloride solutions. In: Normung EV, editor. Deutsches Institut für. German National Standard; 1988.

[15] ISO International Organization for Standardization. ISO 9227, Corrosion tests in artificial atmospheres – salt spray tests; 2006.

[16] UNE-EN 14147: natural stone test methods. Determination of resistance to ageing by salt mist. Madrid: Spanish Association for Standardisation and Certification (AENOR); 1994.

[17] Cardell C. Cristalización de sales en calcarenitas. Aplicación al Monasterio de San Jerónimo, Tesis Doctoral. Granada: University of Granada, Faculty of Science, Department of Mineralogy and Petrology; 1998.

[18] Steiger M, Zeunert K. Crystallisation properties of salt mixtures: comparison of experimental results and models calculations. In: Proceedings of 8th international congress on deterioration and conservation of stone, Berlin, 1996. p. 535–44.

[19] Ruiz-Agudo E, Mees F, Jacobs P, Rodríguez-Navarro C. The role of saline solution properties on porous limestone salt weathering by magnesium and sodium sulfates. Environ Geol 2007;52:269–81.

[20] Pentecost A. The quaternary travertine deposits of Europe and Asia Minor. Quater Sci Rev 1995;14:1005–28.

[21] Ford TD, Pedley HM. A review of tufa and travertine deposits of the world. Earth Sci Rev 1996;41:117–75.

[22] Török Á. Influence of fabric on the physical properties of limestones. In: Kourkoulis SK, editor. Fracture failure of natural building stones. Applications in the restoration of ancient monuments. Dordrecht: Springer-Verlag; 2006. p. 487–97.

[23] Durán-Suárez JA, García-Casco A, Sánchez-Navas A, Rodríguez-Gordillo J. Caracterización de las alteraciones en pilares de travertino de la Iglesia del Salvador (Granada). Propuestas restauradoras. Bol Soc Esp Miner 1993;16:1–12.

[24] Gauri K, Bandyopadhyay JK. Carbonate stone chemical behavior durability and conservation. New York: J. Wiley & Sons; 1999. [25] Demirdag S. The effect of using different polymer and cement based materials in pore filling applications on technical parameters of travertine stone. Constr Build Mater 2009;23:522–30.

[26] Török Á. Surface strength and mineralogy of weathering crusts on limestone buildings in Budapest. Build Environ 2003;38:1185–92.

[27] Török Á. Black crusts on travertine: factors controlling development and stability. Environ Geol 2008;56:583–94.

[28] Voersman F, Baena J. Mapa geológico de España escala 1:50.000. Hoja 1.044 Alhama de Almería. Mapa y memoria. Madrid: Geological and Mining Institute of Spain (IGME); 1983.

[29] García del Cura MA, Sanz-Montero E, Benavente D, Martínez-Martínez J, Bernabéu A, Cueto N. Sistemas travertínicos de Alhama de Almería: características petrográficas y petrofísicas. Geotemas 2008;10:456–9.

[30] García del Cura MA, La Iglesia A, Ordóñez S, Sanz-Montero E, Benavente D. Óxidos de hierro y manganeso en travetinos de Alhama de Almería. Macla 2008;9:107.

[31] Martín Ramos JD. XPowder: a software package for powder X-ray diffraction analysis. Granada: Lgl. Dep. GR 1001/04; 2004.

[32] Sing KSW, Everett DH, Haul RAW, Moscou L, Pierotti RA, Rouquérol J, et al. Reporting physisorption data for gas/solid systems with special reference to the determination of surface area and porosity (recommendations 1984). Pure Appl Chem 1985;57:603–19.

[33] Gregg SJ, Sing KSW. Adsorption surface area and porosity. London: Academic Press; 1982.

[34] Adamson AW, Gast AP. Physical chemistry of surfaces. New York: J. Wiley & Sons; 1997.

[35] Barret EP, Joyner LG, Halenda PP. The determination of pore volume and area distributions in porous substances I. Computations from nitrogen isotherms. J Am Chem Soc 1951;73:373–80.

[36] Tang P, Chew NJK, Chan H-K, Raper JA. Limitation of determination of surface fractal dimension using N_2 adsorption isotherms and modified Frenkel–Halsey–Hill theory. Langmuir 2003;19:2632–8.

[37] Wyszecki G, Stiles WS. Colour science. Concepts and methods, quantitative data and formulae. 2nd ed. New York: J. Wiley & Sons; 1982. [38] Andersson J, Hillborg H, Gubanski SM. Deterioration of internal interfaces between silicone and epoxy resin. In: Conference record of the 2006 IEEE international symposium on electrical insulation; 2006. p. 527–30.

[39] Crnkovic B, Poggi F. Travertine the restoration stone for the Zagreb Cathedral. Mining Geol Petrol Eng Bull 1995;7(1):77–85.

[40] Petrelli M, Perugini D, Moroni B, Poli G. Determination of travertine provenance from ancient buildings using self-organizing maps and fuzzy logic. Appl Artif Intell 2003;17:885–900.

[41] Pentecost A. Travertine. Berlin Heidelberg: Springer-Verlag; 2005.

[42] Rodríguez-Navarro C, Rodríguez-Navarro A, Elert K, Sebastián E. Role of marble microstructure in near-infrared laser-induced damage during laser cleaning. J Appl Phys 2004;95:3350–7.

[43] Sunagawa I. Characteristics of crystal growth in nature as seen from the morphology of mineral crystals. Bull Minéral 1981;104:81–7.

[44] Rodríguez-Navarro C, Doehne E, Sebastián E. How does sodium sulfate crystallize? Implications for the decay and testing of building materials. Cem Concr Res 2000;30:1527–34.

[45] Markov I. Crystal growth for beginners. Fundamentals of nucleation, crystal growth and epitaxy. 2nd ed. Singapore: World Scientific Publishing Company; 2003.

[46] Buck BJ, Van Hoesen JG. Snowball morphology and SEM analysis of pedogenic gypsum, Southern New Mexico, USA. J Arid Environ 2002;51:469–87.

[47] Avnir D, Jaroniec M. An isotherm equation for adsorption on fractal surfaces of heterogeneous porous materials. Langmuir 1989;5(6):1431–3.

[48] Lefebvre Y, Lacelle S, Jolicoeur C. Surface fractal dimensions of some industrial minerals from gas-phase adsorption isotherms. J Mater Res 1992;7:1888–91.

[49] Ruiz-Agudo E, Luque A, Sebastián EM, Rodríguez-Navarro C. Changes in the pore structure of marble after salt decay tests. In: Proceedings of 9th international congress on heritage and building conservation, Seville, 2008. p. 153–8.

[50] Ruiz-Agudo E, Putnis CV, Jiménez-López C, Rodríguez-Navarro C. An atomic force microscopy study of calcite dissolution in saline solutions: The role of magnesium ions. Geochim Cosmochim 2009;73:3201–17.

[51] Xie H, Wang J, Qan P. Fractal characters of micropore evolution in marbles. Phys Lett A 1996;218:275–80.

Chapter 7

Submitted to Construction and Building Materials

An experimental study on sea spray-induced decay in rough and polished low-porous limestone

Maja Urosevic*, Eduardo Sebastián-Pardo, Carolina Cardell

Department of Mineralogy and Petrology, Faculty of Science, University of Granada, Campus Fuentenueva s/n, 18071 Granada, Spain

Article history:

Submitted 22 February 2011

ABSTRACT

Tablets of rough and polished compact dolomite-bearing limestones and a glass crystallizer were aged in a sea-salt spray chamber to explore potentially contrasting weathering response. Salts of diverse composition and habits crystallized as crusts in all substrates. No detachments occurred in stones, though a binding effect and coeval micro-fissure opening were identified in the smallest pores. Also chemical weathering was observed in calcite (unlike dolomite) crystals - mainly in polished samples - revealing that dolomite-rich carbonate stones are less prone to salt decay in coastal areas. Chromatic alterations (bluing) occurred in all limestones, but was more pronounced in polished samples.

KEYWORDS

Salt-spray damage, low-porous limestone, marine environment, ageing test, dolomite.

7.1. Introduction

It has long been recognized that limestones (carbonate rocks composed largely of the mineral calcite, $CaCO_3$) exposed at outdoor environments are more prone to weathering than other stone lithotypes such as sandstones or granites [1]. This is mainly due to water deposition at the limestone surface that acts as a solvent for a series of gaseous substances present in the atmosphere, as well as air pollutants that are very reactive in contact with carbonate minerals [2]. Among other regimes, marine environments are especially aggressive because carbonate dissolution is accelerated by the presence of marine aerosols that can include very reactive sulfate solutions [3-7]. Although in low quantities, marine aerosols may also be transported by winds to inland areas relatively far from the coast [3,8-10] making this issue an important research area to engage future conservation strategies in inland areas.

Pioneering works on the morphological variations of limestone surface under marine environment have stressed a limited weathering effect of condensed water [11,12]. Natural observations, however, suggest that other wet deposition mechanisms must prevail as a large variety of weathering forms in limestone have been described in coastal environments [1,3,5,6,13]. More likely wet surface deposition is produced directly by sea-spray [5,6,14] instead of direct water condensation, as the latter is formed only near 100% relative humidity. Nevertheless, direct condensation of moisture onto cold surfaces (i.e. when the monument temperature is below the dew point) is also very common in coastal areas, where sea-spray causes condensation at RH = 75%, as reported by [15]. Additionally marine aerosol dry deposition must be considered [16].

Recently it has been shown that different surface finishing processes may potentially control contrasting stone decay behavior in porous materials [17]. Moreover, different hydrophilicities at the surface may induce changes in the system evaporation rate and hence modify the precipitation/dissolution cycles of soluble salts [11]. Therefore the surface roughness should also be considered as an important factor as it contributes to different degrees of weathering by promoting long-term interaction with reactive species, or by

changing morphological features of condensed mineral phases. Nevertheless the implications of the surface finishing for the weathering of limestones under marine environments have not been considered so far.

This paper presents a laboratory ageing test using marine spray in a controlled atmosphere chamber to examine the weathering decay in low-porous rough and polished limestone samples. This work is aimed to characterize the condensed phases and their morphological variations, and to explore different deterioration behaviors due to contrasting finishing of stone surfaces.

7.2. Materials and methods

7.2.1. Stone material

This research is focused on a low-porous Jurassic limestone type known as Sierra Elvira stone (SE). This limestone is currently used as a building stone extracted in Andalusia (Granada province, Southern Spain). A similar stone variety in age and geological depositional environment is found in many other Alpine realms and is extensively used throughout Europe. The sawing direction of the selected material is perpendicular to the layering (vein cut). This layering is due to a thin alternation of parallel- to cross-laminated beds that has been interpreted as storm sand layers [18]. Two finishing surface types of the SE limestone are commercialized, namely as rough surface and polished surface. The latter finishing type requires no treatment before the polishing process because of its high strength. In this work, limestone samples with rough and polished surfaces were cut as tablet samples (50 x 50 x 10 mm) for the sea-salt spray ageing test. Later on, the stone samples were prepared according to the requirement of each analytical technique applied, as specified in Section 7.2.3 (Fig. 1a and b).

The SE limestone is a medium-grain limestone mainly composed of well cemented carbonate bioclastic fragments of crinoids (equinoderms). It is by far the most exploited

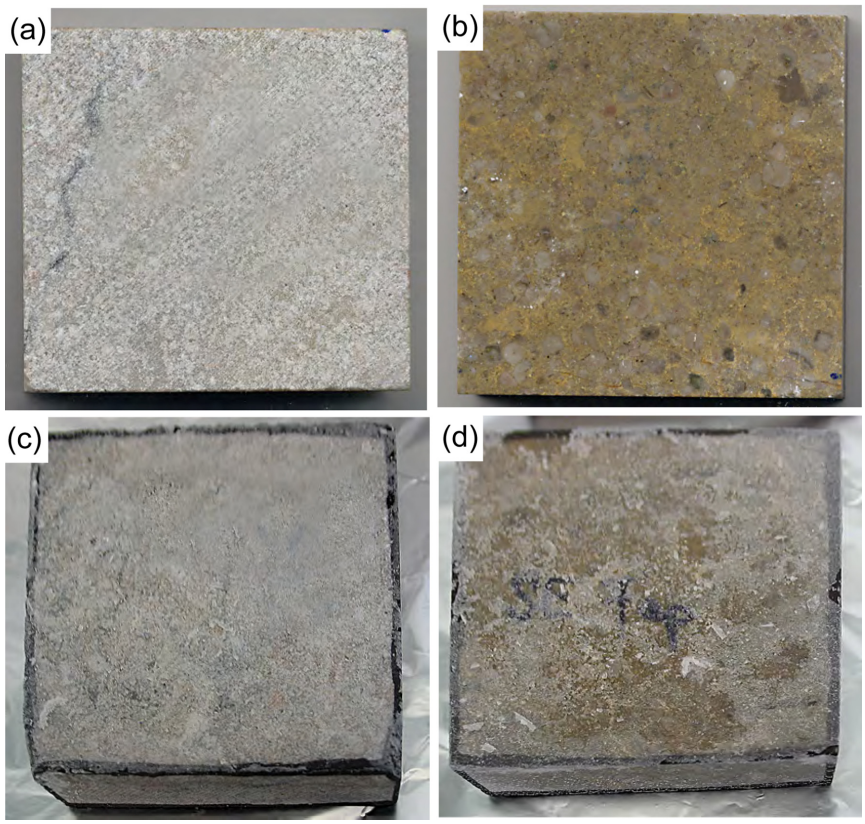

Figure 1. Sierra Elvira limestone: **(a)** rough and **(b)** polished fresh surface before the test, **(c)** rough and **(d)** polished aged surface after the test. Tablets are 5 cm in width.

stone variety in the Granada area and widely used for ornamental purposes in historical monuments and in modern buildings in Andalusia [19]. The SE limestone is classified by means of optical microscopy as a biopelsparite (Ibp) according to Folk's scheme [20], and is comprised chiefly of allochemical constituents (pellets and fragments of fossil equinoderms, molluscs, brachiopods and minor foraminifera) cemented by sparry calcite cement (10-100 μm in size) as shown in Fig. 2. Crinoids (equinoderms) are the main allochemical constituents (50-70%), showing a diameter of 1-2 mm. Stylolites (fine lines, usually brownish in color, formed by pressure-solution) are not rare. A key feature of this limestone is the occurrence of variable amounts of dolomite ($CaMg(CO_3)_2$) crystals which have important implications for the development of weathering patterns (see below). The presence of dolomite produces a relatively high MgO content in the bulk composition (ca. 4 wt.%)

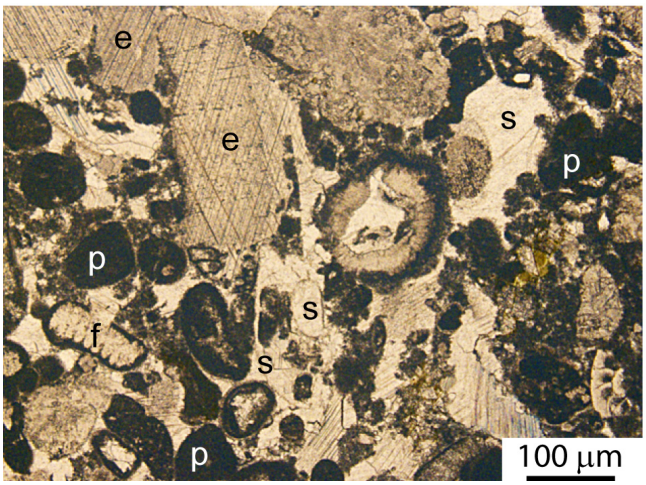

Figure 2. Optical microphotograph showing a representative texture of fresh quarried Sierra Elvira low-porous limestone: fragments of equinoderms (e), pellets (p), and foraminera (f) cemented by sparry calcite (s). Transmitted light, parallel nicols.

Table 1. Representative major bulk rock composition and trace elements of SE limestone (this study) together with mean values of Campanile limestone [21].

wt. %	Sierra Elvira	Campanile
SiO_2	0.52	0.51
TiO_2	0.01	b.d.l.
Al_2O_3	0.21	0.10
Fe_2O_3	0.18	0.09
MnO	0.01	0.10
MgO	4.22	0.86
CaO	50.66	54.54
Na_2O	0.03	0.15
K_2O	0.06	0.02
P_2O_5	0.02	0.03
SO_3	0.03	n.m.
Cl	0.02	n.m.
ppm		
Cu	41	n.m.
Zn	n.m.	n.m.
Sr	132	n.m.
Zr	7	n.m.

Detection limit is 0.005 wt.% for major elements and for trace elements 3 ppm for Zr, 2 ppm for Sr, 1 ppm for Cu, Zn, Zr. b.d.l.: below detection limit, n.m.: not measured.

when is compared to other common limestones [21]. The amount of dolomite in studied limestone is ca. 18 wt.%, based on XRF data (Table 1).

7.2.2. Sea-salt spray ageing test

Limestone tablets were subjected to a modified UNE-EN (14147) ageing test [22] in a saline spray chamber (CCONS series, INELTEC®) to investigate the effect of marine aerosol deposition on the rough and polished stone surfaces. In order to re-create more realistic environmental conditions of coastal areas, seawater was collected from the Mediterranean Sea at Granada coast (Salobreña, Southern Spain). Stone tablets were hung on a nylon thread from plastic bars inside the chamber. The

applied sea-salt ageing test is described in detail by [17]. Each cycle consisted of 3 h of seawater spray followed by 6 h of drying by forced air at 35 ºC and relative humidity of 70 ± 2%. The chamber remained closed throughout the test, thus during spray periods the relative humidity was higher (ca. 98%). The composition of the seawater is shown in Table 2. Cations (Ca^{2+}, K^{+}, Na^{+} and Mg^{2+}) were determined by means of inductively coupled plasma-atomic emission spectrometry (ICP-AES, Leeman Labs PS series) and anions (Cl^{-}, SO_4^{2-} and NO_3^{-}) by ion chromatography (IC, Dionex DX 300). The pH of the seawater was 7.84 at 20 ºC (Eutech 1500). Macroscale observations and photographic records were made throughout the test to determine the presence of efflorescences, evolution of crystalline habits on the stone surfaces, drying and decay of the samples. Moreover, before and after the test the tablets were weighed.

Table 2. Sea-salt water composition (expressed in ppm) used in the artificial ageing test of the present study and from [6].

	This study	[6]
Cl^{-}	12,879	22050
NO_3^{-}	72	50
SO_4^{2-}	2772	2713
Ca^{2+}	330	345
K^{+}	348	1020
Na^{+}	10,030	19920
Mg^{2+}	1069	945
HPO_4^{2-}	-	28

- not measured

7.2.3. Analytical techniques

The mineralogical composition of the SE limestone and the crystallized efflorescences were determined by X-ray powder diffraction (XRD) on a Philips PW-1710 diffractometer equipped with an automatic slit window. Samples were previously milled in an agate mortar to less than 50 μm particle size. Analysis conditions were: radiation Cu Kα (λ: 1.5405 Å), 40 kV voltage, 40 mA current intensity, explored area between 3º and 60º 2θ and goniometer

speed of 0.01º 2θ s^{-1}. Automatic acquisition, evaluation and identification of minerals were performed by the Xpowder software [23]. Major and trace elements of fresh limestone were analyzed using a Bruker S4 Pioneer X-ray fluorescence spectrometer (XRF) with wavelength dispersion equipped with a goniometer that held analyzing crystals (LIF200/PET/OVO-55) and Rh X-ray tube (60 kV, 150 mA).

Petrographic characteristics of fresh and aged limestones presenting rough and polished surfaces were examined under optical microscopy (OM) using an Olympus BX-60 equipped with digital camera (Olympus DP10). To this aim, polished thin sections were prepared with ethanol to avoid salt dissolution, and stained with red alizarin to differentiate calcite from dolomite (calcite tints to red while dolomite remains unstained). Chips of these stone samples were also analyzed with an environmental scanning microscope (ESEM). A Phillips Quanta 400 was used applying 20 kV acceleration voltage, 1 nA probe current and working distance of 10 mm.

The limestone pore system was characterized by means of mercury intrusion porosimetry (MIP) and argon adsorption. Blocks of ca. 2 cm^3 of fresh and aged samples (containing salts) were dried in an oven during 24 h at 60 ºC, and analyzed on a Micromeritics Autopore III model 9410 porosimeter. In addition, aged samples were washed in distilled water during one week after the ageing test, and studied by means of argon adsorption. The Barret–Joyner–Halenda (BJH) method was used to obtain the pore size distribution curves, the pore volume and the mean pore size of the limestone samples [24]. The surface fractal dimension, D_S, was determined from adsorption data and used to characterize the surface roughness. Analysis of the gas adsorption isotherms using a modified Frenkel–Halsey–Hill (FHH) theory [25] allows determination of surface fractal dimension from the slope (A) of the plot of Ln(V) vs. Ln[Ln(P/P_0)], where V is the adsorbed volume of gas, and P and P_0 are the actual and condensation gas pressures. When surface tension (or capillary condensation) effects are important, the relationship between A and D_S is $A = D_S - 3$. Capillary condensation is significant if $\delta = 3(1 + A)-2 < 0$. The pressure range and therefore the thickness range of the adsorbed layer coverage revealed that samples were

purely monolayer (since n = 1–2). This thickness range ensures that the determination of DS is reliable [25].

Chromatic characteristics of rough and polished surface samples before and after the ageing test were determined using a Minolta CR 210 colorimeter, with 0º viewing angle and 50 mm diameter measuring area. The CIE 1976 chromatic scale was used to measure the parameters L*, a* and b* [26].

7.3. Results and discussion

7.3.1. Macroscopic changes

During the sea-salt ageing test no stone detachments were observed. The first efflorescences crystallized as crusts after 48 h of exposure in the test chamber in all samples, most profusely in the rough ones. Salt crusts started to grow at the upper borders of each tablet and afterwards extended and covered the tablets completely (Fig. 1). The weight of all samples slightly increased after the test (+ 0.25% for rough limestone and + 0.40% for polished limestone). This is in agreement with experimental results from [5] and [14] that suggest only very small and gradual change in weight for compact microcrystalline limestone. The salt crust was thicker in the polished limestones (ca. 0.5-1 mm). Furthermore, thin sections prepared perpendicular to the limestone surfaces did not reveal the presence of subefflorescences.

7.3.2. Nature and morphology of crystallized mineral phases

A key finding of this study is the contrasting nature and morphology of the salt crust precipitated onto the rough versus polished aged limestone surfaces observed with ESEM. Crystal morphology reveals the phenomena controlling the process of crystal growth [4,27,28]. These morphologies are described separately in the following paragraphs.

7.3.2.1. Rough surface

A semi continuous, homogeneous and thin halite (NaCl) crust was developed onto the rough limestone surface (Fig. 3a and b). The crust was 50-100 μm thick, relatively flat and with a smooth surface. The only mineral phase identified was halite showing anhedral crystal shapes (no crystal face development). Under ESEM inspection some discontinuities were seen in the crust as shown in Fig. 3b. Here subhedral (poor crystal face development) and small (5-10 μm) halite crystals together with small amount of ferruginous clays usually occur. As stated by [4] and [29], rounded external surfaces of halite crystals are usually formed when ion diffusion controls the growth process suggesting that moderate to low humidity prevailed during crystallization.

In other areas of the rough limestone, where a continuous crust is lacking, evidence of corrosion and alteration of the carbonate phases has been observed. Fig. 3c shows a detail of one of these areas without salt crust formation where micritic calcite (1-4 μm crystal size, centre of the image) shows signs of powdering or sanding. Moreover sparitic calcite cleavage surfaces are profusely affected by micropitting (Fig. 3c). In clear contrast, dolomite cleavage surfaces (dark grey in Fig. 3c) are significantly less damaged. Other salts (e.g. gypsum) expected to crystallize considering the chemistry of the sea water used in the test (Table 2) were not found, but their occurrence under or inside the continuous halite crust is not discarded based on the observations on the polished surface samples (see below).

7.3.2.2. Polished surface

Aged polished surfaces are characterized by higher diversity of crystalline habits and salt species. In contrast with the rough surface samples, the crust is thick and discontinuous; it mostly consists of clusters of large halite single crystals up to 100 μm in size, as observed in Fig. 3d and e. Halite occurs as subhedral to euhedral crystals (well developed crystal

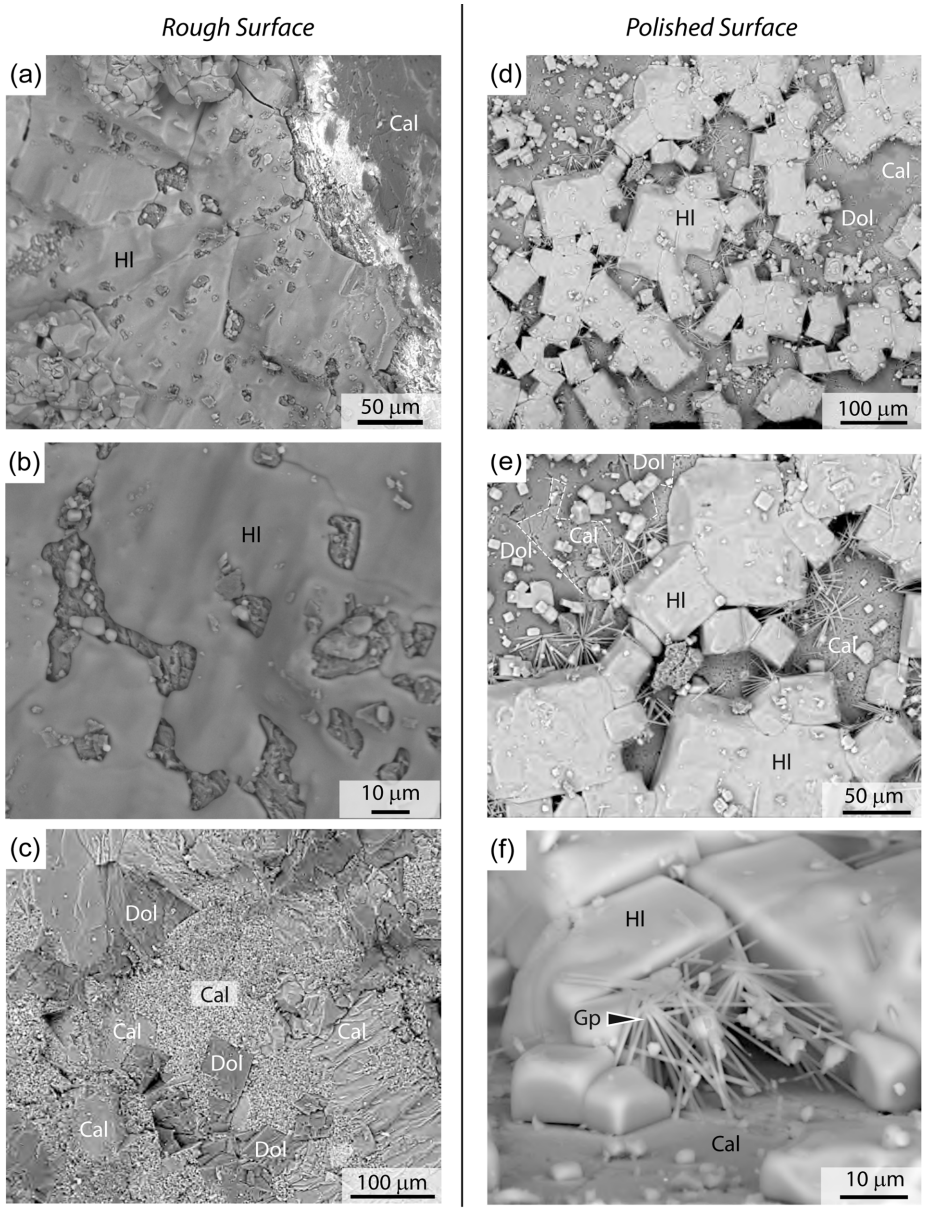

Figure 3. Electron backscattered images taken with ESEM of the aged Sierra Elvira limestone: **(a)** rough surface with massive and homogeneous halite crust, **(b)** detail of halite crust where irregularities on the rough surface inhibited the continuity of the crust, **(c)** micritic calcite (centre) showing signs of powdering or sanding where sparitic calcite cleavage surfaces are profusely affected by micropitting. Note that dolomite cleavage surfaces (in dark grey) are significantly less damaged, **(d)** polished surface covered by tabular euhedric halite and acicular gypsum crystals, **(e)** detail of the crust showing different degree of weathering damage of calcite and dolomite grains, **(f)** detail of radial aggregates of multiple aciculae gypsum crystals partially overgrown by tabular halite crystals. Cal: calcite; Dol: dolomite; Hl: halite; Gp: gypsum.

faces) growing with no crystallographic preferred orientation on the limestone surface. The {100} crystal forms are commonly parallel to the polished surface (Fig. 3d and e). Isometric halite crystals show their specific equilibrium form which indicates that crystal growth was controlled by surface reactions, thus suggesting relatively high humidity values [4,27-29].

Although halite is again the main salt forming the crust, calcium sulfate is also conspicuously present. While in this work the precise composition of the calcium sulfate could not be established with the applied analytical techniques, the experimental conditions of the test (98% RH and T = 35 ºC) imply that gypsum ($CaSO_4 \cdot 2H_2O$) should be the stable phase [30,31], since at room temperature and relative humidity lower than 70% gypsum dehydrates to bassanite ($CaSO_4 \cdot 0.5H_2O$) and anhydrite ($CaSO_4$). Moreover, considering that the kinetics of these dehydration reactions are very slow [30,31] in the following discussion only gypsum will be considered. Gypsum distinctively occurs as radial aggregates of multiple aciculae (slender or needle-like crystals) as can be observed in Fig. 3f. Textural relationships between crystallized salts indicate that gypsum precipitated first and afterwards was overgrown by larger halite crystals. This morphological feature of gypsum crystals on the aged stone samples after a sea salt ageing has not been described so far. It is known that gypsum crystallizing from polluted fog droplets usually occurs as clusters of "rosette" habits [15,32].

As in the aged rough limestones, calcite crystals are more strongly chemically altered than are dolomite crystals. This feature is even enhanced by polishing and can be precisely observed in the ESEM images (Fig. 3d and e) where darker colors of the substrate, which correspond to dolomite, are almost free of dissolution pits. Instead, calcite develops a porous network due to dissolution which is conspicuous even at the observation scale of the ESEM. The modification of the limestone porous system after the ageing test is further confirmed by means of other techniques, as explained below. Extreme corrosion morphologies like deep V-in-V etching or grain boundary widening reported by [2], were not observed however.

7.3.2.3 An ad hoc salt crystallization test onto a glass crystallizer

All the studied limestone samples were aged in the same salt-spray test, so they were subjected to similar experimental conditions (number of cycles, distance from the spray source, temperature, humidity, etc.). Therefore, considering that the stone mineralogy is similar, the above described contrasting salt morphologies observed in the rough and polished surfaces must be related to their surface finishing. In fact, the different surface micro-textures of the limestone samples involve different evaporating and water absorption conditions. Physical interaction between marine aerosol and rock substrates is complex, and the control that these interactions exert on the kinetics of salt crystallization is not fully understood, especially in large heterogeneous systems like porous stones [4,33]. Consequently the relation between surface roughness and salt crust morphologies (that eventually determine stone decay) is not straightforward. For this reason, to further explore the influence of substrates on precipitated salt composition and habits, an *ad hoc* crystallization test was conducted using a glass crystallizer as substrate. The glass was sprayed (inside the test chamber) with the same sea water employed to age the limestone samples, and allowed to completely vaporize. Afterwards the nature and morphology of the crystallized efflorescences were analyzed by means of ESEM.

In the *ad hoc* crystallization test the composition of the salts was more complex. Minerals found with ESEM/EDS analysis included halite, gypsum, silvine (KCl) and epsomite ($MgSO_4 \cdot 7H_2O$). As mentioned above, this technique does not permit identification of the sulfate species, however considering the experimental test conditions we infer that in fact gypsum and epsomite are the mineral phases present [27]. Regarding the observed salt morphologies, these were rather different from those previously described for rough and polished limestone surfaces. Thus, gypsum twinned on {100} crystal planes was the most conspicuous morphology encountered. The twins were composed of two or four crystals with simple habit (tabular on {010} planes with edges bevelled by {120} planes) resulting in swallowtail morphologies (Fig. 4a). Gypsum twins were usually overgrown by halite. Large subhedral halite crystals (ca. 1 mm in size) with typical hopper morphologies (crystal displaying an hourglass shape) were common. The morphology of NaCl crystals grown from

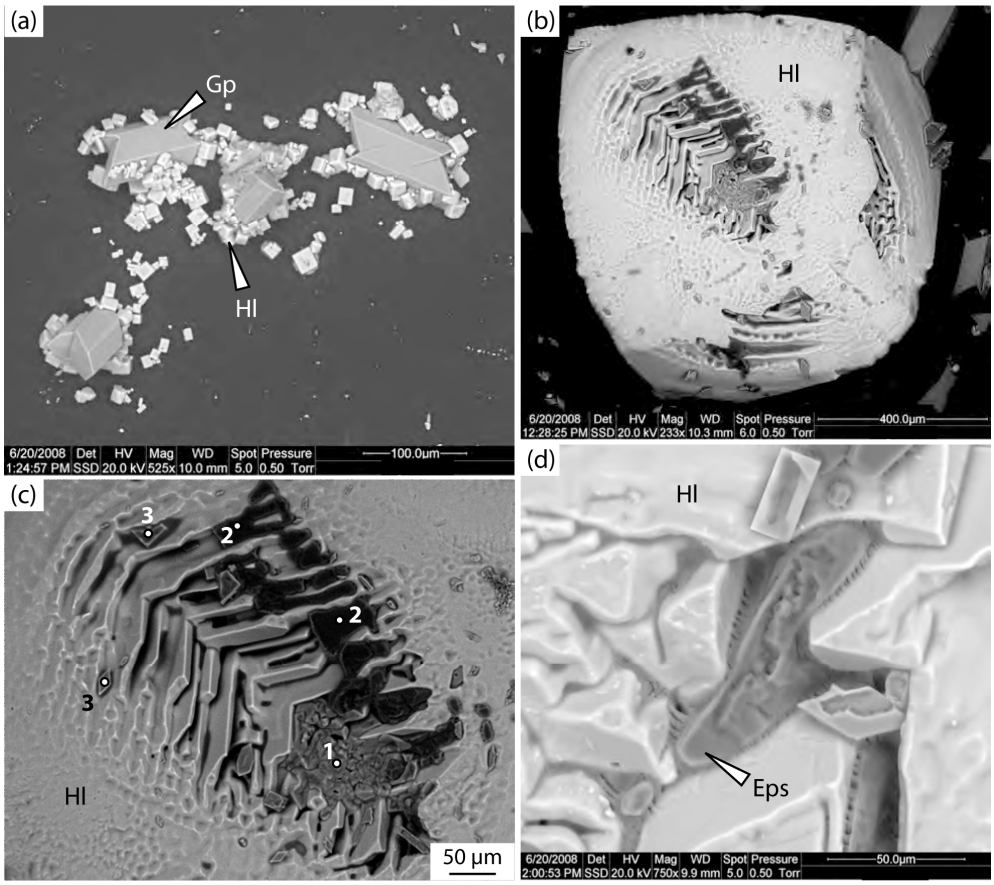

Figure 4. Electron backscattered images of the ad hoc salt crystallization test onto glass crystallizer. **(a)** twinned gypsum (Gp) crystals partially overgrown by euhedral halite (Hl), **(b)** large halite crystal (ca. 800 µm) with hopper morphology, **(c)** enlarged area from **(b)** showing the occurrence of silvine-rich aggregate (1), epsomite (2) and gypsum (3) in to the hopper halite crystal, **(d)** detail of one xenomorphic epsomite (Eps) growing in halite boundary grains.

aqueous solutions in a closed system is mainly controlled by different temperature gradients where both {100} and {111} hopper cubes forms can be developed [34]. In our crystallization test small euhedral {100} forms (< 40 µm in length, Fig. 4a) and large {100} hopper cubes (> 500 µm in length, Fig. 4a) were observed. Small, non-twinned gypsum (20-30 µm in size) usually occurred on the halite surface together with more soluble salts like epsomite and silvine (Fig. 4c and d). Epsomite showed xenomorphic shapes filling open spaces (Fig. 4d).

All these observations clearly indicate that even subtle changes in the nature, roughness and composition of the substrate may induce important changes in the morphology and composition of the crystallized salts. According to [15] hygroscopic and deliquescent salts like epsomite and silvine tend to disappear after numerous spray cycles, thus explaining their lack on the surface of salt-tested rocks due to surface washing. Moreover, according to [15], dissolution of other soluble phases like ammonium, sulfate and nitrate after numerous fog water deposition events are characteristic for more polluted environments.

7.3.3. Modification of the limestone pore system

Comparison of the pore systems before and after the ageing test in the studied limestones enabled evaluation of changes to the pore network due to the salt crystallization only in pores near the stone surface. Moreover, our results revealed that the porosity for both the rough and polished limestones was similar, in contrast with findings obtained in other materials like rough and polished travertines [17]. This suggests that in our compact limestones the surface roughness does not produce a modification of the pore system, which clearly should be attributed to the low porosity of our tested limestone. In the following sections the modification of the pore system for rough and polished samples is described for the pore system range accessible to the MIP and gas adsorption techniques.

7.3.3.1. Mercury intrusion porosimetry (MIP)

Fig. 5 shows the pore size distribution obtained by means of MIP for fresh and all aged samples. The SE limestone is a low porous material [19] and the variation of its pore size distribution is expected to be rather low. The average and the standard deviation (1σ) for four measurements (including rough and polished surface samples) are reported for the fresh samples in order to evaluate the representativeness of changes to the pore systems after the ageing test (Fig. 5 and Table 3). The pore size distribution curve for fresh samples is bimodal and slightly symmetric (Fig. 5). Two groups of pore size ranges have been observed for these samples. The first is comprised of radii between 20 and 110 μm and the second between

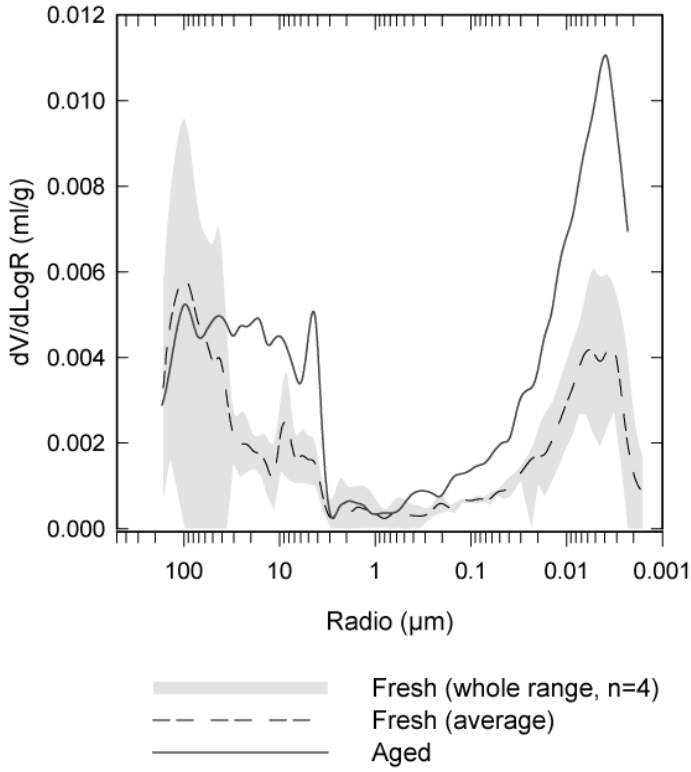

Figure 5. Pore size distribution measured by mercury intrusion porosimetry (MIP) of fresh quarry (continuous line) and aged (dashed line) SE limestone.

0.001 and 0.02 µm. It is important to note that the pore size of the first group is highly variable (high standard deviation, Fig. 5) and is lacking in some samples. By contrast the second group of pore sizes has been detected in all samples and thus is believed to be representative of this limestone.

After the ageing test this pore size distribution is modified. The distribution is still bimodal but is more asymmetric (Fig. 5). The range of the first group of pore sizes is expanded and comprises sizes between 3 and 100 µm, some of them (those comprised between 3 and 20 µm) created after the test and interpreted as due to salt damage. Moreover the proportion of the second group is more important after the ageing test. Salt crystallization induces a substantial increase in the open porosity from 1.64 ± 0.67% to 4.26 ± 0.64% and a slight reduction of the bulk density as shown in Table 3. Modification of the pore system

Table 3. Pore system characteristics determined by mercury intrusion porosimetry (MIP) and Ar adsorption for fresh and aged samples of SE limestone.

Mercury intrusion porosimetry	fresh	aged
Open porosity (%)	1.64 ± 0.67	4.26 ± 0.64
Apparent density (g/cm^3)	2.71 ± 0.04	2.71 ± 0.01
Bulk density (g/cm^3)	2.67 ± 0.02	2.60 ± 0.01
Ar adsorption		
Surface area (m^2/g)	0.4102 ± 0.0627	0.2655 ± 0.0433
Total pore volume (cm^3/g)	0.00042 ± 0.00005	0.00036 ± 0.00007
Average pore diameter (Å)	52.45 ± 3.58	53.61 ± 1.07
Monolayer volume (cm^3/g)	0.1004 ± 0.0064	0.1062 ± 0.0019
Surface fractal dimension (D_S)	2.674 ± 0.015	2.664 ± 0.010
Linear correlation coefficient (r^2)	0.9921	0.9927

Reported values are the mean and standard deviation of four measurements.

induced by salt crystallization is a well known process in porous materials [35] and is especially relevant for calcarenites, porous limestones and sandstones, but is less constrained for low porous material like cemented limestones [6,36,37]. Our results show that this process is also significant in the SE limestone where development of new porous sizes and an increase of open porosity were observed. This observation has important implications, as this damage is not associated with rising moisture (where the ground is the source of humidity and salt solutions). It is relevant to the case when stone surfaces are prone to salt-decay via sea-salt deposition by fog in coastal areas.

7.3.3.2. Argon adsorption

Argon adsorption was applied to investigate the pore sizes between 20 and 100 Å (2-10 nm) of fresh and aged samples (Fig. 6 and Table 3). Representative Ar adsorption isotherms of these samples are shown in Fig. 6a. Both isotherms are of type II [38] and indicate the non-microporous nature of these samples; this is further confirmed by the very low surface area, i.e. 0.4102 ± 0.0627 m^2/g vs. 0.2655 ± 0.0433 m^2/g respectively for fresh and aged

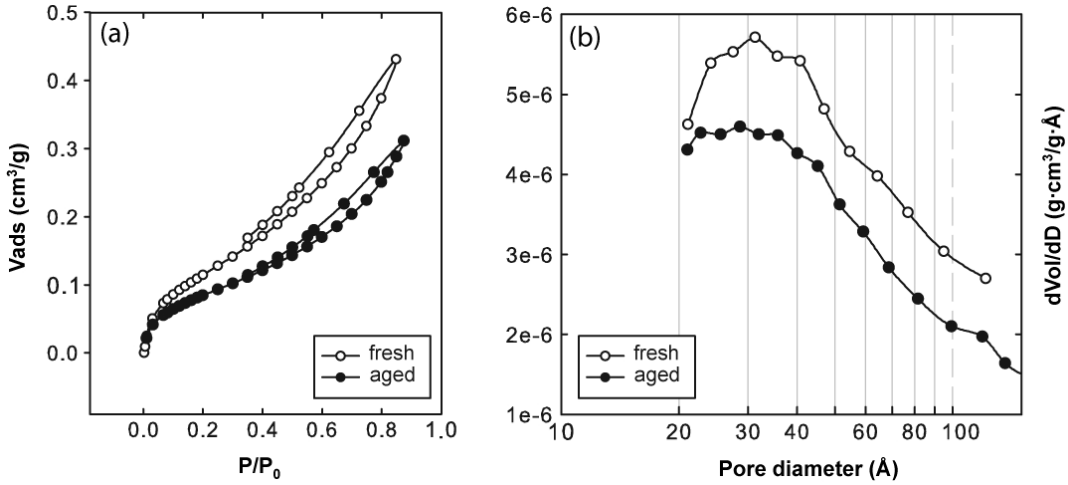

Figure 6. (a) Ar (-196ºC) physisorption and **(b)** BJH pore size distribution plot of Ar physisorption curve isotherms for fresh (empty dots) and aged (filled dots) SE limestone.

samples. Table 3 also shows that the porosity is concentrated in the mesopore range (pore width 20-500 Å, [38]), with an average pore diameter of 52.45 ± 3.58 Å for the fresh samples and 53.61 ± 1.07 Å for the aged samples.

Finally, the BJH plots (pore size distribution curves named after Barret–Joyner–Halenda) are almost equivalent in shape, although the aged samples are displaced to lower values, in agreement with lower surface area and total pore volume (Fig. 6b and Table 3). The reduction of the pore volume is attributed to precipitation of the less soluble salts in the smallest pores. However, the potential inefficiency of salt removal to which this technique is prone (samples must be washed in distilled water during 24 h), can not be excluded. The complexity of the pore system, expressed as the surface fractal dimension (D_S), is slightly reduced after the ageing test (D_S = 2.674 vs. D_S = 2.664 for fresh and aged samples respectively) in agreement with lower surface area of aged samples (Table 3). The reduction in pore system complexity is most likely related to the opening of new microcracks that could also explain the increased proportion of pores between 0.001 and 0.02 μm as measured by MIP (Fig. 5). Therefore salt precipitation in the porous network has flip-side effects: (1) to produce binding and cementing by filling the smallest pores (20-100 Å) and (2) to disrupt the stones by opening microcracks [6,39,40].

7.3.4. Color modification

Chromatic parameters of the rough and polished aged SE limestone surfaces were determined using the following approach: (1) measurements on surfaces covered by salt crusts and (2) measurements on surfaces where efflorescences were mechanically removed. The second approach can be useful to evaluate the efficiency of cleaning interventions to recuperate original stone chromatic characteristics. Table 4 shows the chromatic parameters of all studied samples (these are average values of three measurements for each sample). Perceptible visual changes are achieved only when ΔE* (total color difference = $\sqrt{(\Delta L^*)^2 + (\Delta a^*)^2 + (\Delta b^*)^2}$ exceeds three units. Thus color alterations were observed in all aged samples with exception of the rough ones. Nevertheless, when salts were mechanically removed visual changes were perceptible in both rough and polished samples (Table 4). Furthermore, after the ageing test and mechanical elimination of the salt crusts, the ΔL* (brightness difference) was higher in the polished samples than in the rough ones (15.44 vs. 5.11, Table 4), as can be observed in Fig. 7a. Luminosity increased in both rough and polished samples after mechanical cleaning (Fig. 7a), which can be attributed to the development of salt cleavage planes during surface rasping.

Table 5. Mean values of chromatic parameters and their variations in tested SE limestones, before and after mechanical cleaning of salts on their surfaces.

Surface	Type	L*	a*	b*	C*	H*	ΔL*	Δa*	Δb*	ΔC*	ΔE*
rough	fresh	72.67	-0.24	1.47	1.49	99.13					
	aged	69.90	0.53	1.04	1.17	62.92	-2.77	0.77	-0.43	-0.32	2.90
	rasped	77.78	0.41	1.18	1.25	70.89	5.11	0.65	-0.29	-0.24	5.16
polished	fresh	53.12	1.24	8.61	8.70	81.83					
	aged	63.52	0.96	3.42	3.56	74.28	10.39	-0.27	-5.19	-5.14	11.62
	rasped	68.57	1.04	5.87	5.96	79.98	15.44	-0.20	-2.74	-2.74	15.69

L* brightness; a* red-green components; b* yellow-blue components; C* chroma, $C^*=\sqrt{(a^*)^2+(b^*)^2}$; H* hue; $\Delta E^*=\sqrt{(\Delta L^*)^2+(\Delta a^*)^2+(\Delta b^*)^2}$.

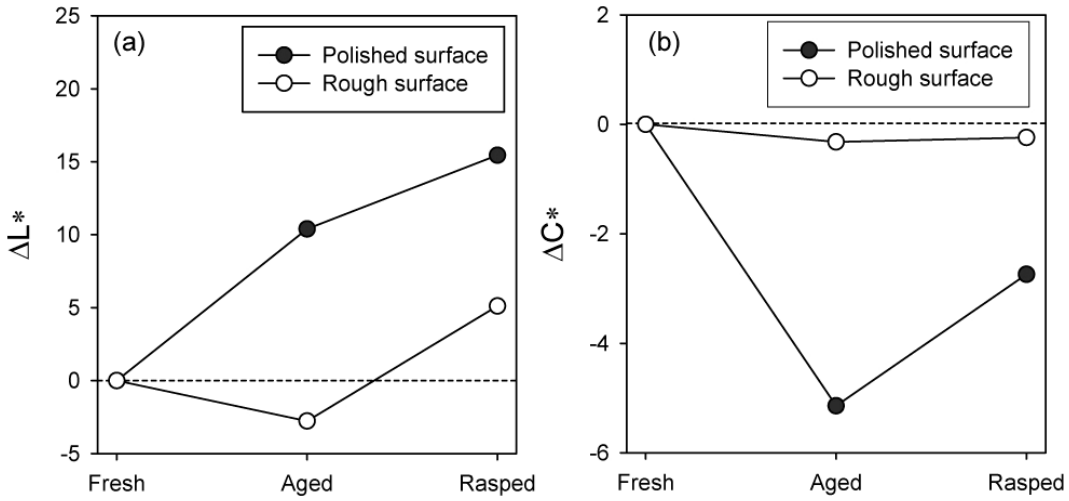

Figure 7. Changes in the chromatic parameters of the limestone with rough (empty dots) and polished surface (filled dots) between fresh samples, aged ones and aged samples after mechanical salt cleaning: **(a)** variation of brightness (ΔL*) and **(b)** variation of chroma (ΔC*).

On the other hand, chromatic parameter variations related to the fresh limestones can be quantified together by means of chroma differences. Fig. 7b shows an important decrease of chroma after the ageing test only for the polished surface limestones, but not for the rough surface samples which remained constant. Moreover, rough and polished samples became more blue after the test as the b* (yellow-blue) component decreased in both cases. On the contrary, the a* (red-green) component decreased only in the polished aged samples that became more green, while it increased in the rough aged samples towards more red values (Table 4).

7.4. Conclusions

A practical sea-salt spray test has been conducted in rough and polished surface tablets of a low-porous dolomite-bearing limestone (Sierra Elvira, SE, limestone) widely used as a building and decorative stone in Andalusia (Southern Spain). Macroscopic observation revealed that no stone detachments occurred during the test in any of the samples, irrespective of their surface finishing. This is attributed to the fact that SE limestone is a

compact, low-porous and homogeneous rock with an interlocking crystalline texture that prevents intensive salt weathering. However salts precipitated as crusts in both rough and polished limestones, though with contrasting compositions and morphologies. These results indicate that stone surface finishing strongly controlled salt-spray absorption and salt crystallization onto the stone surfaces. Thus, while a thin and continuous crust made of halite (as anhedral crystals) covered the rough samples, in polished samples a thick and discontinuous crust composed of halite (isometric crystals) and minor amounts of gypsum (needle-like crystals) was formed.

Although macroscopic evidences suggested that development of efflorescences only had an aesthetic impact – since no other alteration forms were observed – at the microscopic level dissolution patterns (e.g. micropitting) were detected mainly in calcite crystals compared to dolomite crystals, particularly in polished samples. Thus, it is inferred that the presence of dolomite in carbonate rocks has a crucial influence on their chemical weathering response when subjected to saline solutions. Moreover, results clearly indicate that dissolution processes are modified by polishing treatments of limestone surfaces.

On the other hand, the stone porous system analysis before and after the salt test revealed development of new pore sizes and increased open porosity. Moreover, a binding effect and coeval opening of micro-fissures were identified in the smallest pores (20-100 Å) thanks to the gas adsorption technique.

To further explore the influence of substrates on the nature and habits of precipitated salts due to a sea-salt spray, a salt crystallization test onto a glass crystallizer was conducted. Results showed that salt composition was more complex and habits were different. Thus, this work shows that different surface finishing treatments in commercial stones not only lead to contrasting decay responses in coastal environments, but also have implications in surface color modifications attained after salt precipitation and subsequent cleaning. In this regard, after the salt test all of our studied samples became more blue (cold tone), and luminosity and chroma strongly decreased specifically in the polished SE limestone. Thus, the valued warm tonality was lost, which is a non desirable aesthetic side-effect.

7.5. References

[1] Smith BJ, Gómez-Heras M, Viles HA. Underlying issues on the selection, use and conservation of building limestone. In: Smith BJ, Gómez-Heras M, Viles HA, Cassar J, editors. Limestone in the Built Environment: Present-Day Challenges for the Preservation of the Past. London: Geological Society; 2010. v. 331, p. 1–11.

[2] Thornbush MJ, Viles HA. Simulation of the dissolution of weathered versus unweathered limestone in carbonic acid solutions of varying strength Earth Surf Process Land 2007;32:841–52.

[3] Zezza F, Macrì F. Marine aerosol and stone decay. Sci Total Environ 1995;167:123-43.

[4] Theoulakis P, Moropoulou A. Salt crystal growth as weathering mechanism of porous stone on historic masonry. J Porous Mater 1999;6:345-58.

[5] Cardell C, Delalieux F, Roumpopoulos K, Moropoulou A, Auger F, Van Grieken R. Salt-induced decay in calcareous stone monuments and buildings in a marine environment in SW France. Constr Build Mater 2003;17:165–79.

[6] Cardell C, Rivas T, Mosquera MJ, Birginie JM, Moropoulou A, Prieto B, Silva B, Van Grieken B. Patterns of damage in igneous and sedimentary stones under conditions simulating sea-salt weathering. Earth Surf Process Land 2003;28:1–14.

[7] Angeli M, Hébert R, Menéndez B, David C, Bigas JP. Influence of temperature and salt concentration on the salt weathering of a sedimentary stone with sodium sulphate. Eng Geol 2010;115:193-9.

[8] Silva B, Rivas T, García-Rodeja E, Prieto B. Distribution of ions of marine origin in Galicia (NW Spain) as a function of distance from the sea. Atmos Environ 2007;41:4396-407.

[9] Meira GR, Andrade C, Alonso C, Padaratz IJ, Borba JC. Modelling sea-salt transport and deposition in marine atmosphere zone - A tool for corrosion studies. Corr Sci 2008;50:2724-31.

[10] Anwar Hossain KM, Easa SM, Lachemi M. Evaluation of the effect of marine salts on urban built infrastructure. Build Environ 2009;44:713–22.

[11] Zendri E, Biscontin G, Kosmidis P, Bakolas A. Characterization and physico-chemical action of condensed water on limestone surfaces. In: Vasco F, editor. Proceedings of the 9th international congress on deterioration and conservation of stone. Amsterdam: Elsevier Science BV; 2000. p. 647-56.

[12] Zendri E, Biscontin G, Kosmidis P. Effects of condensed water on limestone surfaces in a marine environment. J Cult Herit 2001;2:283-89.

[13] Chabas A, Jeannette D, Lefèvre RA. Crystallization and dissolution of airborne sea-salts on weathered marble in a coastal environment at Delos (Cyclades-Greece). Atmos Environ 2000;34:219-24.

[14] Silva ZSG, Simão JAR. The role of salt fog on alteration of dimension stone. Constr Build Mater 2009;23:3321-7.

[15] Del Monte M, Rossi P. Fog and gypsum crystals on building materials. Atmos Environ 1997;31:1637-46.

[16] Stefanis N-A, Theoulakis P, Pilinis C. Dry deposition effect of marine aerosol to the building stone of the medieval city of Rhodes, Greece. Build Environ 2009;44:260–70.

[17] Urosevic M, Sebastián-Pardo E, Cardell C. Rough and polished travertine building stone decay evaluated by a marine aerosol ageing test. Constr Build Mater 2010;24:1438-48.

[18] Dabrio CJ, Polo D. Interpretación sedimentaria de las calizas de crinoides del Carixiense Subbético. Mediterránea 1985;4:55-77.

[19] Sebastián Pardo E, Cultrone G, Garibaldi V, Rodríguez Navarro C, De la Torre MJ, Valverde I. La Caliza de Sierra Elvira: comportamiento petrofísico de una piedra significativa del Patrimonio Arquitectónico Andaluz. Mater Construcc 2008;58:51-63.

[20] Folk RL. The Petrology of Sedimentary Rocks. Austin, Texas: Hemphill Publishing Company; 1980. 182 p.

[21] Buj O, Gisbert J, Franco B, Mateos N, Bauluz B. Decay of the Campanile limestone used as building material in Tudela Cathedral (Navarra, Spain). In: Smith BJ, Gómez-Heras M, Viles HA, Cassar J, editors. Limestone in the Built Environment: Present-Day Challenges for the Preservation of the Past. London: Geological Society; 2010. v. 331; p. 195-202.

[22] UNE-EN 14147: natural stone test methods. Determination of resistance to ageing by salt mist. Madrid: Spanish Association for Standardisation and Certification (AENOR); 1994.

[23] Martín Ramos JD. XPowder: a software package for powder X-ray diffraction analysis. Granada: Lgl. Dep. GR 1001/04; 2004.

[24] Barret EP, Joyner LG, Halenda PP. The determination of pore volume and area distributions in porous substances I. Computations from nitrogen isotherms. J Am Chem Soc 1951;73:373–80.

[25] Tang P, Chew NJK, Chan H-K, Raper JA. Limitation of determination of surface fractal dimension using N2 adsorption isotherms and modified Frenkel–Halsey–Hill theory. Langmuir 2003;19:2632–8.

[26] Wyszecki G, Stiles WS. Colour science. Concepts and methods, quantitative data and formulae. 2nd ed. New York: J. Wiley & Sons; 1982.

[27] Zehnder K, Arnold A. Crystal growth in salt efflorescence. J Cryst Growth 1989;97:513–21.

[28] Cardell-Fernández C, Rodríguez-Gordillo J. A comparative study of calcarenite SALT crystallisation and weathering in laboratory conditions and in a monument. In: Proceedings of 8th international conference on non destructive investigations and microanalysis for the diagnostics and conservation of the cultural and environmental heritage, Lecce (Italy), 2005. p. 1-15.

[29] Moropoulou A, Theoulakis P, Tsiourva T, Kourteli C, Labropoulos K. Salt and humidity impact on porous stone masonries in marine environment. In: Druzik JR, Vandiver PB, editors, Materials Issues in Art and Archaeology IV. Pitsburg: Publ. Materials Research Society; 1995. v. 352, p. 893.

[30] Charola A, Pühringer J, Steiger M. Gypsum: a review of its role in the deterioration of building materials. Environ Geol 2007;52:339-52.

[31] Kramar S, Urosevic M, Pristacz H, Mirtič B. Assessment of limestone deterioration due to salt formation by micro-Raman spectroscopy: application to architectural heritage. J Raman Spectrosc 2010;41:1441-8.

[32] Simão J, Ruiz-Agudo E, Rodriguez-Navarro C. Effects of particulate matter from gasoline and diesel vehicle exhaust emissions on silicate stones sulfation. Atmos Environ 2006;40:6905-17.

[33] Kubik J, Kucharczyk A. Salt solution flows in walls of monumental buildings. Bauphysik 2008;30:426-30.

[34] Aquilano D, Pastero L, Bruno M, Rubbo M. {1 0 0} and {1 1 1} forms of the NaCl crystals coexisting in growth from pure aqueous solution. J Cryst Growth 2009; 311:399-403.

[35] Scherer GW. Crystallization in pores. Cem Concr Res 1999;29:1347-58.

[36] Cardell C, Benavente D, Rodríguez Gordillo J. Weathering of limestone building material by mixed sulfate solutions. Characterization of stone microstructure, reaction products and decay forms. Mater Charact 2008;59:1371–85.

[37] Kramar S, Mladenović A, Urosevic M, Mauko A, Pristacz H, Mirtič B. Deterioration of Lesno Brdo limestone on monuments (Ljubljana, Slovenia). RMZ – Mater Geoenviron 2010;57:53–73.

[38] Sing KSW, Everett DH, Haul RAW, Moscou L, Pierotti RA, Rouquérol J, Siemieniewska,T. Reporting physisorption data for gas/solid systems with special reference to the determination of surface area and porosity (recommendations 1984). Pure Appl Chem 1985;57:603–19.

[39] Ruiz-Agudo E, Mees F, Jacobs P, Rodríguez-Navarro C. The role of saline solution properties on porous limestone salt weathering by magnesium and sodium sulfates. Environ Geol 2007;52:269–81.

[40] Angeli M, Benavente D, Bigas J-P, Menéndez B, Hébert R, David C. Modification of the porous network by salt crystallization in experimentally weathered sedimentary stones. Mater Struct 2008;41:1091-108.

Chapter 8

Submitted to Geochimica et Cosmochimica Acta

In situ nanoscale observations of the dissolution of {10-14} dolomite cleavage surfaces

Maja Urosevic[1], Carlos Rodriguez-Navarro[1], Christine V. Putnis[2], Carolina Cardell[1], Andrew Putnis[2] and Encarnación Ruiz-Agudo[1,2]*

[1] Department of Mineralogy and Petrology, Faculty of Science, University of Granada, Campus Fuentenueva s/n, 18071 Granada, Spain.

[2] Institut für Mineralogie, Universität Münster, Corrensstrasse 24, 48149 Münster, Germany.

Article history

Submitted 19 April 2011

ABSTRACT

Knowledge of the kinetics and mechanisms of carbonate dissolution is essential, for instance, to determine the contribution of carbonate-fluid reactions to the global carbon cycle and CO_2 sequestration strategies, as well as to design new methods that mitigate the effects of weathering processes on carbonate stones. There is a significant lack of understanding of the molecular-scale reaction mechanisms of dolomite ($CaMg(CO_3)_2$), particularly in comparison to other common carbonates such as calcite ($CaCO_3$). Here we present a systematic *in situ* Atomic Force Microscopy (AFM) study of dolomite dissolution in the pH range 3-10 aimed at improving our understanding of the nanoscale processes governing dolomite-fluid interactions. The results of this study indicate that the overall dolomite dissolution rate is controlled by the removal of dolomite layers by spreading and coalescence of shallow etch pits, nucleated at point defects and/or in defect-free areas. Our results also suggest that at all pH (and particularly at pH < 5) and under conditions of relatively slow solution flow, dolomite dissolves via a dissolution-precipitation reaction with the formation of an Mg-rich surface precipitate. As a consequence, the effluent solution shows Ca/Mg ratios > 1. This explains why in the past the dolomite dissolution was considered to be "incongruent". *In situ*, direct observations of the reacting mineral surfaces are important to unambiguously ascertain the kinetics and mechanism of mineral dissolution. In fact, direct observations allow quantification of the kinetics of the process from the measurement of etch pit spreading rates, which are unaffected by the formation of a secondary precipitate whose existence has been neglected in the past.

KEYWORDS

Dolomite, incongruent dissolution, AFM, pH dependence, dissolution kinetics, dissolution-precipitation.

8.1. Introduction

Dissolution of carbonate minerals is one of the main chemical reactions occurring at shallow levels in the crust of the Earth and has a paramount importance for a wide range of geological and biological processes. In particular, carbonate dissolution plays a key role in a large spectrum of scenarios such as landscape modelling and carbonate aquifer development (i.e. Karst geomorphology, e.g. Ford and Williams, 2007), the chemistry of marine waters and global carbon cycle (Oelkers and Schott, 2005; Millero, 2007), in engineering science (e.g. carbonate dissolution enhances permeability and increases oil reservoir productivity, Lund et al., 1973), cultural heritage and building stone preservation (Bell, 1993; Charola and Ware, 2002; Cardell-Fernández et al., 2002; Hoke and Turcotte, 2004), and biomineralization (Mann, 2001). Calcite ($CaCO_3$), and to a lesser extent dolomite ($CaMg(CO_3)_2$), are the major carbonate minerals in sedimentary rocks. The dissolution of calcite has been thoroughly investigated over a range of conditions and solution compositions (see Morse et al., 2007 for a comprehensive review). In contrast, dolomite dissolution studies have been traditionally hampered by its low reaction rates compared to calcite and its poorly constrained relationship between cation ordering and reactivity (e.g. Morse and Arvidson, 2002; Lüttge et al., 2003).

Dolomite dissolution rate is a complex function of saturation state, pH, temperature, ionic strength, total dissolved carbonate, aqueous calcium and magnesium activities, organic and inorganic ligand concentration and hydrodynamic conditions (Busenberg and Plummer, 1982; Herman and White, 1985; Chou et al., 1989; Orton and Unwin, 1993; Pokrovsky and Schott, 2001; Pokrovsky et al., 2005; Gautelier et al., 2007). Most of these relationships have been derived experimentally by monitoring the evolution of the composition of the bulk solution using macroscopic flow-through or batch reaction devices. Direct observations of mineral growth and dissolution by real-time nanometer-resolution imaging techniques such as *in situ* Atomic Force Microscopy (AFM), Lateral Force Microscopy (LFM) and Vertical Scanning Interferometry (VSI) have proven to be critical for determining the mechanism and kinetics of mineral dissolution, as they facilitate a precise and representative analysis of mineral-water interactions (see for example Ruiz-Agudo et al., 2009 and refs. therein).

Despite the existence of several macroscopic studies dealing with dolomite dissolution, very little work has been done towards the understanding of the reactivity of dolomite interfaces at the molecular scale (Lüttge et al., 2003; Higgins and Hu, 2005; Hu et al., 2005; Kaczmarek and Sibley, 2007; Fenter et al., 2007; Higgins et al., 2007; Ruiz-Agudo et al., 2011). Although these nanoscale resolution studies have provided new insights into the kinetics and mechanisms of dolomite dissolution there is still a significant lack of understanding of the molecular-scale reaction mechanisms of dolomite, particularly in comparison to other common carbonates such as calcite (Fenter et al., 2007).

All previous nanoscale studies of dolomite dissolution rates have been conducted at fixed pH conditions and, to date, there is not a systematic study of the dependence of dissolution rates on pH as in the case of macroscopic flow-through or batch reaction experiments (e.g. Chou et al., 1989; Gautelier et al., 1999; Pokrovsky et al., 1999; Pokrovsky and Schott, 2001). Moreover, there is a significant scattering on the published data of macroscopic dolomite dissolution rates as a function of pH, in many cases due to the fact that these studies are performed under different hydrodynamic conditions, ionic strength and/or pCO_2. Nevertheless, all these works agree that the dolomite dissolution reaction is complex compared to other common carbonates such as calcite, aragonite or magnesite, as reflected for example in the determined fractional-order dependence of the dolomite dissolution rate on H^+ activity (at low pH and in the absence of CO_2) (c.f. Busenberg and Plummer, 1982; Chou et al., 1989; Orton and Unwin, 1993).

The aim of this paper is to present a systematic *in situ* AFM study of dolomite dissolution in the pH range 3-10 in order to improve our knowledge of the nanoscale processes governing dolomite-fluid interactions. Experiments were carried out far from equilibrium (no calcium, magnesium, bicarbonate or carbonate in the inlet solutions) and at low ionic strength. A better understanding of the kinetics and mechanisms of dolomite dissolution at different pH is essential, for instance, to determine the contribution of dolomite-fluid reactions to the global carbon cycle and CO_2 sequestration strategies (c.f. Oelkers and Schott, 2005; Gautelier et al., 2007), as well as to design new methods that mitigate the effects of acid rain on carbonate stone.

8.2. Methodology

8.2.1. Atomic force microscopy (AFM)

High purity, optical grade dolomite crystals from Eugui, Navarra (Spain) were cleaved with a knife blade to obtain mm-size (ca. 3 × 3 × 1 mm) fragments. Crystallinity of the sample was checked previously by powder X-ray diffraction (XRD) that showed the presence of strong cation ordering (or superstructure) reflections (i.e., those with indexes (*h0l*) and (*0kl*), with odd-numbered l, such as (101), (015), and (107); Lipmann, 1973) confirming its crystalline perfection. Due to its chemical purity and crystalline perfection dolomite single crystals from this locality in Navarra have been used in several studies of dolomite dissolution (e.g., Busenberg and Plummer, 1982; Orton and Unwin, 1993; Lüttge et al., 2003). AFM *in situ* dissolution experiments were carried out by passing solutions of fixed pH over dolomite $\{10\bar{1}4\}$ cleavage surfaces. Solutions used in the experiments were prepared using double-deionized water (resistivity > 18 $m\Omega^{-1}$) and the solution pH was adjusted from 3 to 10 using HCl or NaOH. Each solution was prepared immediately before the experiment to avoid equilibration with the ambient air, especially at higher pH values. Therefore, the amount of carbonate and bicarbonate ions in solution is considered to be negligible. The absence of calcium and magnesium in the input solutions ensured constant far-from-equilibrium conditions with respect to dolomite. *In situ* observations and measurements were performed using an AFM equipped with a fluid cell of a Digital Instruments Nanoscope III Multimode AFM working in contact mode under ambient conditions (T = 20 ºC). The solutions flowed continuously for 30 min at ca. 100 mL h^{-1} 120 from a syringe coupled to an O-ring-sealed fluid cell containing the sample crystal. The scanned areas were typically 9 (3 × 3) μm^2. AFM images were collected using Si_3N_4 tips (Veeco Instruments, tip model NP-S20) and analyzed with the Nanoscope software (Version 5.12b48). Measurements of step retreat velocity (or etch pit spreading rate, v_{sum}) were made from sequential images scanned in the same direction. The retreat velocity given by $v_{sum} = (v_+ + v_-)$, where v_+ and v_- represent the retreat velocities of + and - steps, respectively (see Paquette and Reeder (1995) for a comprehensive description of the morphology and nomenclature of rhombohedral carbonate etch pits). v_{sum} values were calculated by

measuring the length increase per unit time between opposite parallel steps in sequential images. Overall dissolution rates, R_{AFM} (in mol cm^{-2} s^{-1}), were calculated as follows: if there are N_{pit} etch pits per square centimeter of surface, then for a shallow rhombohedral etch pit, the volume loss (ΔV) after the time between two sequential images t_2-t_1, can be approximated by

$$\Delta V = (w_2 \cdot u_2 - w_1 \cdot u_1) \cdot h \qquad (1)$$

where *w*, *u* and *h* are the etch pit width, length and depth, respectively, in sequential images after that time duration, $t_2 - t_1$. Therefore, the overall dissolution rate (mol cm^{-2} s^{-1}) can be calculated as

$$R_{AFM} = \frac{\Delta V \cdot N_{pit}}{V_{dol} \cdot (t_2 - t_1)} \qquad (2)$$

where V_{dol} is the molar volume of dolomite (64.34 cm^3 mol^{-1}). N_{pit} used in the calculation of the overall dissolution rates is the average observed for each experiment.

Additionally, after flowing through the fluid cell 10 mL aliquots of effluent solution were collected for calcium and magnesium analysis by inductively coupled plasma optical emission spectrometry, ICP-OES (Varian Vista proaxial). In flow through experiments performed in AFM, variations and uncertainties related to the reacting surface area contribute to significant error in macroscopic rate determinations, leading to an overestimation of macroscopic dissolution rates (Duckworth and Martin, 2004; Ruiz-Agudo et al., 2010, 2011). The very low amount of calcium and magnesium in the outlet solution (a few mmol L^{-1}) precludes obtaining reliable concentration values (Arvidson et al., 2006). Nevertheless, here we present a few selected measured values of macroscopic dissolution rates only for comparison purposes. Macroscopic dissolution rates of dolomite, R_{MAC} (mol cm^{-2} s^{-1}) were calculated as follows:

$$R_{MAC} = \frac{Ca_T Q}{A} \qquad (3)$$

where Ca_T is the total calcium in the effluent solution (mol L^{-1}), Q is the solution flow rate (L s^{-1}) and A is the geometric surface area of dolomite exposed to the solution (cm^2).

8.2.2. Analysis of surface precipitates

AFM flow-through experiments were reproduced at macroscale and after flowing deionized water (pH 2.84) over the crystal for 30 minutes (flow rate of ca. 100 mL h^{-1}) the crystals were analyzed by X-ray diffraction (XRD), using a Philips PW XPERT-PRO diffractometer (Department of Mineralogy and Petrology, University of Granada). In order to maximize the signal from the thin surface layer of the precipitate and minimize the penetration depth of the X-rays into the dolomite substrate, data were obtained in grazing incident angle mode (GIAXRD), by carrying out 2θ scans at a fixed small incident angle of the X-ray beam on the substrate surface. Analysis conditions were: radiation Cu Kα (λ: 1.5405 Å), 45 kV voltage, 40 mA current intensity, and goniometer speed of 0.01º 2θ/s using Si-detector X'Celerator. The grazing angle (ω) was 2º and the investigated area between 5º and 60º 2θ. The study of diffractograms was performed using the computer program X'Pert Plus V.1.0 (1999, PANalytical). The crystals were also analyzed by X-ray photoelectron spectroscopy (XPS). We used a Physical Electronic PHI 5701 spectrometer equipped with a multi-channel hemispherical electroanalyzer. Non-monochromatic Mg Kα X-ray radiation (300 W, 15 kV, 1253.6 eV) was 173 used as the excitation source. The spectrometer energy scale was calibrated using Cu 2p3/2, Ag 3d5/2, and Au 4f7/2 photoelectron lines at 932.7, 368.3 and 84.0 eV, respectively. The binding energy of photoelectron peaks was referenced to C 1s core level for adventitious carbon at 284.8 eV. High resolution spectra were recorded at a given take-off angle of 45º by a concentric hemispherical analyzer operating in the constant pass energy mode at 29.35 eV and using a 400 μm diameter aperture. The residual pressure in the analysis chamber was maintained below 1.33 x 10^{-7} Pa during spectra acquisition. The PHI ACCESS ESCA-V8.0C software package was used for acquisition and data analysis. Recorded spectra were fitted using Gauss-Lorentz curves in order to accurately determine the binding energy of the different element core levels. After a Shirley-type background subtraction, atomic concentration percentages of the dolomite elements were determined from high-resolution spectra and the corresponding area sensitive factor for

every photoelectron line was taken into account (Moulder et al., 1992). Survey and multiregion spectra were recorded for C 1s, O 1s, Ca 2p and Mg 2p photoelectron peaks. A depth profiling (up to 6 nm deep) was carried out by 4 keV Ar^+ bombardment. The at-depth scale of 3 nm min^{-1} is assumed to be equivalent to the sputter rate of Ta_2O_5 under the same sputter conditions. Differences in sputtering yield between the sample under study and Ta_2O_5 were not considered. Additionally, the microscopic surface features of dolomite crystals subjected to dissolution were observed using an optical microscope (Olympus BX60) equipped with a digital microphotography unit (Olympus DP10). Observations were performed both under transmitted and reflected (polarized) light.

8.3. Results and discussion

8.3.1. General features of dolomite dissolution

Dolomite dissolved on $\{10\bar{1}4\}$ cleavage surfaces by the formation and spreading of etch pits after the injection of highly undersaturated solutions into the fluid cell. Immediately after injection, the dolomite surface developed shallow (~ 0.3 nm height) rhombohedral pits at all values of pH tested (Fig. 1). This etch pit morphology is typically observed in other carbonates such as calcite during dissolution studies. Angles between steps delimiting etch pits were found to be ~77° and ~103°. The length ratio of the rhombus diagonals was found to be 0.92 ± 0.05, which differs from the value (~0.72) observed in the regular rhombohedral etch pits formed at all pH values on cleavage surfaces of single-cation $R\bar{3}c$ carbonates such as calcite and rhodochrosite ($MnCO_3$) (e.g. Pérez-Garrido et al., 2007). These distorted rhombohedral etch pits were typically less than 200 nm wide before they coalesced and a one unit-cell layer was removed. Then new etch pits nucleated and spread, repeating the process (Fig. 2). The measured etch pit density was approximately constant from pH 3 to pH 10 and equal to $1.94 \cdot 10^9$ ($\pm$ $0.25 \cdot 10^9$) cm^{-2} , which is ca. 4 orders of magnitude higher than that observed by Lüttge et al. (2003) at acidic pH (~ 3) conditions using VSI. However, their study focused on deep etch pits (depth up to 2 μm), most probably nucleated at dislocations (McInnis and Brantley, 1992). The observed average values of nucleation density were

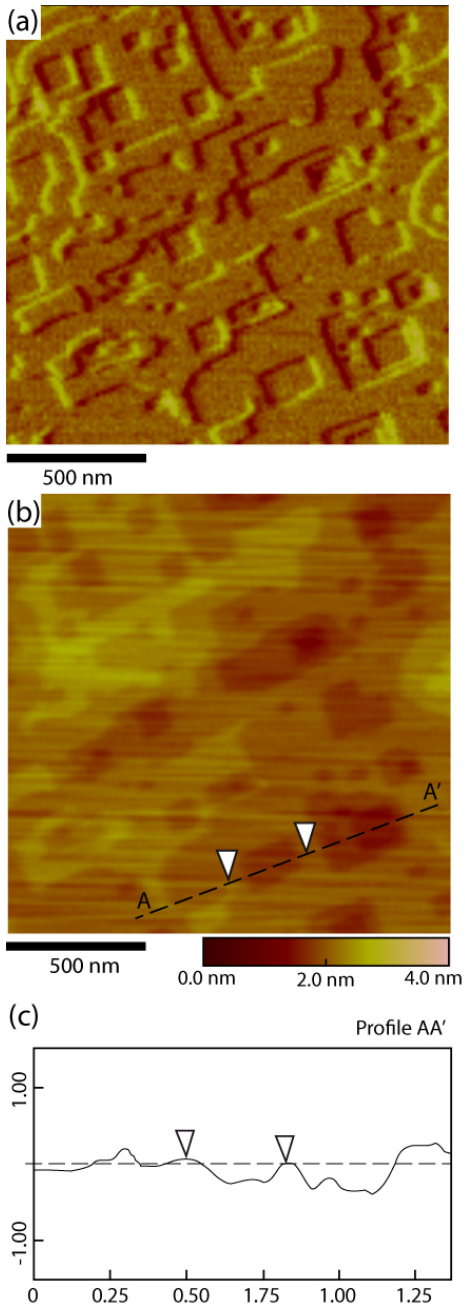

Figure 1. AFM deflection **(a)** and topographic **(b)** images showing shallow, rhombohedral etch pits developed on $\{10\bar{1}4\}$ dolomite surface at pH 8. **(c)** Depth profile in section AA' of the corresponding topographic image.

roughly one order of magnitude higher than those generally reported for calcite during dissolution in pure, deionized water (Teng, 2004; Ruiz-Agudo et al., 2009). Shallow etch pits, such as those observed here during dolomite dissolution, nucleate at point defects (McInnis and Brantley, 1992) as well as on defect-free surfaces, provided a sufficiently high undersaturation is reached (Teng, 2004; Ruiz-Agudo et al., 2009). Examination under the optical microscope of Eugui dolomite single crystals subjected to dissolution (pH 3) showed the formation of scarce (~ $0.5 \cdot 10^4$ cm^{-2}) deep rhombohedral etch pits (Fig. 3). However, such deep etch pits were not present after flowing the acid solution for 30 min, but only visible after long term (> 48 h) dissolution (pH 3) in a batch reactor. The measured low density of deep etch pits is consistent with the low density of dislocations in Eugui dolomite (Barber et al., 1981). The lower density of line defects in Eugui dolomite compared with calcite (ca. 10^6 cm^{-2}; Bisschop et al., 2006) may explain why deep etch pits are rarely observed here as well as in other dissolution studies where Eugui dolomite crystals have been used (e.g.,

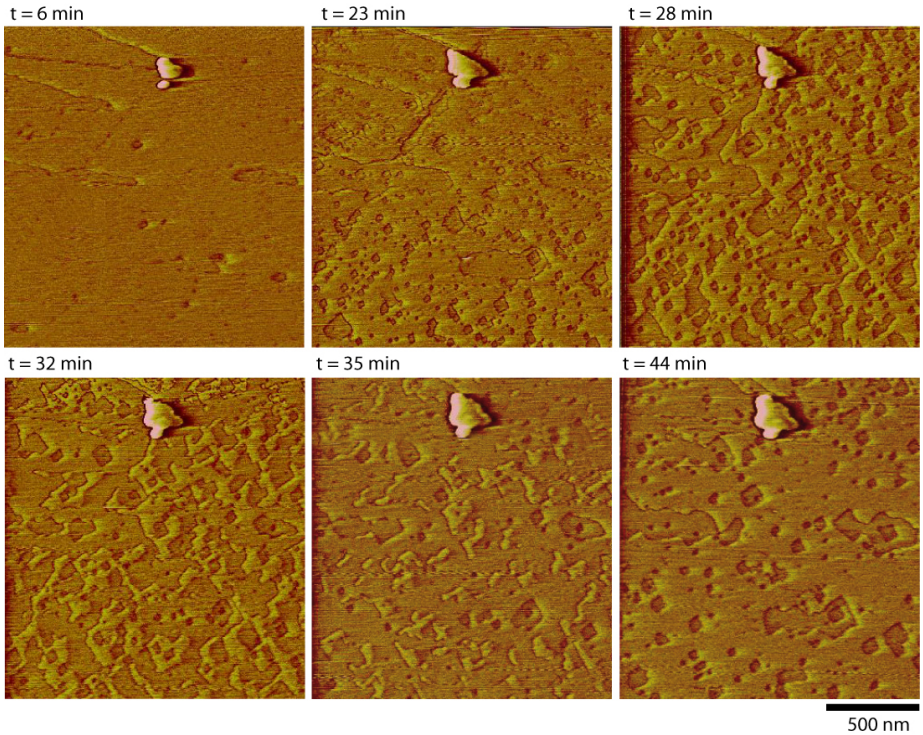

Figure 2. AFM deflection images of a dolomite (10-14) surface exposed to deionized water for increasing periods of time. Average etch pit depth ~ 0.3 nm. Note the complete removal of an atomic layer after 35 min. and the nucleation and spreading of new shallow pits in the newly exposed layer after 44 min.

Ruiz-Agudo et al., 2011). In contrast, shallow etch pits were highly abundant and their nucleation and spreading appeared to control the dissolution of dolomite.

Overall, dolomite dissolution shows characteristics of both Type I (Ca, Mn) and Type II (Fe, Mg) carbonates, according to the classification of Duckworth and Martin (2004). Flat surfaces with well-formed shallow etch pits such as those observed in our dissolution experiments are typically reported during dissolution of stoichiometric and well-ordered dolomite (Kaczmarek and Sibley, 2007). The observation of aspect ratios different from that of the perfect rhombohedrom can be explained considering the lower symmetry of dolomite structure if compared with that of calcite. Dolomite crystallizes in the space group $R\bar{3}$, which differs from the $R\bar{3}c$ space group of calcite-type carbonates in the lack of the c-glide and diad axes (Reeder, 1983). Thus, the two obtuse steps are structurally different, as well as

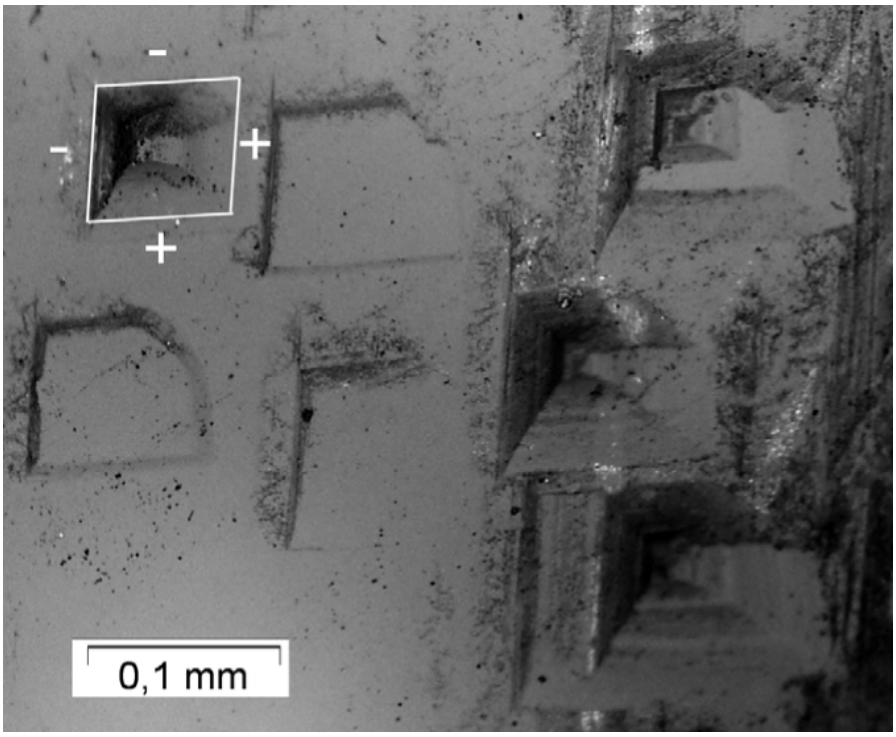

Figure 3. Reflected light optical microscopy image of the dolomite (10-14) surface exposed to pH 3 solution for 48 h. Deep rhombohedral etch pits are observed (the acute – and obtuse + step edges are indicated).

the acute steps (Fig. 4). Therefore, the etch pits may show non-regular rhombohedral geometries (Higgins and Hu, 2005). Due to the lower symmetry of dolomite if compared with calcite, four distinct step velocities are needed to define the spreading of the etch pits formed on dolomite cleavage surfaces (Higgins and Hu, 2005). However, differences found between etch pit spreading rates along $[\bar{4}41]$ and $[48\bar{1}]$ directions (Fig. 4) were within the experimental error of the measurements and thus the etch pit spreading rate values, v_{sum}, reported in this work refer on average to the rate of change in etch 247 pit length along either $[\bar{4}41]$ or $[48\bar{1}]$ directions.

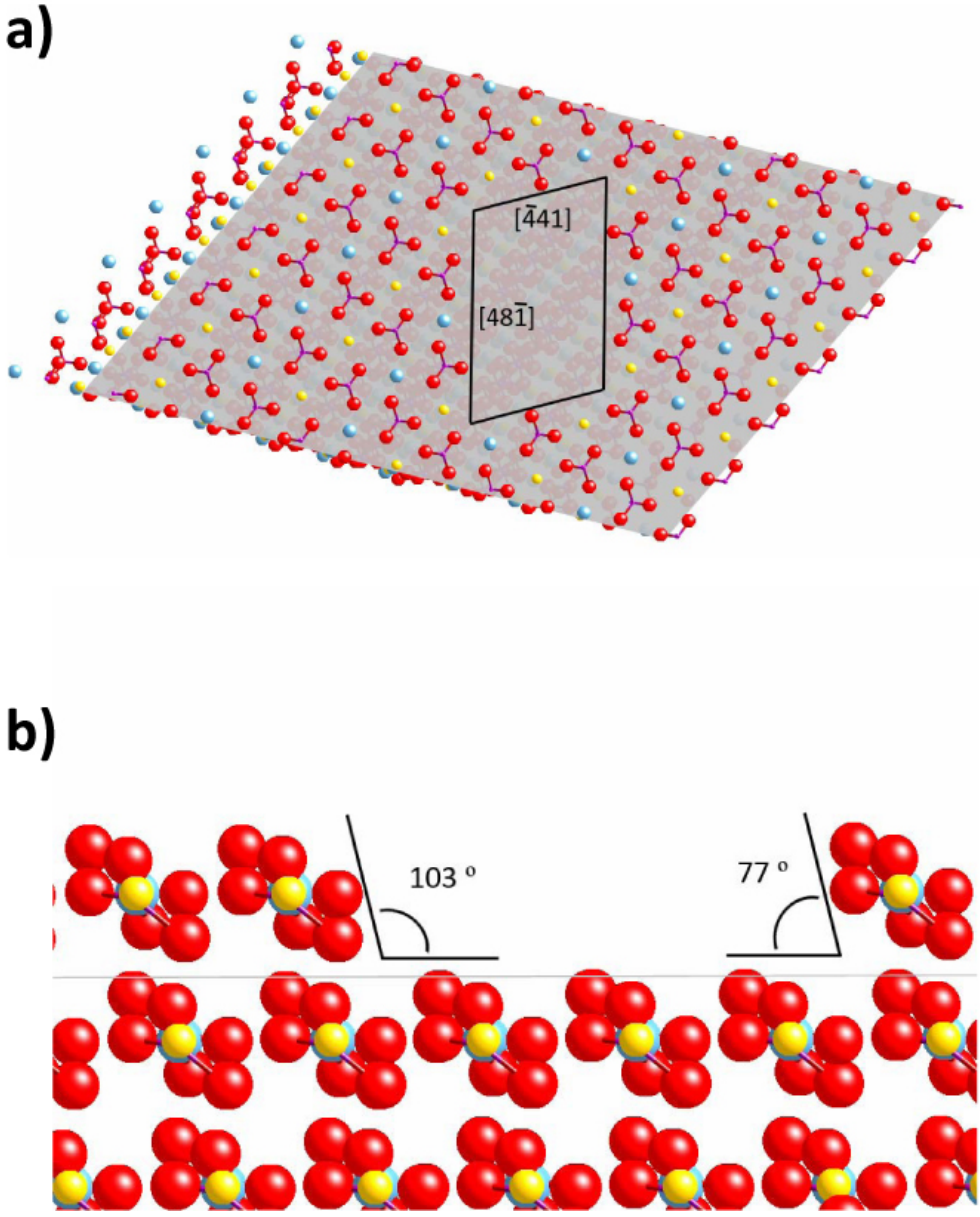

Figure 4. (a) Normal view of the atomic arrangements in the cleavage plane of dolomite. **(b)** Sketch showing a cross-section of an etch pit, with the obtuse and acute step edges indicated. Color code: calcium (blue), magnesium (yellow), oxide (red), carbon (purple).

8.3.2. Dissolution kinetics: comparison with previous dissolution studies

Table 1 shows etch pit spreading rates (v_{sum}) as well as overall dissolution rates (R_{AFM}) calculated from AFM measurements according to equations (1) and (2) for the different pH values tested. Ca and Mg concentrations in the outflow solutions are also shown in Table 1. Non-stoichiometric Ca/Mg ratios were found (i.e. Ca/Mg in the effluent solution was different from that of the solid). This observation will be further discussed in Section 8.3.3. To compare with R_{AFM}, macroscopic dissolution rates (R_{MAC}) were calculated according to equation (3) using Ca concentrations in the outlet solutions (Table 1).

Table 1. Etch pit spreading rates (v_{sum}), density of etch pits and overall dissolution rates (R_{AFM}) on dolomite cleavage surface as a function of pH, and concentrations of Ca^{2+} and Mg^{2+} in the outlet solutions and bulk dissolution rates (R_{MAC})

pH	V_{sum} (nm s^{-1})	Density (nm^{-2})	R_{AFM} (mol cm^{-2} s^{-1})	Ca^{2+} (mg L^{-1})	Mg^{2+} (mg L^{-1})	R_{MAC} (mol cm^{-2} s^{-1})
3	0.0885 ± 0.0012	17.26	$16.80\ 10^{-13} \pm 3.05\ 10^{-13}$	2.455	0.018	$3.420\ 10^{-9}$
4	0.0615 ± 0.0017	17.61	$10.40\ 10^{-13} \pm 1.95\ 10^{-13}$	0.475	0.002	$0.658\ 10^{-9}$
5	0.0538 ± 0.0021	15.96	$9.21\ 10^{-13} \pm 2.32\ 10^{-13}$	0.170	0.000	$0.237\ 10^{-9}$
7	0.0581 ± 0.0036	22.51	$7.42\ 10^{-13} \pm 1.62\ 10^{-13}$	0.195	0.001	$0.272\ 10^{-9}$
8	0.0473 ± 0.0016	18.48	$9.28\ 10^{-13} \pm 2.66\ 10^{-13}$	0.145	0.000	$0.202\ 10^{-9}$
9	0.0441 ± 0.0014	22.04	$8.43\ 10^{-13} \pm 2.19\ 10^{-13}$	0.160	0.000	$0.223\ 10^{-9}$
10	0.0448 ± 0.0014	18.98	$8.81\ 10^{-13} \pm 2.47\ 10^{-13}$	0.010	0.000	$0.014\ 10^{-9}$

Figure 5a summarizes some of the dolomite dissolution rate data published in the literature. In the present study, R_{AFM} of dolomite in deionized water (neutral pH) was found to be $7.42 \cdot 10^{-13}$ ($\pm$ $1.62 \cdot 10^{-13}$) mol cm^{-2} s^{-1}. As can be seen in Fig. 5a, R_{AFM} values were nearly pH-independent in the range 5 to 10, while a slight increase in R_{AFM} values was observed at pH < 5. The spreading rate showed a similar trend, with a tendency to increase for pH < 5 (Fig. 5b).

To our knowledge only three previous studies have explored the kinetics of dolomite dissolution at the micro- and nanoscale. Ruiz-Agudo et al. (2011) carried out a systematic study of ion-specific effects on dolomite dissolution using *in situ* AFM, showing that

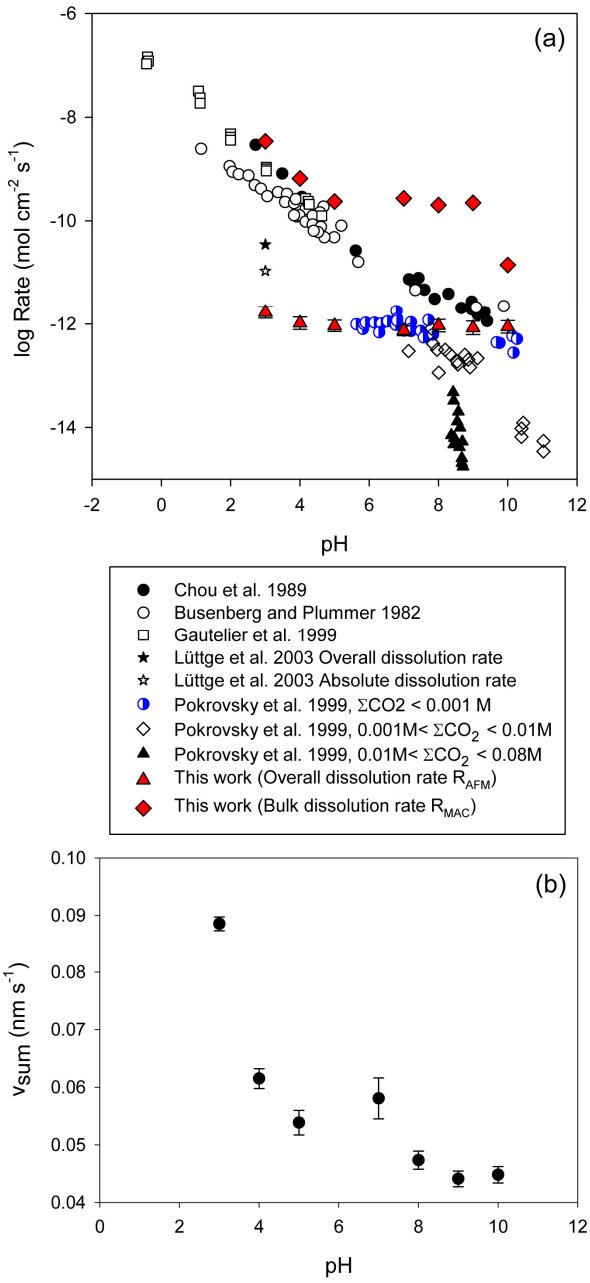

Figure 5. (a) Comparison of AFM-derived (R_{AFM}) and macroscopic (R_{MAC}) dolomite dissolution rates of the present work with those obtained from previous studies as a function of pH. **(b)** Etch pit spreading rates, v_{sum}(nm s^{-1}) on dolomite cleavage surfaces as a function of pH.

different electrolytes modify dolomite dissolution kinetics, expressed as etch pit spreading rates, when compared with pure deionized water. Trends observed for the different electrolytes can be interpreted in terms of characteristic parameters of background ions, according to the way in which these electrolytes modify solute hydration and water structure dynamics. The etch pit spreading rate in deionized water (pH = 7) reported in that paper (0.09 ± 0.01 nm s^{-1}) is of the same order of magnitude than that found in the present study (0.0581 ± 0.0036 nm s^{-1}).

Hu et al. (2005) performed an *in situ* AFM study of the reactivity of cleavage surfaces of dolomite. However, they reported dissolution rates that cannot be directly compared with our data, as they worked under different conditions of undersaturation. They obtained values for v_{sum} and R_{AFM} of 3.4 nm h^{-1} (0.0012 nm s^{-1}) and 4.4·10^{-15} mol cm^{-2} s^{-1} (SI = -2.98) and 1.2 nm h^{-1} (0.0003 nm s^{-1}) and 1.5·10^{-15}

mol cm^{-2} s^{-1} (SI = -1.17), at high pH (9) and 0.01 ionic strength (NaCl). The overall dolomite R_{AFM} dissolution rate measured at pH 3 in our study (calculated from etch pit density and spreading rate) is ca. 25 times lower than that reported at the same pH by Lüttge et al. (2003) determined using VSI ($4 \cdot 10^{-11}$ mol cm^{-2} s^{-1}). This difference is not unexpected, as they measured dissolution rates in deep etch pits most probably originated at dislocations which represent regions of unusually high strain. The same authors calculated an absolute dissolution rate from surface retreat of $1.08 \cdot 10^{-11}$ mol cm^{-2} s^{-1}. This value is closer to our measured value. Lüttge et al. (2003) compared their rate values with some published bulk measurements, such as those determined by Busenberg and Plummer (1982), Chou et al. (1989) and Gautelier et al. (1999), showing clear disagreements between them (bulk values were between one and two orders of magnitude higher than that obtained by VSI). Our macroscopic dissolutions rates (R_{MAC}), show similar disagreement with Lüttge at al. (2003) VSI measurements, as well as with our own R_{AFM} values (Fig. 5a). As Lüttge at al. (2003) indicated, there are several reasons for the disagreement between bulk/macroscopic and nanoscale dissolution rates, including errors associated with the normalization of rates by inferred geometric areas and the use of mineral powders which are likely to expose highly reactive surfaces to the solution (see also Lüttge, 2005).

Pokrovsky et al. (1999) and Pokrovsky and Schott (2001) performed a comprehensive study of dolomite dissolution using mixed-flow reactors under different conditions of pH, ionic strength (NaCl) and undersaturation. These authors showed that below ca. pH 5.4, dissolution rates increase with decreasing pH whereas above this value they are pH independent in CO_2-poor solutions and decrease sharply with increasing pH in CO_2 enriched solutions. Under conditions of circumneutral to alkaline pH, low ionic strength (0.001) and low total dissolved carbonate (< 0.001 M), they obtained values which are in remarkably good agreement with the R_{AFM} values reported in our study (see Fig. 5a). This agreement between macroscopic and AFM-calculated dissolution rates seems to indicate that the removal of dolomite layers by spreading and coalescence of shallow etch pits controls the overall dolomite dissolution rate and that the contribution of step retreat from deep pits is limited (under neutral to slightly alkaline pH conditions).

Mineral dissolution rates can be determined by the kinetics of the surface reaction and/or the mass transport of the dissolved species from the crystal surface towards the bulk. The slowest of these processes will control the dissolution rate. It is generally accepted that, in contact with the mineral surface and separating it from the well-mixed, turbulent bulk solution, there is a "boundary layer" with a different composition from the bulk (Putnis et al., 2005). If the solution flow is slow, this boundary layer is thick and the time for the solutes to be transported through the layer is long and it can become the rate-limiting step in the dissolution process (Liu and Dreybrodt, 2001). Although the early macroscopic studies of dolomite dissolution (such as those published by Lund et al., 1973; Busenberg and Plummer, 1982 and Chou et al., 1989) suggested that the kinetics of the dissolution process is controlled by the surface reaction even at low pH (Orton and Unwin, 1993), later studies have shown that, as in the case of calcite, the kinetics of dolomite dissolution is diffusion controlled at acidic pH. Orton and Unwin (1993) provided evidence of mass-transport control on dolomite dissolution rates at low pH, even at fast flow rates (up to 0.125 $cm^3\ s^{-1}$ in their channel-flow set up). Liu and Dreybrodt (2001) showed that the presence of a diffusion boundary layer in contact with the mineral surface can significantly reduce dolomite dissolution rates. Furthermore, some of the studies reporting surface control on the kinetics of dolomite dissolution, such as those by Herman and White (1984) and Chou et al. (1989), were performed under conditions of high partial pressure of CO_2 ($pCO_2 > 1$ atm). However, it has been suggested that, for low partial pressures of CO_2, the mechanism controlling the kinetics of the reaction is different, and the rates become mass-transport controlled (Liu and Dreybrodt, 2001). All in all, these observations give evidence of the relevance of mass transport and the diffusion boundary layer during the dissolution of dolomite at acidic pH.

Mass transport control on dissolution rates (reflected as a flow rate dependence on the velocity of step spreading) at acidic pH (< 5.3) has been reported for other carbonates, such as calcite, up to flow rates of 119 mL h^{-1} in AFM experiments (Shiraki et al., 2000). In the case of dolomite, this threshold could be even higher, considering that Mg^{2+} diffuses at slower rates than Ca^{2+} in aqueous solutions due to its stronger hydration (diffusion coefficients: Ca^{2+}, 0.40 to $0.55 \cdot 10^{-5}$ $cm^2\ s^{-1}$ and Mg^{2+} 0.45 to $0.60 \cdot 10^{-5}$ $cm^2\ s^{-1}$, depending on the ion-water potential model used in the calculation; the experimental values are 0.71 and

$0.79 \cdot 10^{-5}$ cm^2 s^{-1} for Mg^{2+} an Ca^{2+}, respectively – Guárdia et al., 1999). Therefore, under our experimental conditions, and despite the fact that we used a relatively high flow rate of ca. 100 mL h^{-1} (a value double that used by Ruiz-Agudo et al., 2009, to fully ensure a reaction-controlled mechanism in the case of calcite dissolution), it seems that the dolomite dissolution reaction is mass transport controlled at acidic pH.

8.3.3. Surface precipitates during the "incongruent" dissolution of dolomite

The dissolution of dolomite was accompanied by nucleation of a new phase on the dolomite surface (Fig. 6). This could well explain why Ca/Mg ratios in the effluent solution were different than that of the solid and much higher than 1, which itself suggests that the precipitating phase was a Mg-rich carbonate. The precipitation of this secondary phase was particularly evident at acidic pH (pH 3 and 4). The precipitated nuclei or three-dimensional islands rarely showed well-defined straight edges and reached a thickness of 2.2 ± 0.3 nm during the very early stages of their formation. The growth of this new phase occurred by lateral spreading of the 3D islands leading eventually to their coalescence, without a significant increase in their height, that remained approximately constant during the whole growth process. Initially, the growth of this layer avoided the areas where etch pits previously existed, leading to the formation of a surface that reproduced the original dolomite surface.

One frequent source of divergence between dissolution rates determined in bulk and nanoscale experiments could arise from the fact that dissolution rates obtained from solution chemistry may be influenced by dolomite "incongruent" or "non-stoichimetric" dissolution. Several macroscopic dissolution studies have reported non-stoichiometric dissolution of dolomite, particularly in the first stages of the dissolution experiments (i.e., during the removal of up to two atomic layers of the solid surface). Busenberg and Plummer (1982) and later Pokrovsky and Schott (2001) and Zhang et al. (2006) suggested that preferential dissolution of the Ca-component and the formation of a Ca-depleted surface could explain the fact that Ca/Mg ratios in solution were initially higher than those of the bulk solid. The preferential release of the calcium component to the solution was explained on the basis of

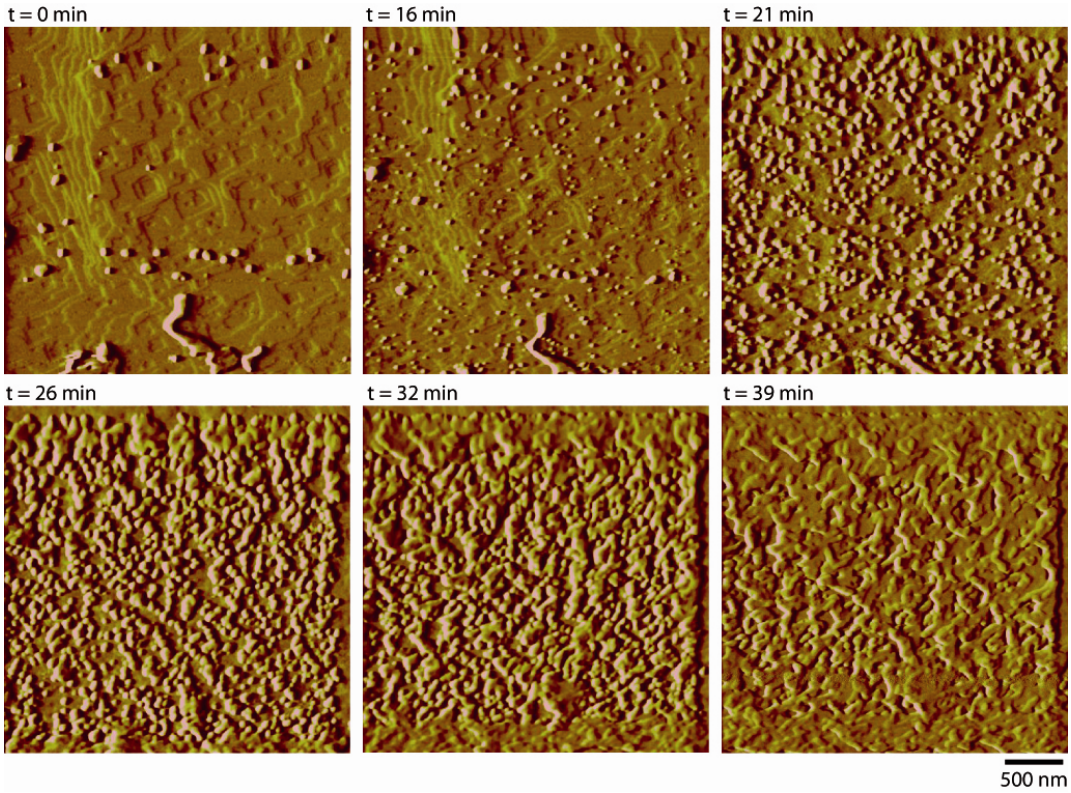

Figure 6. Sequential AFM deflection images showing the formation of a Mg-rich phase on a dolomite cleavage surface at pH 3.

the much lower hydration energy of Ca^{2+} if compared with Mg^{2+} and thus its lower stability at the dolomite/water interface (Pokrovsky and Schott, 2001). A similar mechanism has been proposed to explain the non-stoichiometric dissolution behavior of other minerals, such as wollastonite ($CaSiO_3$), although in this case the possibility of a precipitation event was not ruled out (Green and Lüttge, 2007). However, from our *in situ*, nanoscale observations of the reacting surface we found no experimental evidence that supports the hypothesis of a preferential release of calcium. Moreover, our AFM results clearly indicate that this "incongruent" behavior (non-stoichiometric dissolution) is the result of a dissolution-precipitation process, as reflected in the height profiles shown in Figure 7, where the newly-formed topographic features are clearly the result of a growth process.

According to our observations, dolomite dissolution occurs at step edges parallel to $<\bar{4}41>$, and dissolution at such step edges is a stoichiometric process, i.e. equal amounts of

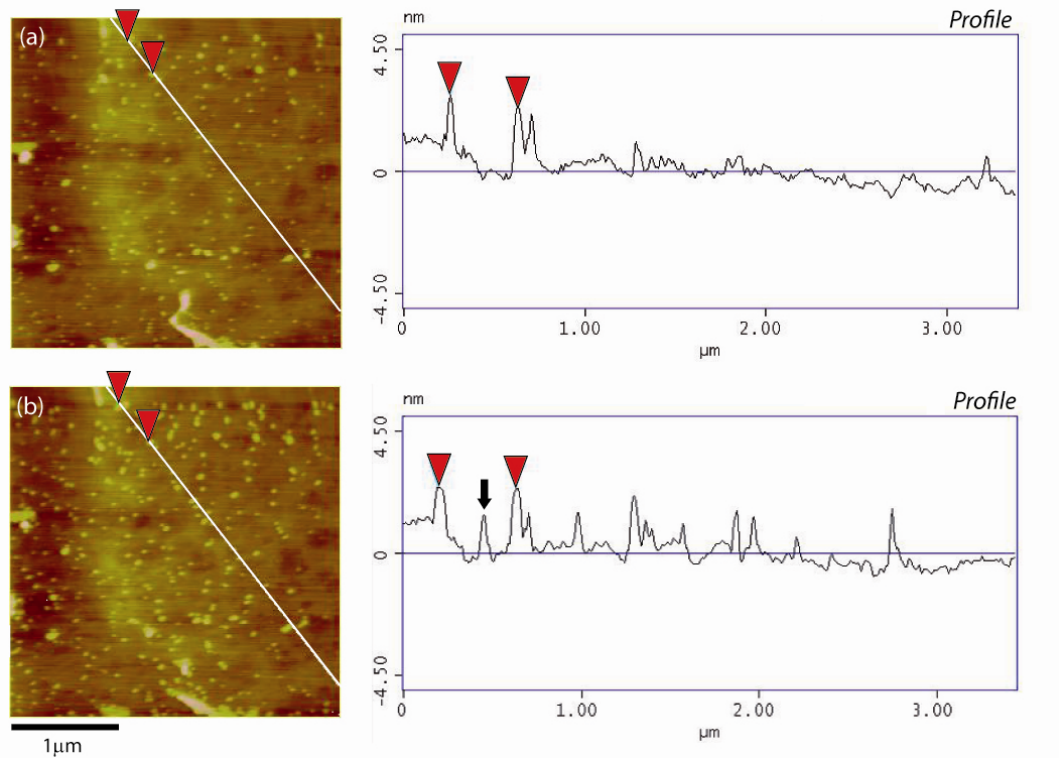

Figure 7. Sequential AFM height images showing the formation of surface precipitates.The depth profiles show the upward growth (i.e., height increase indicated with black arrow) of such a newly formed phase. The time lapse between images is 104 s.

Ca^{2+} and Mg^{2+} are present along such steps and thus are equally released to the solution as the steps spread. Hu et al. (2006) indicated that a possible pathway for the generation of Mg-enriched surfaces during dolomite dissolution could be the preferential detachment of calcium ions from terraces, generating point defects at these flat surfaces. Etch pits would immediately nucleate at these defects, and in fact this could possibly explain the higher etch pit density observed in the case of dolomite compared to calcite. However, this would just be a transient stage, and the immediate spreading of these newly formed etch pits would lead to stoichiometric dissolution. Nevertheless, it is plausible that the detachment, hydration (Hu et al. 2006) and/or diffusion to the bulk of the magnesium ions adsorbed at the dolomite surface is sufficiently slow to result in a magnesium enrichment of the dolomite surface or the solution layer immediately in contact with the surface. This is supported by the lower rate of desorption and smaller diffusion coefficient (Guárdia et al., 1999), as well as the higher residence time at the mineral/solution interface (Kerisit and Parker, 2004) of magnesium if

compared with calcium. All in all, any of these effects could lead to the development of steep concentration gradients close to the surface of the mineral, as observed by Putnis et al. (2005) during mineral dissolution/replacement reactions using real time phase-shift interferometry. The authors reported that dissolution of a parent phase (KBr) in a saturated KCl solution results in an interfacial fluid layer that is supersaturated with respect to a different solid composition (K(Br,Cl)), while the bulk solution is undersaturated with respect to such a phase. As a result, a tightly coupled dissolution/precipitation reaction at the mineral-fluid interface occurs. In our system, supersaturation with respect to a secondary Mg-rich phase could have been locally reached following the formation of a similar interfacial fluid layer with composition different from the bulk, leading to the eventual formation of such a surface precipitate. If dolomite dissolves and instantaneously equilibrates with the bulk solution, thermodynamic calculations performed using PHREEQC indicate that the bulk solution is undersaturated with respect to all possible phases except magnesite ($MgCO_3$). Due to the short contact time between the solid and the fluid in our flow-through set up, equilibrium with respect to dolomite is not expected to be reached and this is just considered as a reference or threshold case for our experiments. It is well known that, despite being the stable Mg-carbonate form, the precipitation of magnesite under normal P-T conditions of the Earth surface is virtually impossible (Hänchen et al., 2008). Thus the formation of this phase may be disregarded in our experiments. Mg-carbonate precipitation is strongly kinetically controlled, and it has been suggested that the highly hydrated character of the Mg^{2+} ion in aqueous solution is responsible for the difficulty in precipitating anhydrous Mg-bearing carbonates (magnesite and dolomite) (Sayles and Fyfe, 1973). Most commonly, nesquehonite ($MgCO_3 \cdot 3H_2O$), hydromagnesite ($(MgCO_3)_4 \cdot Mg(OH)_2 \cdot 4H_2O$) and landsfordite ($MgCO_3 \cdot 5H_2O$) are formed in laboratory studies under ambient conditions (see for example Hänchen et al., 2008 and refs. therein). The scarcity of well formed peaks in the XRD pattern of dolomite crystals treated with HCl aqueous solutions (pH 3) obtained by the grazing incident angle method (GIAXRD) precludes the unambiguous identification of the Mg-rich phase formed. However, the peaks present in the XRD pattern shown in Figure 8 match those of nesquehonite. Unfortunately, this could not be fully confirmed by XPS (Table 2), possibly due to the low percentage of the dolomite surface covered by this secondary phase. The XPS results nevertheless confirm the

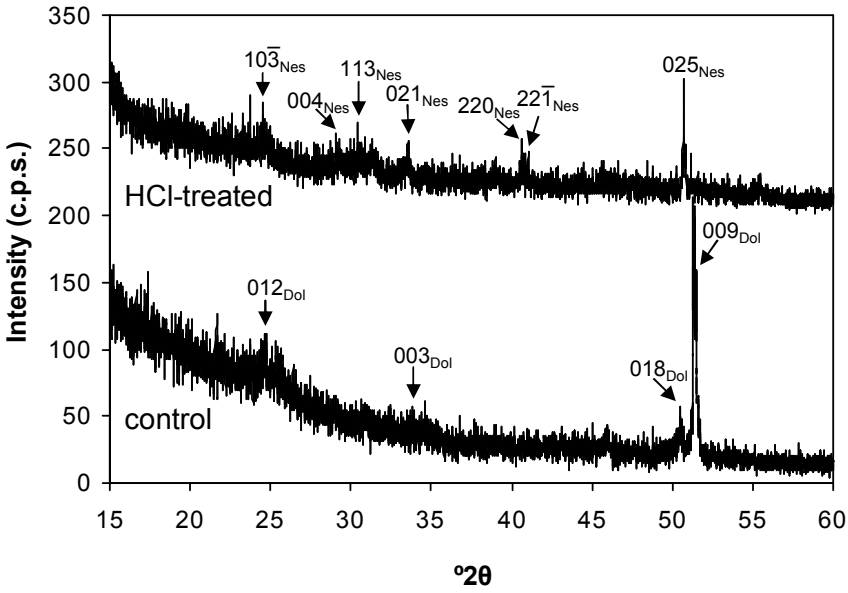

Figure 8. Grazing angle X-ray diffraction patterns of dolomite (10-14) surface before dissolution (control) and following dissolution at pH 3 (HCl-treated). Bragg peaks of dolomite (hkl_{dol}) and nesquehonite (hkl_{nes}) are indicated.

purity and stoichiometry of the dolomite used in our experiments. As stated above, development of a concentration gradient and magnesium enrichment at the dolomite/solution interface is likely to occur, resulting in the fluid being locally supersaturated with respect to nesquehonite. Supersaturation with respect to other phase/s could also be reached at the interface, but the precipitation of this/these other phase/s may be kinetically unfavorable for unknown reasons.

Table 2. Ca/Mg atomic ratios measured by X-ray photoelectron spectroscopy (XPS) in raw and partially dissolved samples as a function of depth.

Depth	Dolomite Control	Dolomite HCl
surface	0.924	0.935
3 nm	0.999	0.996
6 nm	1.058	1.014

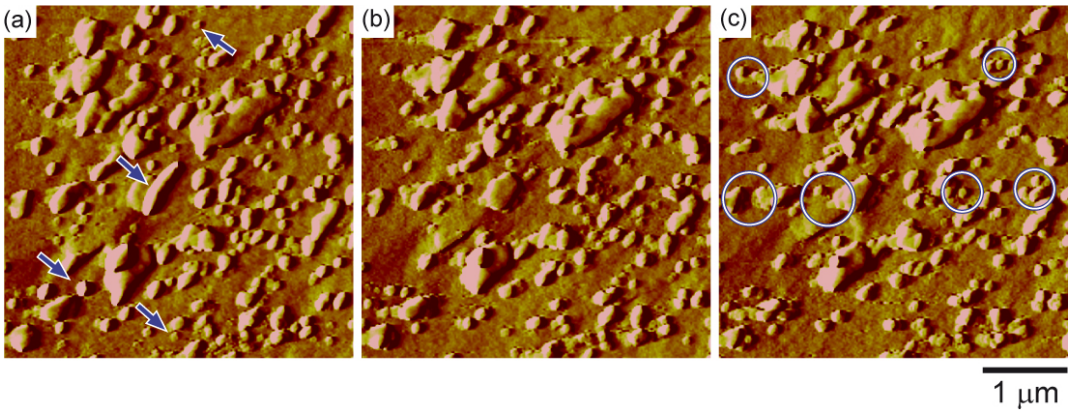

Figure 9. Sequential AFM height images showing the **(a)** dissolution of some of the precipitates covering the surface (blue arrows) when compared with **(b)** and **(c)** the growing and nucleation of precipitates (circles). The time lapse between images is 101 s.

Thus, our experimental results suggest that this interface-coupled dissolution-precipitation reaction (Putnis and Putnis, 2007) is controlled by the fluid composition in a boundary layer at the interface with the solid dolomite substrate. This boundary layer will have a different composition to the fluid in the bulk because, on dissolution of the substrate, it becomes supersaturated with respect to a new phase which then precipitates simultaneously, or is coupled to further dolomite dissolution. Therefore, according to our observations we suggest that the interaction of dolomite with aqueous solutions is a two-step process: (i) **congruent** dissolution of the primary mineral by formation and spreading of shallow (i.e. 0.3 nm deep) etch pits and (ii) subsequent precipitation of a Mg-rich phase. The fact that growth initially stops at the edges of dolomite etch pits, reproducing the topography of the parent solid (i.e. the template effect, Astilleros et al., 2003), indicates a crystallographic mismatch between the substrate and the overgrowth.

Note that it has been reported that the so-called "incongruent" dissolution is a transient stage, typically observed during the early stages of dolomite dissolution (Busenberg and Plummer, 1982). Over time, the solution Ca/Mg ratio approaches unity. This implies that the newly formed Mg-rich surface layer we have observed should redissolve as dissolution progresses. This is actually what we have seen under the AFM (Figure 9), where the newly formed precipitate continuously dissolves and reprecipitates during the course of the

experiment. This is not unexpected as the steep concentration gradient existing at the dolomite-solution boundary layer will be changed due to the precipitation of this phase and the supply of fresh solution, thus promoting the dissolution of this phase. In fact, PHREEQC thermodynamic calculations show that the bulk solution is undersaturated with respect to this Mg-rich carbonate phase (most probably nesquehonite, as indicated by XRD analysis). We suggest that a steady-state equilibrium should be reached between Ca and Mg release from both the dolomite surface and the newly formed Mg-rich carbonate layer which might explain why a nearly constant Ca/Mg ratio close to 1 is eventually reached (Busenberg and Plummer, 1982; Zhang et al., 2006). This implies that the formation of such a Mg-rich layer will not be limited to the very early stages of dolomite dissolution, only affecting a few (one or two) atomic layers as suggested by Busenberg and Plummer (1982); rather, it will affect an undetermined number of atomic layers as the reaction front penetrates within the dolomite crystal. In fact, it is difficult to envision a mechanistic scenario explaining why either the first layer or the first two atomic layers of the dolomite surface will be the only ones involved in the so-called "non-stoichimetric" or "incongruent" dissolution of dolomite as suggested by Busenberg and Plummer (1982) and Pokrovsky and Schott (2001).

In summary, this discussion highlights the importance of using techniques such as AFM that allow *in situ*, direct nanoscale observations of the mineral surface during dissolution to ascertain the mechanism and kinetics of mineral dissolution.

8.4. Conclusions

The results of this study suggest that the overall dolomite dissolution rate under circumneutral to alkaline conditions is controlled by the removal of dolomite layers by spreading and coalescence of shallow etch pits rather than by step retreat from deep pits nucleated at high energy points (dislocations). Our results also suggest that dolomite dissolution rates obtained from measurements of the solution chemistry could be misestimated both due to an underestimation of reactive surface area, and as a consequence of the precipitation of a secondary phase, particularly at acidic pHs. This process is a coupled

dissolution-precipitation reaction, ultimately controlled by the hydrodynamic conditions of the system and the formation of a boundary layer where supersaturation with respect to a secondary phase is reached. *In situ*, direct observations of the reacting mineral surface become critical in systems where "incongruent" dissolution is assumed, in order to unambiguously ascertain the mechanism and kinetics of mineral dissolution. For this reason, *in situ* AFM is a valuable tool in mineral dissolution studies as it allows quantification of the kinetics of the process from the measurement of etch pit densities and spreading rates, which are unaffected by the formation of any secondary precipitates. AFM in turn helps identifying the formation of secondary precipitates during dissolution, thus yielding critical mechanistic information.

8.5. References

Astilleros J.M., Pina C.M., Fernández-Díaz L. and Putnis A. (2003) Metastable phenomena on calcite {10-14} surfaces growing from Sr^{2+}–Ca^{2+}–CO_3^{2-} aqueous solutions. Chem. Geol. 193, 93-107.

Barber, D.J., Heard, H.C. and Wenk, H.R. (1981) Deformation of dolomite single crystals from 20-800 ºC. Phys. Chem. Minerals 7, 27l-286.

Bell F.G. (1993) Durability of carbonate rock as building stone with comments on its preservation. Environ. Geol. 21(4), 187-200.

Bisschop, J., Dysthe, D.K., Putnis, C.V. and Jamtveit, B. (2006) *In situ* AFM study of the dissolution and recrystallization behaviour of polished and stressed calcite surfaces. Geochim. Cosmochim. Acta 70, 1728-1738.

Busenberg E. and Plummer L.N. (1982) The kinetics of dissolution of dolomite in CO_2-H_2O systems at 1.5 to 65 degrees C and O to 1 atm pCO_2. Am. J. Sci. 282(1), 45-78.

Cardell Fernández C., Vleugels G., Torfs K. and Van Grieken R. (2002) The process dominating Ca dissolution of limestone when exposed to ambient amospheric conditions as determined by comparing dissolution models. Environ. Geol. 43, 160-171.

Charola A.E. and Ware R. (2002) Acid deposition and the deterioration of stone: a brief review of a broad topic. In: Natural stone, weathering phenomena, conservation strategies and case

studies (eds. Siegesmund, S., Weiss, R. and Vollbrecht, A.), Geol. Soc. Lond. Spec. Publ. 205(1), 393–406.

Chou L., Garrels R.M. and Wollast R. (1989) Comparative study of the kinetics and mechanisms of dissolution of carbonate minerals. Chem. Geol. 78(3-4), 269-282.

Duckworth O.W. and Martin S.T. (2004) Dissolution rates and pit morphologies of rhombohedral carbonate minerals. Am. Mineral. 89(4), 554-563.

Fenter P., Zhanga Z., Parka C., Sturchio N.C., Hu X.M. and Higgins S.R. (2007) Structure and reactivity of the dolomite (104)-water interface: New insights into the dolomite problem. Geochim. Cosmochim. Acta 71(3), 566-579.

Ford D.C. and Williams P. (2007) Karst Hydrogeology and Geomorphology. Wiley-Blackwell, 576 pp.

Gautelier M., Oelkers E.H. and Schott J. (1999) An experimental study of dolomite dissolution rates as a function of pH from -0.5 to 5 and temperature from 25 to 80°C. Chem. Geol. 157(1-2), 13-26.

Gautelier M., Schott J. and Oelkers E.H. (2007) An experimental study of dolomite dissolution rates at 80 °C as a function of chemical affinity and solution composition. Chem. Geol. 242(3-4), 509-517.

Green E. and Lüttge A. (2006) Incongruent dissolution of wollastonite measured with vertical scanning interferometry. Am. Mineral. 91(2-3), 430-434.

Hänchen M., Prigiobbe V., Baciocchi R. and Mazzotti M. (2008) Precipitation in the Mg-carbonate system—effects of temperature and CO2 pressure. Chem. Eng. Sc. 63, 1012-1028.

Herman J.S. and White W.B. (1985) Dissolution kinetics of dolomite: Effects of lithology and fluid flow velocity. Geochim. Cosmochim. Acta 49(10), 2017-2026.

Higgins S.R. and Hu X. (2005) Self-limiting growth on dolomite: Experimental observations with in situ atomic force microscopy. Geochimica Geochim. Cosmochim. Acta 69(8), 2085-2094.

Higgins S.R., Hu X. and Fenter P. (2007) Quantitative Lateral Force Microscopy Study of the Dolomite (104)−Water Interface. Langmuir 23(17), 8909-8915.

Hoke G.D. and Turcotte D.L. (2004) The weathering of stones due to dissolution. Environ. Geol. 46(3), 305-310.

Hu X., Grossie D.A. and Higgins S.R. (2005) Growth and dissolution kinetics at the dolomite-water interface: An *in-situ* scanning probe microscopy study. Am. Mineral. 90, 963-968.

Kaczmarek S.E. and Sibley D.F. (2007) A comparison of nanometer-scale growth and dissolution features on natural and synthetic dolomite crystals: implications for the origin of dolomite. J. Sed. Res. 77(5), 424-432.

Kerisit S. and Parker S.C. (2004) Free energy of adsorption of water and metal ions on the {10 4} calcite surface. J. Am. Chem. Soc. 126, 10152-10162.

Lippman F. (1973) Sedimentary carbonate minerals. Springer-Verlag, Berlin.

Liu Z. and Dreybrodt V. (2001) Kinetics and rate-limiting mechanisms of dolomite dissolution at various CO_2 partial pressures. Sci. China(B) 44(5), 500–509.

Lund K., Fogler H.S. and McCune C.C. (1973) Acidization--I. The dissolution of dolomite in hydrochloric acid. Chem. Eng. Sci. 28(3), 691-700.

Lüttge, A. (2005) Etch pit coalescence, surface area, and overall mineral dissolution rates. Am. Mineral. 90, 1776-1783.

Lüttge A., Winkler U. and Lasaga A.C. (2003) Interferometric study of the dolomite dissolution: a new conceptual model for mineral dissolution. Geochim. Cosmochim. Acta 67(6), 1099-1116.

Mann S. (2001) Biomineralization: principles and concepts in bioinorganic materials chemistry. Oxford University Press, Oxford, 216 pp.

MacInnis I.N. and Brantley S.L. (1992) The role of dislocations and surface morphology in calcite dissolution. Geochim. Cosmochim. Acta 56, 1113-1126.

Millero F.J. (2007) The marine inorganic carbon cycle. Chem. Rev. 107(2), 308-341.

Morse J.W. and Arvidson R.S. (2002.) The dissolution kinetics of major sedimentary carbonate minerals. Earth Sci. Rev. 58(1-2), 51-84.

Morse J.W., Arvidson R.S. and Lüttge A. (2007) Calcium carbonate formation and dissolution. Chem. Rev. 107(2), 342-381.

Moulder J.F., Stickle W.F., Sobol P.E. and Bomben, K.D. (1982) Handbook of X-ray photoelectron spectroscopy. Chastain, J. Ed. Minneapolis, Perkin-Elmer Corporation.

Oelkers E.H. and Schott J. (2005) Geochemical aspects of CO_2 sequestration. Chem. Geol. 217(3-4), 183–186.

Orton R. and Unwin P.R. (1993) Dolomite dissolution kinetics at low pH: a channel-flow study. J. Chem. Soc. Faraday Trans. 89(21), 3947-3954.

Paquette J. and Reeder R.J. (1995) Relationship between surface structure, growth mechanism, and trace element incorporation in calcite. Geochim. Cosmochim. Acta 59, 735-749.

Pérez-Garrido C., Fernández-Díaz L., Pina C.M. and Prieto M. (2007) *In situ* AFM observations of the interaction between calcite (10-14) surfaces and Cd-bearing aqueous solutions. Surf. Sci. 601, 5499-5509.

Pokrovsky O.S., Golubev S.V. and Schott J. (2005) Dissolution kinetics of calcite, dolomite and magnesite at 25 °C and 0 to 50 atm pCO_2. Chem. Geol. 217(3-4), 239-255.

Pokrovsky O.S. and Schott J. (2001) Kinetics and mechanism of dolomite dissolution in neutral to alkaline solutions revisited. Am. J. Sci. 301(7), 597-626.

Pokrovsky O.S., Schott J. and Thomas F. (1999) Dolomite surface speciation and reactivity in aquatic systems. Geochim. Cosmochim. Acta 63(19-20), 3133-3143.

Putnis A. and Putnis C.V. (2007) The mechanism of reequilibration of solids in the presence of a fluid phase. J. Solid State Chem. 180, 1783-1786.

Putnis C.V., Tsukamoto K. and Nishimura Y. (2005) Direct observations of pseudomorphism: compositional and textural evolution at a fluid-solid interface. Am. Mineral. 90, 1909-1912.

Reeder R.J. (1983) Crystal chemistry of the rhombohedral carbonates. *In* Carbonates: mineralogy and chemistry (ed. R. J. Reeder); Rev. Mineral. 11, 1–47. Mineralogical Society of America.

Ruiz-Agudo E., Kowacz M., Putnis C.V. and Putnis A. (2010) The role of background electrolytes on the kinetics and mechanism of calcite dissolution. Geochim. Cosmochim. Acta 74(4), 1256-1267.

Ruiz-Agudo E., Putnis C.V., Jiménez-López C. and Rodríguez-Navarro C. (2009) An atomic force microscopy study of calcite dissolution in saline solutions: The role of magnesium ions. Geochim. Cosmochim. Acta 73(11), 3201-3217.

Ruiz-Agudo E., Urosevic M., Putnis C.V., Rodríguez-Navarro C., Cardell C. and Putnis A. (2011) Ion-specific effects on the kinetics of mineral dissolution. Chem. Geol. 622 281(3-4), 364-371.

Sayles F.L. and Fyfe W.S. (1973) The crystallization of magnesite from aqueous solution. Geochim. Cosmochim. Acta 37, 87-99.

Shiraki R., Rock P.A. and Casey W.H. (2000) Dissolution kinetics of calcite in 0.1 M NaCl solution at room temperature: An atomic force microscopic (AFM) study. Aq. Geochem. 6, 87-108.

Teng H.H. (2004) Control by saturation state on etch pit formation during calcite dissolution. Geochim. Cosmochim. Acta 68, 253-262.

Zhang R., Hu S., Zhang X. and Yu W. (2007) Dissolution kinetics of dolomite in water at elevated temperatures, Aq. Geochem. 13(4), 309–338.

Chapter 9

Submitted to Science of the Total Environment

Black soiling of an architectural limestone during a long-term urban polluted air exposure in the city of Granada (S Spain)

Maja Urosevic[1,*], Africa Yebra-Rodríguez[2], Eduardo Sebastián-Pardo[1] and Carolina Cardell[1]

[1] Dept. Mineralogy and Petrology, Faculty of Science, University of Granada, Campus Fuentenueva s/n, 18071 Granada, Spain.

[2] Dept. Geology-Associated Unit IACT (CSIC-UGR), Faculty of Experimental Science, University of Jaén, Campus Las Lagunillas s/n, 23071 Jaén, Spain.

Article history

Submitted 5 May 2011

ABSTRACT

A long-term ageing test was carried out on a building limestone (i.e. carbonate stone named *Escúzar* calcarenite) under different polluted urban conditions in the city of Granada (Southern Spain) to assess its Cultural Heritage sustainability. To this end stone tablets were placed vertically at four sites with contrasting local pollution micro-environments, and different conditions of exposure (rain-sheltered and unsheltered). The back (rain-sheltered) and the front (rain-unsheltered) faces of the stone tablets were studied for each site. The soiling process (surface blackening) on the stone surfaces was monitored through lightness (ΔL^*) and chroma changes (ΔC^*). Additionally atmospheric particles deposited on the aged calcarenite surfaces and on particulate matter PM10 filters during the time of exposure were studied through a multianalytical approach including scanning electron microscopy with energy-dispersive X-ray analyzer (SEM-EDX), transmission electron microscopy (TEM) and micro-Raman spectroscopy.

The identified atmospheric particles (responsible for stone soiling) were mainly soot particles (C-rich particles), and soil dust particles; also fly ash and aged salt particles were found. The calcarenite soiling process was related to surface texture, exposure conditions and proximity to dense traffic streets. On the front faces of all stones, black soiling and surface roughness promoted by differential erosion between micritic and sparitic calcite were noticed. Moreover, it was found that surface roughness enhanced a feedback process that triggers further black soiling. After the first year of urban exposure, gypsum crusts (thickness ca. 100 μm) embedding variable amount of dust and soot particulates, developed on both the front and back faces of all calcarenites (except in the lowest polluted site). The estimated soiling coefficients (SC = 4.9 to 6.4 x 10^{-2} $days^{-1/2}$ $\mu g^{-1/2}$ $m^{3/2}$) were slightly lower than those reported in other cities of Spain. However, the calculated effective coverage area of blackening particles (EAC) ranged from 10.2 to 20.4%, exceeding by far the established value of 2% EAC which is the limit perceptible by the human eye. Indeed, after two years of exposure to the Granada urban air, the darkening of the white *Escúzar* calcarenite surface has resulted in an undesired aesthetical problem that will required frequent cleaning actions (evaluation of ca. 17 years), in addition to trigger further stone degradation.

KEYWORDS

Building limestone, black soiling, air pollution, atmospheric particulates, spectrophotometry, architectural heritage.

9.1. Introduction

Stone decay in polluted urban atmosphere is an outstanding problem with paramount cultural and economic consequences which have attracted the attention of intensive research during decades (see Doehne & Price, 2010 for a comprehensive review). In fact, the effect of air pollution on stone decay is still a major problem even though the acidic pollutant levels have been considerably reduced since the early 1990s (Doehne & Price, 2010). The danger to the Cultural Heritage from air pollution comes from several main sources such as the increasing of corrosion induced by gases from the atmosphere (Charola & Ware, 2002; Cardell-Fernández et al., 2002), the soiling of light colored stone surfaces due to black particles (e.g. Grossi et al., 2003, Hamilton & Crabbe, 2009), and the crystallization of soluble and insoluble salts inside the porous network that eventually leads to stone disaggregation and surface recession (Scherer, 1999; Doehne, 2002 and references therein). The development of black crust is a well-known process associated with surface deposition of complex mixtures of atmospheric particles and gases derived from the combustion of fossil fuels together with a range of environmental dusts, a variety of salts including marine aerosols, and microbial fauna (Watt, 2009 and references therein). The blackness of these gypsum crust layers are commonly explained by absorption of carbonaceous particles such as soot. Additionally, it has been argued that carbon soot and metal-rich particles (e.g. V, Fe, Ni, Cu, Mn and Cr-rich particles derived from anthropogenic sources) exert a critical catalytic action in the oxidation of SO_2 (Camuffo et al., 1984; Rodríguez-Navarro & Sebastián-Pardo, 1996; Maravelaki-Kalaitzaki & Biscontin, 1999; Böke et al., 1999, 2002; Maravelaki-Kalaitzaki, 2005), although the additional catalytic effect of bacteria is not discarded.

Most of these studies have addressed the above issues by combining (1) detailed observations of already weathered construction materials from polluted cities with (2) *ad hoc* experiments under controlled laboratory conditions (e.g. Rodríguez-Navarro & Sebastián, 1996; Simão et al., 2006). Experimental data are later extrapolated to 'real' urban conditions. The diversity of tested stone materials under different environmental conditions has provided a considerable understanding of their main weathering mechanisms. However to unsure

measurable results in relatively short times, these experiments are usually conducted under extreme environmental conditions which are usually far from those prevailing in urban conditions. Therefore a direct extrapolation to the nature is not straightforward and leads to several uncertainties in the estimation of decay rates which are an important issue in the sustainability of Cultural Heritage. Furthermore there are still many intrinsic factors (stone-related properties) and extrinsic factors (environmental-related variables such as exposure and micro climatic conditions, pollution, etc.) that are challenging to be reproduced experimentally. Therefore long-term ageing tests would be of benefit to address long-term sustainability of architectural materials, eventually controlled by all these intrinsic and extrinsic factors (Delalieux et al., 2002). Pioneering long-term ageing tests designed to study the soiling effect of atmospheric aerosols on building stones were conducted by Beloin and Haynie (1975) using changes in reflectance to asses the stone weathering process. Similar studies were carried out by Creighton et al. (1990), Hamilton & Mansfield (1992) and Pio et al. (1998) which discussed several fitting equations of experimental data relating reflectance decrease and time of exposure. However, these kinds of studies are still limited in many places around Europe with an outstanding and vulnerable Cultural Heritage legacy such as Spain (nevertheless see Grossi et al., 2003), even thought are essential to design conservation policies (Grossi & Brimblecombe, 2004; Brimblecombe & Grossi, 2005, 2007).

This study is aimed to investigate the black soiling of a carbonate stone (i.e. a calcarenite used to replace similar historic carbonate stones in monuments in Andalusia, South Spain) under Granada urban condition during a long-term exposure test (period of 2008 and 2009). Although the city of Granada is considered a relatively non-polluted city, most of its architectural heritage, built with carbonate stones, is prone to weathering under its urban conditions. Assessment of soiling was qualitatively and quantitatively estimated by chromatic changes on the calcarenite surfaces through spectrophotometric measurements. Additionally, atmospheric aerosols deposited on the stone surfaces and filters were analyzed by scanning electron microscopy (SEM), transmission electron microscopy (TEM) and micro-Raman spectroscopy (MR). Calculated total soiling (ΔL^*), soiling coefficient (SC) and effective area coverage by dark particles (EAC) enabled estimation of cleaning actions on the SP calcarenite.

9.2. Materials and methods

9.2.1. Materials

A limestone (carbonate stone) was selected for this study, namely *Escúzar* calcarenite exploited in the *Escúzar* quarry situated ~ 20 km to the SW from the city of Granada, Southern Spain (Urosevic et al., 2011). This calcarenite is commonly used in modern architecture in Andalusia as well as in monuments replacing the historic *La Escribana* calcarenite commonly used in ancient buildings of the city of Granada such as the Cathedral, the Charles V Palace and the San Jerónimo Monastery (Rodríguez-Navarro, 1994; Rodríguez-Navarro & Sebastián, 1996; Cardell, 1998; Rodríguez-Navarro et al., 2008).

The calcarenite can be classified as a coarse calcarenite or fine calcirudite (Folk, 1981). This calcarenite is texturally very heterogeneous, highly porous (29.30 ± 7.6% in average) and scarcely cemented (calcitic cement), showing fragments of bioclasts (mainly molluscs, echinoderms, briozoan, red algae and foraminifera) with sizes normally ranging from 2 to 5 mm, although they also can attain up to 2 cm (Urosevic et al., 2011). These features, together with the high calcite proportion in its matrix, make this stone very prone to weathering due to dissolution processes, e.g. salt damage and gypsum crust formation, especially under polluted environments.

9.2.2. Environment and sample location

Granada is a non industrialized, medium size city in Southern Spain with a population of around 300,000 (ca. 600,000 inhabitants of the entire urban area). It is about 50 km from the Mediterranean Sea and around 200 km from the African continent. Granada is located in an intraorogenic basin surrounded by mountains with the highest elevations (up to 3,500 m) located at the southeast of the basin. Due to its topography in combination with the prevailing low wind speeds, heavy traffic and intensive construction works (e.g. Metropolitan works during the period of the test, i.e. years 2008 and 2009), pollutants and soot particles often accumulate in the air of Granada. Indeed, around 9% of black carbon

particles (soot particles) were detected in the city center by Kontozova-Deutsch and co-workers (2010). Granada has a near-continental climate with cool winters, hot summers, and high diurnal temperature variability. Most rainfall occurs during winter and spring seasons, leading to re-suspension of dust particles predominantly in the dry seasons. The average annual precipitation in the area during the test was 427 L m^{-2}. When the wind direction is southerly (S and SW are the prevailing wind directions) marine particles can be expected. Additionally meteorological conditions prevailing in spring and summer favors the arrival of Saharan and Sahel air masses. During autumn and winter the number of Saharan dust episodes is reduced while Atlantic and continental air mass are dominant (Lyamani et al., 2004, 2008, 2010). Regarding atmospheric pollutants, the European legal limits for SO_2, CO, and NO_2 emissions were not surpassed during the test in clear contrast to the O_3, PM10 (particulate matter with an aerodynamic size ca. 10 μm) and soot particles emissions, particularly these two latter (Lyamani and Brava, 2008, 2009).

For the long-term test, calcarenite tablets of 10 × 10 × 2 cm (cut from the same calcarenite slab) were placed vertically at four different sites in the city of Granada (see Fig. 1 for sample location and Table 1 for details). The selected site locations ensure a representative spectrum of microclimatic conditions and thus stone weathering environments ranging from very high (site 4), high (site 1) to low polluted areas (sites 2 and 3), as inferred from the proximity to heavy traffic streets and data monitored through several stations placed in the city (Fig. 1). Outdoor- and indoor-looking stone faces (here named 'front face' and 'back face' respectively) were distinguished for each site. Comparatively the back faces were more sheltered from rain-wash and sun light exposure than the front faces. In this work the term "black soiling" always refers to blackening of stones (Grossi et al., 2003) and was related to chromatic changes of lightness or luminosity (L^*) on stone surfaces. The discussion of the results was done considering the impact of atmospheric particles on the calcarenite surfaces and taking into account their conditions of exposure (sheltered and unsheltered from rain-wash). However we are aware that soiling also depends on other factors among which surface roughness, humidity and sun light irradiation are under investigation. Moreover, during the period of stone exposure, PM10 filters were collected at

the roof of the Andalusian Centre for Environmental Studies (CEAMA), located in Granada (Fig. 1) and analyzed.

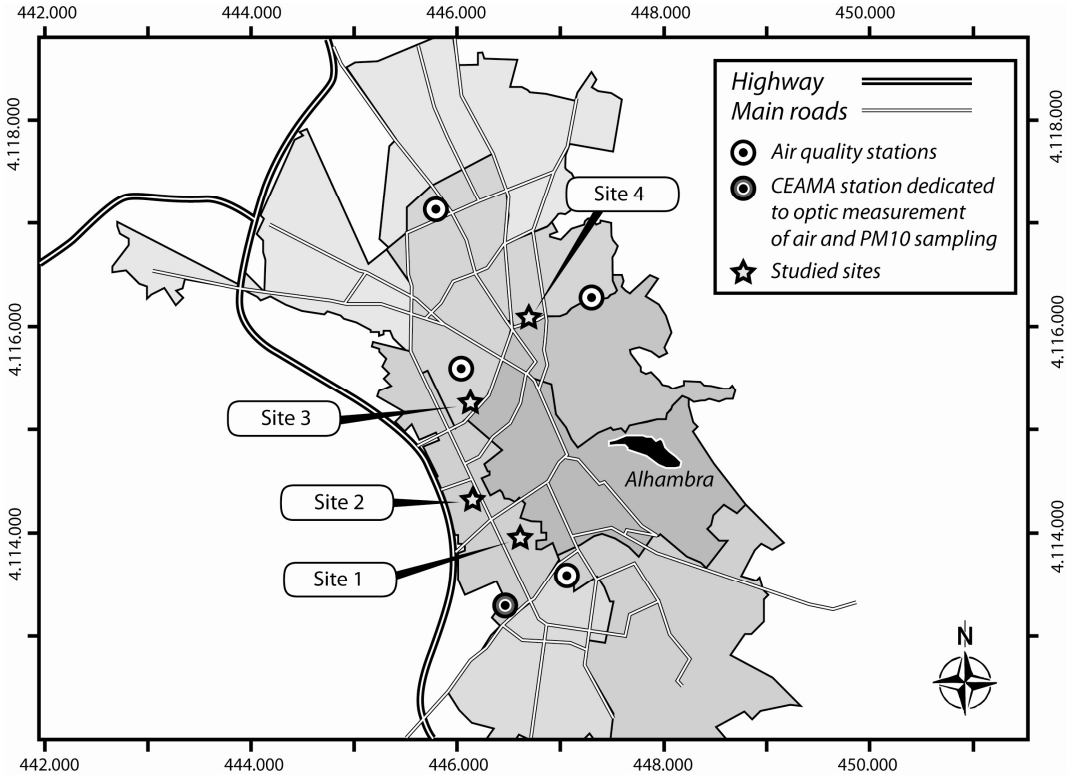

Fig. 1. Location of the sites where calcarenite tablets were placed for the long-term ageing test (stars) in Granada (Spain). Several suburbs of Granada's city are depicted in grey scale. Highways and main roads are also shown. Location of air quality stations (dotted circle) and particulate matter sampling (CEAMA station, grey dotted circle) are shown.

9.2.3. Analytical techniques

Chromatic changes in the calcarenite tablets due to urban air exposure were measured with a Minolta CM-700d spectrophotometer using a 8 mm measuring aperture. The measurements were performed on a regular grid consisting of 18 or 24 points on both back and front faces for each stone tablet. D65 illuminant, known as standard daylight illuminant

Table 1. Location and description of sites where calcarenite tablets were placed in the city of Granada.

Site location	Exposure conditions	Orientation	Exposure days
1	Unroofed balcony at ~20 m from ground level (g.l.). High traffic density, next to metropolitan works.	ENE	673
2	Roofed balcony at ~7 m g.l. Medium traffic.	NNE	587
3	Unsheltered roof at ~18 m g.l. Medium traffic.	SSE	700
4	Window embrasure at ~2 m g.l. Very high traffic density in narrow and steep street.	S	825

(color temperature: 6504 K), was applied. The CIE 1976 chromatic scale was used to measure the chromatic parameters L^*, a^* and b^* (Wyszecki & Stiles, 1982). L^* is luminosity or lightness which varies from black with a value of 0 to white with a value of 100); a* varies from +a* (red) to -a* (green) and b* ranges from +b* (yellow) to -b* (blue).

Chips samples of fresh and aged calcarenite tablets were analyzed with an environmental scanning microscope (ESEM). A Phillips Quanta 400 was used applying 20 kV acceleration voltage, 1 nA probe current and working distance of 10 mm. In addition, carbon coated polished thin sections (prepared from aged stone tablets) were studied with a LEO 1430VP scanning electron microscope (VPSEM), coupled with an EDX microanalyzer (Inca 350 version 17, Oxford Instruments). Pinpoint analyses were done using a 500 pA filament current and 10 eV/ch resolution, while for X-ray maps acquisition working conditions were 1 nA filament current and 20 eV/ch resolution. The high-resolution X-ray maps (1024 × 768 pixels) were obtained in selected areas with 500 frames acquired over 16h. Furthermore, the *Phasemap* tool implemented in the INCA 350 version was applied to

identify mineral phases using ternary element plots of specific pixel information from montaged X-ray maps (Cardell et al., 2009a, b).

The composition and morphology of the atmospheric particles deposited on the stone surfaces and those collected by filters were studied at nanoscale by transmission electron microscopy (TEM). A Philips CM20 equipped with an EDAX solid-state ultrathin-window energy dispersive X-ray (EDX) detector was used. The acceleration voltage of the microscope was 200 kV, and a lens aperture of 40 μm was employed as a compromise between amplitude and phase contrast for the images. The identification of mineral phases was facilitated by collecting selected area electron diffraction (SAED) patterns. Prior to TEM analysis, particles were dispersed in ethanol, sonicated for 30 s, and placed on Formvar© and C-coated Cu grids.

Micro-Raman spectroscopy was applied to distinguish tiny crystals precipitated onto the calcarenite tablets. A Renishaw RM1000 dispersive spectrometer equipped with a Leica DMLM optical microscope, a grating with 1200 grooves/mm and a Peltier-cooled CCD detector was used. Raman spectra were obtained with the 785 nm emission of a diode laser with 30 mW laser power. Leica 20 × and 50 × objectives were employed. The system was operated in the confocal mode, resulting in an approximate lateral resolution of ca. 3 μm.

9.3. Results and discussion

9.3.1. Characterization of fresh calcarenite surface

At surface the *Escúzar* calcarenite is very heterogeneous in texture and composed by micritic calcite (ca. 3-5 μm in size) showing large cavities of ca. 100-300 μm in length, which can attain up to 1 cm in length. The larger cavities are covered by sparry calcite (ca. 20-40 μm) and often Fe-rich framboids and Fe-rich tubes occur. Fe-rich framboids comprise small spherules (with diameters of 1-2 μm) forming aggregates of 5-15 μm in length as shown in Fig. 2a. The framboids are mainly composed of Fe and Si, and Al in minor

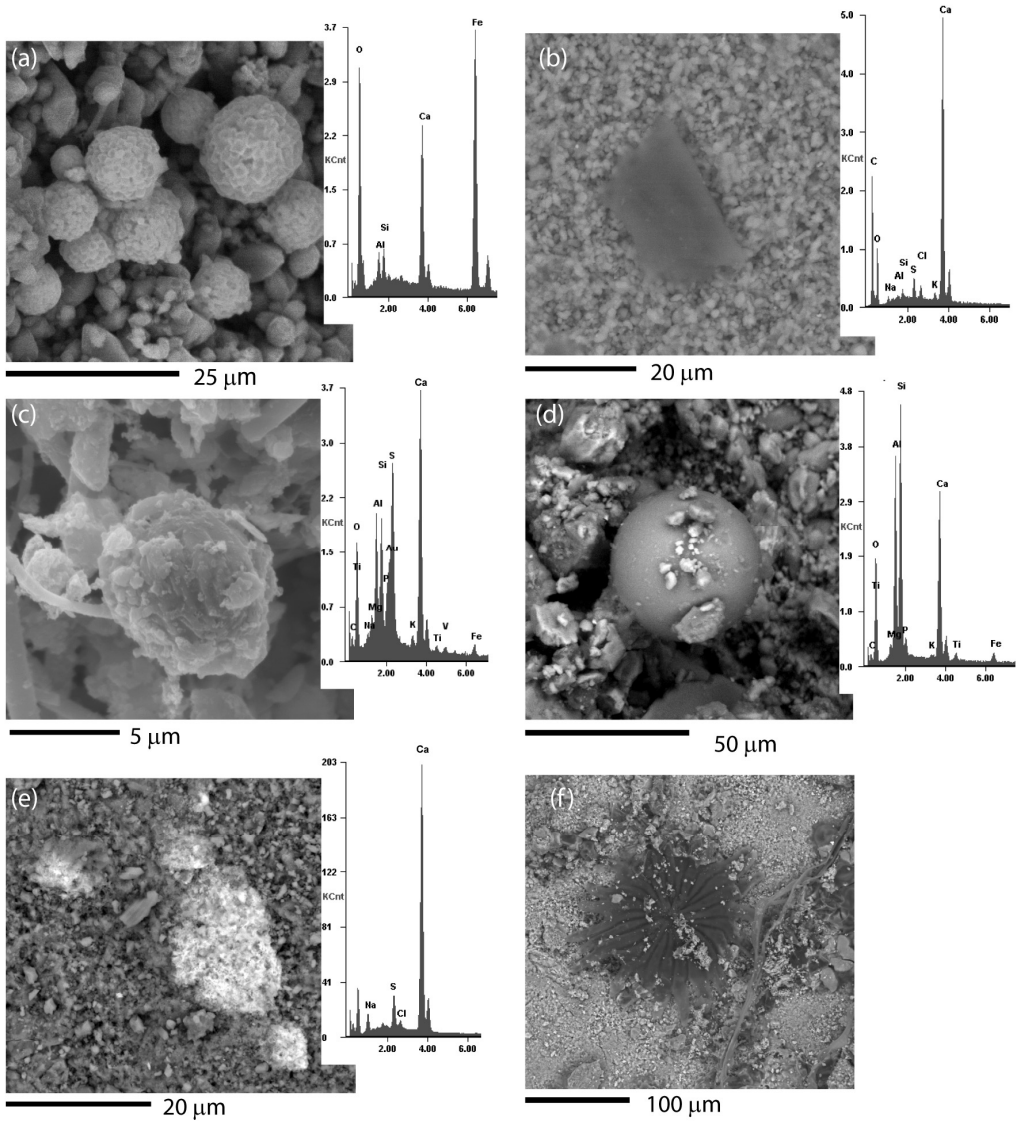

Fig. 2. Representative SEM images and corresponding SEM-EDX spectra of *Escúzar* calcarenite and particulate matter filters. **(a)** Aggregate of several Fe-rich framboids on fresh (quarried) stone sample. **(b)** C-rich particle mixed with clay minerals and phyllosilicates, NaCl and Ca-sulfate on stone tablet at site 4. **(c)** Phyllosilicates and clay minerals mixed with Ca-sulfate and traces of V and Ti in PM10 filter. **(d)** Si-Al-rich spherical particle on stone tablet at site 1. **(e)** Porous aggregate of sea-salt particles (NaCl) mixed with Ca-sulfate on stone tablet at site 2. **(f)** Biogenic particle (Leaf Trichome) in the center and fungal hyphaea (right) on stone tablet at site 1.

proportions; S is scarce and not always present (see spectrum in Fig. 2a). Based on the Fe-rich framboids morphology and their location in the larger cavities, we suggest that they can be oxyhydroxides pseudomorphs of former framboidal pyrites originated by oxidation and sulfur loss during early stages of diagenesis (e.g. Merinero et al., 2009). Fe-rich tubes are likewise interpreted. Additionally the fresh stones may contain clay minerals (hydrous aluminium phyllosilicates with particle size < 2 μm) and occasionally sphalerite (Zn,Fe)S.

9.3.2. Atmospheric particles deposited on the calcarenite tablets and filters

In the following paragraphs a simple classification of the identified atmospheric particles deposited on the aged calcarenite surfaces and the PM10 filters collected at the CEAMA station are presented (Table 2). However it is noteworthy to note that complex mixtures between these groups are very common.

Soil dust particles: Phyllosilicates (parallel sheets of silicate tetrahedra with Si_2O_5 or a 2:5 ratio) with sizes commonly ranging from 40 to 100 μm, and clay minerals are by far the most common particles found in all sites (Table 4). These particles have both primary and secondary (airborne) origins. Although pure phyllosilicates and clay minerals were observed (probably those corresponding with a primary origin), most commonly they form complex mixtures with other atmospheric particles. For example, Fig. 2b shows a C-rich particle mixed with NaCl and Ca-sulfate and phyllosilicate particles. This mixture also was observed in the filters, possible indicating an airborne origin of the phyllosilicates (Fig. 2c). At nanoscale (e.g. Fig. 3a) the mixture is more obvious, including variable amounts of C, Cl, Ca-sulfate and CaMg-sulfate and occasionally NaCl. Based on the chemical composition, the observed clay minerals comprise several phyllosilicates such as illite $(K,H_3O)(Al,Mg,Fe)_2(Si,Al)_4O_{10}[(OH)_2,(H_2O)]$, paragonite $NaAl_2(Si_3Al)O_{10}(OH)_2$, smectite $(Na,Ca)(Al,Mg)_6(Si_40_{10})_3(OH)_6\text{-}nH_20$, kaolinite $Al_2Si_2O_5(OH)_4$ and chlorite $(Mg,Fe)_3(Si,Al)_4O_{10}(OH)_2\cdot(Mg,Fe)_3(OH)_6$, as reported elsewhere for the city of Granada (Rodríguez-Navarro & Sebastián, 1996; Kontozova-Deutsch et al., 2010).

Table 2. Summary of the identified atmospheric particles by SEM-EDX and TEM onto the studied calcarenite tablets at the different sites and the filters collected at the CEAMA station in the city of Granada (Southern Spain).

	Fresh	Site 1	Site 2	Site 3	Site 4	Filter
Fe-rich framboids	●	●	●	○	●	○
Fe-rich tubes	●	●	○	○	●	○
Atmospheric Particles						
Dust particles (phyllosilicates and clay minerals)	●	●	●	●	●	●
Fly ash particles (Si-Al-rich)	○	●	●	○	●	○
Fe-rich particles	○	○	○	○	●	○
Soot particles (C-rich)	○	●	●	●	●	●
Salt particles	○	○	●	○	○	○
Other particles						
Dolomite	○	●	●	○	●	●
Calcite	●	●	●	●	●	●
Fe-Ti-oxide	○	○	●	○	○	○
Fe-oxide	○	●	●	○	○	○
Sphalerite	○	○	●	○	○	○
Barite	○	○	●	○	○	●
Feldspar	○	○	●	○	●	○
Chalcopyrite	○	●	○	○	○	○
Rutile	○	○	○	○	○	●
Quartz	○	○	○	○	●	○
Biogenic particles						
Fungal hyphae	○	●	●	●	●	○
Leaf Trichome	○	●	●	○	●	○
Black gypsum crust	○		○	●	●	○

● observed ○ not observed

Fly ash particles: These silicon- and aluminium-rich particles are perfectly spherical with smooth surface (Fig. 2d). They contain minor amounts of Mg, Fe, Ti, K, S and occasionally Cl, showing a wide range in sizes that goes from 2 to 40 μm. Similar particles have been observed elsewhere and are commonly interpreted as derived from coal combustion (Kindratenko et al, 1994; Xie et al., 1994; Katrinak et al., 1995; Rodríguez-Navarro & Sebastián, 1996; Esbert et al., 2001, Kontozova-Deutsch et al., 2010).

Iron-rich particles: These particles are generally rounded in shape and can be related to diesel exhaust, mainly composed of soot and metallic particles bearing Fe and Fe-S as major elements. Metal-rich particles are important in the development of black crust since they usually contain several metals such as V, Co, Ni, Cu, Mn and Cr that, together with carbonaceous particles, catalyze the oxidation and hydrolysis of atmospheric SO_2 (Rodríguez-Navarro & Sebastián, 1996 and reference therein).

Soot particles: These carbon-rich particles were observed on all stones, usually mixed with clay minerals. C-rich particles with detectable amounts of Na, K and Cl also were observed by means of SEM-EDX analyses and more precisely by TEM. These particles comprise both organic matter (made up of hundreds of individual carbon compounds) and elemental carbon (soot) forming the fine and ultrafine particulate matter fraction (e.g. Esbert et al., 2001; Murr & Bang, 2003). TEM observations of particles collected from the filters revealed the widespread occurrence of soot particles (Fig. 3a and b) with fractal geometries, i.e. concentric graphene-like layers, which are wrapped into spherules that aggregate into characteristic branching clusters of hundreds of carbonaceous spherules (e.g. Katrinak et al., 1995; Pósfai et al., 1999; Murr & Bang, 2003; Simão et al., 2006; Pósfai & Buseck, 2010). Individual carbonaceous spherules range in size from 20 to 60 nm with an average value of 32 ± 11 nm matching those observed from diesel particulate matter (Simão et al., 2006). The SAED patterns are dominated by diffuse (non-crystalline) carbon reflections although occasionally diffuse rings at 0.12, 0.21 and 0.34 nm (Fig. 3b inset) indicate the occurrence of graphite (Murr & Bang, 2003; Simão et al., 2006). Micro-Raman analyses further confirmed the occurrence of soot as revealed by the two broad bands around 1300 and 1600 cm^{-1} attributed to the D (disordered) and G (graphitic) bands typical of soot particles (Fig. 4). Additionally the high luminescence of the Raman spectrum also suggests the occurrence of organic matter or organic carbon.

Salt particles: Highly porous Na and Cl rich particles (up to 20 μm in length) were occasionally observed (Fig. 2e). These particles have compositions similar to aged sea salts which are characterized by a decrease on the ratio Cl/S due to particle modification during long-term transport in the atmosphere (Esbert et al., 2001). It is worth to note that sea salt

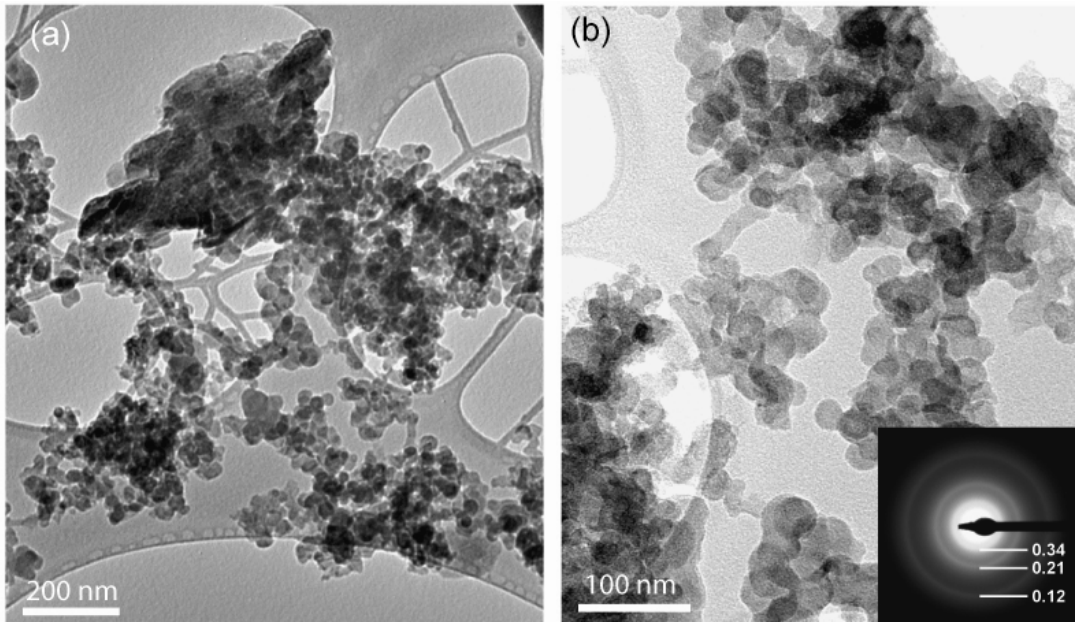

Figure 3. Examples of particulate matter (PM10) on filter. **(a)** Clay minerals mixed with Ca-sulfate (upper left) and soot with fractal geometry. **(b)** Detailed of soot particles composed of irregular C-rich spherules leading to a high porous aggregates. Inset: SAED pattern showing graphitic carbon reflections corresponding to carbon-layer spacings.

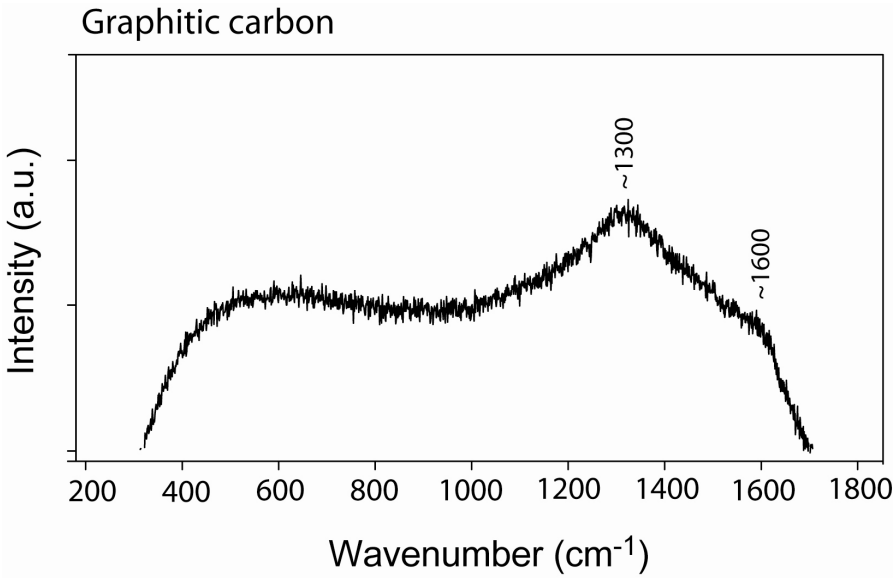

Figure 4. Example of Raman spectrum of black particles deposited on calcarenite surface. Note the broad bands around 1300 and 1600 cm^{-1} attributed to the D (disordered) and G (graphitic) bands, respectively, indicating graphitic carbon derived from atmospheric soot particles.

particles are reported in other near-continental areas of Spain (e.g. Querol et al., 2004) including the city of Granada (Kontozova-Deutsch et al., 2011; Horemans et al., submitted).

Other particles: Under this category a wide spectrum of observed mineral dust particles are classified, including dolomite ($CaMg(CO_3)$ and fibrous calcite ($CaCO_3$), barite ($BaSO_4$), Fe-oxides, sphalerite, Fe-Ti particles (ilmenite and/or rutile, TiO_2), chalcopyrite ($CuFeS_2$), feldspar $(Na/K/Ca)Al_{(1-2)}Si_{(3-2)}O_8$, and quartz Si_2O.

Biogenic particles: Evidence of biological colonization was found on stones located in all sites mainly in the form of lichens and fungal hyphae, the latter showing elongated structures ca. 50 mm wide by more than 500 μm long (Fig. 2f). Also it should be noted the widespread occurrence (Table 2) of radial and starry shape organic structures (200 μm in length) which are tentatively classified here as *olive leaf trichome* (e.g. Filippou et al., 2007).

9.3.3. Black soiling

After ca. 2 years of exposure to the Granada urban air, macroscopic changes on both the front and back faces of almost all calcarenite surfaces were evident, namely color modification and darkening, edges rounding of the stone tablets and minor organic colonization. As an example, Fig. 5 shows the surface modification of the calcarenite tablet placed at site 1 (high polluted area) after two years of urban exposure. Surface roughness was higher in the front face (Fig. 5a) than in the back face (Fig. 5b), that was attributed to the more intense rain wash-out of the front stone side which in turn promote differential erosion between micritic and sparitic calcite (with crystal sizes < 4 μm and > 10 μm respectively) areas (Vendrell et al., 1996; Viles, 2005). Differential erosion is typical of bioclastic limestones (such as the *Escúzar* calcarenite) with texture showing very clear distinction between sparitic areas (in bioclasts) and the micritic matrix. Indeed, in the matrix the higher specific surface area enhances calcite dissolution compare with the less reactive sparitic domains. Additionally it should be noted that rain-sheltered areas are more suitable for gypsum crust development which in turn may explain smooth surfaces (Delalieux et al., 2001). Also it is worth to mention that in the calcarenites surface blackening was

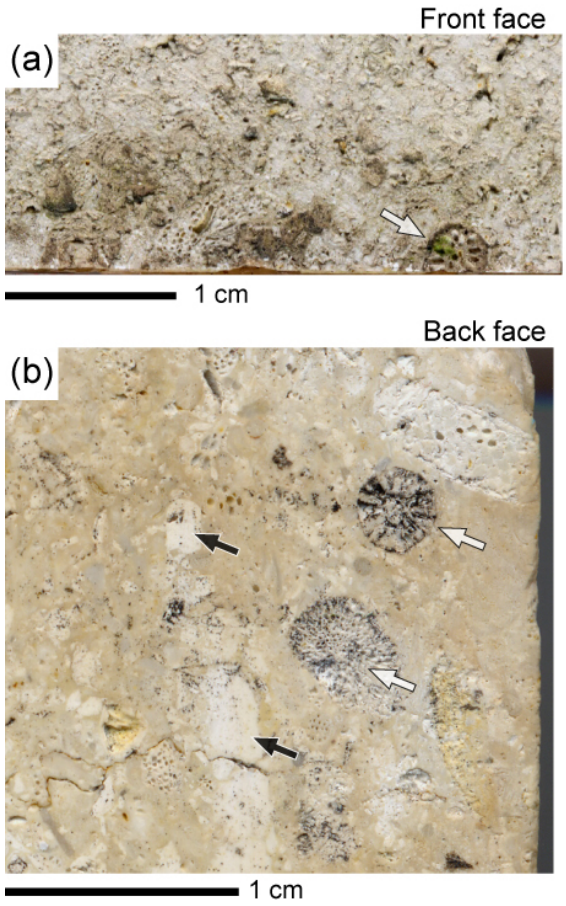

Figure 5. Scanned surface of calcarenite tablet place at site 1 after the on-site long-term test. **(a)** Front face; note the surface roughness compared to the back face. The white arrow shows one bioclast (bryozoan) partially colonized by organic material. **(b)** Back face; the white arrows indicate two blackened bioclasts (bryozoans). Other bioclasts (e.g. red algae, black arrows) are less or not blackened.

heterogeneous at the centimeter scale, and more obvious in certain types of bioclasts displaying abundant intraclast porosity, such as bryozoans (Fig. 5b).

In order to assess the soiling process of the *Escúzar* calcarenite under Granada urban conditions, chromatic changes on the front and back stone faces were measured using spectrophotometry. Table 3 shows mean values and standard deviation of L^*, a^*, b^* and C^* for the *Escúzar* calcarenite. Black soiling can be estimated by measuring the decrease in L^* at a certain time (L_t^*) with respect to the initial conditions L_0^*, namely final soiling, $\Delta L^* = L_t^* - L_0^*$ (e.g. Grossi et al., 2003). As Table 3 displays absolute ΔL^* between fresh and aged calcarenite tablets indicate a decrease in lightness (i.e. blackening) on both the back and front stone faces at all sites (Table 3). Black soiling was particularly evident at site 4 (ΔL^* = -10.84 on front face and -11.53 on back face) and site 1 (ΔL^*= -8.12 vs. -5.97 units for front and back faces respectively) which correspond to the most polluted areas (see Table 1). Moreover, Table 3 reveals a statistically significant increase in the chromatic parameters a^* and b^* on all studied calcarenite tablets (on both back and front faces) which result in a displacement towards more red and yellow tonalities (i.e. warmer colors) of the stones.

Table 3. Lightness (L*), a* and b* parameters and chroma (C* = $\sqrt{(a^*)^2+(b^*)^2}$) for SP calcarenite in fresh tablet and aged tablets after exposure to urban environment in several sites of Granada (see Fig. 1 and Table 1 for locations). ΔL* and ΔC* mean difference in lightness and chroma with respect to the fresh quarried calcarenite sample.

Front face											
	n	L*	σ	a*	σ	b*	σ	C*	σ	ΔL*	ΔC*
Fresh	24	91.00	0.56	0.34	0.17	5.90	0.40	5.91	0.40		
Site1	24	82.89	2.10	1.57	0.23	9.79	1.19	9.91	1.21	-8.12	4.00
Site2	18	87.00	0.59	0.67	0.07	7.39	0.58	7.42	0.58	-4.01	1.51
Site3	22	86.34	1.47	0.66	0.12	6.39	0.74	6.42	0.74	-4.66	0.51**
Site4	20	80.16	5.93	1.41	0.96	10.13	3.79	10.24	3.89	-10.84	4.33
Back face											
	n	L*	σ	a*	σ	b*	σ	C*	σ	ΔL*	ΔC*
Fresh	24	90.86	0.81	0.55	0.12	7.48	0.92	7.50	0.92		
Site1	24	84.89	2.83	1.05	0.38	11.44	3.39	11.49	3.41	-5.97	4.00
Site2	22	89.81	0.78	0.52	0.14	6.80	0.58	6.82	0.59	-1.05	-0.67**
Site3	22	85.33	1.46	0.78	0.07	6.99	0.76	7.03	0.76	-5.53	-0.47**
Site4	24	79.33	5.24	1.47	0.82	11.20	3.24	11.30	3.32	-11.53	3.81

n = number of measurements, σ = standard deviation. All differences are statistically significant at P = 0.01 except for those marked with two asterisks.

In order to better appreciate the effect of black soiling on the *Escúzar* calcarenite, the L^*, a^*, b^* and C^* values were plotted as shown in Fig. 6. The degree of chromatic modification can be estimated by comparing the scattering of the data between the fresh tablet and the aged stone tablets. Fig. 6a shows that parameters a^* and b^* were modified to some extend in the front faces particularly on stones placed at sites 1 and 4, where differences of up to 3 and 10 units for a^* and b^* respectively were found. For the back faces (Fig. 6b) data were more scattered though again calcarenites located at the most polluted areas (sites 1 and 4) showed the highest tonalities changes compare to the fresh stone tablet.

Variations on lightness (L^*) relative to chroma (C^*) are displayed in Figs. 6c and d, where a negative correlation can be seen appointing for a black soiling process (soiling tends to increase C^*, i.e. color intensity, when L^* decreases). Once again results show that stone soiling was more acute in sites 1 and 4 (polluted areas) in both the front and back stone

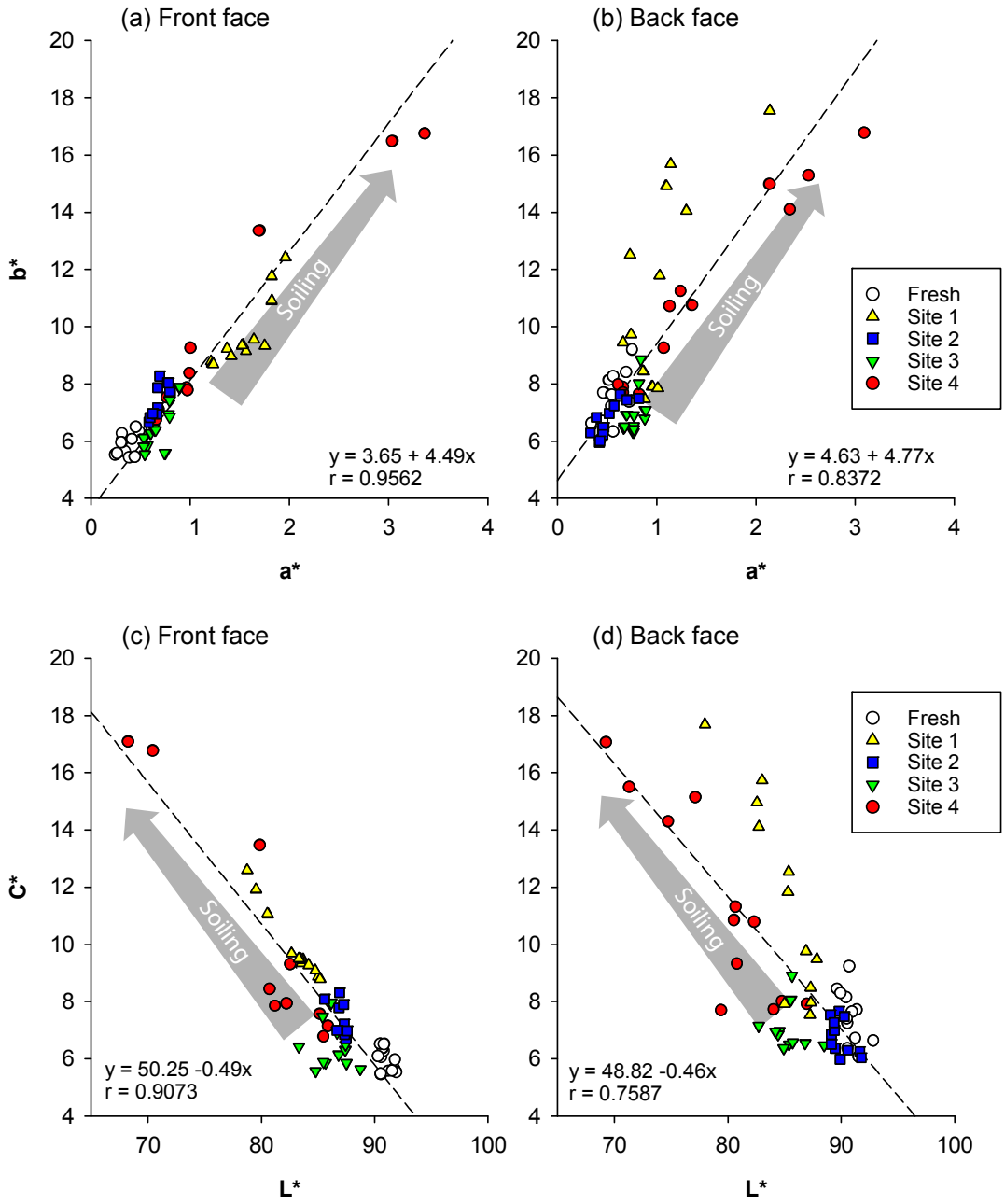

Figure 6. Variations in the absolute chromatic values a* relative to b* components in **(a)** front faces and **(b)** back faces for different locations exposed at the urban Granada conditions. Initial values are those corresponding to the quarried stone slab (black dots). Variations in lightness (L*) relative to chroma (C*) in **(c)** front faces and **(d)** back faces. Dashed lines are linear fit of the data. Fit equation and correlation coefficients are shown in each figure.

faces, though data were more scattered in the back stone faces (Fig. 6d). As previously noted the scattering of the chromatic data can be related to a differential erosion process of the stone related to the calcarenite heterogeneous texture (uneven distribution of micritic matrix and diverse types of bioclasts – sparitic areas–; see Figs. 5a and b). However, as mentioned before, surface roughness on front stone surfaces is more flat than the back faces, which might favor less scattered chromatic data.

Lightness (ΔL^*) and chroma (ΔC^*) absolute differences for all aged calcarenite tablets (on both front and back faces) were plotted respect to the fresh quarried stone tablet as Fig. 7 exhibits. In the CIELAB color space a perceptible color change - to the human eye - is defined by lightness and chroma differences greater than 3 units (Völz, 2001). In this work a perceptible negative change in lightness was observed on both the front and back faces of all stones indicating a perceptible stone darkening, except on the back face of calcarenite placed at site 2 (Fig. 7a). Regarding chroma variations, only visual changes were noticed on stones placed in the most polluted sites ($\Delta C^* > 3$) and with little difference between the front and back faces (Fig. 7b).

On the other hand, the area of a stone surface covered by atmospheric particles (i.e. effective area coverage, ECA) can be estimated from the following expression (Pio et al., 1998; Grossi et al., 2003):

$$\frac{L_t^*}{L_0^*} = (1 - AC) + \frac{L_p^*}{L_0^*} AC \qquad (1)$$

where AC is the fraction of the area covered by particles and L_p^* is the lightness of the settled particles (which here is assumed to be 30 for simplicity, Grossi et al., 2003). Table 4 shows the estimated EAC values (EAC = 100 · AC) for the front and back faces of all tested calcarenites. Those stones placed next to dense traffic streets (sites 1 and 4) exhibited the highest EAC values on both the front and back faces (ranging from 10.2% to 20.4%) compared to stones located at lower polluted areas with EAC values ranging from 1.7 to

9.4%. It is considered that EAC values above 2% are perceptible for the human eye and values up to 5% would trigger public complaints (in Grossi et al., 2003). In this work, all calcarenite surfaces (rain-sheltered and unsheltered) exposed to the urban environment of Granada in a two years time span (except one) have surpassed this value.

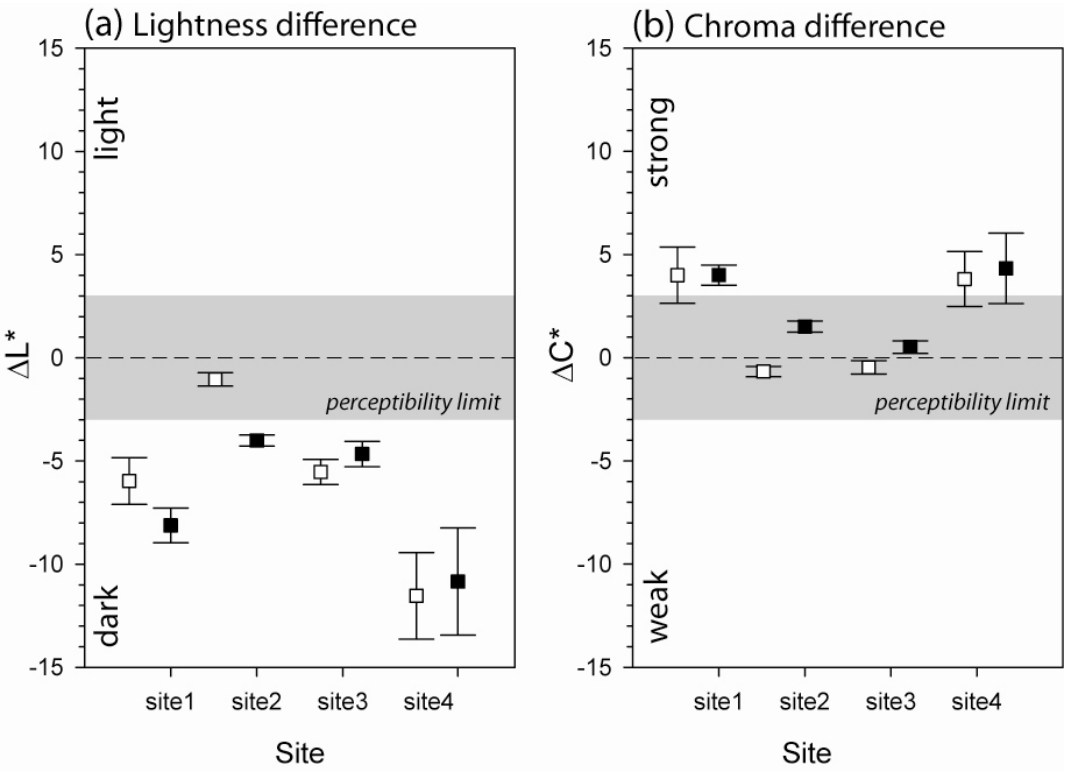

Figure 7. (a) Lightness and **(b)** chroma absolute differences with respect to the fresh quarried calcarenite slab. Empty and filled symbols are back and front faces respectively. Squares are mean values and bars are the confidence intervals for the mean at 95 %. Data outside the grey area (absolute change greater than ± 3 units) are considered to be perceptible.

The soiling coefficient (capacity of soiling of a stone independently of time and total suspended particulate, TSP, concentration) of building stone surfaces can be further determined by measuring changes in reflectance (lightness) through time when the concentration of the blackening agent in the air is known (e.g. Pio et al., 1998; Grossi et al., 2003). In this way, the change in reflectance at a certain time is linearly related to the square root of time (t) and the amount of TSP by the following expression,

$$L_t^* = L_0^* - SC\sqrt{TSP \cdot t}\,, \qquad (2)$$

where SC is the soiling coefficient. Grossi et al. (2003) found that each stone has a characteristic SC and that mainly depends on the initial stone lightness L_0^* (SC is higher when L_0^* is higher). Therefore, high SC values indicate that the blackening rate (negative changes in ΔL^* through time) of the stone surface is very high at constant TSP concentration. The most difficult parameter to constrain in equation (2) is TSP, and even more challenging is to estimate the TSP proportion responsible for blackening which is commonly associated to elemental carbon or black carbon (Pio et al., 1998; Grossi et al., 2003; Grossi & Brimblecombe, 2004, 2005; Brimblecombe, 2011). In this study the mean PM10 concentrations measured during the 2008 and 2009 atmospheric aerosols campaigns conducted in the city of Granada were used (see Fig. 1 for location of air quality stations). In these air quality stations black carbon particles were not directly measured but inferred from absorbers aerosols (Lyamani and Bravo Aranda, 2009, 2010).

From the specific literature it is clear the high proportion of black particles in the city of Granada. Based on light scattering and absorption properties of aerosol particles, Lyamani and co-workers (2008) found seasonal and diurnal variations of the single scattering albedo indicating fluctuation in the proportion of scattering (relate to sulfates) and strong absorbers aerosols (related to black carbon). Average values of single scattering albedo ranged from 0.5 to 0.8, indicating that about 35% of the aerosol light extinction was due to absorption, and thus to black carbon particles (Lyamani et al., 2008, 2010). On the other hand, Querol et al. (2004) observed that elemental carbon and organic carbon concentrations in Spain accounted for 10–25% (2.5–4.5 $\mu g \cdot m^{-3}$) of the regional PM10, 35% (~ 5 $\mu g \cdot m^{-3}$) of the urban background and 43% (~ 4 $\mu g \cdot m^{-3}$) of the urban kerbside site levels from Mediterranean and Atlantic regions. Only very recently direct measurements of black carbon concentration in the city of Granada have been provided (Horemans et al., submitted) revealing daily black carbon fluctuation with maximum ranging from 3 to 15 $\mu g \cdot m^{-3}$ and with average values of ~ 12-30% of PM10.

Table 4. Relative lightness difference (ΔL*), effective area coverage (EAC), time of exposure under urban conditions (t), particulate matter less than 10 μm (PM10) and estimated soiling coefficient (SC) for the front and back faces of the exposed SP calcarenite tablets in the studied sites.

	ΔL* (%)	EAC (%)	t (days)	PM10* $\mu g \cdot m^{-3}$)	SC x 10^{-2} ($days^{-1/2} \mu g^{-1/2} m^{3/2}$)
Front face					
Site1	-8.9	14.0	673	41	4.9
Site2	-4.4	6.7	587	35	2.8
Site3	-5.1	7.8	700	40	2.8
Site4	-11.9	19.0	825	39	6.0
Back face					
Site1	-6.6	10.2	673	41	3.6
Site2	-1.2	1.7	587	35	0.7
Site3	-6.1	9.4	700	40	3.3
Site4	-12.7	20.4	825	39	6.4

* Daily mean values for 2008/2009 of closest air quality stations (Lyamani et al., 2010).

In this work, a rough estimation of SC for both the front and back faces of all studied calcarenites was computed based on PM10 concentrations. The results are shown in Table 4. SC values for the front faces ranged from 2.8 to 6.0 x 10^{-2} $days^{-1/2}$ $\mu g^{-1/2} m^{3/2}$ (higher in polluted sites) whereas in back faces the range was wider (0.7 to 6.4 x 10^{-2} $days^{-1/2}$ $\mu g^{-1/2} m^{3/2}$). These values are comparable (though lower) to those values obtained for other types of bioclastic calcarenite placed in urban conditions in Atlantic (from 8.8 to 10.2 x 10^{-2} $days^{-1/2}$ $\mu g^{-1/2} m^{3/2}$) and continental climates (from 5.0 to 8.1 x 10^{-2} $days^{-1/2}$ $\mu g^{-1/2} m^{3/2}$) (Grossi et al., 2003). Furthermore, as Table 4 shows minor differences in SC were found between the front and back faces of all stones except the one placed at site 2. Considering that SC refers to the soiling capability of a stone and thus is independent of time and TSP concentration, the differences noticed here should be attributed to other(s) factor(s). As mentioned above differences in surface roughness between the front and back faces due to different conditions of exposure controlling stone differential erosion would play an important role.

On the other hand, the knowledge of SC is important to design cleaning policies if the aesthetic threshold of the lightness is provided (usually assumed to be $\Delta L^* = 35\%$, as described in Grossi et al., 2003 and Brimblecombe & Grossi, 2005). In this study a rough

appraisal of calcarenite cleaning frequency was done considering the highest estimated SC value (6.4 x 10^{-2} $days^{-1/2}$ $\mu g^{-1/2} m^{3/2}$, Table 4) and a constant PM10 concentration of 40 $\mu g\, m^{-3}$. Thus a reduction of 35% of the initial SP calcarenite lightness will happen after 17 years to urban exposure in Granada requiring cleaning actions.

9.3.4. Gypsum crust formation

Gypsum crusts (i.e. black crusts) were found in all sites with the exception of site 2. The occurrence of gypsum was confirmed by means of micro-Raman spectroscopy as shown in Fig. 8. SEM observation revealed that gypsum crystals varied from tabular (rose-shape) to more massive morphologies (Fig. 9). Small and euhedral (well-formed crystals) calcite rombohedrons (up to 5 μm) were often seen mantled by the gypsum crust. More likely the occurrence of these euhedral calcite crystals may result from the disintegration of the calcitic

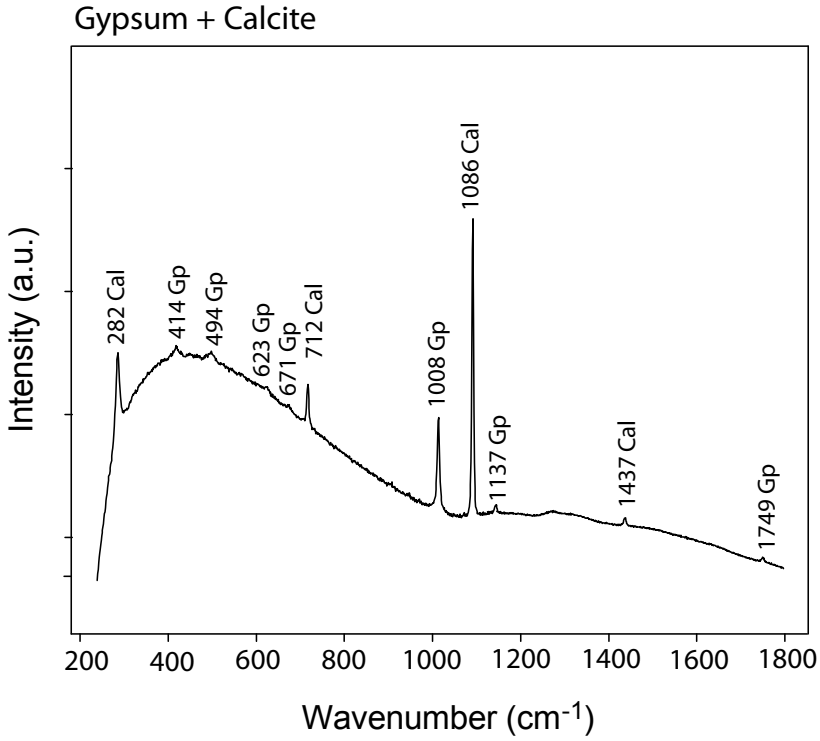

Figure 8. Raman spectrum of the stone crust showing the occurrence of a mixture of gypsum (Gp) and calcite (Cal).

matrix, however it cannot be discharged to result from dissolution-precipitation processes associated to the gypsum crust formation. Fig. 9 shows two SEM images of the aged calcarenite tablet (back face) placed at site 1 (high polluted area) during the ageing test. The gypsum crust was developed after the first year of exposure, with mean value of gypsum crystal size of 4.7 ± 1.4 μm (Fig. 9a). After the second year of exposure more abundant and bigger gypsum crystals, up to 12 μm, were formed as observed in Fig. 9b (and corresponding histogram).

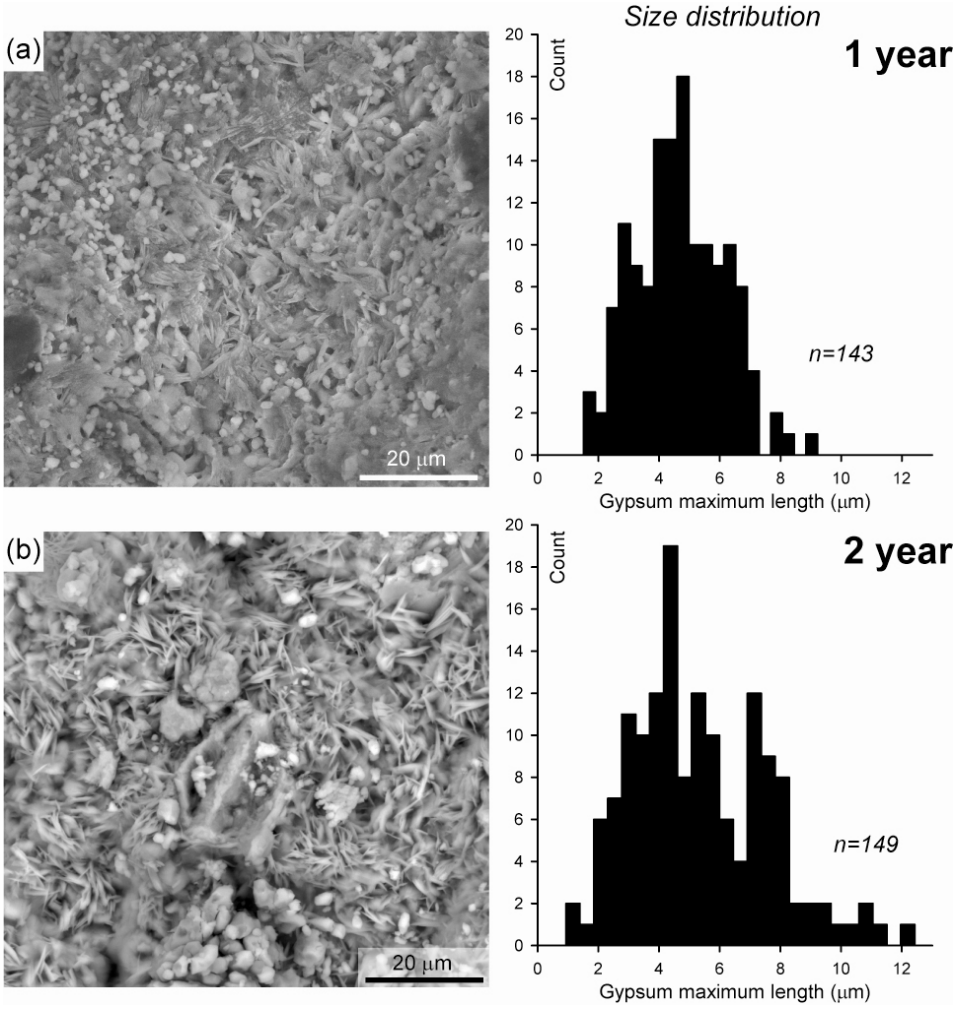

Figure 9. SEM images showing the black crust formed on the back surface of the calcarenite tablet placed at site 1 (high polluted area) after **(a)** one year and **(b)** two years of urban exposition. Note the tabular and more massive gypsum crystals developed after two years of test. Right: histograms obtained by image analysis from the corresponding SEM pictures showing gypsum crystal size distribution.

At the end of the test the thickness of all gypsum crusts were determined by means of SEM-EDX elemental mapping obtained from thin sections elaborated normal to the aged stones. Fig. 10 shows a false-color mineral map elaborated from a SEM-EDX elemental mapping of the aged calcarenite placed at site 1 (back face). It can be observed that the gypsum crust formation is controlled by the surface roughness of the stone, which is eventually related to the occurrence of bioclasts with intraclastic porosity. Here the thickness of the gypsum crust attained ca. 50 µm (Fig. 9a), though thickness ca. 100 µm were found in the front face of other calcarenites. Gypsum crystals also were detected filling calcarenite pores at depths of ca. 500-700 µm (Fig. 9a and b). Average spectra (Fig. 9a, b) obtained from the gypsum crust indicate the occurrence of Si, Al, K and C suggesting that mineral dust particles and soot particles are mixed with the gypsum to form the black crust.

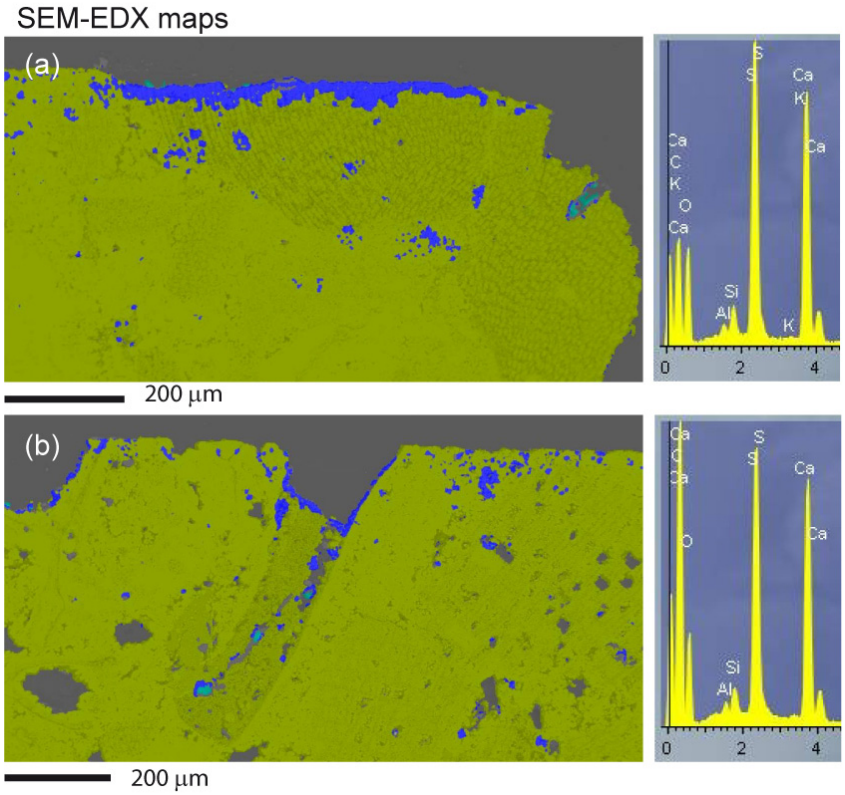

Figure 10. False-color mineral maps elaborated from SEM-EDX elemental mappings from thin sections cut normal to calcarenite tablet place at site 1 (back face). Pistachio represents calcite and blue gypsum. **(a)** Gypsum crust is preferentially developed over bioclasts. **(b)** Gypsum crust is irregularly developed on the surface of a large cavity and filling deeper porous. Right: corresponding average spectra of gypsum-rich areas (blue areas).

9.4. Concluding remarks

In this work the black soiling of the building *Escúzar* calcarenite (i.e. limestone) was estimated after a long-term exposure (ca. 2 years) under different contaminated urban conditions in the city of Granada (Southern Spain). The final goal was to evaluate the Cultural Heritage suitability of this stone to replace similar historic limestones in monuments in Andalusia, and its endurability in present civil buildings. The soiling process was studied by measuring variations in chromatic parameters, particularly in lightness (L^*, whose decrease indicates blackening of stones) on the front (rain-unsheltered) and back (rain-sheltered) calcarenite faces. Atmospheric particles responsible for stone soiling also were analyzed. Results revealed that soot particles (black carbon particles) and soil dust particles were the most abundant particles in the Granada air intensifying the stone darkening. After the first year of urban exposure, gypsum crusts developed on both front and back calcarenite faces in all tested sites with diverse pollution levels (except one site). Calculated total soiling (ΔL^*) corroborated black soiling of stones in all sites, though particularly at the most polluted areas and on rain-unsheltered (front) stone faces. In fact, on front faces surface roughness was higher than in back faces, fostering more intense differential erosion which in turn promotes a feedback process that would trigger further black soiling.

In a two years time span of exposure to the urban environment of Granada, rain-sheltered and unsheltered calcarenite surfaces placed in all sites (except one), surpassed the 2% EAC value (percentage of stone area covered by black particles or effective area coverage) which is considered to be the limit perceptible for the human eye. Indeed the EAC values obtained in this work range from 7.8 to 20.4%. The soiling coefficient (used to predict the frequency of stone cleaning practices) calculated in this work suggested that the *Escúzar* calcarenite will suffer a 35% reduction of its lightness after ca. 17 years to urban exposure in Granada, then requiring cleaning actions. This kind of study would help restorers to be aware of the most vulnerable areas for architectural stones in polluted cities. Furthermore, cleaning policies can be better planned based on these valuable data.

9.5. References

Beloin NJ, Haynie FH. Soiling of building surfaces. J Air Poll Control Assoc 1975 ; 25:393-403.

Böke H, Göktürk EH, Caner-Saltik EN, Demirci S. Effect of airborne particle on SO_2-calcite reaction. Appl Surf Sci 1999;140:70-82.

Böke H, Hale Göktürk EH, Caner Saltik EN. Effect of some surfactants on SO2-marble reaction. Mat Letters 2002;57:935-939.

Brimblecombe P, Grossi CM. Aesthetic thresholds and blackening of stone buildings. Sci Total Environ 2005;349:175-189.

Brimblecombe P, Grossi CM. Damage to buildings from future climate and pollution. APT Bull 2007;38:13-18.

Brimblecombe P. Environment and architectural stone. In: Siegesmund S, Snethlage, R, editors. Stone in architecture: properties, durability, Springer; 2011. p. 317-346.

Camuffo D, Del Monte M, Ongaro A. The pH of the atmospheric precipitation in Venice, related to both the dynamics of precipitation events and the weathering of monuments. Sci Total Environ 1984;40:125-139.

Cardell C. Cristalización de sales en calcarenitas: aplicación al monasterio de San Jerónimo, Granada (Spain). PhD Thesis, Dept. Mineralogy and Petrology, University of Granada, Granada. 1998.

Cardell C, Vleugels G, Torfs K, Van Grieken R. The processes dominating Ca dissolution of limestone when exposed to ambient atmospheric conditions as determined by comparing dissolution models. Environ Geol 2002;43:160-171.

Cardell C, Benavente D, Rodriguez-Gordillo J. Weathering of limestone building material by mixed sulfate solutions. Characterization of stone microstructure, reaction products and decay forms. Mater Charact 2008;59:1371-1385.

Cardell C, Guerra I, Romero-Pastor J, Cultrone G, Rodriguez-Navarro A. Innovative analytical methodology combining micro-X-ray diffraction, scanning electron microscopy-based mineral maps, and diffuse reflectance infrared Fourier transform spectroscopy to characterize archeological artifacts. Anal Chem 2009a;81:604-611.

Cardell C, Guerra I, Sánchez-Navas A. SEM-EDX at the service of archaeology to unravel historic technology. Microscopy Today 2009b;17:28-33.

Charola AE, Ware R. Acid deposition and the deterioration of stone: a brief review of a broad topic. Geological Society, London, Special Publications 2002;205:393-406.

Creighton PJ, Lioy PJ, Haynie FH, Lemmons TJ, Miller JL, Gerhart J. Soiling by atmospheric aerosols in an urban industrial area. J Air Waste Manag Assoc 1990;40:1285–1289.

Delalieux F, Cardell-Fernández C, Torfs K, Vleugels G, Van Grieken R. Damage functions and mechanism equations derived from limestone weathering in field exposure. Water Air Soil Poll 2002;139:75–94.

Doehne E. Salt weathering: a selective review. In: Siegesmund S, Weiss T, Vollbrecht A, editors. Natural stone, weathering phenomena, conservation strategies and cases studies. Geological Society of London, Special Publications; 2002. p. 51-64.

Doehne E, Price C. Stone conservation: an overview of current research. (2nd ed.). Getty Conservation Institute: Los Angeles. 2010.

Esbert RM, Daz-Pache F, Grossi CM, Alonso FJ, Ordaz J. Airborne particulate matter around the Cathedral of Burgos (Castilla y Leon, Spain). Atmos Environ 2001;35:441-452.

Filippou M, Fasseas C, Karabourniotis G. Photosynthetic characteristics of olive tree (Olea europaea) bark. Tree Phys 2007;27:977-984.

Folk RL. The petrology of sedimentary rocks. Hemphill Publishing Company, Austin, Texas. 1981.

Grossi CM, Brimblecombe P. Aesthetics of simulated soiling patterns on architecture. Environ Sci Techn 2004;38:3971-3976.

Grossi CM, Esbert RM, Díaz-Pache F, Alonso FJ. Soiling of building stones in urban environments. Buil Environ 2003;38:147-159.

Hamilton R, Crabbe H. Environment, pollution and effects. In: Watt J, Tidblad J, Kucera V, Hamilton R, editors. The effects of air pollution on Cultural Heritage. Springer, Boston, MA; 2009. p 1-28.

Hamilton RS, Mansfield TA. The soiling of materials in the ambient atmosphere. Atmos Environ A. 1992;26:3291-3296.

Katrinak KA, Anderson JR, Buseck PR. Individual particle types in the aerosol of Phoenix, Arizona. Environ Sci Techn 1995;29:321-329.

Kindratenko VV, Van Espen PJM, Treiger BA, Van Grieken R. Fractal dimensional classification of aerosol particles by computer-controlled scanning electron microscopy. Environ Sci Techn 1994;28:2197-2202.

Kontozova-Deutsch V, Moreton Godoi RH, Worobiec A, Spolnik Z, Krata A, Deutsch F, Van Grieken R. Investigation of gaseous and particulate air pollutants at the Basilica Saint-Urbain in Troyes, related to the preservation of the medieval stained glass windows. Microch Acta 2008;162:425-432.

Kontozova-Deutsch V, Cardell C, Urosevic M, Ruiz-Agudo E, Deutsch F, Van Grieken R.. Characterization of indoor and outdoor atmospheric pollutants impacting architectural monuments: the case of San Jerónimo Monastery (Granada, Spain). Environ Earth Sci 2010;DOI 10.1007/s12665-010-0657-5

Lyamani H, Olmo FJ, Alados-Arboledas L. Long-term changes in aerosol radiative properties at Armilla (Spain). Atmos Environ 2004;38:5935-5943.

Lyamani H, Olmo FJ, Alados-Arboledas L. Light scattering and absorption properties of aerosol particles in the urban environment of Granada, Spain. Atmos Environ 2008;42:2630-2642.

Lyamani H, Bravo Aranda JA. Informe de calidad del aire de Granada: año 2008. Informe interno, Universidad de Granada, Granada (Spain). 2008. 61pp.

Lyamani H, Bravo Aranda JA. Informe de calidad del aire de Granada: año 2008. Informe interno, Universidad de Granada, Granada (Spain). 2009. 53pp.

Lyamani H, Olmo FJ, Alados-Arboledas L. Physical and optical properties of aerosols over an urban location in Spain: seasonal and diurnal variability. Atmos Chem Physics 2010;10:239–254.

Maravelaki-Kalaitzaki P. Black crusts and patinas on Pentelic marble from the Parthenon and Erechtheum (Acropolis, Athens): characterization and origin. Anal Chim Acta 2005;532:187-198.

Maravelaki-Kalaitzaki P, Biscontin G. Origin, characteristics and morphology of weathering crusts on Istria stone in Venice. Atmos Environ 1999;33:1699-1709.

Merinero R, Lunar R, Somoza L, Diaz-del-Rio V, Martinez-Frias J. Nucleation, growth and oxidation of framboidal pyrite associated with hydrocarbon-derived submarine chimneys: lessons learned from the Gulf of Cadiz. Eur J Min 2009;1:947-961.

Murr LE, Bang JJ. Electron microscope comparisons of fine and ultra-fine carbonaceous and non-carbonaceous, airborne particulates. Atmos Environ 2003;7:4795-4806.

Pio CA, Ramos MM, Duarte AC. Atmospheric aerosol and soiling of external surfaces in an urban environment. Atmos Environ 1998;2:1979-1989.

Pósfai M, Buseck PR. Nature and climate effects of individual tropospheric aerosol particles. Ann Rev Earth Plan Sc 2010;8:17-43.

Pósfai M, Anderson JR, Buseck PR, Sievering H. Soot and sulfate aerosol particles in the remote marine troposphere. J Geophys Res Lett 1999;104:21685-21693.

Querol X, Alastuey A, Viana MM, Rodriguez S, Artiñano B, Salvador P, Garcia do Santos S, Fernandez Patier R, Ruiz CR, de la Rosa J, Sanchez de la Campa A, Menendez M, Gil JI. Speciation and origin of PM10 and PM2.5 in Spain. J Aer Sci 2004;5:1151-1172.

Rodríguez-Navarro C, 1994. Causas y mecanismos de alteración de los materiales calcáreos de la catedrales de Granada y Jaén. Tesis Doctoral, Universidad de Granada, Granada, 435 pp.

Rodríguez-Navarro C, Sebastián E. Role of particulate matter from vehicle exhaust on porous building stones (limestone) sulfation. Sci Total Environ 1996;87:79-91.

Rodríguez-Navarro C, Sebastián-Pardo E, Ruiz-Agudo E. Plan Director del Hospital Real: Estudio de materiales, formas y mecanismos de alteración". Informe interno Universidad de Granada, Granada. 2008.

Scherer GW. Crystallization in pores. Cem Concr Res 1999;29:1347-1358.

Simão J, Ruiz-Agudo E, Rodriguez-Navarro C. Effects of particulate matter from gasoline and diesel vehicle exhaust emissions on silicate stones sulfation. Atmos Environ 2006;40:6905-6917.

Urosevic M, Sebastián-Pardo E, Ruiz-Agudo E, Cardell C. Physical properties of carbonate rocks used as a modern and historic construction material in Eastern Andalusia, Spain. Mat Constr 2011;61:93-114.

Vendrell-Saz M, Garcia-Vallès M, Alarcón S, Molera J. Environmental impact on the Roman monuments of Tarragona, Spain, Environ Geol 1996;27:263-269.

Viles HA. Can stone decay be chaotic? Geol Soc Amer Special Papers 2005;390:11-16.

Watt J, Tidblad J, Kucera V, Hamilton R. The effects of air pollution on Cultural Heritage. Springer;2009.

Wyszecki G, Stiles WS. Colour science. Concepts and methods, quantitative data and formulae. 2nd ed. J. Wiley & Sons, New York; 1982.

Xie Y, Hopke PK, Wienke D. Airborne particle classification with a combination of chemical composition and shape index utilizing an adaptive resonance artificial neutral network. Environ Sci Techn 1994;28:1921-1928.

Chapter 10

GENERAL CONCLUSIONS and FUTURE WORK PERSPECTIVES

General conclusions

This last chapter briefly summarizes the main conclusions of this PhD Thesis, which address the physico-chemical decay of carbonate stones caused by air pollution and mineral dissolution processes. This PhD study focused on the city of Granada (Southern Spain) as an outstanding example where carbonate stones constitute a considerable part of its Architectural Heritage. Therefore, most of its historic buildings are exposed to weathering, mainly caused by mineral dissolution-precipitation processes and atmospheric aerosols impact in this medium-polluted urban environment.

This PhD Thesis presents a detailed petrographic and physico-mechanical characterization of two fresh carbonate stones (*Escúzar* calcarenite and *Olivillo* travertine) which are currently quarried and can potentially replace two stones extensively used in the architectural heritage of Granada, i.e. *La Escribana* calcarenite and *Alfacar* travertine respectively. As a common practice in restoration works, strongly weathered stones from historic buildings are usually replaced. When it is possible the stone is replaced by the same material (if the ancient/historic quarry is known and still active) or most frequently by

similar geological materials. The petrophysical characterization of the latter materials is crucial for restorers and conservators to better design replacement strategies when a deteriorated stone building of cultural interest needs to be repaired. The comparison of the physical properties of the *Escúzar* calcarenite and the *Olivillo* travertine with those from the original/historic quarries has enabled to establish their suitability as replacement stones. The *Escúzar* calcarenite has larger pore cavities and higher open porosity than *La Escribana* calcarenite. From a chromatic point of view both calcarenites are rather similar. This is of particular interest because the stone replacement would have no detriment to the overall aesthetic view of the repaired historic building or monument. Nevertheless, the higher anisotropy of the *Escúzar* calcarenite and, to a lesser extent its different hydraulic behavior must be taken into account in restoration projects. Regarding, the *Olivillo* travertine, this stone exhibits much lower free water absorption/desorption and effective porosity values than the historic *Alfacar* variety, along with higher Young's modulus indicating the excellent mechanical properties of the *Olivillo* stone. However, the significant chromatic differences between both travertines point to reduced suitability of the *Olivillo* travertine as substitutive material for the *Alfacar* stone.

In addition to the above described intrinsic factors related to the physico-mechanical properties stones, extrinsic factors also play an important role in the weathering of stones under polluted urban conditions. Extrinsic factors are associated (among other agents) with concentrations of atmospheric gaseous pollutants, and composition, size and morphology of particulate matter which interacts with the stone surface. Furthermore these extrinsic factors are different at indoor and outdoor environments and can be highly variable at different sites of a city. In this Thesis the constraining of these parameters at indoor and outdoor conditions was performed at the monastery of San Jerónimo in Granada (Southern Spain). This is the first air quality study performed in a monument in the city of Granada with the aim of developing a strategy for preventive conservation. Moreover, it should be note that other research groups from the University of Granada study atmospheric aerosols, though mainly focusing on their optical and physical properties and concentrations of gaseous pollutants. Thus, the contribution of this Thesis to the knowledge of the elemental and mineralogical

composition, and morphological characteristics of particulate matter in the city of Granada is noteworthy.

Abundant soil dust particles (aluminosilicates, calcite, dolomite, quartz and clay minerals) and ca. 9% of black carbon particles (soot particles) were detected outside the monastery of San Jerónimo. Chloride, sulfate and ammonium-rich salts and minor amounts of Br and spherical Fe-rich particles (related to traffic) were also observed. Inside the church of San Jerónimo, relatively high NO_2 and SO_2 concentrations were detected, implying an indoor–outdoor air exchange. Particulate matter composition at indoor air was similar than outside though inside the building high levels of S, Pb, and chloride- and sulfate-rich aerosols were identified. These findings suggest that the source of these particles is related to the intense weathering of the construction and decorative materials of the church, as well as the copious efflorescences in its interior. Indeed, chemical reactions between chloride-rich salts and Fe-rich pigments from the paintings were identified through the recognition of iron chloride particles. All of these particles promote a feedback process that triggers further weathering of the mentioned indoor materials. Moreover, it was found that the unfortunate cleaning habits (i.e. dusting) in the monastery fostered blackening of distant and isolated surface decorative materials via particle re-suspension. On the other hand, an important finding in this investigation was the detection of marine aerosols (mainly in the form of aged salts, Ca–K–S and Ca–Na–K–S particles) as part of middle sized and coarse fraction of the particulate matter at outdoor conditions. This demonstrates that, in fact, influx of marine particles due to the prevailing S and SW wind patterns enables the transport of sea-salt particles towards the city of Granada (ca. 50 km from the Mediterranean Sea). Although in low quantities, these particles may interact with stone surface and led to weathering due to moist/dry cycles.

Therefore, the effect of marine aerosol on the decay of diverse carbonate stones was experimentally reproduced in a controlled chamber in order to understand how these salt dissolution and precipitation cycles led to salt damage of stone material. Additionally, this ageing test was performed on two contrasting stone finishing surfaces, namely rough and polished surfaces, with the aim to survey the effect of commercial finishing. The results

reveal that the polished finishing of studied *Olivillo* travertine is combined with a gypsum-based plaster and an epoxy silicone resin infilling that protects the travertine against marine salt corrosion. On the basis of surface fractal dimension analyses, it is clear that this finishing process effectively blocks the pore system in the near-surface zone of the travertine, thus preventing penetration of the sea-salt spray into the stone. By contrast, on the irregular rough travertine surfaces, salt crystallization was more abundant and induced larger open porosity which in turn makes it more vulnerable to further salt spray attack. On the one hand, this work emphasizes the need to perform *ad hoc*, realistic long-term salt-spray ageing tests on construction and decorative materials for the design of proper processing, protection, maintenance and intervention protocols for civil and historic buildings. On the other hand, this study aware that prior to establishing conservation or maintenance practices, it is advisable to characterize the materials used in filled stones, since undesirable infilling products such as gypsum can activate weathering mechanisms.

In addition, the same test was also applied to a compact, low porous dolomite bearing limestone (*Sierra Elvira* limestone). It was found that contrasting sequence of salt precipitation and allied morphologies were developed on polished and rough limestone surfaces. The obtained results suggested that the stone surface finishing strongly controlled the absorption of the sea-salt spray and salt crystallization onto the stone surface. Detailed observation of the limestone surface after the ageing test also revealed the occurrence of micropitting on calcite cleavage surfaces, thus indicating active dissolution processes of carbonates. This chemical interaction was, however, more limited for dolomite where dissolution evidence on its surfaces was far less common. Chemical dissolution and crystallization of soluble salts in building materials play a critical role in the decay of carbonate stone. However the physical and chemical processes behind this decay are not completely well understood especially in carbonate minerals such as dolomite.

Literature agrees that dolomite dissolution reaction is complex compared to other common carbonates. To improve our knowledge of the nanoscale processes governing dolomite-fluid interactions, a systematic *in situ* Atomic Force Microscopy (AFM) study was performed in this PhD Thesis to estimate the dissolution rate of dolomite in the pH range 3-

10. All previous nanoscale studies of dolomite dissolution rates were conducted at fixed pH conditions and, to date, a systematic study of the dependence of dissolution rates on pH as in the case of macroscopic flow-through or batch reaction experiments was not reported. The results of this study showed that the overall dolomite dissolution rate was controlled by the removal of dolomite layers by spreading and coalescence of shallow etch pits, nucleated at point defects and/or in defect-free areas. Moreover, results also suggested that at all pH (and mainly at pH < 5) and under conditions of relatively slow solution flow, dolomite dissolves via a dissolution-precipitation reaction with the formation of an Mg-rich surface precipitate (most probably nesquehonite $MgCO_3 \cdot 3H_2O$). The growth of this new phase occurred by lateral spreading of 3D islands leading eventually to their coalescence, without a significant increase in their height. This finding is crucial to better understand the kinetics and mechanisms of carbonate dissolution which may help to determine the contribution of carbonate-fluid reactions to the global carbon cycle and CO_2 sequestration strategies, as well as to design new methods that mitigate the effects of acid rain on carbonate stones.

The danger to the Cultural Heritage from air pollution comes from several main sources such as the crystallization of soluble and insoluble salts inside the porous network, the increasing of corrosion induced by gases from the atmosphere, and the soiling of light colored stone surfaces due to black particles. They eventually lead to undesired chromatic changes, stone disaggregation, surface recession and development of black crust, among other deterioration forms. The above issues are addressed in the literature by combining (1) *ad hoc* experiments under controlled laboratory conditions, and (2) detailed observations of already weathered construction materials from polluted cities. However to unsure measurable results in relatively short times, these experiments are usually conducted under extreme environmental conditions which are usually far from those prevailing in urban conditions. Therefore a direct extrapolation to the nature is not simple and leads to several uncertainties in the estimation of decay rates which are an important issue in the sustainability of Cultural Heritage.

The last part of this PhD Thesis is aimed to investigate the black soiling of the *Escúzar* calcarenite (used to replace similar historic carbonate stones in monuments in Andalusia

such as the Cordoba mosque) under Granada urban air during a long-term exposure test (period of 2008 and 2009). The soiling process was studied by measuring changes in lightness, L* (whose decrease indicates stone blackening) on rain-unsheltered and sheltered stone faces placed at four sites with *a priori* contrasting local pollution micro-environments. Atmospheric particles (responsible for stone soiling) deposited on the stone surfaces and filters also were analyzed. Soot particles (black carbon particles) and soil dust particles (phyllosilicates and clay minerals mixed with NaCl, Ca-sulfate salts and C-rich particles) were the most abundant particulate matter, intensifying stone darkening. Gypsum crusts developed on both the front and back calcarenite faces in all tested sites (except one) after one year of urban exposure mainly over calcarenite intraclast porosity. Indeed *total soiling* (ΔL^*) corroborated black soiling of stones at all sites, particularly in the most polluted areas (heavy traffic and proximity to metropolitan construction), and on rain-unsheltered (front) stone faces. On the front faces high surface roughness foster more intense differential erosion than in back faces, which in turn promote a feedback process that trigger further black soiling.

In a two years time span of exposure to the urban environment of Granada, both rain-sheltered and unsheltered calcarenite surfaces placed in all sites (except one), surpassed the 2% EAC value (percentage of stone area covered by black particles or effective area coverage) which is considered to be the limit perceptible for the human eye. Indeed the EAC values obtained in this work ranged from 7.8 to 20.4 %. The estimated *soiling coefficient* (used to predict the frequency of stone cleaning practices) suggested that the *Escúzar* calcarenite will suffer 35 % reduction of its lightness after ca. 17 years to urban exposure in Granada, then requiring cleaning actions.

All results presented in this PhD Thesis have been obtained by means of multianalytical approaches from nano- to macroscale. The use of numerous complementary techniques is essential to understand in depth the chemical and physical factors controlling stone decay. They include conventional techniques (e.g. XRD, SEM-EDX, porosity, ultrasonic or chromatic measurements), and more advanced analytical techniques such as micro-Raman spectroscopy and cutting-edge techniques like AFM or VSI.

Future Perspectives

Cultural Heritage Science comprises several research fields that involve an increasing number of specialists from different backgrounds. The transfer of knowledge from different disciplines is still challenging but future collective efforts can enhance our knowledge to find the most suitable strategies for preservation of our cultural legacy under urban polluted conditions. One of the main issues for an effective Cultural Heritage sustainability that need to be addressed in the future is to find the link between experimental data on stone decay rate and decay rate under actual urban environment. For instance, carbonate dissolution rates are fairly well known under well constrained laboratory conditions but their extrapolations to weathering rates of historic building made of carbonate stones are still poorly constrained. Accordingly two approaches should be followed:

- Identification of the main variables that control carbonate dissolution prevailing at different scales (from the experimental nanoscale to the macroscopic scale of the building stone). On this regard, vertical scanning interferometry (VSI) is a promising technique that will provide in the next future the unique opportunity to link nanoscale observations (e.g. AFM) and bulk dissolution experiments (e.g. batch reactors).
- Monitoring of the main identified variables controlling the decay rate at the sites where weathering under polluted environments is taking place.

Whereas the first point requires a considerable investment in instrumental equipment, the second point is relatively easy to tackle. Surprisingly there are still little systematic *in situ* studies in urban conditions addressing this issue. The indoor and outdoor monitoring of atmospheric gases and sampling of particulate matter in outstanding historic buildings for instance, is an essential step on this matter. Long-term studies, similar to those presented in this PhD Thesis, will be also of benefice. More ambitious *in situ* experiments could also include the estimation of precise soiling rates by placing stone samples near to existing air quality station and additionally monitoring other important variables such as pluviometry or sun irradiation. The latter has been traditionally neglected but the direct effect of sun

irradiation, especially in cities like Granada with hot summers and an important daily thermal amplitude, contributes to a great extend to aesthetic chromatic modifications. The air quality station network of Granada has one station located at the Granada coast (Motril). Long-term studies on this station are very important to understand how the decay pattern and decay rates are modified due to higher influence of marine aerosols related to the inland situation of the city of Granada.

On the other hand, *in situ* observations of gypsum and allied black crust development are required to better understand the details of this process, which include complex mineral dissolution and precipitation steps. The use of novel analytical techniques of micro-sized precipitates observed in nature such as the structural and chemical analyzer namely SCA by *Renishaw* (use of VPSEM and Raman spectroscopy in tandem), will improve our ability to characterize more precisely minor mineral phases like oxalates in black crusts, in addition to organic compounds. Moreover this technique also permits to identify the spatial distribution of precipitate phases through micro-Raman mapping. Therefore, the distribution of soot particles on the surface and its connection with gypsum development can be easily tracked even at slow reaction rates that are typical of urban conditions.

Chapter 11

CONCLUSIONES GENERALES y PERSPECTIVAS FUTURAS

En este último capítulo se presentan de manera resumida las principales conclusiones derivadas de esta Tesis Doctoral, en la que se ha abordado el estudio del deterioro físico-químico de rocas carbonatadas como consecuencia de la contaminación atmosférica y los procesos de disolución mineral. Este trabajo doctoral se ha centrado en la ciudad de Granada (Sur de España) ya que esta ciudad alberga una gran cantidad de Patrimonio Arquitectónico construido con rocas carbonatadas. Es por ello que la mayoría de estos edificios están sujetos a alteración, principalmente debido a procesos de disolución-precipitación así como al impacto de la contaminación atmosférica existente en el contexto urbano de esta ciudad.

En primer lugar, este trabajo de investigación presenta una detallada caracterización petrofísica y físico-mecánica de dos rocas carbonatadas (la calcarenita de *Escúzar* y el travertino *Olivillo*) explotadas en la actualidad, y que potencialmente pueden utilizarse como material de sustitución de rocas tradicionalmente utilizadas en el Patrimonio Arquitectónico de Granada, i.e. la calcarenita de *la Escribana* y el travertino de *Alfacar*, pero también de otros monumentos de Andalucía. Una práctica habitual en los trabajos de restauración es el reemplazamiento de materiales altamente deteriorados. Cuando es posible, las partes alteradas son sustituidas por el mismo material (cuando la cantera original se conoce y sigue

siendo activa en la actualidad) o, de manera más habitual, son sustituidas por materiales geológicos similares. En el último caso, la caracterización petrofísica de los materiales que potencialmente se pueden utilizar en la sustitución es crucial para que arquitectos y restauradores diseñen estrategias óptimas de reemplazamiento.

La comparación de las propiedades físicas de la calcarenita de *Escúzar* y del travertino *Olivillo* con los materiales procedentes de las canteras históricas ha permitido establecer la idoneidad de estas rocas como material de sustitución. La calcarenita de *Escúzar* posee cavidades de mayor tamaño, así como una mayor porosidad comparadas con la calcarenita de *la Escribana*. Desde el punto de vista cromático ambas calcarenitas son muy similares. Este hecho es de particular interés ya que el reemplazamiento de un material pétreo por otro no debe producir un detrimento en la percepción estética del edificio o monumento que ha de ser reparado. Sin embargo, la mayor anisotropía de la calcarenita de *Escúzar* y, en menor medida, las diferencias de comportamiento hídrico deben ser tenidas en cuenta en los futuros proyectos de restauración. Por su parte, el travertino *Olivillo* exhibe una menor capacidad de absorción/desorción libre de agua, así como una menor porosidad efectiva en relación al travertino tradicional de *Alfacar*. A estas propiedades se le une el hecho de que la piedra *Olivillo* presenta mayores valores del módulo de Young indicando unas excelentes cualidades mecánicas. Sin embargo las importantes diferencias cromáticas entre los dos travertinos reducen la idoneidad del travertino *Olivillo* como material de reemplazamiento de la piedra de *Alfacar*.

Además de los factores intrínsecos relacionados con las propiedades físico-mecánicas mencionados anteriormente, determinados factores extrínsecos juegan un papel primordial en el deterioro de la piedra en ambientes urbanos contaminados. Los factores extrínsecos están asociados (entre otros agentes) con la concentración de gases contaminantes en la atmósfera, así como con la composición, tamaño y morfología de las partículas en suspensión que interaccionan con la superficie de la roca. Además, estos factores extrínsecos difieren en el interior y exterior de edificios históricos y pueden variar de manera considerable en diferentes puntos de la ciudad. En esta Tesis Doctoral varios de estos parámetros se han cuantificado en el ambiente interior y exterior del monasterio de San

Jerónimo, en la ciudad de Granada. Este es el primer estudio de este tipo realizado en esta ciudad con el objetivo de desarrollar políticas preventivas de conservación. Cabe destacar que otros grupos de investigación de la Universidad de Granada están activamente involucrados en el estudio de aerosoles atmosféricos, aunque principalmente enfocados en su caracterización a través de sus propiedades ópticas, así como en la determinación de la concentración de gases contaminantes. Es por ello que esta Tesis, que presenta datos sobre la composición elemental, mineralógica y características morfológicas de las partículas en suspensión de la ciudad de Granada, contribuye a un mejor conocimiento de las mismas.

En esta investigación se han detectado abundantes partículas de polvo terrígeno *(soil dust particles*), i.e. aluminosilicatos, calcita, dolomita, cuarzo y minerales de arcilla y aproximadamente un 9% de partículas carbonáceas (hollín) en el exterior del monasterio de San Jerónimo. Así mismo se han identificado aerosoles compuestos por cloruros, sales sulfatadas y sales ricas en amonio, y cantidades menores de Br y partículas esféricas ricas en hierro que deben relacionarse con el tráfico. Dentro de la iglesia de San Jerónimo, se han detectaron cantidades relativamente altas de NO_2 y SO_2, indicando un eficiente intercambio de aire entre el exterior e interior del edificio. La composición de las partículas en suspensión fue similar a la observada en el exterior, con la salvedad de altos niveles de S, Pb y aerosoles ricos en cloruros y sulfatos. Estas observaciones sugieren que el origen de estas partículas está relacionado con una intensa alteración de los materiales de construcción y decorativos de la iglesia, así como de numerosas eflorescencias de sales solubles e insolubles en su interior. De hecho se han identificado partículas de cloruro ferroso como producto de reacción entre las sales ricas en cloruro y los pigmentos a base de hierro procedentes de las pinturas del templo. Todas estas partículas propician un proceso de retroalimentación que produce a su vez una mayor degradación de los materiales mencionados del interior de la iglesia. Igualmente, se ha observado que los desafortunados hábitos de limpieza en el monasterio propician el ennegrecimiento de sus materiales constructivos y decorativos, incluso en zonas distantes y aisladas debido a la resuspensión de partículas. Por otra parte un hallazgo importante fue la determinación de aerosoles marinos (principalmente en forma de sales marinas evolucionadas, y partículas de Ca-K-S y Ca-Na-K-S) en la fracción media y gruesa de las partículas en suspensión en el exterior del edificio. Esto demuestra que los

vientos predominantes del S y SO permiten el transporte de aerosoles marinos desde la costa a la ciudad de Granada, situada a unos 50 km del mar Mediterráneo. Aunque en bajas cantidades, estas partículas pueden interaccionar con la superficie de la roca y ocasionar su deterioro como consecuencia de ciclos de humedad y secado.

Por otra parte, para poder comprender el efecto que los ciclos de disolución y precipitación de estos aerosoles marinos tienen en el deterioro de rocas carbonatadas, en esta Tesis se ha realizado un estudio experimental de envejecimiento en una cámara de niebla salina. Los ensayos de deterioro se realizaron sobre las rocas carbonatadas estudiadas con dos acabados superficiales diferentes, i.e. superficie pulida y rugosa, con el objetivo de determinar el efecto del acabado comercial en la degradación del material. Los resultados han revelado que el proceso de pulido comercial del travertino *Olivillo* está combinado con un relleno de los poros mediante una masilla que contiene yeso y una resina de silicona. A partir del análisis de la dimensión fractal de la superficie del entramado poroso del travertino, se ha comprobado que el proceso de pulido produce una reducción del sistema poroso cerca de su superficie, y por tanto evita la penetración del aerosol marino. Por el contrario, en la superficie irregular del acabado rugoso la cristalización de sales es mucho más abundante como consecuencia de una mayor porosidad libre que hace que este acabado sea más vulnerable al ataque del spray marino. Por otra parte, este trabajo pone de relieve la necesidad de realizar experimentos especialmente diseñados y de larga duración sobre materiales decorativos y de construcción con el fin de evaluar su respuesta frente a agentes de alteración. Los resultados de estos experimentos deben permitir diseñar protocolos de procesamiento, protección y mantenimiento de los materiales pétreos que constituyen las edificaciones históricas y civiles. Además este estudio enfatiza la importancia de caracterizar las masillas utilizadas por los fabricantes para rellenar los poros de rocas muy porosas (como el travertino), ya que la presencia de productos indeseables como el yeso puede activar procesos de alteración a medio plazo.

El test anterior ha sido aplicado también a una caliza compacta de baja porosidad y con cantidades apreciables de dolomita (caliza de *Sierra Elvira*). Se ha encontrado que la secuencia de cristalización y morfología de las sales precipitadas difiere entre las superficies

rocosas pulidas y rugosas. Los resultados obtenidos sugieren que el acabado superficial de las rocas controla fuertemente la absorción del spray marino y la cristalización de sales en superficie. Igualmente se ha puesto de manifiesto la acción de procesos de disolución mediante la existencia de micropicoteos (*micropitting*) en las superficies de exfoliación de la calcita tras el test de envejecimiento. Sin embargo, esta alteración química ha sido más limitada en el caso de los cristales de dolomita, donde apenas se han encontrado evidencias de procesos de disolución. La disolución química y la cristalización de sales solubles en el seno de materiales utilizados en la construcción juegan un papel crítico en el deterioro de materiales rocosos carbonatados. No obstante, los procesos físicos y químicos asociados a este deterioro aún no son del todo conocidos para el caso de rocas carbonatadas como la dolomita.

Existen numerosos estudios que demuestran que la reacción de disolución de la dolomita es mucho más compleja que la de otros carbonatos comunes como, por ejemplo, la calcita. Para tratar de comprender las complejas interacciones que tienen lugar en la interfase fluido-dolomita, se ha realizado un estudio sistemático a nanoescala utilizando un microscopio de fuerza atómica (AFM), determinándose la cinética y mecanismo de disolución de la dolomita en soluciones con pH comprendido entre 3 y 10. Todos los estudios previos sobre la disolución de la dolomita a nanoescala se habían realizado para un valor de pH fijo y, hasta la fecha, no se había realizado un estudio sistemático que relacionase velocidades de disolución con el pH, como en el caso de los experimentos de disolución en reactores de flujo. Los resultados de este trabajo muestran que la velocidad de disolución de la dolomita está controlada por la eliminación de capas atómicas mediante la propagación y coalescencia de pozos de disolución que nuclean en áreas libres de defectos. Por otra parte, los resultados sugieren que a todos los pH (y principalmente para pHs menores de 5) y bajo condiciones de flujo lento de la solución, la dolomita se disuelve mediante reacciones acopladas de disolución-precipitación que conllevan la formación de un precipitado superficial rico en magnesio (muy probablemente nesquehonita $MgCO_3 \cdot 3H_2O$). El crecimiento de esta nueva fase tuvo lugar por la propagación lateral y coalescencia de islas tridimensionales, sin un incremento significativo de su altura. Esta observación es crucial para poder comprender la cinética y los mecanismos de disolución de carbonatos que

pueden ayudar a determinar de la contribución de las reacciones fluido-carbonato en el ciclo global del carbono y en estrategias de secuestro de CO_2, así como para poder diseñar nuevos métodos para mitigar el efecto de la lluvia ácida sobre rocas ornamentales carbonatadas.

El impacto de la contaminación atmosférica en el Patrimonio Arquitectónico se debe a varias causas, como son la cristalización de sales solubles e insolubles dentro del sistema poroso rocoso, el aumento de corrosión inducida por gases atmosféricos, y el ennegrecimiento de las superficies pétreas debido al depósito de partículas contaminantes. Estas partículas finalmente causan cambios cromáticos no deseados, desagregación del material pétreo, erosión de la superficie y el desarrollo de costras negras, entre otras formas del deterioro. Los problemas mencionados anteriormente se intentan resolver mediante (1) aplicación de experimentos *ad hoc* en el laboratorio en condiciones climáticas controladas, y (2) observaciones detalladas de los materiales de construcción ya alterados por contaminantes atmosféricos. Sin embargo, para obtener resultados relevantes en un corto periodo de tiempo, estos experimentos se llevan a cabo normalmente en condiciones ambientales extremas que muchas veces no se acercan a las condiciones reales urbanas. Por tanto, la extrapolación directa de datos del laboratorio a los obtenidos en la naturaleza no es fácil y suele conllevar incertidumbres en la estimación de los grados de deterioro, que son importantes para la sostenibilidad del Patrimonio Arquitectónico.

La última parte de esta Tesis Doctoral presenta el estudio del proceso de ennegrecimiento de la calcarenita de *Escúzar* (usada para reemplazar similares materiales pétreos en monumentos de Andalucía, como es el caso de la Mezquita de Córdoba) expuesta a las condiciones urbanas de la ciudad de Granada durante un periodo de 2 años (2008 y 2009). El proceso de ennegrecimiento se ha estudiado a través de las medidas de cambios de luminosidad, L^* (la disminución indica el ennegrecimiento de la piedra) en caras rocosas expuestas y protegidas de la lluvia de los materiales pétreos colocados en cuatro sitios de la ciudad con contrastados microclimas y contaminación local. Se han analizado las partículas atmosféricas (responsables para el ennegrecimiento pétreo) depositadas en las superficies de las muestras de calcarenita, y en filtros específicos para tal fin. Las partículas de hollín (*soot*, i.e. partículas carbonáceas) y de polvo terrígeno (*soil dust particles*, e.g. filosilicatos y

minerales de arcilla mezclados con NaCl, sales de sulfatos de Ca y partículas ricas en carbono) fueron las partículas sólidas más abundantes identificadas, las cuales contribuyen decisivamente al ennegrecimiento del material pétreo. Tras un año de exposición en la atmósfera urbana granadina se desarrollaron costras de yeso en ambas caras de la calcarenita (expuestas y protegidas de la lluvia) en todos los sitios examinados (excepto en aquel donde la contaminación es menor). Las costras de yeso se formaron principalmente en las zonas de la calcarenita con porosidad intraclástica, e.g. en los bioclastos, frente a las zonas de matriz. El ennegrecimiento total (ΔL^*) estimado confirmó el oscurecimiento de todas las calcarenitas estudiadas, particularmente de las que estaban expuestas a las zonas más contaminadas (con tráfico intenso y cercanas a la construcción del tranvía metropolitano) y no protegidas de la lluvia. Los resultados han revelado que en las caras frontales la elevada rugosidad superficial ha favorecido una erosión diferencial más intensa que en las caras posteriores (protegidas de la lluvia). Este hecho promueve un proceso de retroalimentación en las caras frontales por cuanto favorece a su vez la intensificación de los procesos de alteración superficial por ennegrecimiento (*black soiling*).

En un plazo de tiempo de exposición de 2 años en la atmósfera urbana de la ciudad de Granada, se ha encontrado que todas las calcarenitas ensayadas (tanto en sus caras protegidas de la lluvia, como las expuestas), excepto en el emplazamiento urbano menos contaminado, han sobrepasado el límite del 2 % permitido de área de piedra cubierta por partículas negras o área de cobertura efectiva (EAC) que corresponde al valor perceptible de ennegrecimiento por el ojo humano. De hecho los valores obtenidos en esta tesis, comprendidos entre 7.8 % y 20.4 % (según los sitios estudiados) sobrepasan con creces tal límite. El coeficiente de ennegrecimiento (*soiling coefficient,* usado para predecir la frecuencia de limpieza de los materiales pétreos) calculado en esta investigación sugiere que la calcarenita de *Escúzar* sufrirá una reducción del 35 % de su luminosidad inicial (límite establecido para iniciar prácticas de limpieza) tras aproximadamente unos 17 años de exposición a la atmósfera urbana de la ciudad de Granada.

Los resultados obtenidos en esta Tesis Doctoral se han obtenido aplicando una combinación de técnicas analíticas tanto convencionales como novedosas que abarcan desde

la información a nanoescala a la macroescala. El uso de técnicas analíticas complementarias es fundamental para entender en profundidad los factores físico-químicos que controlan la alteración de rocas. Entre estas técnicas cabe mencionar las técnicas convencionales como la difracción o fluorescencia de rayos-X, las microscopías ópticas y electrónicas como el SEM;-EDX y el TEM, las medidas de porosidad, ultrasonidos y cromáticas de las rocas), así como técnicas analíticas más novedosas (e.g. microscopía Raman) o de última generación como la microscopía de fuerza atómica (AFM) o las técnicas de interferometría de barrido vertical (VSI).

Perspectivas futuras de trabajo

Actualmente, la ciencia del Patrimonio Cultural involucra varios campos de investigación y a un número creciente de especialistas con diferentes formaciones científicas y académicas. La transferencia de conocimiento entre estos campos de investigación no siempre es sencilla pero los esfuerzos de colaboración permitirán en el futuro un gran avance en nuestra capacidad para encontrar las estrategias más adecuadas para proteger nuestro legado cultural en ambientes contaminantes como el urbano. Uno de los puntos clave para una mejora en la sostenibilidad del Patrimonio Arquitectónico que necesita ser abordado en el futuro, es la búsqueda de factores de escala entre los datos experimentales sobre la velocidad de deterioro y la velocidad de degradación en ambientes urbanos reales. En este sentido, a pesar de que las velocidades de disolución de carbonatos son relativamente bien conocidas en condiciones experimentales de laboratorio, su extrapolación en velocidades de deterioro en edificios históricos construidos con rocas carbonatadas es aún, hoy día, muy limitada. Dos aproximaciones podrían seguirse para poder abordar esta problemática en el futuro:

- Identificación de las principales variables que controlan la disolución de carbonatos teniendo en cuenta varias escalas espaciales de observación (desde la escala nanoscópica experimental a la escala macroscópica de la piedra de construcción). En este sentido, la interferometría vertical de barrido (VSI) es una técnica prometedora,

ya que permitirá relacionar las observaciones a nanoescala (e.g. AFM) con los experimentos de disolución en reactores de flujo.

- Monitorización de las variables identificadas que controlan la velocidad de deterioro en aquellos lugares del ambiente urbano donde la alteración está teniendo lugar.

Mientras que el primer punto requiere una considerable inversión en equipamiento instrumental, el segundo es relativamente fácil de ejecutar. Sorprendentemente, aún existen pocos estudios sistemáticos *in situ* que aborden este aspecto en condiciones urbanas. La monitorización de los gases atmosféricos y el muestreo de las partículas en suspensión en zonas de interior y exterior de edificios históricos significativos es un paso esencial en este sentido. Asimismo, estudios *in situ* de alteración a largo plazo, como el presentado en esta Tesis Doctoral pueden ser muy útiles para avanzar en este aspecto. En el futuro se podrían abordar estudios *in situ* de este tipo más ambiciosos, con el objetivo de poder estimar coeficientes de ennegrecimiento (*soiling coefficient*) más precisos colocando muestras (pétreas y de otro tipo de material histórico) cerca de estaciones de calidad del aire, y monitorizando otras variables de especial interés como la pluviometría o la irradiación solar. Este último factor ha sido tradicionalmente poco considerado, pero es evidente que el efecto de la radiación solar, especialmente en ciudades como la de Granada, con veranos muy calurosos y una importante amplitud térmica diaria, contribuye en gran medida a las modificaciones cromáticas y estéticas del material pétreo. Es interesante mencionar que la red de estaciones de calidad de aire en la provincia de Granada incluye una estación costera (Motril). Estudios de larga duración en esta estación podrían ser muy importantes para poder comprender como los patrones y velocidades de deterioro pueden ser modificadas en ambientes con una alta influencia de aerosoles marinos, en comparación con las condiciones de interior de la ciudad de Granada.

Por otra parte, el estudio del desarrollo *in situ* de costras de yeso y costras negras es esencial para poder comprender en detalle los procesos de alteración que incluyen complejas reacciones de disolución y precipitación mineral. El uso de técnicas analíticas novedosas como el analizador estructural y químico *SCA* desarrollado por *Renishaw* (que combina la espectroscopia micro Raman con un microscopio electrónico de tipo VPSEM) en el estudio

de estos agregados de tamaño de grano muy fino, mejorará de manera sustancial nuestra capacidad para caracterizar de manera precisa los componentes minoritarios como oxalatos en las costras negras, así como la presencia de compuestos orgánicos. Además esta técnica puede permitir la identificación de la distribución espacial de los diferentes tipos de precipitados mediante mapas de micro-Raman. Por tanto, la distribución de las partículas de hollín en la superficie y la conexión de éstas con el desarrollo de costras de yeso pueden ser fácilmente identificadas incluso teniendo en cuenta las lentas velocidades de reacción propias de condiciones urbanas.

Chemical Geology 281 (2011) 364–371

Contents lists available at ScienceDirect

Chemical Geology

journal homepage: www.elsevier.com/locate/chemgeo

Research papers

Ion-specific effects on the kinetics of mineral dissolution

Encarnación Ruiz-Agudo [a,*], Maja Urosevic [b], Christine V. Putnis [a], Carlos Rodríguez-Navarro [b], Carolina Cardell [b], Andrew Putnis [a]

[a] Institut für Mineralogie, Universität Münster, Corrensstrasse 24, 48149, Münster, Germany
[b] Department of Mineralogy and Petrology, University of Granada, Campus Fuentenueva s/n, 18071, Granada, Spain

ARTICLE INFO

Article history:
Received 14 October 2010
Received in revised form 2 January 2011
Accepted 3 January 2011
Available online 7 January 2011

Editor: J. Fein

Keywords:
Dolomite dissolution
In situ AFM
Background electrolytes

ABSTRACT

Specific effects of background electrolytes on mineral growth and dissolution can be interpreted on the basis of the ability of ions to modify solute hydration, in a similar way to the systematic effects of inorganic ions on precipitation, structure and function of organic macromolecules (i.e., the Hofmeister effect). Here, the effect of a range of background electrolytes (sodium and chloride salts) on dolomite ($Ca_{0.5}Mg_{0.5}CO_3$) reactivity was investigated as a model system by measuring dissolution rates using in-situ Atomic Force Microscopy. The systematic trends found for the different ions are interpreted in terms of characteristic parameters of background ions such as effective hydrated radii. Entropic effects associated with the ordering of solvent molecules induced by constituting cations from the crystal ultimately dictate how electrolytes affect dissolution rates. In dilute electrolyte solutions, ion–ion interactions dominate and the stabilisation of the solvation shell of ions constituting the crystal, by counter-ions present in solution enhances the unfavourable entropic effect on dolomite dissolution. The tendency for electrolytes to form ion pairs in solution reduces such an effect, thus leading to an inverse correlation between dissolution rates and background ion separation in solution. On the other hand, in concentrated saline solutions the interaction between background ions and water molecules determines the hydration of a constituent ion immersed in an electrolyte solution. In this case, dissolution rates correlate with the mobility of background ions and, therefore, with their effective hydration radii. The observed effects of background ions on growth and dissolution could be applicable for other inorganic systems where the Hofmeister effect has been reported.
© 2011 Elsevier B.V. All rights reserved.

1. Introduction

It has long been recognised that specific ions at moderate to high concentrations in aqueous solutions can play important but very different roles on the crystallisation, structure and function of proteins (Kunz et al., 2004a; Zhang et al., 2005). It is also well known that most of these effects correlate with water affinity of the respective ions and follow a trend known as the lyotropic or Hofmeister series (Kunz et al., 2004b; Dove and Craven, 2005). Current research in this field suggests that the control that electrolytes exert on water structure is limited to the local environment surrounding the ion and is not related to long-range electric fields emanating from the ions but results from effects associated with the hydration shell(s) of the ions (Collins et al., 2007) and the ions' capacity to "break" or "structure" water (i.e., chaotropic and kosmotropic ions, respectively) (Parsons et al., 2010). Hofmeister effects are ubiquitous and numerous cases in which they apply can be found in biological systems. Examples of processes following the Hofmeister series include enzyme activity, protein stability, protein–protein interactions, protein crystallisation or optical rotation of sugars and amino acids (see Kunz et al., 2004a; Zhang et al., 2005 and Zhang and Cremer, 2006). Although there is still an on-going debate about the origin of these salt-specific effects (see for instance Cappa et al., 2006), their relation to hydration characteristics of ions is commonly accepted (Collins and Washabaugh, 1985; Collins et al., 2007). However, attempts to relate the Hofmeister effect to thermodynamic solvation properties of ions (e.g., enthalpy and entropy of hydration), generally yield no conclusive results. In fact, no single thermodynamic property associated with the solvation of ions has yet been found to unambiguously explain their hydration characteristics (Marcus, 1994a).

In the case of inorganic solids, the effect of ionic strength on growth and dissolution rates has been traditionally attributed to changes in solubility (i.e. a thermodynamic effect). The strong long-range electric fields emanating from the ions of the background electrolyte reduce the activity of the ions building the crystal due to charge screening, hence increasing its solubility. Nevertheless, several studies have shown that the dependence of growth or dissolution rates of minerals on ionic strength is complex, and is not independent of the ionic species producing it (Dove and Czank, 1995; Weaver et al., 2007; Kowacz and Putnis, 2008; Ruiz-Agudo et al., 2009,

* Corresponding author. Tel.: +49 251 83 36107; fax: +49 251 83 38397.
E-mail addresses: eruiz_01@uni-muenster.de, encaruiz@ugr.es (E. Ruiz-Agudo), maja@ugr.es (M. Urosevic), putnisc@uni-muenster.de (C.V. Putnis), carlosrn@ugr.es (C. Rodríguez-Navarro), cardell@ugr.es (C. Cardell), putnis@uni-muenster.de (A. Putnis).

0009-2541/$ – see front matter © 2011 Elsevier B.V. All rights reserved.
doi:10.1016/j.chemgeo.2011.01.003

2010). Ions having different surface charge density exert different effects that cannot be simply explained by continuum electrostatics models (i.e. those considering the ions as point charges). This suggests that purely thermodynamic considerations may not be enough to explain ion specific effects on mineral dissolution and growth and that kinetics may play a key role.

The systematic study of specific ion effects on the growth and dissolution of minerals has so far received little attention. Several experimental and computational studies have shown that crystal growth and dissolution rates of sulphates and carbonates are actually controlled by cation hydration–dehydration dynamics (Dove and Czank, 1995; Pokrovsky and Schott, 2002; Piana et al., 2006). Thus, any factor affecting cation solvation should alter growth and dissolution rates. A few recent studies have proposed that the specific effects of background electrolytes on the kinetics of crystal growth and dissolution can be interpreted on the basis of the ability of such electrolytes to modify hydration of the crystal constituting ions (i.e., the building units) (Kowacz and Putnis, 2008; Ruiz-Agudo et al., 2010). These experiments validate such an approach, and demonstrate the need for the inclusion of specific ion effects in the development of a predictive model that describes crystal growth and dissolution in complex systems, such as those found in nature (e.g., ocean water and rock pore solutions). However, there are several critical aspects that need further clarification in order to ensure the global character of this theory. In the previous studies, calcite ($CaCO_3$) and barite ($BaSO_4$) showed opposite trends in reactivity with respect to ion type, thus suggesting that the hydration characteristics of the crystal building units have a dramatic effect on the systematic trends observed for the different background salts. In this sense, with the presence of magnesium, in addition to calcium, in its structure, dolomite ($Ca_{0.5}Mg_{0.5}CO_3$) represents an ideal system to test this hypothesis. The high charge density of Mg^{2+} leads to a very strong solvation, higher than that of other alkali-earth cations (i.e., Ca^{2+} and Ba^{2+}) and may shed light on the ultimate mechanism and factors governing the interactions in solution of background ions with the constituting ions of a mineral. Furthermore, it is important to define relationships between crystal reactivity and fundamental parameters of the background ions that will enable extrapolation of these results to other systems. Here, we address the basic hypotheses that (i) the effect of electrolytes on mineral dissolution is governed by similar principles to those which apply in the case of organic macromolecules (e.g., Hofmeister effect on proteins salting-out) and are related to fundamental properties of the background ions in solution, and (ii) the systematic trends observed in mineral reactivity for the different background salts are determined by the hydration characteristics of the crystal building units.

To test these hypotheses, in-situ flow-through dissolution experiments were conducted using Atomic Force Microscopy (AFM) on dolomite cleavage surfaces in the presence of different 1:1 sodium and chloride salts. In the last 15 years the study of fluid–mineral interactions has experienced a considerable advance, largely due to the use of in-situ AFM. Using this technique, nanoscale real-time observations of crystal surfaces reacting with fluids can be performed, thus representing a valuable tool for precise and representative analysis of fluid–mineral interactions (Hillner et al., 1992; Putnis et al., 1995; Hall and Cullen, 1995; Jordan and Rammensee, 1997; Shtukenberg et al., 2005; Shiraki et al., 2007). Also, it allows quantification of the kinetics of these processes. The reactivity of carbonates can be optimally studied by means of AFM as most carbonate minerals have perfect cleavage, facilitating the study of nearly atomically flat surfaces. Furthermore, the dissolution of carbonates occurs by the retreat of unit-cell high steps and/or formation and spreading of etch pits, processes that are easily observed and quantified by AFM. The experimental approach presented in this study has enabled us to obtain quantitative information on the behaviour of dolomite in a range of solution compositions, with the aim of determining reactivity trends and ascertaining the principles that define changes in the kinetics of dissolution induced by background ions.

Our results show that the experimentally determined dependence of dolomite dissolution rates on ion type in concentrated solutions is ultimately related to the hydrated volume of the background ion, as an indicator of the strength of the interactions between background ions and the solvent molecules. Moreover, by comparison with other divalent carbonates and sulphates, it seems that the systematic of this dependence is controlled by the hydration characteristics of the cation building the crystal. In dilute solutions, the volume of solvent affected by the electrolytes is reduced and ion–ion interactions dominate.

2. Methodology

Optically transparent dolomite crystals from Eugui (Navarra, Spain) were cleaved in air along $\{10\bar{1}4\}$ planes with a knife blade. Dolomite crystals from Eugui have been commonly used in crystal chemistry studies of dolomite due to its high purity and perfection (Barber et al., 1981; Reeder and Nakajima, 1982; Spinolo and Anselmi-Tamburini, 1984). The crystals, ca. $3\times3\times1$ mm in size, were examined by optical microscopy to ensure that the cleavage surfaces were free of macroscopic steps and small particles. Crystals were cleaved immediately before each experiment. In-situ AFM dissolution experiments were carried out by passing prepared salt solutions of LiCl, NaCl, KCl, CsCl, NaI, NaF and $NaNO_3$ at different ionic strengths (IS = 0.001, 0.01, 0.1 and 1) over dolomite $\{10\bar{1}4\}$ cleavage surfaces. Na^+ and Cl^- ions are the most suitable counter ions to investigate the effects of different hydration properties of anions and cations on mineral dissolution, as they have been shown to have the least structural effects on the solvent (at room temperature) (Jákli, 2007). Table 1 shows experimental conditions for each saline solution. The natural pH of concentrated (IS = 1) LiCl, KCl, CsCl and $NaNO_3$ solutions was slightly acidic (pH<5.3), and it was adjusted to 7 using NaOH. PHREEQC (Parkhurst and Appelo, 1999) was used to calculate the ionic strength of the solutions. Deionised water (resistivity>18 $m\Omega^{-1}$) was passed over the surfaces before each experiment to clean the cleaved surface, as well as to adjust the AFM parameters as in Arvidson et al. (2006). Solutions were prepared immediately before the experiments to avoid the equilibration with CO_2 in the ambient air. Therefore, the amount of carbonate and bicarbonate ions in solutions is considered to be negligible. The absence of calcium and magnesium in the input solutions as well as the constant solution flow during the experiments ensured constant far-from-equilibrium conditions with respect to dolomite.

An Atomic Force Microscope (Digital Instruments Nanoscope III Multimode) equipped with an O-ring sealed fluid cell working in contact mode was used to study dolomite dissolution under ambient conditions (T = 20 °C). The scanning frequency was 4 Hz, giving an average time of 1.5 min per scan over 4 (2×2) and 9 (3×3) μm^2 dolomite surfaces. Solution flow rate (20 $\mu L\ s^{-1}$) was controlled by syringe injections. AFM images were collected using Si_3N_4 tips (Veeco Instruments, tip model NP-S20) and analysed with the Nanoscope software (Version 5.12b48). Measurements of step retreat velocity (or etch pit spreading rate) were made from sequential images scanned in the same direction. The retreat velocity, v_{sum}, was calculated by measuring the length increase per unit time between opposite parallel steps in sequential images.

3. Results

3.1. Dissolution features of etch pits

Dolomite dissolved on $\{10\bar{1}4\}$ cleavage surfaces by the formation and spreading of etch pits after contact with deionised water (pH 7) in the fluid cell. The etch pits were shallow (~0.3 nm height) rhombohedral pits at circumneutral pH (Fig. 1). This is the typical

etch pit morphology observed on dolomite surfaces in contact with highly undersaturated solutions (Higgins and Hu, 2005). No significant change in etch pit morphology was observed in the presence of the different background electrolytes tested. Angles between steps defining the etch pits were found to be ~77° and ~104°. The average etch pit density measured in deionised water was 2.25×10^9 cm^{-2}, which is 4 orders of magnitude higher than that observed by Luttge et al. (2003) at acidic pH (~3) using Vertical Scanning Interferometry (VSI). However, their study focussed on deep etch pits (depth up to 2 μm), most probably nucleated at dislocations (MacInnis and Brantley, 1992). The shallow etch pits considered in our study are nucleated either on point defects or, as the experiments were performed under far-from-equilibrium conditions, on defect-free areas of the surface. At the AFM scale, dolomite dissolution shows characteristics of Type I (Ca, Mn) carbonates, according to the classification of Duckworth and Martin (2004). These authors classified five isostructural carbonate minerals (Ca, Mn, Fe, Mg and Zn carbonates) into three different groups according to similarities in the dissolution behaviour. Type I carbonates show widespread distributed shallow rhombohedral pits, which are densely clustered and seem to be initiated by groups of point defects. However deep, isolated etch pits associated with the presence of line dislocations are observed on a larger scale (Luttge et al., 2003), and are typically reported for Type II (Fe, Mg) carbonates.

3.2. Dissolution kinetics

In flow-through experiments performed in AFM, the very low amount of calcium and magnesium in the outlet solution precludes obtaining reliable macroscopic dissolution rates from measurements of cation concentrations in the output solution (Arvidson et al., 2006). Furthermore, variations and uncertainties related to the reacting surface area contribute to significant error in macroscopic rate determinations, leading to an overestimation of macroscopic dissolution rates (Duckworth and Martin, 2004; Ruiz-Agudo et al., 2010). Thus, etch pit spreading rates determined from measurements of length changes in consecutive AFM images allow a more precise comparison between different solution compositions and, accordingly, comparative etch pit spreading rates have been measured for this study.

Values of the retreat velocity, v_{sum}, reported in this work refer to rate of change in etch pit length along either $[\bar{4}41]$ or $[4\,8\bar{1}]$ directions (Fig. 1). In deionised water, $v_{sum} = 0.09 \pm 0.01$ nm s^{-1}. Table 1 and Fig. 2 show v_{sum} as a function of ionic strength for the electrolytes tested. Although there is some scatter in the published data of dolomite dissolution rates as a function of pH, it seems that under conditions of low pCO_2 (total carbon<0.001 M), dolomite dissolution rates showed, in general, little change with solution pH for $5.4 \le pH \le 8$ (and total carbon<0.001 M) (see Pokrovsky et al., 1999 and Pokrovsky and Schott, 2001). For lower pH values, dissolution rates increase with decreasing pH. Most of the electrolyte solutions tested showed $5.6 \le pH \le 7$ (Table 1). The pH of KCl solutions at IS = 0.01 and IS = 0.1 is 5.3 and 5.4, respectively, so pH could have influenced the measured rate to some extent. Nevertheless, the rates in these cases were not faster than those measured in other electrolyte solutions of higher pH at the same IS. This suggests that the differences observed are not due to differences in solution pH. The average etch pit spreading velocity on the dolomite cleavage surface varied according to the nature of the background electrolyte at a low and constant ionic strength (IS = 0.001), increasing in the order $CsCl < NaNO_3 < LiCl \approx NaCl < NaI < KCl < NaF$. Note that the spreading rate in CsCl and $NaNO_3$ solution is lower than that observed in pure water, thus suggesting some kind of inhibitory effect on dolomite dissolution. The step retreat rate increased with increasing ionic strength for NaCl, CsCl and $NaNO_3$. However, in the case of KCl, LiCl and NaI, spreading rates were observed to remain constant or to slightly decrease when increasing the ionic strength from 0.01 to 1. In concentrated saline solutions (IS = 1), the etch pit spreading rate v_{sum} increased in the order $LiCl < CsCl < KCl < NaCl$ and $NaI < NaCl < NaNO_3$. Note that in the case of NaF, it was not possible to quantify the etch pit spreading rate at ionic strengths higher than 0.001 as they coalesced faster than the scanning rate. Additionally, extensive formation of precipitates (likely CaF_2 and/or MgF_2) was observed.

4. Discussion

Specific effects of background electrolytes on crystal dissolution can be interpreted on the basis of the ability of ions to modify solute hydration. Hydration of an ion in pure, deionised water is the result of a competition between ion–water (electrostatic) and water–water (hydration forces) interactions. Both can be affected when a background ion is present in solution (Kowacz and Putnis, 2008; Ruiz-Agudo et al., 2010). Solute–water and water–water interactions will determine the relative influence of electrolytes on dissolution rates at low and high ionic strength, respectively. In principle, dissolution should be favoured by a stronger hydration of the constituting ions and thus by increasing affinity of the water solvent to the building units of the dolomite crystal (increasing solute–water interactions) and/or by decreasing solvent affinity to the other solvent molecules (decreasing water–water interactions) in the respective salt solutions. However, as discussed in the next sections, entropic effects associated with the strong hydration of Ca^{2+} and Mg^{2+} dictates how electrolytes affect the kinetics of dolomite dissolution. Information about ion–solvent interactions is usually obtained either

Table 1
Average etch pit spreading rates (v_{sum}/nm s^{-1}) on dolomite cleavage surfaces for different background electrolytes as a function of ionic strength (IS).

IS	LiCl			KCl			CsCl			NaCl		
	pH	Mean	Std	pH	Mean	Std	pH	Mean	Std	pH	Mean	Std
Water	7.0	0.094	0.006	7.0	0.094	0.006	7.0	0.094	0.006	7.0	0.094	0.006
0.001	6.4	0.088	0.012	6.0	0.129	0.006	6.2	0.037	0.001	5.7	0.089	0.030
0.01	5.7	0.174	0.012	5.4	0.211	0.012	5.8	0.041	0.002	7.0	0.113	0.012
0.1	5.8	0.131	0.014	5.3	0.195	0.013	5.6	0.062	0.002	7.0	0.282	0.029
1	7.0[a]	0.070	0.039	7.0[a]	0.085	0.015	7.0[a]	0.080	0.027	7.2	0.290	0.052

IS	NaI			$NaNO_3$			NaF		
	pH	Mean	Std	pH	Mean	Std	pH	Mean	Std
Water	7.0	0.094	0.006	7.0	0.094	0.006	7.0	0.094	0.006
0.001	6.0	0.119	0.012	6.2	0.078	0.004	6.9	0.136	0.008
0.01	7.0	0.194	0.010	6.2	0.145	0.007			
0.1	7.4	0.171	0.020	5.6	0.341	0.018			
1	7.4	0.041	0.013	7.0[a]	0.430	0.083			

[a] pH adjusted using NaOH.

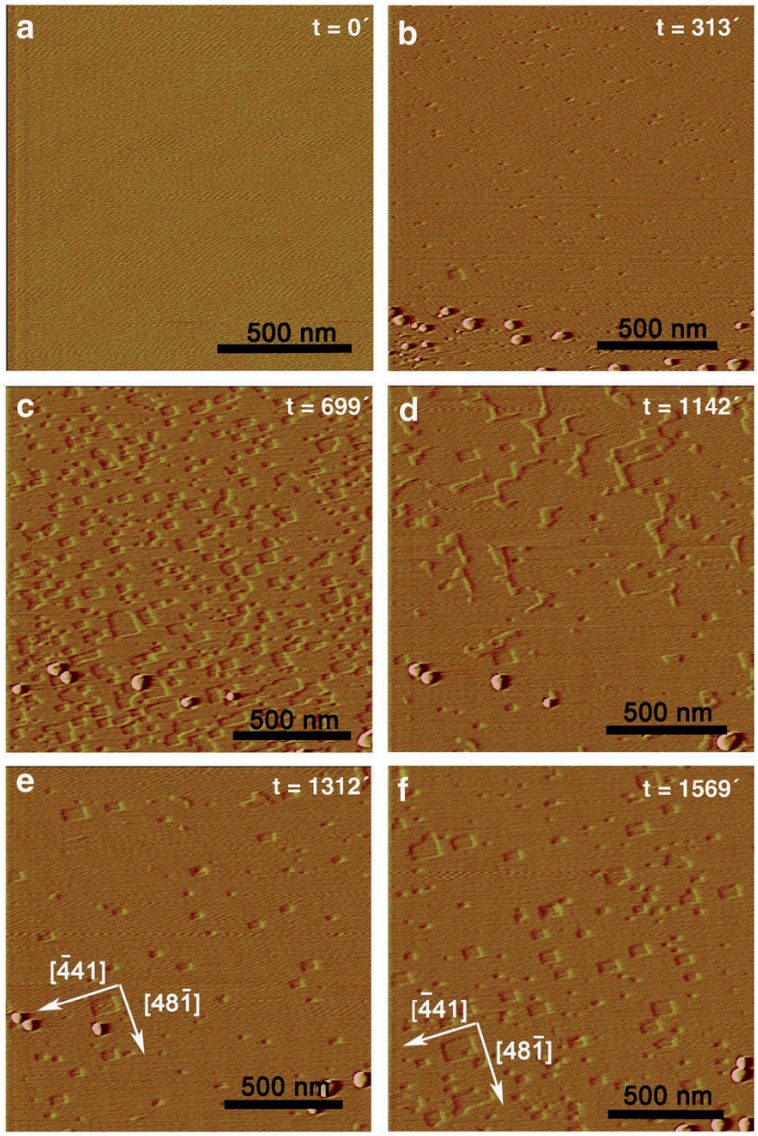

Fig. 1. AFM deflection images of a dolomite ($10\bar{1}4$) surface exposed to a highly undersaturated solution for increasing periods of time. Shallow etch pits with edges parallel to [$\bar{4}$41] and [4 8$\bar{1}$] form and spread as dissolution proceeds. Average etch pit depth ~0.3 nm. Background electrolyte: $NaNO_3$ (IS = 0.1).

from measurements of thermodynamic functions of hydration or from irreversible ionic transport processes such as conductance and ionic mobility (Nightingale, 1959). In the discussion below, we use the data obtained from transport processes in order to derive fundamental relationships between the impact of specific electrolytes on dissolution rates and characteristic properties of these background ions.

4.1. Dissolution at low ionic strength: stabilisation of Ca^{2+}/Mg^{2+} hydration shells by background electrolytes

The interaction between a solute ion and the water molecules in its hydration shell is stronger in dilute electrolyte solutions than in pure water, because the water molecules in the hydration shell are stabilised by their electrostatic attraction with the counter-ions in the solution (Samoilov, 1967; Samoilov, 1971). This effect is reduced by the tendency of the background cations and anions to pair in solution. When two ions are close in solution, their combined electric fields are screened and consequently their electrostatic influence on hydration water diminishes. Differences in the degree of ion pairing of the background salt in solution can be related to differences in diffusion coefficients (ΔD) of the ionic salt constituents in solution: increased ion pairing leads to smaller differences in ionic diffusivity between the cation and anion and should lead to a decrease in dissolution rate (Ruiz-Agudo et al., 2010). This is the trend observed in the dissolution of barite (Kowacz and Putnis, 2008). However, Fig. 3a shows that dolomite dissolution rates at low ionic strength (0.001) decrease with *increasing* differences in diffusion coefficients (ΔD) i.e. *decreasing* ion-pairing and thus, with increasing stabilisation of water in the solute-cation hydration shell. Values of ionic diffusion coefficients were taken from Koneshan et al. (1998) (Table 2). Due to the large uncertainties in the published values of ionic diffusion coefficients for Cs^+ and K^+, in the case of like-hydrated electrolytes such a trend is best observed if we use the solubility of the background salt as a rough "proxy" of ion separation in solution (Fig. 3b). The less

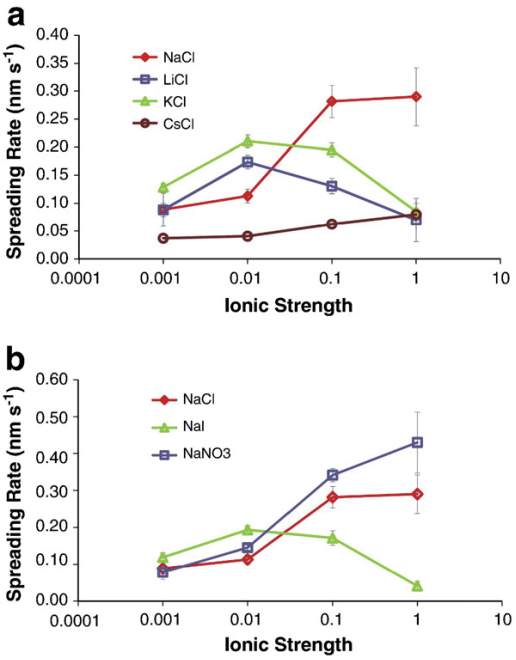

Fig. 2. Etch pit spreading rates (v_{sum}/nm s^{-1}) on dolomite cleavage surfaces versus ionic strength for a series of (a) chloride and (b) sodium salts.

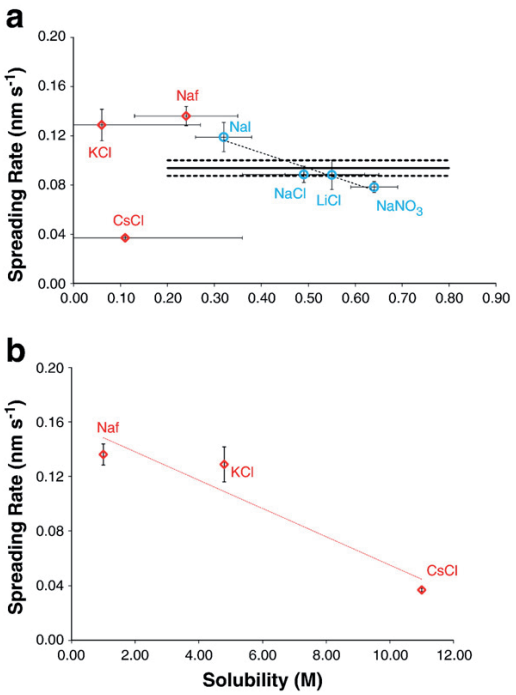

Fig. 3. Etch pit spreading rates (v_{sum}/nm s^{-1}) on dolomite cleavage surfaces at IS = 0.001 in different background salts as a function of (a) the difference in the diffusion coefficients (ΔD) of ions composing the respective salt and (b) solubility. The horizontal black line corresponds to etch the pit spreading rate in pure water, and the dotted line represents the standard deviation of this value.

Table 2
Diffusion coefficients (D, 10^{-5} cm^2 s^{-1}) for selected ions. Koneshan et al., 1998.

	$D \cdot 10^{-5}$ (cm^2 s^{-1})	
	Mean	Std
F^-	1.04	0.06
Cl^-	1.77	0.08
I^-	1.60	0.01
NO_3^-	1.92[a]	
Li^+	1.22	0.02
Na^+	1.28	0.05
K^+	1.83	0.13
Cs^+	1.88	0.17

[a] Parsons, R. *Handbook of Electrochemical Constants;* Buttersworth Scientific Publication: London, 1959; p 79.

paired the salt constituents are in solution, the more soluble is the salt (Collins, 1997). The lower dissolution rates are observed for the less ion-paired electrolytes (CsCl, $NaNO_3$). This is exactly the opposite trend to that observed during barite dissolution (Kowacz and Putnis, 2008).

The reason for this difference between the effect of background electrolytes on barite dissolution and dolomite dissolution cannot therefore be related to the factors discussed above. As shown for calcite (Ruiz-Agudo et al., 2010), although stabilisation of water molecules on the hydration shells of calcium (and, in the present case, magnesium as well as calcium) by the presence of electrolytes should make dissolution more favourable, there is a strong negative entropic effect due to increased ordering in the water molecules as they arrange in solution around strongly hydrated calcium and magnesium ions, compared to weakly-hydrated Ba^{2+}. The stabilisation of the hydration shell of water molecules around Ca and Mg ions by the presence of background salts augments this negative entropic effect upon calcite and dolomite dissolution relative to barite, thus making the overall process less favourable. This is reflected in the observed decrease in the dissolution rate with increasing ion separation in solution.

4.2. Dissolution at high ionic strength: impact of background anions on water structure dynamics

At high ionic strength, stabilisation of the solute-ion hydration shells by background electrolyte ions will be counterbalanced by the high concentration of like-charges, which increase the potential energy of hydration due to electrostatic repulsion between the like-charge ions and the solvent dipoles. Moreover, the interactions between background ions and solvent molecules will be progressively increased with increasing salt concentration due to the increase in the volume of water affected by the electrolyte. These interactions will change water structure dynamics (i.e. water–water interactions), thus modifying the hydration of solute ions and will become the controlling factor on the resulting dolomite dissolution rates in the different electrolyte solutions.

The strength of the interaction between an ion in solution and the solvent molecules can be related to its intrinsic mobility (μ_0). It is a function of its charge and a frictional drag. To a first approximation, we can consider that the mobility of univalent anions is inversely related to the effective radius of hydrated ions (r_H), according to the Hückel equation

$$\mu_0 = \frac{q}{6\pi\eta r_H}$$

where q is the charge of the ion and η is the viscosity of the solvent (Mbuna et al., 2004). From literature values of r_H (Nightingale, 1959)

Table 3
Effective radii of hydrated ions, r_H (Nightingale, 1959) ionic mobilities, μ_0 (cations: Koneshan et al. (1998); anions: Mbuna et al. (2004)) and Δr (Marcus (1994a)).

	r_H (Å)	$\mu_0 \cdot 10^{-4}$ ($cm^2V^{-1}s^{-1}$)	Δr (Å)
$Fe(CN)_6^{3-}$	4.22	8.10	0.16
ReO_4^-	3.52	5.43	0.15
I^-	3.31	7.70	0.26
Br^-	3.30	7.74	0.35
BrO_3^-	3.51	5.60	0.38
IO_3^-	3.74	3.99	0.43
NO_3^-	3.35	7.14	0.44
Cl^-	3.32	7.48[a]	0.43
Li^+	3.82	4.75	1.72
Na^+	3.58	4.98	1.16
K^+	3.31	7.12	0.74
Rb^+	3.29	7.71	0.64
Cs^+	3.29	7.32	0.49

[a] Value estimated from the linear correlation for other monovalent anions.

and mobilities (Mbuna et al., 2004) (Table 3), Fig. 4a shows that this linear relationship is fulfilled for monovalent anions. The hydrated size of ions specifies the distance over which the electric field of the ion controls solvent behaviour; in other words, identifies the volume of water molecules affected by the presence of the ion (Kiriukhin and Collins, 2002). Low ion mobility is the result of a strong interaction with water molecules (i.e., more water molecules are affected by the ion resulting in a more structured solvent). The competition for hydration water between the bulk and the building units of the dissolving crystal will be higher in a more structured solvent, thus leading to an increase in the frequency of water exchange around the latter. Dissolution will be then more favourable as the above-mentioned unfavourable entropic effect upon calcium and magnesium hydration will be reduced.

Ion mobility in water increases in the order $NO_3^- < Cl^- < I^-$ (Koneshan et al., 1998; Lucy, 1999). Hence, water is less mobile around NO_3^- and, thus, more mobile around Ca^{2+} and Mg^{2+}. Accordingly, the unfavourable entropic effect on dolomite dissolution is progressively reduced in the order $I^- < Cl^- < NO_3^-$ due to an increasing frequency of water exchange around calcium and magnesium ions, which leads to the observed increase in dissolution kinetics in the same order. From the above discussion, it seems clear that the correlation between ion mobility and the effective radius of the hydrated ions, r_H, (Fig.4a and Table 3) can be directly related to the dissolution rates (Fig. 5a). Thus the results show that it is possible to correlate the observed dissolution rates with an intrinsic parameter of the ion, such as its effective hydration radius, and in particular the thickness of the hydrated layer, hence representing a valuable tool for establishing predictive trends for other inorganic systems. This trend could not be predicted based solely on thermodynamic properties of the ions in the system. The fact that the effect of different anions on dolomite dissolution rates does not follow the typical Hofmeister series ($I^- < NO_3^- < Cl^-$) (Zhang and Cremer, 2006) may be because the traditional ordering of anions in the Hofmeister series is based only on thermodynamic properties.

4.3. Dissolution at high ionic strength: impact of background cations and the lithium anomaly

The most significant differences in the dissolution kinetics of dolomite should be observed in the presence of different background anions, as they will determine the solvent structure around Ca^{2+} and

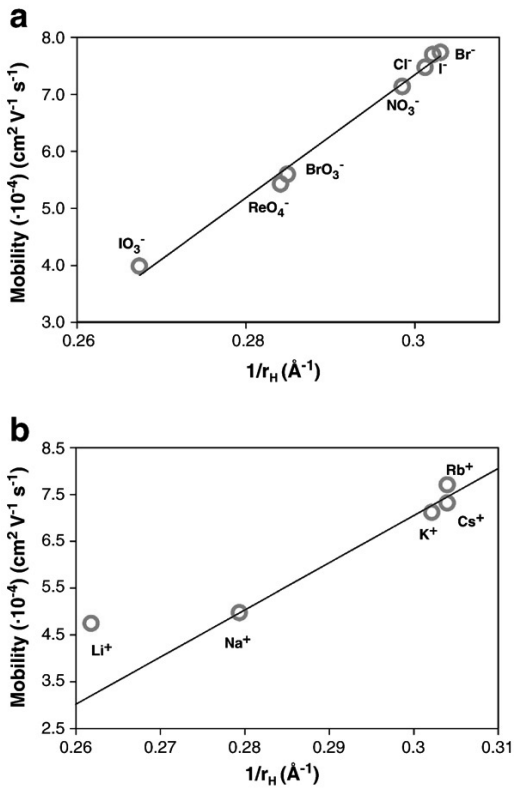

Fig. 4. Mobility (μ_0) of selected (a) anions and (b) cations as a function of effective hydration radius (r_H). Effective hydration radii are taken from Nightingale (1959) and mobilities are those reported by Koneshan et al. (1998) (cations) and Mbuna et al. (2004) (anions). Note the deviation from the linear trend of Li^+ having higher mobility than expected according to its r_H.

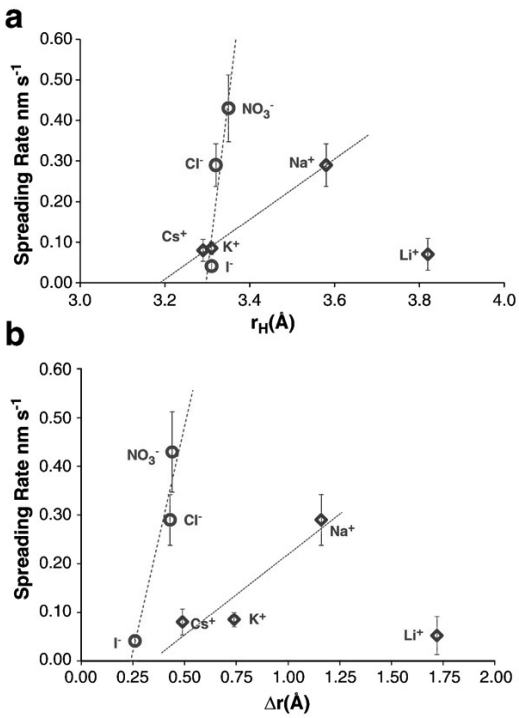

Fig. 5. Etch pit spreading rates (v_{sum}/nm s^{-1}) on dolomite cleavage surfaces at IS = 1 in different background electrolyte solutions as a function of (a) effective hydration radius (r_H) and (b) thickness of the hydration layer (Δr). Note that sodium and chlorine salts follow different trends with dissolution rates having a weaker dependence for Cl-salts.

Mg^{2+} and solvation of the constituting cation is believed to be the rate limiting step in growth and dissolution of inorganic solids (Dove and Czank, 1995; Pokrovsky and Schott, 2002; Piana et al., 2006). Therefore, chloride salts (LiCl, NaCl, KCl and CsCl) should have a similar effect on the dissolution rates of carbonates at high ionic strengths. This has been observed for example for calcite (Ruiz-Agudo et al., 2010). However, in the case of dolomite, the nature of the background counter cation also appears to have an impact on the dissolution rate, which was not clearly appreciated in the case of calcite. This is reasonable as Mg^{2+} hydration is even higher than Ca^{2+}, and therefore solvent structuring effects induced by the cation building the crystal are expected to be more important.

As in the case of anions, cations with the larger effective hydration radius are expected to show the strongest interaction with water dipoles. Therefore, dissolution rates should be expected to increase with r_H, and hence in the order CsCl < KCl < NaCl < LiCl (i.e. following a reverse Hofmeister series). With the exception of LiCl, this series is followed here as shown by Fig. 5a. A similar relationship was found between dissolution rates and Δr, which is the thickness of the region surrounding an ion in which the water molecules are translationally immobilised and electrostricted (Fig. 5b). Values of Δr were obtained from Marcus (1994b) (Table 3). Both r_H and Δr refer to similar concepts and in general correlate well with charge density, with higher charge density being associated with higher r_H and Δr values. The correlation of dissolution rates with both parameters clearly shows that the critical parameter controlling the observed behaviour is the volume of water that is affected by the presence of the background ions. The dependence of dissolution rate upon the hydration characteristics of the ions is weaker for cations compared to anions, as expected from the fact that anions will have the stronger influence in the solvation environment of the constituting cations (i.e., Mg and Ca).

Lithium is an exception to this trend. Despite its high effective hydration radius, the water molecules in its solvation shell are less electrostricted than around sodium (Hibrar et al., 2002). Its hydration co-sphere in transport processes is the largest among the alkali cations (Jákli, 2007) (as reflected by its lower ionic mobility compared to the rest of alkali cations) and therefore it should be expected to strongly structure the solvent. However, it always shows the smallest interactions with the solvent (Fortier et al., 1974). The unique hydration properties of lithium are most probably due to its tetrahedral first hydration shell, which fits well into the water structure thus resulting in only weak structural perturbations (Hibrar et al., 2002; Jákli, 2007). This may explain why LiCl does not follow the Hofmeister series observed for dolomite dissolution rates in the presence of other alkali chlorides, showing lower dissolution rates than NaCl or KCl. Also, as shown in Fig. 4b, this may explain the deviation of lithium from the linear relationship between mobility and r_H, with lithium having higher mobility (and, thus, weaker ion–water interactions) than expected from its hydrated radius.

Finally, K^+, Li^+ and I^- weaken the structure of the solvent (overwhelming the effect of the respective counter ions, Cl^- and Na^+). In this case, the competition for water of hydration between the bulk and the solute ions will be lower than in a strongly structured solvent, resulting in a decrease in the frequency of water exchange around the solution ion. This will result in a less positive entropy upon ion hydration and, therefore, a less favourable process. Such an effect seems to be more important in dolomite than in calcite, leading to the observed decrease in dissolution rate in these salts when increasing the ionic strength from 0.01 to 1. As mentioned above, the stronger hydration of Mg^{2+} compared to Ca^{2+} may explain the observation that water structuring effects have a higher impact on dissolution rates.

5. Conclusions

Although it has been known for more than a century that the behaviour of organic macromolecules in aqueous solutions is affected by background ions in a systematic sequence (lyotropic or Hofmeister series) based on ion hydration characteristics, similar effects on the growth and dissolution of inorganic solids are still not well documented. Here, the dissolution of dolomite has been studied as a model system to obtain insights into the principles governing ion specific effects in crystal reactivity, representing a relatively simple test of systematic trends in dissolution rates upon ion type. Pairing of background ions reduces the electrostatic stabilisation of water molecules in the hydration shells of a solute ion induced by the background electrolyte. This effect is thought to control ion-specific effects in dilute solutions. The role of background ions in crystal dissolution at high ionic strength is proposed to be determined by their affinity for water, the effective radius of the hydrated ions being a measure of such affinity. Furthermore, our results support the hypothesis that the response of the system to changes in hydration being induced by specific background ions depends on the hydration characteristics of the cations building the crystal (here calcium and magnesium). To our knowledge, this is one of the few systematic studies which provides a conceptual model that correlates dissolution rates of ionic inorganic solids with a fundamental property of the background ions, that is, the effective hydration radius. The volume of water affected by the background ions is the critical parameter to understand their effects on crystal dissolution in concentrated saline solutions, and the observed trends cannot be predicted or explained only in terms of the thermodynamic properties of ion solvation. It is likely that this model will be suitable for other inorganic systems where the Hofmeister effect occurs. Similar correlations have been shown for oxide minerals (Dove and Nix, 1997), therefore supporting the validity of our qualitative model for general dissolution processes. This study extends our ability to predict crystal reactivity in the fluids of both engineering and natural systems. As an example, from our conclusions we can hypothesise that ion-assisted dehydration of relevant cations could occur in biological systems thus affecting growth and weathering rates of biominerals as well as trace metal incorporation.

Acknowledgments

This work was carried out within the EU Initial Training Network Delta-Min (Mechanisms of Mineral Replacement Reactions) grant PITN-GA-2008-215360. Experimental facilities in Münster are supported by the Deutsche Forschungsgemeinschaft (DFG). M. Urosevic acknowledges the Spanish Ministry of Innovation, Science and Technology for financial support through a FPU grant (AP2006-060). Additional funding was provided by the research group RNM-179 (Junta de Andalucía, Spain) and the Spanish government under grant MAT2009-11332. We thank two anonymous referees and Dr. Fein for the constructive comments that have helped to improve the overall quality of our paper.

References

Arvidson, R.S., Collier, M., Davis, K.J., Vinson, M.D., Amonette, J.E., Luttge, A., 2006. Magnesium inhibition of calcite dissolution kinetics. Geochimica et Cosmochimica Acta 70, 583–594.

Barber, D.J., Heard, H.C., Wenk, H.R., 1981. Deformation of dolomite single crystals from 20–800 °C. Physics and Chemistry of Minerals 7, 27l–286l.

Cappa, C.D., Smith, J.D., Messer, B.M., Cohen, R.C., Saykally, R.J., 2006. Effects of cations on the hydrogen bond structure of liquid water. The Journal of Physical Chemistry. B 110, 5301–5309.

Collins, K.D., 1997. Charge density-dependent strength of hydration and biological structure. Biophysical Journal 72, 65–76.

Collins, K.D., Washabaugh, M.W., 1985. The effect and behaviour of water interfaces. Quarterly Review of Biophysics 18, 323–422.

Collins, K.D., Neilson, G.E., Enderby, J.E., 2007. Ions in water: characterizing the forces that control chemical processes and biological structure. Biophysical Chemistry 128, 95–104.

Dove, P.M., Craven, C.M., 2005. Silica surface charge in alkali chloride solutions reveals roots of ionic specificity. Geochimica et Cosmichimica Acta 69, 4963–4970.

Dove, P.M., Czank, C.A., 1995. Surface chemical controls on the dissolution kinetics of the isostructural sulfates: barite, celestite and anglesite. Geochimica et Cosmichimica Acta 59, 1907–1915.
Dove, P.M., Nix, C.J., 1997. Role of solvent-surface interactions in the electrolyte catalyzed kinetics of quartz dissolution. Geochimica et Cosmochimica Acta 61, 3329–3340.
Duckworth, O.W., Martin, S.T., 2004. Dissolution rates and pit morphologies of rhombohedral carbonate minerals. American Mineralogist 89, 554–563.
Fortier, J.-L., Philip, P.R., Desnoyers, J.E., 1974. Thermodynamic properties of alkali halides. III. Volumes and heat capacities of transfer from H2O to D2O at 25 °C. Journal of Solid State Chemistry 3, 523–538.
Hall, C., Cullen, D.C., 1995. Scanning force microscopy of gypsum dissolution and crystal growth. AIChE Journal 42, 232–238.
Hibrar, B., Southall, N.T., Vlachy, V., Dill, K.A., 2002. How ions affect the structure of water. Journal of the American Chemical Society 124, 12,302–12,311.
Higgins, S.R., Hu, X., 2005. Self-limiting growth on dolomite: experimental observations with in situ atomic force microscopy. Geochimica et Cosmochimica Acta 69, 2085–2094.
Hillner, P.E., Gratz, A.J., Manne, S., Hansma, P.K., 1992. Atomic-scale imaging of calcite growth and dissolution in real time. Geology 20, 359–362.
Jákli, G., 2007. The H_2O–D_2O solvent isotope effects on the molar volumes of alkali-chloride solutions at T = (288.15, 298.15, and 308.15) K. The Journal of Chemical Thermodynamics 39, 1589–1600.
Jordan, G., Rammensee, W., 1997. Growth and dissolution on the CaF2 (111) surface observed by scanning force microscopy. Surface Science 371, 371–380.
Kiriukhin, M.Y., Collins, K.D., 2002. Dynamic hydration numbers for biologically important ions. Biophysical Chemistry 99, 155–168.
Koneshan, S., Rasaiah, J.C., Lynden-Bell, R.M., Lee, S.H., 1998. Solvent structure, dynamics, and ion mobility in aqueous solutions at 25 °C. The Journal of Physical Chemistry. B 102, 4193–4204.
Kowacz, M., Putnis, A., 2008. The effect of specific background electrolytes on water structure and solute hydration: consequences for crystal dissolution and growth. Geochimica et Cosmichimica Acta 72, 4476–4487.
Kunz, W., Henle, J., Ninham, B.W., 2004a. Zur Lehre von der Wirkung der Salze' (about the science of the effect of salts): Franz Hofmeister's historical papers. Current Opinion in Colloid and Interface Science 9, 19–37.
Kunz, W., Lo Nostro, P., Ninham, B.W., 2004b. The present state of affairs with Hofmeister effects. Current Opinion in Colloid and Interface Science 9, 1–18.
Lucy, C.A., 1999. Factors affecting selectivity of inorganic anions in capillary electrophoresis. Journal of Chromatography A 850, 319–337.
Luttge, A., Winkler, U., Lasaga, A.C., 2003. Interferometric study of the dolomite dissolution: a new conceptual model for mineral dissolution. Geochimica et Cosmochimica Acta 67, 1099–1116.
MacInnis, I.N., Brantley, S.L., 1992. The role of dislocations and surface morphology in calcite dissolution. Geochimica et Cosmochimica Acta 56, 1113–1126.
Marcus, Y., 1994a. A simple empirical model describing the thermodynamics of hydration of ions of widely varying charges, sizes, and shapes. Biophysical Chemistry 51, 111–127.
Marcus, Y., 1994b. Viscosity B-coefficients, structural entropies and heat capacities, and the effects of ions on the structure of water. Journal of Solid State Chemistry 23, 831–848.
Mbuna, J., Takayanagi, T., Oshima, M., Motomizu, S., 2004. Evaluation of weak ion association between tetraalkylammonium ions and inorganic anions in aqueous solutions by capillary zone electrophoresis. Journal of Chromatography A 1022, 191–200.
Nightingale Jr., E.R., 1959. Phenomenological theory of ion solution. Effective radii of hydrated cations. The Journal of Physical Chemistry 63, 1381–1387.
Parkhurst, D.L., Appelo, C.A.J., 1999. Users Guide to PHREEQC (version 2) — A Computer Program for Speciation, Batch Reaction, One Dimensional Transport, and Inverse Geochemical Calculations. U.S. Geological Survey Water-Resources Investigation Report 99-4259. 312 pp.
Parsons, D.F., Boström, M., Maceina, T.J., Salis, A., Ninham, B.W., 2010. Why direct or reversed Hofmeister Series? Interplay of hydration, non-electrostatic potentials, and ion size. Langmuir 26, 3323–3328.
Piana, S., Jones, F., Gale, J.D., 2006. Assisted desolvation as a key kinetic step for crystal growth. Journal of the American Chemical Society 128, 13,568–13,574.
Pokrovsky, O.S., Schott, J., 2001. Kinetics and mechanism of dolomite dissolution in neutral to alkaline solutions revisited. American Journal of Science 301, 597–626.
Pokrovsky, O.S., Schott, J., 2002. Surface chemistry and dissolution kinetics of divalent metal carbonates. Environmental Science & Technology 36, 426–432.
Pokrovsky, O.S., Schott, J., Thomas, F., 1999. Dolomite surface speciation and reactivity in aquatic systems. Geochimica et Cosmochimica Acta 63, 3133–3143.
Putnis, A., Junta-Rosso, J.L., Hochella Jr., M.F., 1995. Dissolution of barite by a chelating ligand: an atomic force microscopy study. Geochimica et Cosmochimica Acta 59, 4623–4632.
Reeder, R.J., Nakajima, Y., 1982. The nature of ordering and ordering defects in dolomite. Physics and Chemistry of Minerals 8, 29–35.
Ruiz-Agudo, E., Putnis, C.V., Jiménez-López, C., Rodríguez-Navarro, C., 2009. An atomic force microscopy study of calcite dissolution in saline solutions: the role of magnesium ions. Geochimica et Cosmichimica Acta 73, 3201–3217.
Ruiz-Agudo, E., Kowacz, M., Putnis, C.V., Putnis, A., 2010. Role of background electrolytes on the kinetics and mechanism of calcite dissolution. Geochimica et Cosmichimica Acta 74, 1256–1267.
Samoilov, O.Ya., 1967. The theory of salting out from aqueous solutions — I. General problems. Journal of Structural Chemistry 7, 12–19.
Samoilov, O.Ya., 1971. Theory of salting out from aqueous solutions. Journal of Structural Chemistry 11, 929–931.
Shiraki, R., Rock, P.A., Casey, W.H., 2007. Dissolution kinetics of calcite in 0.1 M NaCl solution at room temperature: an atomic force microscopic (AFM) study. Aquatic Geochemistry 6, 87–108.
Shtukenberg, A.G., Astilleros, J.M., Putnis, A., 2005. Nanoscale observations of epitaxial growth of hashemite on barite (001). Surface Science 590, 212–223.
Spinolo, G., Anselmi-Tamburini, U., 1984. Dolomite decomposition to (Ca,Mg)O solid solutions: an X-ray diffraction study, part I. Naturforsch Pt A 39a, 975–980.
Weaver, M.L., Qiu, S.R., Hoyer, J.R., Casey, W.H., Nancollas, G.H., De Yoreo, J.J., 2007. Inhibition of calcium oxalate monohydrate growth by citrate and the effect of the background electrolyte. Journal of Crystal Growth 306, 135–145.
Zhang, Y., Cremer, P.S., 2006. Interactions between macromolecules and ions: the Hofmeister Series. Current Opinion in Chemical Biology 10, 658–663.
Zhang, Y., Furyk, S., Bergbreiter, D.E., Cremer, P.S., 2005. Specific ion effects on the water solubility of macromolecules: PNIPAM and the Hofmeister Series. Journal of the American Chemical Society 127, 14,505–14,510.

Appendix II

Comparative study of dolomite dissolution rate measured by atomic force microscopy (AFM) and vertical scanning interferometry (VSI)

1. Introduction and experimental strategy

Chapter 8 and Appendix 1 have shown the application of the AFM technique in the study of dolomite dissolution. This technique facilitates a precise and representative analysis of mineral-water interactions as well as the quantification of the kinetics of the dissolution processes from the measurements of etch pit densities and spreading rates formed on small surfaces (typically from 4 up to 400 μm^2). Several authors have stressed, however, that the dissolution features developed on dissolving surfaces may be quite heterogeneous in depth and density when larger spatial scales are considered, because these etch pits can be nucleated in different kinds of surface defects (Lasaga & Lüttge, 2001). Vertical scanning interferometry, thus, represents an valuable tool to explore these surface heterogeneities and their influence on dissolution rates due to its larger field of view compared to AFM (from ~22,000 μm^2 up to 250,000 μm^2) and its high (~2 nm) vertical resolution (e.g. Lüttge *et al.*, 2003; Arvidson *et al.*, 2004).

The AFM data shown in Chapter 8 suggest that the controlling mechanism on dolomite dissolution at neutral to slightly alkaline pHs is the removal of dolomite layers by spreading and coalescence of shallow etch pits (~ 0.3 nm height). Overall dissolution rates estimated using AFM (R_{AFM}) are calculated from the measurements of the etch pit density and the change in width and length of the etch pits in the time lapse between two sequential images (see Chapter 8).

Although the same procedure can be applied using the VSI technique, the occurrence of one reference surface enables an unambiguous quantification of the absolute dissolution rate based on the normal surface retreat. Absolute rates are measured with this technique using the average height difference ($\overline{\Delta z}$) between the reacted surface and a reference surface (Arvidson *et al.*, 2003, 2004; Arvidson & Lüttge, 2010). The reference surface is usually obtained by masking the flat pristine surface with an inert adhesive access (silicone polymer or multicomponent epoxy resin) to prevent the contact of the solution with the mineral surface. The dissolution rate based on VSI data is then calculated using the following expression:

$$R_{VSI} = \frac{\overline{\Delta z}}{\Delta t \cdot V_{dol}} \qquad (1)$$

where V_{dol} is the molar volume of dolomite (64.34 cm^3 mol^{-1}) and Δt is the time lapse between two sequential images. The aim of this brief note is to highlight the complexity of the dissolution features developed on dolomite $(10\bar{1}4)$ cleavage surfaces when different spatial scales are considered using VSI observations (Fig. 1). Freshly cleaved dolomite surfaces were exposed to deionized water during prolonged times (up to 142 h). For a description of VSI technique the reader is referred to the section 3.5.3 of this PhD Thesis. An outline of the main results is presented in the following paragraphs.

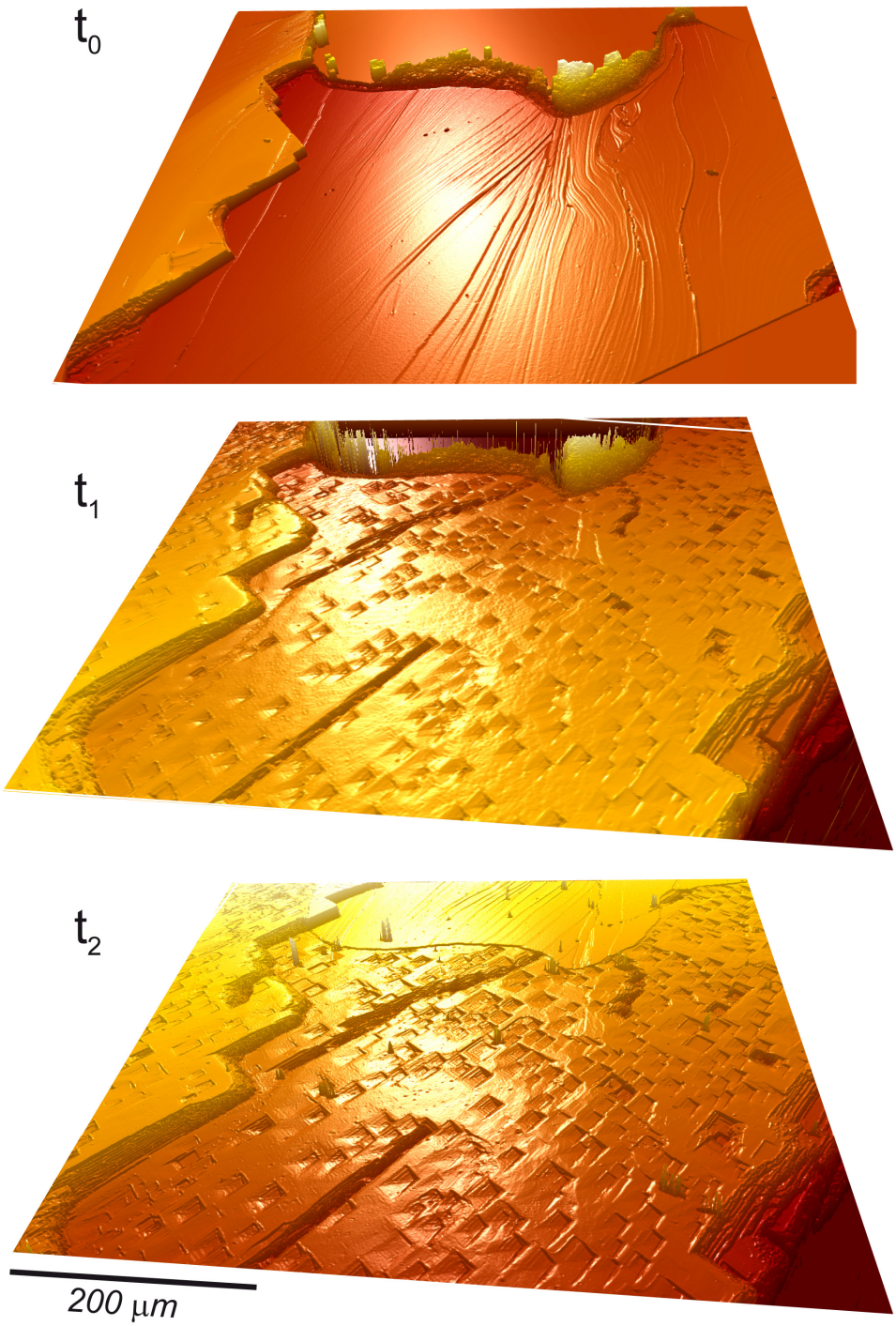

Figure 1. 3D representation of the (10-14) dolomite cleavage surface based on VSI data for initial conditions (t_0), after 72 h (t_1) and 142 h (t_2) of dissolution in pure, deionized water at neutral pH. The masked region is placed at the northern side.

2. Results

2.1. Surface morphology evolution

Figure 1 shows the evolution of a dolomite cleavage surface during the dissolution process. After cleavage (t_0) the surface is almost flat with a high density of straight and curved steps with different orientations. Deep walls (left side of Fig. 1 at t_0) define two main flat terraces. Several deep pits or holes can also be observed which in some cases are gathered following a certain direction.

After 72 h of dissolution the original step density was almost vanished and pseudo-rhombohedral deep etch pits appeared widespread distributed on formerly flat terraces. The length of the long diagonal of these deep pits was found to be around 25-35 μm. This size clearly contrasts to that of the etch pits observed using AFM (< 200 nm). The length ratio of the etch pit diagonals (0.93 ± 0.05) was however very similar to that measured in the AFM images (Chapter 8). A notorious new feature is the development of very deep trench (see below) parallel to the $<\bar{4}\,41>$ directions. The width of these trenches is similar to those of other pits (~ 20 μm) and their length can reach up to 400 μm. Detailed observation of the original surface reveals that these trenches were developed on the originally present round pits or holes described above, thus suggesting that these features where lines of dislocations that act as nucleation points for dissolution pits.

After 142 h of contact with deionized water, etch pits continue expanding whereas the nucleation of new pits was rarely observed. The final distribution of etch pits on the surface is rather homogenous although the density seems to be lower closer to deep walls dividing the two terraces (left side, Fig. 1).

2.2 Dissolution rate

Two different profiles were selected to illustrate the heterogeneity of dissolution features developed on the initially flat dolomite cleavage surface after 142 h (Fig. 2). These

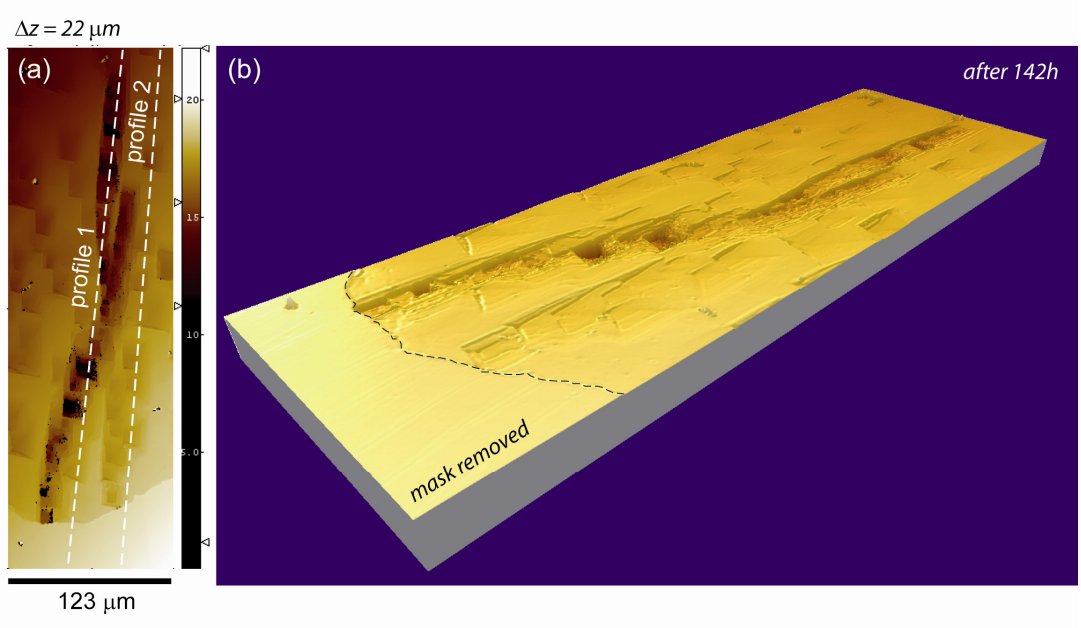

Figure 2. Close view of the dolomite surface after 142 h of contact with deionized water (pH 7) near the masked region used as the initial surface reference (see Fig. 1 at t_2 for location). (a) 2D VSI image depicting the two selected cross section profiles. Note that profile 1 intersects the trench whereas profile 2 only intersects rhombohedral etch pits. (b) 3D reconstruction of the studied area showing the location or the deep trench and dissolution etch pits.

two profiles were used to estimate dissolution rates based on surface normal retreat (equation 1). The average retreat was estimated by fitting a straight line with the VSI data collected over the protected region (and later unmasked) used as a reference (dashed lines in Fig. 3).

It is interesting to note that certain areas of the reacted surface were indeed coincident with the initial surface (Figs. 3a and b) thus suggesting that these areas were scarcely affected by the dissolution process at the resolution of VSI. Other areas were strongly affected by the dissolution process leading to very deep etch pits with depth up to 8 μm (Fig. 3a). The etch pit depth distribution is clearly more regular in the case of profile 2 than in the profile 1 corresponding with the trench. Dissolution rate was found to be 0.36×10^{-11} mol cm^{-2} s^{-1} and 0.13×10^{-11} mol cm^{-2} s^{-1} for profile 1 and 2 respectively. These values are of one order of magnitude lower than those measured by Lüttge *et al.*, (2003) at pH 3 using the same technique (1.08×10^{-11} mol cm^{-2} s^{-1}). This difference was expected as that dolomite dissolution rates are known to increase with decreasing pH (see Chapter 8 and references

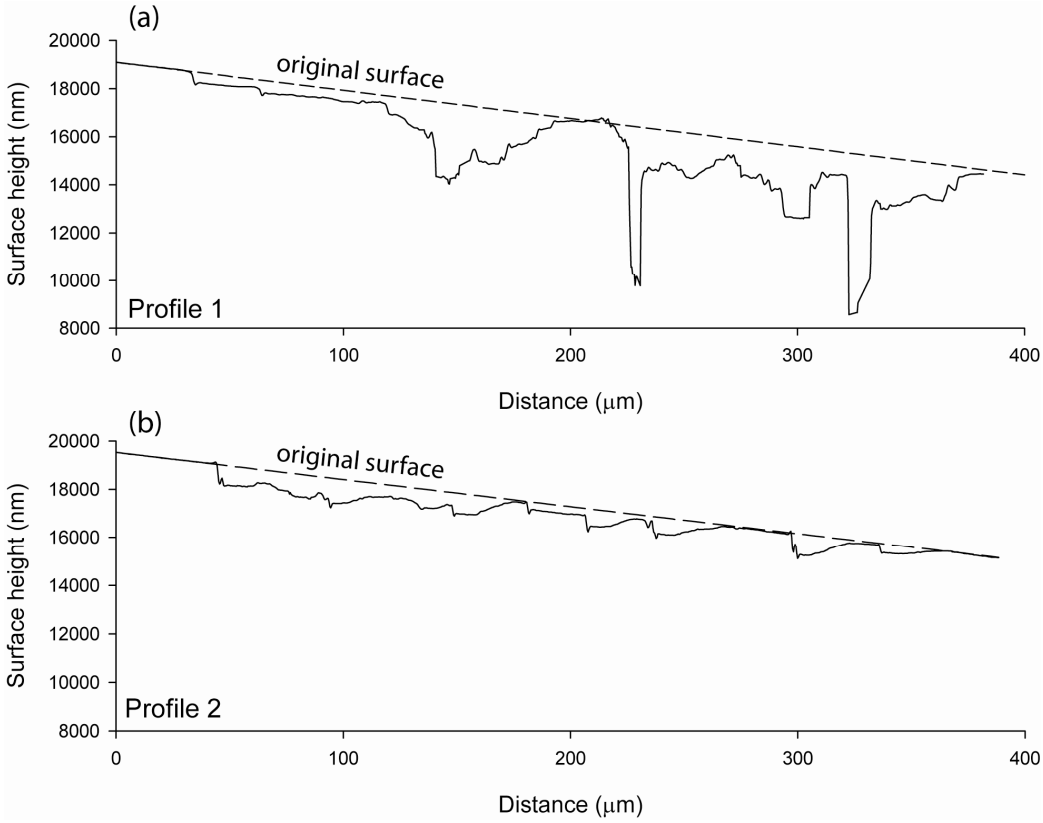

Figure 3. Cross section profiles corresponding to profile 1 (a) and profile 2 (b). See Fig. 2 for location.

therein). A value of $7.42 \times 10^{-13} \pm 1.62\ 10^{-13}$ mol cm^{-2} s^{-1} at pH 7 was found based on AFM observations and the spreading of shallow etch pits, most probably nucleated at point defects or even on defect-free surfaces (see Chapter 8 for more details). This value is more than one order of magnitude lower than that reported here, determined using VSI at the same pH and calculated from observations and measurements of deep etch pits (nucleated at dislocations). Dissolution rates estimated using AFM and VSI are therefore measured using dissolution features that are nucleated on surface defects with different energies, and thus it is not unexpected that they propagate (parallel and perpendicularly to the dissolving surface) at contrasting rates. The differences found between rates measured these two techniques illustrate the complexity of the dissolution process and the dependence of its kinetics on the surface feature considered (Lüttge *et al.*, 2003).

3. Afterthoughts

The simple observations shown in this brief note illustrate the difficulty of relating dissolution mechanisms and rates at different observational (spatial) scales. AFM observations are related to small areas which are typically defect-free surfaces or show point defects, whereas the large field of view typical of VSI enables observations of how dissolution is modified by the occurrence of dislocations.

Defects contribute to local excursion of the reaction overstep and thus to the reaction rate (Arvidson & Lüttge, 2010). Larger reaction rates are thus expected in areas with a high population of defects such as outcropping dislocations along subgrain boundaries or weak planes. These boundaries could correspond to the deep trenches observed in this study (Fig. 3) where the dissolution rate is enhanced. On the other hand, randomly distributed etch pits (much deeper than those observed with AFM) could also correspond with outcropping isolated dislocations or impurities randomly distributed on the mineral surface. It has been suggested that the dissolution of dolomite is controlled by the deepening of these deep etch pits and the retreat of shallow steps emerging from these pits which finally results in the removal of a entire layer of the mineral surface (e.g. the Dissolution Stepwave Model, Lasaga & Lüttge, 2001; Lüttge *et al.*, 2003; Lasaga & Lüttge, 2003).

REFERENCES

Arvidson, R.S., Ertan, I.E., Amonette, J.E. and Luttge, A., 2003. Variation in calcite dissolution rates: A fundamental problem? Geochimica et Cosmochimica Acta, 67(9): 1623-1634.

Arvidson, R.S. and Luttge, A., 2010. Mineral dissolution kinetics as a function of distance from equilibrium - New experimental results. Chemical Geology, 269(1-2): 79-88.

Lasaga, A.C. and Lüttge, A., 2003. A model for crystal dissolution. Eur J Mineral, 15(4): 603-615.

Lasaga, A.C. and Luttge, A. 2001. Variation of crystal dissolution rate based on a dissolution stepwave model. Science 291, 2400-2404.

Lüttge, A., Winkler, U. and Lasaga, A.C., 2003. Interferometric study of the dolomite dissolution: a new conceptual model for mineral dissolution. Geochimica et Cosmochimica Acta, 67(6): 1099-1116.

Research Article

Journal of RAMAN SPECTROSCOPY

Received: 2 December 2009 Accepted: 6 April 2010 Published online in Wiley Online Library: 31 May 2010

(wileyonlinelibrary.com) DOI 10.1002/jrs.2700

Assessment of limestone deterioration due to salt formation by micro-Raman spectroscopy: application to architectural heritage†

Sabina Kramar,[a]* Maja Urosevic,[b] Helmut Pristacz[c] and Breda Mirtič[d]

Salt crystallisation is a principal deterioration factor of many stone monuments. In this study, samples of weathering products of two baroque monuments in Ljubljana, Slovenia (the Fountain of Three Carniolian Rivers and the side altar of the Church of St. James), as well as the limestone used in their construction (Lesno Brdo limestone) were investigated in order to ascertain the main mineral phases produced during the weathering process. A combination of micro-Raman spectroscopy and X-ray powder diffraction was successfully applied to identify micrometre-size minor components in the limestone and the weathering product phases. In addition to calcite and dolomite as the main components of the Lesno Brdo limestone, quartz, anatase, goethite, haematite and phyllosilicates were also determined as minor limestone minerals. The limestone was found to be extensively deteriorated in both outdoor and indoor environments in the studied historical monuments, showing flaking, subflorescence, efflorescences, crumbling and black and white crusts as a result of the deterioration phenomena. Among these weathering forms, efflorescences were found to be more complex in terms of mineral assemblage, where gypsum was associated to hexahydrite, pentahydrite, and nitre. In contrast to the efflorescences, the mineralogy of subflorescences as well as that of white and black crust from outdoor and indoor conditions was rather simple, composed of only gypsum. The results showed that gypsum also crystallised under the surface as subflorescence, which eventually led to the flaking and crumbling of the limestone. **Copyright © 2010 John Wiley & Sons, Ltd.**

Supporting information may be found in the online version of this article.

Keywords: limestone; salt weathering; deterioration; micro-Raman spectroscopy; historical monuments

Introduction

Limestone has been one of the most commonly used building stones worldwide since prehistoric times. Although limestone is composed mainly of calcite, it may show significant variations in minor mineral composition and texture, resulting in a complex and contrasting weathering behaviour. Salt crystallisation is a frequently encountered problem in the field of cultural heritage and is considered to be one of the most powerful weathering factors of carbonate stones.[1–5] Salts are known to damage porous materials through a range of mechanisms, such as production of physical stress resulting from the crystallisation of salts in pores, differential thermal expansion, hydration pressure and enhanced wet/dry cycling caused by deliquescent salts.[1,3] Depending on the environmental factors and type of solution, salts can crystallise under the surface (subflorescence, cryptoefflorescence) or on the surface, forming either efflorescences or compact crusts. These mechanisms lead to various deterioration patterns, i.e. flaking, alveolar weathering, crumbling, loss of material or dissolution. Therefore, a precise determination of the salt mineral assemblage must be given the first priority when exploring the physical factors producing stone damage. Unfortunately, the small size of the weathering products prevents an accurate assessment of the crystallised phases in pores or fragile aggregates in natural weathered stones by conventional techniques.

In the field of cultural heritage, vibrational spectroscopic techniques, particularly Raman spectroscopy, have been extensively applied for typifying art materials such as pigments and other painting materials,[6–11] glasses[12–14] and ceramics.[15,16] Moreover, vibrational spectroscopy has been applied along with other innovative techniques to resolve complex characterisation of archaeological artefacts.[17,18] Although the spatial resolution of modern micro-Raman systems has also proved to be useful in the identification of micrometre-sized weathering products of natural stones used in architectural heritage,[19–22] more work is

* *Correspondence to: Sabina Kramar, Institute for the Protection of Cultural Heritage of Slovenia, Restoration Centre, Poljanska 40, 1000 Ljubljana, Slovenia. E-mail: sabina.kramar@rescen.si*

† *Paper published as part of the Art and Archaeology 2009 special issue.*

a *Restoration Centre, Institute for the Protection of Cultural Heritage of Slovenia, Poljanska 40, 1000 Ljubljana, Slovenia*

b *Faculty of Science, Department of Mineralogy and Petrology, University of Granada, Avda. Fuentenueva s/n, 18071 Granada, Spain*

c *Institute of Mineralogy and Crystallography, University of Vienna, Althanstrasse 14, 1090 Vienna, Austria*

d *Faculty of Natural Sciences and Engineering, Department of Geology, University of Ljubljana, Aškerčeva 12, 1000 Ljubljana, Slovenia*

Copyright © 2010 John Wiley & Sons, Ltd.

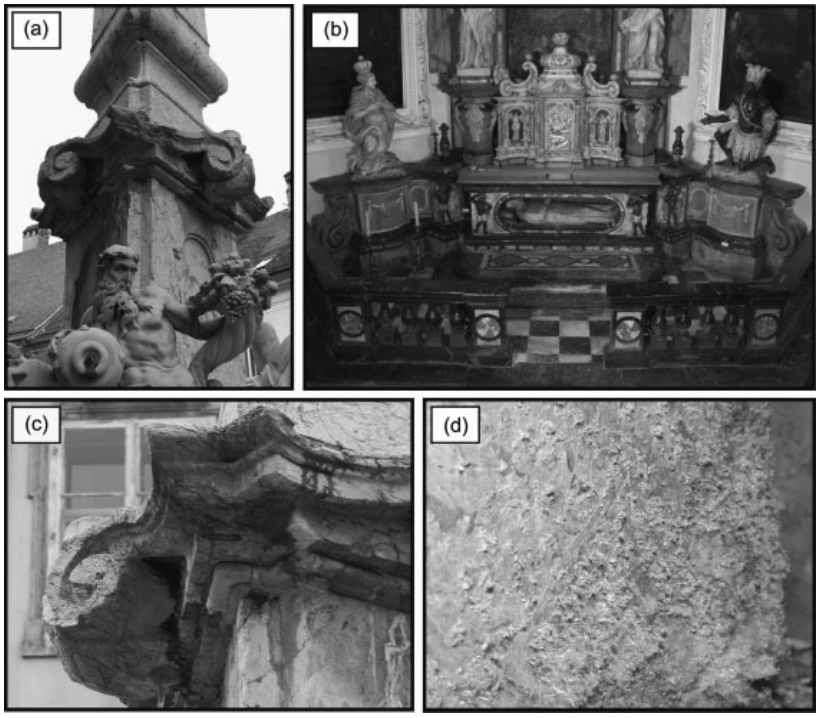

Figure 1. Selected monuments and weathering forms of Lesno Brdo limestone. (a) Details of the Fountain of the Three Carniolian Rivers. The obelisk is made of Lesno Brdo limestone and the statues of Carrara marble. (*Photo: Valentin Benedik*). (b) Details of the altar of the St. James Church. Some of its stone elements in the lower parts are made of Lesno Brdo limestone (*Photo: Valentin Benedik*). (c) Black crusts are compact aggregates of salt minerals, occurring on a surface. The figure shows a detail of the fountain. The image is about 40 cm in width. (d) Fluffy efflorescence appearing as very loosely coherent aggregates of acicular and long hair-like crystals. The figure shows a detail of the altar. The image is about 10 cm in width.

needed in order to better ascertain the mechanism and origin of the weathering[23] and, more importantly, to design suitable restoration and preservation strategies.[24,25]

In this study, micro-Raman spectroscopy together with X-ray powder diffraction was used to characterise a quarried Lesno Brdo limestone[26] that is frequently used in the construction of Slovenian historical monuments as well as modern buildings. Additionally, weathering products of two selected Slovenian monuments made of Lesno Brdo limestone were analysed.

Experimental

Sampling

Samples of fresh limestone were collected from the currently active quarry Lesno Brdo near Ljubljana (Central Slovenia). This Triassic reef limestone is heterogeneous, being composed of intraclasts, pellets and fossil fragments. Coloured (violet, red, green and white) veins and stylolites are also present. Moreover, large yellow or violet crystals can be commonly found.[27]

In order to investigate and compare the deterioration effects of the Lesno Brdo limestone when used as a building material exposed to diverse environments, samples were taken from two baroque monuments from Ljubljana, Slovenia, namely the Fountain of Three Carniolian Rivers, constructed during 1743–1751 (Fig. 1(a)), and the altar in the Chapel of St. Francis Xavier of the Church of St. James, constructed during 1709–1722 (Fig. 1(b)). Elements of the fountain consist of four different natural stones. The architectural part is made of two different Slovenian limestones and conglomerate, whereas the three statues are sculptured from Carrara marble. The Lesno Brdo limestone is used for the construction of the obelisk. The altar in the Chapel of the St. James Church consists of 18 different natural stones, where the Lesno Brdo limestone is used for construction of lower parts of the altar. A total of 15 samples from both selected monuments were carefully collected, paying special attention to sampling the different textures of the weathering forms and the degree of damage. Detailed information regarding fresh and weathered samples is provided in Table 1.

Analytical methods

Polished thin sections of unweathered limestone samples from the quarry were studied with optical microscopy using an Olympus BX-60 instrument equipped with a digital camera (Olympus JVC3-CCD).

The mineral composition of both unweathered limestone and the weathering products was determined by X-ray powder diffraction, using a Philips PW3710 X-ray diffractometer equipped with Cu Kα radiation and a secondary graphite monochromator. Data were collected at 40 kV and a current of 30 mA in the range from 2 to 70° 2θ. In order to verify the possible epsomite dehydration, large crystals of epsomite were prepared by dissolving anhydrous magnesium sulfate in H_2O and evaporating subsequently. Single-crystal X-ray data of a clear crystal with homogenous optical extinction grown from solution were measured on a Nonius KappaCCD diffractometer in order to verify the presence

Copyright © 2010 John Wiley & Sons, Ltd.

Journal of RAMAN SPECTROSCOPY

Table 1. Summary of investigated samples, their related weathering forms and mineralogy determined by micro-Raman spectroscopy and X-ray powder diffraction

Natural stone	Location	Investigated samples	Primary mineralogy
Lesno Brdo limestone	Lesno Brdo quarry	LB1, LB2, LB3, LB4, LB5	Calcite, dolomite, quartz, anatase, muscovite, haematite, goethite
Weathering type	**Location**	**Investigated samples**	**Weathering products**
Black crust	Fountain	RO2, RO4	Gypsum
Subflorescence	Fountain	RO1, RO2, RO3	Gypsum
Subflorescence	Altar	JAL1, JAL8	Gypsum
Efflorescence	Altar	JAL2, JAL6, JAL7	Nitre, gypsum, hexahydrite, pentahydrite,
Crumbling	Altar	JAL5, JAL9	Gypsum
White crust	Altar	JAL1, JAL3, JAL4	Gypsum

of epsomite. The mineral composition of the synthesised crystals was then determined directly from the solution and after 4 days at room conditions with X-ray powder diffraction.

Polished thin sections of quarried and weathered limestone as well as unprepared samples (crystals of salts) were examined with micro-Raman spectroscopy. Oil was used during the preparation of polished thin sections of the weathered limestone samples to avoid the dissolution of the salts. Raman spectra were obtained with a Renishaw RM1000 dispersive spectrometer equipped with a Leica DMLM optical microscope, a grating with 1200 grooves/mm and a Peltier-cooled CCD detector. Spectra were excited with the 632.8 nm emission of a He–Ne laser (8 mW measured behind the objective), and a Leica 50× objective (NA 0.75) was used. The wavenumber accuracy was better than 1 cm^{-1} and the spectral resolution was about 2.5 cm^{-1}. The system was operated in the quasi-confocal mode, resulting in an approximate lateral resolution of *ca* 3 μm.

Results and Discussion

Unweathered limestone

Petrographic characterisation

All samples from Lesno Brdo quarry were classified as micritic with transition to microsparitic limestone with pellets, intraclasts and some fragments of fossils. Microscopic examination showed that the limestone was very heterogeneous because of the occurrence of coarse-grained crystals, veins and stylolites (Fig. 2(a)). Coarse-grained crystals of dolomite were partially or completely replaced by calcite. Furthermore, iron oxides and hydroxides were present in stylolites, being distributed on the rims of coarse-grained dolomite crystals. Phyllosilicates (e.g. sericite) were present in veins or stylolithes and in the inter-granular spaces between the coarse-grained dolomite and calcite grains. Quartz occurs as single crystals or between sparitic grains, sometimes as terrigenous grains or in veins as polycrystalline quartz.

X-ray powder diffraction

The results of the X-ray diffraction analysis of the limestone indicate the presence of calcite and dolomite. Among non-carbonate component quartz and phyllosilicates as illite/muscovite are present. A detailed characterisation of phyllosilicates with X-ray diffraction was not possible.

Micro-Raman characterisation: mineral composition

Raman spectra obtained from polished thin sections of limestone samples allowed us to identify the occurrence of single mineral phases of the limestone. The results of the detailed mineral composition with its characteristic bands are shown in Table S1.

Calcite, the main mineral of the Lesno Brdo limestone, was identified according to the main Raman active bands at 155, 282, 712 and 1086 cm^{-1} (CO_3 symmetric stretching) and sometimes at 1437 and 1748 cm^{-1} (Fig. 2(b)). The Raman spectrum of dolomite (Fig. 2(c)) is generally similar to that of calcite; however, the internal CO_3 vibrations are slightly shifted because of the different average size of the neighbouring cations[28]; for instance, the symmetric CO_3 stretching of dolomite appears at 1098 cm^{-1} (Fig. 2(c)).

Among the non-carbonate compounds, α-quartz was identified on the basis of its main Raman bands at 128 and 207 cm^{-1} and the most significant band at 465 cm^{-1} (Fig. 3(a)). Some spectra also yielded other minor bands at 265, 355 (394, 404 cm^{-1}) doublet, 696, 807 cm^{-1} and the asymmetric stretches of the silica tetrahedra[29] at 1082 and 1162 cm^{-1}. Besides polycrystalline quartz occurring in the veins or mono-crystalline terrigenous grains, as determined by optical microscopy, Raman spectroscopy of unweathered Lesno Brdo limestone samples also confirmed the occurrence of quartz spots homogeneously distributed over the sample.

The observed Raman bands at 103, 198, 217, 263 and 704 cm^{-1} for muscovite correspond to the wavenumbers of the Raman active modes listed by McKeown *et al*.[30] According to Loh,[31] among the phyllosilicates, only dioctahedral phyllosilicates exhibit extra strong bands in the region 200–300 cm^{-1}, assigned to internal vibrations of an O–H–O isosceles triangle. Phyllosilicates have complex structures and highly variable compositions and consequently complex peak patterns.[32]

Some other minor mineral species that were not identified or detected by optical microscopy or X-ray diffraction were confirmed by Raman spectroscopy. Haematite was identified according to the bands at 223, 243, 290, 406, 495 and 606 cm^{-1}, assigned to Fe–O symmetric bending and stretching vibrations, and the broad band at 1302 cm^{-1}. α-Goethite was determined according to the characteristic bands at 224, 294, 394 and 478 cm^{-1} and the Fe–OH asymmetric stretch at 554 cm^{-1}. The yellow spots around the coarse-grained dolomitic grains were found to be goethite, while the red brownish ones were assigned to haematite. Small grains distributed in phyllosilicates were identified as anatase (Fig. 3(b)), determined according to the main band at 143 cm^{-1}, followed by minor bands at 195, 396, 515 and 638 cm^{-1}.

 Copyright © 2010 John Wiley & Sons, Ltd.

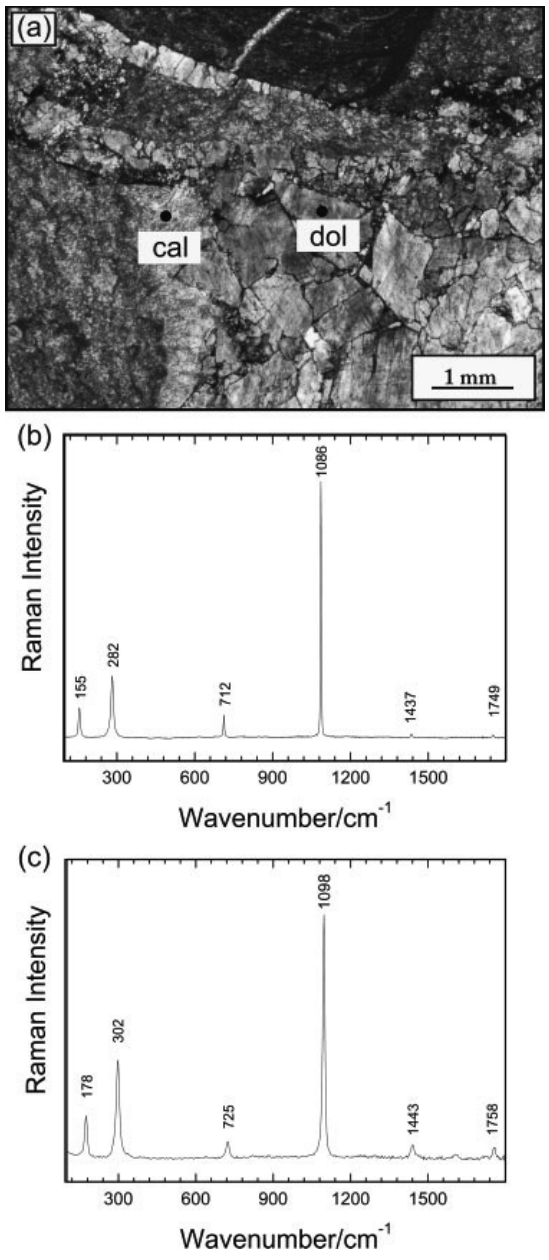

Figure 2. (a) Photomicrograph of the studied limestone, showing micritic calcite (1) and brown coarse-grained dolomitic grains (2). Sample LB5. Transmitted light, parallel polarised light. (b) Raman spectrum of calcite. (c) Raman spectrum of dolomite.

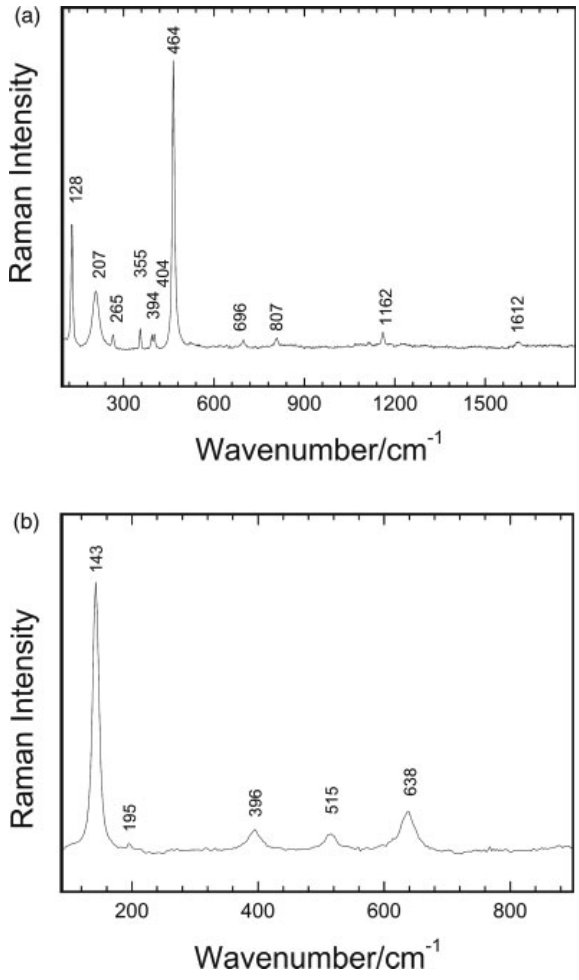

Figure 3. Raman spectra of some minor limestone minerals. (a) Raman spectrum of polycrystalline quartz occurring in the veins of the limestone in sample LB1 and (b) Raman spectrum of anatase, which is distributed as single grains in the veins of phyllosilicates in sample LB1.

Weathered limestone

Weathering forms: macroscopic description

As part of broader conservation/restoration projects, *in situ* investigation of the monuments by means of monument mapping has pointed out several types of deterioration phenomena. Limestone was found to be extensively deteriorated in both outdoor and indoor environments (Fig. 1), salts being the main weathering products. The fountain (outdoor location) showed several types of deterioration phenomena, which were documented according to the Fitzner classification[33]: for example flaking (Fig. S1(a)), subflorescence, crumbling and black crusts (Fig. 1(c)). Flaking leads to loss of material through back weathering. A wide range of weathering forms related to the salt crystallisation have been recognized also in indoor conditions, e.g. flaking (Fig. S1(b)), sub- and efflorescence (Fig. 1(d)), crumbling (Fig. S1(c)) and white crust formation (Fig. S1(d)). Identification of salts of these weathering forms is described in the following sections.

Observation with optical microscope

White and black crusts consist of crystals up to 100 μm in size that are orientated parallel to the surface. Single calcite grains are trapped in the gypsum crystals. The boundary between the salt crystals in the black crust and limestone is extremely irregular, showing that chemical dissolution of calcite grains is in progress. Crystallisation of soluble salts under the surface results in disruption of the limestone. A system of fissures is present

Copyright © 2010 John Wiley & Sons, Ltd.

Journal of RAMAN SPECTROSCOPY

100–150 μm under the surface, while the fissures are 20- to 30-μm thick. Salt crystals of fluffy efflorescences occur as very loosely coherent aggregates of long hair-like needles and fibres. Efflorescence consists of a curled bundle of parallel grown fibres (whiskers) that are about 150- to 500-μm long. Elongated and prismatic crystals were also observed. Whisker growth indicates a slightly humid to nearly dry surface substrate where crystals grow on a solution film into the air.[34]

X-ray powder diffraction

X-ray diffraction data evidence the presence of gypsum, nitre (KNO_3), and the soluble salts of the $MgSO_4 \cdot nH_2O$ series such as pentahydrite and hexahydrite in the altar samples. In samples taken from outdoors, only gypsum is present. Gypsum occurs as white and black crust as well as subflorescence and part of efflorescence. Moreover, three different mineral assemblages have been observed in the efflorescences: (1) nitre and gypsum (sample JAL2); (2) nitre, gypsum or magnesium sulfate hydrates (sample JAL7) and (3) gypsum and magnesium sulfate hydrates (sample JAL6). On the contrary, nitre and magnesium sulfate hydrates were absent in subflorescence.

Gypsum is found to be one of the most common soluble salts in the deterioration of building materials.[35] Moreover, the origin and growth of the black crusts that contribute to limestone deterioration on monuments have been widely studied in the past.[36–40] Salt crusts normally form in damper areas and are generally formed by less soluble salts such as gypsum.[41] Gypsum crystallisation under the surface results in scaling and crumbling of the limestone and indicates that the evaporation flux is higher with respect to capillary transfer of the solution.[42] In addition, black gypsum crust formed outside and white gypsum crust inside.

Hexahydrite and epsomite are common hydrates on the Earth's surface that occur in moderate and elevated relative humidity (RH) at ambient temperature.[43] With the exception of hexahydrite-epsomite, transformations between the various species of the $MgSO_4.nH_2O$ series involve more than simple removal of water and require significant crystal structure rearrangement and the overcoming of activation energy barriers. Close to room temperature, epsomite is the stable form in the presence of liquid water. Under dry conditions, epsomite can dehydrate to hexahydrite and finally to the monohydrate kieserite.[44] The situation was also proved by the experiment, where single-crystal measurement of the synthesised crystal showed the crystal structure of epsomite[45]: $P2_12_12_1$, $a = 11.868$ (10) Å, $b = 11.996$ (10) Å, $c = 6.858$ (7) Å; $V = 976$ Å^3, $Z = 4$, and further analysis with X-ray diffraction determined the presence of epsomite. The X-ray diffraction measurement of the sample after 4 days revealed the presence of hexahydrite and pentahydrite, suggesting that epsomite is stable in the presence of liquid water and then dehydrated into magnesium sulfate hydrates with various amounts of water. Crystallisation of these salts and hydration–dehydration transformations depend mainly on the RH and temperature. As joint mortars between the stone elements of the altar contain high quantities of soluble calcium and magnesium,[46] they are thus considered as a potential source of these damaging salts.

The presence of nitre may be attributed to the solutions containing alkali potassium and nitrate that are present in the ground and transported by capillary rise.[47] Nitre could also be the result of the weathering of K-bearing phyllosilicates in the limestone.

The behaviour of multi-component salt mixtures is extremely complex. Even in a comparably simple four-component system, several possible sequences of salt deposition and phase transformation have to be considered. The salt species that grow in efflorescences depend on the composition of the salt solution, on the properties of the substrate and on the environmental conditions during growth.[2] Charola[1] reported that in normal outdoor environmental conditions most salts remained in solution, except the rather insoluble gypsum that crystallises first from the solution. Magnesium sulfate hydrates and nitre, which are more soluble compared to gypsum, are transported to the evaporation zone at the limestone surface, and therefore are commonly found in the efflorescences. Although some studies[4,48–50] have reported that crystallisation of epsomite caused several damaging effects of the investigated stones, the situation in the altar did not reveal any visible damage of the limestone, where conditions allowed crystallisation of these salts at the limestone surface. The conditions that govern the position of crystallisation depend to some extent on the nature of the salts that are present, but also on the texture of the material and on the conditions of evaporation.[51] The cycles of dissolution and recrystallisation of these salts are considered to be related to the environmental conditions within the church, particularly in relation to the fluctuation in RH. This latter factor seems to be an important issue in the present case, as, during the 1-year monitoring period in the chapel, the RH ranged from a maximum of 100% to a minimum of 40%.[52]

Micro-Raman characterisation of the weathering products

Raman spectroscopy was used to identify the single crystals of soluble salts, which were found to be the main weathering products of limestone deterioration. The results are shown in Table 1, together with the mineral composition of the unweathered Lesno Brdo limestone.

In agreement with the above X-ray diffraction data, Raman spectroscopy showed that gypsum is stable as the weathering product in both outdoor and indoor conditions. Gypsum in the samples was identified mainly from its main Raman band at 1008 cm^{-1} and some minor bands, such as doublets at 414, 494 cm^{-1} and 623, 671 cm^{-1}, assigned to ν_2 symmetric and ν_4 antisymmetric bending of the SO_4 tetrahedra, respectively (Fig. 4(a)). The ν_3 antisymmetric stretching vibration of the SO_4 tetrahedra at 1137 cm^{-1} was also observed in the spectra. In the high wavenumber Raman spectra, two bands were observed at 3405 and 3492 cm^{-1}, which are due to the ν_1 symmetric and ν_3 antisymmetric stretching vibration of water, respectively. Samples from the black crust in particular showed high luminescence (Fig. S2(a)) due to the organic matter of the crusts, but showed enough Raman scattering to give measurable signals. Some spectra of the black crust yielded two additional broad bands at around 1308 and 1600 cm^{-1} attributed to the D (disordered) and G (graphitic) band, respectively, indicating graphitic carbon, derived probably from atmospheric soot particles (Fig. S2(b)).[19,20,53]

Raman spectroscopy revealed the presence of magnesium sulfate hydrates as part of the efflorescence in samples taken from the lower parts of the altar (indoors), supporting X-ray diffraction data. Moreover, the lack of these magnesium sulfate hydrates in the outdoor environment was also confirmed. The most significant band in the investigated samples for hexahydrite was the SO_4^{2-} -associated ν_1 symmetric stretching band at 983 cm^{-1} as shown in Fig. 4(b). The doublets at 218 and 250 cm^{-1} are assigned to O–H···O (sulfate) entities in the crystal structure. The Raman

 Copyright © 2010 John Wiley & Sons, Ltd.

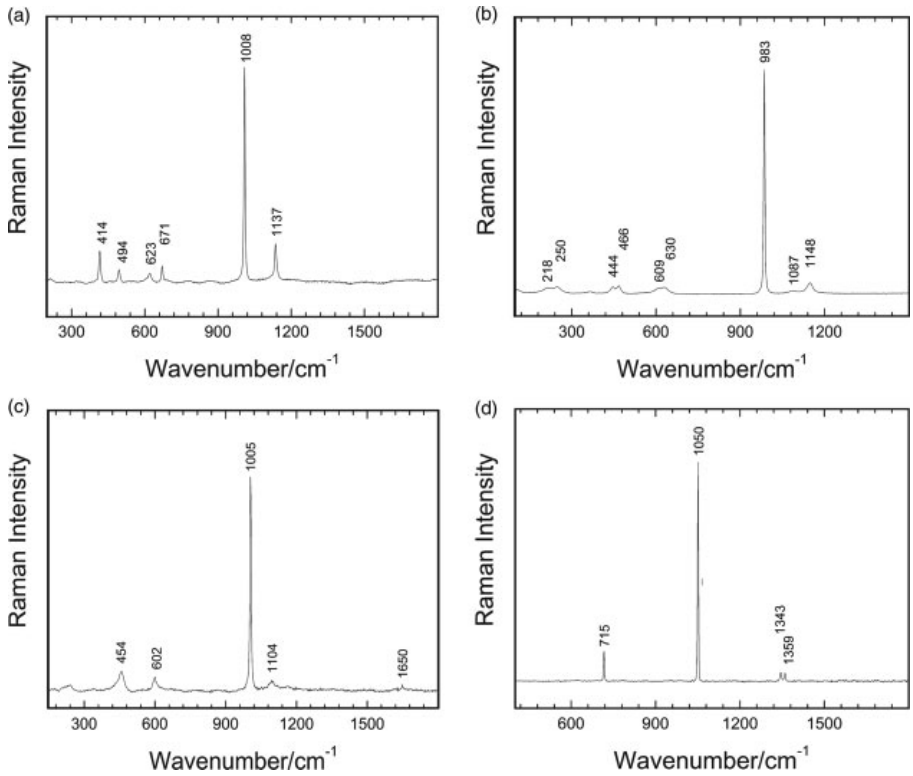

Figure 4. Raman spectra of soluble salts present in the monuments. (a) Raman spectrum of platy gypsum in white crust in sample JAL1. (b) Raman spectrum of prismatic hexahydrite occurring in efflorescence (sample JAL7). (c) Raman spectrum of pentahydrite that occurs in efflorescence (sample JAL7). (d) Raman spectrum of nitre that occurs as fibrous crystals in efflorescence (sample JAL2).

band at 365 cm^{-1} present in some spectra is attributed, according to Makreski *et al*.,[54] to the symmetric metal–oxygen stretching vibration (O–Mg–O deformations). A sulfate mode is observed as two doublets at 444, 466 cm^{-1} and at 609, 630 cm^{-1}. Both the bands observed at 1087 and 1148 cm^{-1} are expected to come from ν_3 sulfate modes. The bending modes of intra-crystalline water are observed at 1614 and 1648 cm^{-1}. Due to the involvement of water in hydrogen bonding (water incorporated into the lattice), the water stretching vibrations manifest as a complex band in the 3000–3600 cm^{-1} region with a maximum at around 3424 cm^{-1} and two shoulders at 3251 and 3547 cm^{-1}.

Wang *et al*.[55] reported that the symmetric stretching vibration ν_1 mode of SO_4 tetrahedra shifts towards higher wavenumbers generally following a decrease in the degree of hydration, which in our case is expressed as a shift from 983 cm^{-1} in hexahydrite to 1005 cm^{-1} in pentahydrite. Figure 4(c) shows the additional sulfate vibration modes of pentahydrite that are observed at 454 (ν_2), 602 (ν_4) and 1104 cm^{-1} (ν_3 mode). Moreover, bands in the region 1000–1800 cm^{-1} at 1151 and 1650 cm^{-1} can also be present. The band at 119 cm^{-1} is ascribed to an external vibration. In the 2500–4000 cm^{-1} spectral region, a broad Raman band is observed which consists of bands at 3287, 3341, 3405, 3510 and 3560 cm^{-1}. The observed bands for both hexahydrite and pentahydrite are in agreement with the literature data reported by Wang *et al*.[55]

Difficulties in the characterisation of the minerals of the $MgSO_4.nH_2O$ series are often encountered. The Raman spectrum of hexahydrite was frequently ascribed to epsomite, since the possibility of dehydration under the room conditions was not considered. To prevent eventual dehydrations that may also occur while acquiring the spectra, researchers have studied the Raman spectra at low temperatures.[56] A systematic Raman study of hydration states of magnesium sulfates was made by Wang *et al*.,[55] where the differences between the hydrates were clearly described.

Furthermore, in some samples of the efflorescence from the bottom of the altar (indoor conditions), nitre was detected by its dominant symmetric NO stretch (ν_1) at 1050 cm^{-1} and the antisymmetric NO stretch (ν_3), which appears as two bands centred at 1343 and 1359 cm^{-1}, and a band at 715 cm^{-1} (Fig. 4(d)).

Conclusions

In this work, micro-Raman spectroscopy together with X-ray powder diffraction was successfully used to study the occurrence of mineral phases in limestone samples and their weathering products from buildings and monuments. Furthermore, tiny crystals that could not be analysed by other techniques such as X-ray diffraction analysis, because of the impossibility of separation or preparation of such diminutive amounts, were identified.

Salt crystallisation led to several deterioration patterns on the studied historical monuments, both indoors as well as outdoors. Indoors, gypsum occurs as a white crust, subflorescence and part of efflorescence, together with nitre and the soluble salts

Copyright © 2010 John Wiley & Sons, Ltd.

of the $MgSO_4.nH_2O$ series such as pentahydrite and hexahydrite. In samples taken from the fountain outdoors, only gypsum is present occurring as a black crust and subflorescence. Whereas in the outdoor monument the deterioration seems to be mainly related to the air pollution, in the case of indoors it is attributed to the surrounding building materials (mortars) and solutions from the ground. Crust occurs in damper areas, suggesting sufficient water supply in that area of the altar, while outdoors it occurs in sheltered areas. It appears that the deterioration of the stonework is mainly due to the cycles of crystallisation/dissolution of soluble salts. Gypsum crystallisation under the surface results in scaling and crumbling of the limestone, both outdoors and indoors. High damage at the lower part of the altar is associated with rising dampness. Crystallisation of nitre and magnesium sulfate hydrate on the surface of the limestone does not contribute to visible mechanical damage of the limestone.

The results provided by this study are important for suitable conservation/restoration interventions. The results could contribute to better decision making regarding the method to remove or extract soluble salts from the stonework and to consider preventive conservation, for example in the chapel, in order to arrange the source moisture from the ground or to stabilise the internal environmental conditions to avoid RH fluctuations.

Acknowledgements

This research was financially supported by the Slovenian Research Agency contract number 321-05-000545. M. Urosevic is supported by a fellowship from the Spanish Science Ministry (AP2006-036). The authors are also grateful to Jože Drešar for performing the necessary sampling works on the selected monuments. The Institute of Mineralogy and Crystallography, University of Vienna, is gratefully acknowledged for providing experimental support. The authors are greatly indebted to professor Lutz Nasdala for his helpful comments.

Supporting information

Supporting information may be found in the online version of this article.

References

[1] E. A. Charola, *J. Am. Inst. Conserv.* **2000**, *39*, 327.
[2] C. Bläuer-Böhm, A. Küng, K. Zehnder, *CHIMIA Int. J. Chem.* **2001**, *55*, 996.
[3] E. Doehne, *Geol. Soc. Spec. Publ.* **2002**, *205*, 51.
[4] C. Cardell, D. Benavente, J. Rodríguez-Gordillo, *Mater. Charact.* **2008**, *59*, 1371.
[5] M. Urosevic, E. Sebastián-Pardo, C. Cardell, *Constr. Build. Mater.* **2010**, *24*, 1438.
[6] C. Coupry, A. Lautié, M. Revault, J. Dufilho, *J. Raman Spectrosc.* **1994**, *25*, 89.
[7] A. Perardi, L. Appolonia, P. Mirti, *Anal. Chim. Acta* **2003**, *480*, 317.
[8] J. Ambers, *J. Raman Spectrosc.* **2004**, *35*, 768.
[9] N. Civici, O. Demko, R. J. H. Clark, *J. Cult. Herit.* **2006**, *6*, 157.
[10] L. Bellot-Gurlet, S. Pagès-Camagna, C. J. Coupry, *J. Raman Spectrosc.* **2006**, *37*, 962.
[11] A. M. Correia, R. J. H. Clark, M. I. M. Ribeiro, M. L. T. S. Duarte, *J. Raman Spectrosc.* **2007**, *38*, 1390.
[12] A. Bertoluzza, S. Cacciari, G. Cristini, C. Fagnano, A. Tinit, *J. Raman Spectrosc.* **1995**, *26*, 75.
[13] P. Ricciardi, P. Colomban, A. Tournié, V. J. Milande, *J. Raman Spectrosc.* **2009**, *40*, 604.
[14] L. Robinet, C. Coupry, K. Eremin, C. J. Hall, *J. Raman Spectrosc.* **2006**, *37*, 1278.
[15] P. Colomban, G. Sagon, X. Faurel, *J. Raman Spectrosc.* **2001**, *32*, 351.
[16] P. Colomban, F. J. Treppoz, *J. Raman Spectrosc.* **2001**, *32*, 93.
[17] G. D. Smith, J. H. Clark, *J. Archaeol. Sci.* **2004**, *31*, 1137.
[18] C. Cardell, I. Guerra, J. Romero-Pastor, G. Cultrone, A. Rodriguez-Navarro, *Anal. Chem.* **2008**, *81*, 604.
[19] S. S. Potgieter-Vermaak, R. H. M. Godoi, R. Van Grieken, J. H. Potgieter, M. Oujja, M. Castillejo, *Spectrochim. Acta, Part A* **2005**, *61*, 2460.
[20] A. Sarmiento, M. Maguregui, I. Martinez-Arkarazo, M. Angul, K. Castro, M. A. Olazábal, L. A. Fernández, M. D. Rodríguez-Laso, A. M. Mujika, J. Gòmez, J. M. Madariaga, *J. Raman Spectrosc.* **2008**, *39*, 1042.
[21] M. J. Campos-Suñol, A. Domínguez-Vidal, M. J. Ayora-Cañada, M. J. de la Torre-López, *Anal. Bioanal. Chem.* **2008**, *391*, 1039.
[22] M. Ostroumov, *Spectrochim. Acta, Part A* **2009**, *73*, 498.
[23] P. Maravelaki-Kalaitzaki, *Anal. Chim. Acta* **2005**, *532*, 187.
[24] B. Doherty, M. Pamplona, C. Miliani, M. Matteini, A. Sgamellotti, B. Brunetti, *J. Cult. Herit.* **2005**, *8*, 186.
[25] M. F. La Russa, S. Ruffolo, G. Barone, G. Crisci, P. Mazzoleni A. Pezzino. *Int. J. Spectrosc.* **2009**, *2009*, 1.
[26] S. Buser, A. Ramovš, D. Turnšek, *Facies* **1982**, *6*, 15.
[27] A. Ramovš, *Podpeški in Črni ter pisani lesnobrdski apnenec skozi Šas*, Mineral d.o.o, Ljubljana, **2000**.
[28] L. Nasdala, D. C. Smith, R. Kaindl, M. Ziemann, in *Spectroscopic Methods in Mineralogy, EMU Notes in Mineralogy*, vol. 6 (Eds: A. Beran, E. Libowitzky), European Mineralogical Union, University of Vienna: Vienna, Austria, **2004**, pp 281.
[29] Q. Williams, in *Mineral Physics and Crystallography. A Handbook of Physical Constants*. American Geophysical Union: Santa Cruz, CA, **1995**, pp 291.
[30] D. A. McKeown, M. I. Bell, E. S. Etz, *Am. Mineral.* **1999**, *84*, 1041.
[31] E. Loh, *J. Phys. C: Solid State Phys.* **1973**, *6*, 1091.
[32] A. Wang, J. Freeman, K. E. Keubler, *Lunar Planet. Sci.* **2002**, *43*, 1347.
[33] B. Fitzner, K. Heinrichs, in *Proceedings of the International Conference "Stone Weathering and Atmospheric Pollution Network (SWAPNET 2001)"* (Eds: R. Poikřyl, H. A. Viles), Karolinum Press, Charles University: Prague, **2002**, pp 11.
[34] K. Zehnder, A. Arnold, *J. Cryst. Growth* **1989**, *97*, 513.
[35] E. A. Charola, J. Pühringer, M. Steiger, *Environ. Geol.* **2007**, *52*, 339.
[36] V. Vergès-Belmin, *Atmos. Environ.* **1994**, *28*, 295.
[37] C. Giavarini, M. Incitti, M. L. Santarelli, R. Natalini, V. Furoholt, *J. Cult. Herit.* **2008**, *9*, 14.
[38] G. Aberg, D. E. Stijfhoorn, K. Iden, R. Lofvendahl, *Atmos. Environ.* **1999**, *33*, 1399.
[39] K. Malaga-Starzec, I. Panas, O. Lindquist, *Appl. Surf. Sci.* **2004**, *222*, 82.
[40] D. Camuffo, M. Del Monte, C. Sabbioni, *Water Air Soil Pollut.* **1983**, *19*, 351.
[41] A. Arnold, A. Kueng. *7th International Congress on Deterioration and Conservation of Stone*, Presses Polytechniques Romandes: Lausanne, **1985**, pp 255.
[42] S. Z. Lewin, in *Conservation of Historic Stone Buildings and Monuments* (Ed.: S. M. Barkin), National Academy of Science: Washington, DC, **1982**, pp 120.
[43] S. J. Chipera, D. T. Vaniman, *Geochim. Cosmochim. Acta* **2007**, *71*, 241.
[44] H. Juling, D. Kirchner, S. Brüggerhof, K. Linnow, M. Steiger, A. El Jarad, G. Gülker, in *10th International Congress on the Deterioration and Conservation of Stone* (Eds: D. Kwiatkowski, R. Löfvendahl), ICOMOS: Stockholm, **2000**, pp 187.
[45] W. H. Baur, *Acta Cryst.* **1963**, *17*, 1361.
[46] S. Kramar, B. Mirtič, M. Gregerovà, *Geophys. Res. Abstr.* **2007**, *9*, a04712.
[47] A. Goudie, H. Viles, *Salt Weathering Hazards*, John Wiley & Sons: New York, **1997**.
[48] E. Ruiz-Agudo, F. Mees, P. Jacobs, C. Rodriguez-Navarro, *Environ. Geol.* **2007**, *52*, 269.
[49] P. Lopez-Arce, J. Garcia-Guinea, D. Benavente, L. Tormo, E. Doehne, *Const. Build Mater.* **2009**, *23*, 846.
[50] E. N. Caner, S. Demirci, A. G. Türkmenoglu, in *Proceedings of 5th International Congress on Deterioration and Conservation of Stone,* vol. 1 (Ed.: G. Félix), Presses Polytechniques Romandes: Lausanne, **1985**, pp 299.

 Copyright © 2010 John Wiley & Sons, Ltd.

[51] G. G. Amoroso, V. Fassina, *Stone Decay and Conservation, Atmospheric Pollution, Cleaning, Consolidation and Protection*, Elsevier Science Publishers: Amsterdam, **1983**.
[52] I. Kolenc, *St. James Church, Measurements of Temperature and Relative Humidity Fluctuations* (in Slovene), Restoration Centre: Ljubljana, **2006**.
[53] S. Mertes, B. Dippel, A. Schwarzenböck, J. *Aerosol Sci.* **2004**, *35*, 347.
[54] P. Makreski, G. Jovanovski, S. Dimitrovska, *Vib. Spectrosc.* **2005**, *39*, 229.
[55] A. Wang, J. J. Freeman, B. L. Jolliff, I. M. Chou, *Geochim. Cosmochim. Acta* **2006**, *70*, 6118.
[56] F. E. Genceli, M. Lutz, A. L. Spek, G. J. Witkamp, *Cryst. Growth Des.* **2007**, *7*, 2640.

Copyright © 2010 John Wiley & Sons, Ltd.